
Numerical methods for strongly correlated many-body systems with bosonic degrees of freedom

Florian Günter Dorfner



München 2016

Numerical methods for strongly correlated many-body systems with bosonic degrees of freedom

Florian Günter Dorfner

Dissertation
an der Fakultät für Physik
der Ludwig-Maximilians-Universität
München

vorgelegt von
Florian Günter Dorfner
aus München

München, den 14. Dezember 2016

Erstgutachter: Priv.-Doz. Dr. Fabian Heidrich-Meisner

Zweitgutachter: Prof. Dr. Eric Jeckelmann

Datum der mündlichen Prüfung: 23. Februar 2017

Zusammenfassung

Jüngste experimentelle Fortschritte erlauben die Beobachtung von elektronischen Relaxationsprozessen in Festkörpern in Echtzeit. Nach der optischen Anregung eines Systems relaxiert dieses in einen Gleichgewichtszustand. Die Dynamik des Systems während des Relaxationsprozesses ist von den vorherrschenden mikroskopischen Wechselwirkungen zwischen den Konstituenten des Systems abhängig. Die Wechselwirkung zwischen Elektronen und Gitterschwingungen – den Phononen – ist allgegenwärtig in Festkörpern, weshalb sie einer der wichtigsten Relaxationskanäle ist. Eine analytische Beschreibung der Relaxationsdynamik ist schwierig, und nur wenige exakte Lösungen existieren, selbst für die Beschreibung von Gleichgewichtsproblemen. Prinzipiell sind numerische Methoden in der Lage, eine Lösung sowohl für Gleichgewichts- als auch für Nichtgleichgewichtssituationen zu finden. Methoden wie die exakte Diagonalisierung oder die Dichtematrix-Renormierungsgruppenmethode, die mit Wellenfunktionen arbeiten, skalieren jedoch ungünstig mit der Dimension des lokalen Hilbertraumes. Dies ist besonders problematisch bei der Studie von Elektron-Phonon gekoppelten Systemen, bei der im allgemeinen besonders große lokale Basen benötigt werden.

Für Grundzustandsprobleme gibt es zwei unabhängige Vorgehensweisen, um dem entgegenzuwirken: die Ein-Gitterplatz Dichtematrix Renormierungsgruppenmethode, die linear in der lokalen Dimension skaliert, sowie die Implementierung eines Schemas, das die Dimension der lokalen Basis verringert, indem es im Eigenraum der lokalen reduzierten Dichtematrix trunkiert was auf sogenannte optimale Moden führt. In dieser Dissertation kombinieren wir diese Strategien zu einer Methode, die linear in der Dimension der optimierten lokalen Basis anstelle der vollen lokalen Dimension skaliert. Wir demonstrieren das verbesserte Skalierungsverhalten der Methode anhand des Holstein-Polaron und des halb gefüllten Hubbard-Holstein Modells. Zudem beschreiben wir die Implementierung einer optimalen Phononbasis in den Time-Evolving Block Decimation Algorithmus, um das Skalierungsverhalten dieser Methode mit der lokalen Dimension zu verbessern. Für die Simulation des Polaron-Problems auf einer unendlich langen Kette hat sich die Krylovraum Zeitentwicklung in einem limitierten funktionalen Raum, als effizient herausgestellt. Wir adaptieren diese Methode für periodische Randbedingungen und endliche Systemgröße.

Außerdem betrachten wir die Eigenschaften der lokalen reduzierten Dichtematrix als Funktion der Modellparameter und in Nichtgleichgewichtssituationen in drei Modellen: dem Bose-Bose Resonanz-Modell, dem Holstein Modell und dem Hubbard-Holstein Modell. Für fermionische und Spin-Modelle weiß man, dass die lokale von Neumann Entropie ein Indikator für Phasenübergänge ist. Für das Bose-Bose Resonanzmodell finden wir, dass die beiden Größen, lokale von Neumann Entropie und Eigenzustände der lokalen Dichtematrix, besondere Eigenschaften an Phasenübergängen zeigen. Wir finden außerdem, dass die Struktur der optimalen Moden sich als Funktion der Zeit in der Nichtgleichgewichtsdynamik ändert.

Desweiteren beschäftigen wir uns mit der Relaxationsdynamik eines einzigen Elektrons

gekoppelt an Holstein-Phononen. Im adiabatischen Fall finden wir einen Netto-Energiefluss von dem Elektron zu den Phononen und wir leiten einen analytischen Ausdruck für die Relaxationszeit des Elektrons im schwach wechselwirkenden, adiabatischen Fall her. Ein weiteres Hauptthema dieser Dissertation ist die Thermalisierung in geschlossenen Quanten-Vielteilchensystemen. Unser erstes Beispiel ist der Zerfall der Néel Ordnung unter Zeitentwicklung im eindimensionalen Fermi-Hubbard Hamiltonian. Wir finden, dass die Relaxation spin-verwandter Observablen von Spin-Anregungen kontrolliert werden und dass die Doppelbesetzung nicht im Sinne der Eigenzustands-Thermalisierungs-Hypothese thermalisiert, da das System nicht ergodisch ist. Als zweites Beispiel behandeln wir Vielteilchenlokalisierung in einem eindimensionalen System von attraktiv wechselwirkenden Fermionen, das im Grundzustandsphasendiagramm auch mit Unordnung eine delokalisierte Phase zeigt. Wir untersuchen diesen Phasenübergang mit modernen Hilfsmitteln, die auf den Verschränkungseigenschaften und der Existenz von Quasiteilchen in lokalisierten Phasen beruhen.

Abstract

Recent experimental advances allow the observation of electronic relaxation processes in solid-state systems in real time. After an initial excitation with an optical pulse, the relaxation depends on the microscopic interactions present in the system. The interaction of electrons with lattice degrees of freedom – the phonons – is ubiquitous in solids and, thus, it represents one of the most important relaxation channels. An analytic description of relaxation dynamics is hard to come by and very few exact solutions exist even for the equilibrium situation. Numerical methods are, in principle, able to solve the problem in both, equilibrium and out-of-equilibrium situations. However, wavefunction-based methods like exact diagonalization or the density matrix renormalization group method scale unfavorably in the number of local basis states. For electron-phonon coupled systems, the situation is especially severe because the local basis dimension can get very large depending on model parameters or in far-from-equilibrium situations.

For groundstate problems, two independent strategies exist for density matrix renormalization group methods: the strictly single-site density matrix renormalization group method that scales linearly in the local dimension and the use of a local basis optimization scheme which truncates the local basis to a subset of the eigenstates of the local reduced density matrix with the largest eigenvalues – the optimal mode basis. In this thesis, we combine these two strategies in an improved algorithm which reduces the scaling from linear in the local dimension of the phonon occupation number basis to linear in the dimension of a smaller optimal mode basis. We demonstrate the improved scaling of this method on the example of the Holstein polaron and the half-filled Hubbard-Holstein model. We further describe an algorithm that combines the time-evolving block decimation method with a local basis optimization to lower the scaling with the local dimension also during time evolution. For the polaron problem on an infinite chain Krylov-space time evolution in a limited functional space has been shown to be very efficient. We adapt this algorithm to periodic boundary conditions and show that it is the most efficient method compared to standard Krylov space time evolution and the time-evolving block decimation method.

We also study the properties of the local reduced density matrix as a function of model parameters and under non-equilibrium conditions in three different models: the Bose-Bose resonance model, the Holstein model and the Hubbard-Holstein model. It was shown for fermionic and spin models that the single-site von Neumann entropy is an indicator for phase transitions. In the Bose-Bose resonance model we find that both, the local von Neumann entropy and the eigenstates of the local reduced density matrix show features in the vicinity of a phase boundary. Also, we find that the eigenstates of the local reduced density matrix depend on time in quantum quench dynamics.

Further, we study the relaxation dynamics of a single electron coupled to Holstein phonons in all parameter regimes. In the adiabatic case a net energy transfer from electron to phonons

happens and we provide an analytic formula for the relaxation time in the weak-coupling adiabatic regime. Another main topic in this thesis is thermalization in closed quantum many-body systems. Our first example is the temporal decay of Néel order in the one-dimensional Fermi-Hubbard model. We find evidence that the relaxation dynamics of spin-related quantities are, in the long-time regime, controlled by spin excitations. Further, we study the thermalization of the double occupancy in the framework of the eigenstate thermalization hypothesis and find that it does not thermalize due to integrability of the model. As a second example, we consider many-body localization in a one-dimensional system of spinless fermions with attractive interactions. It is known for the ground-state phase diagram of this model that a delocalized phase survives for moderate disorder strength in the attractive regime. We use modern tools to analyze this transition exploiting the entanglement properties and the existence of quasi-particles in localized phases.

List of Publications

Various parts of this thesis are published as follows. The method described in Sec. 1.4.2 is published in:

- C. Brockt, F. Dorfner, L. Vidmar, F. Heidrich-Meisner, and E. Jeckelmann, *Matrix-product-state method with a dynamical local basis optimization for bosonic systems out of equilibrium*, Phys. Rev. B **92**, 241106(R) (2015).

The project described in Chapter 3 is published in the paper:

- F. Dorfner, L. Vidmar, C. Brockt, E. Jeckelmann and F. Heidrich-Meisner, *Real-time decay of a highly excited charge carrier in the one-dimensional Holstein model*, Phys. Rev. B **91**, 104302 (2015).

Chapter 4 is published in:

- F. Dorfner and F. Heidrich-Meisner, *Properties of the single-site reduced density matrix in the Bose-Bose resonance model in the ground state and in quantum quenches*, Phys. Rev. A **93**, 063624 (2016).

Chapter 5 is published in the paper:

- A. Bauer, F. Dorfner, and F. Heidrich-Meisner, *Temporal decay of Néel order in the one-dimensional Fermi-Hubbard model*, Phys. Rev. A **91**, 053628 (2015).

Contents

Introduction	1
1 Numerical methods	7
1.1 Exact diagonalization methods	10
1.1.1 Basics of exact diagonalization	10
1.1.2 Krylov-space time-evolution	13
1.1.3 Exact diagonalization in a limited functional space	14
1.2 Density matrix renormalization group algorithm with local subspace expansion	15
1.2.1 Density matrix renormalization group	16
1.2.2 DMRG with subspace expansion	29
1.3 Local optimal mode states in DMRG with subspace expansion	34
1.3.1 The OBB-VMPS optimization procedure	35
1.3.2 DMRG3S-LBO bond update	40
1.4 Time-evolving block decimation with dynamic local basis optimization	42
1.4.1 Time-evolving block decimation	42
1.4.2 Local basis optimization in TEBD	45
2 Optimal modes in the one-dimensional Hubbard-Holstein model	49
2.1 Implementation of the Hubbard-Holstein model	50
2.2 One electron	52
2.2.1 Weight spectrum	52
2.2.2 Tests of the DMRG3S-LBO method	52
2.3 Half filling	55
2.3.1 Weight spectrum	55
2.3.2 Tests of the DMRG3S-LBO method	56
2.4 Conclusion	60
3 Real-time decay of a highly excited charge carrier in the one-dimensional Holstein model	63
3.1 The one-dimensional Holstein model	67
3.2 Ground-state properties	69
3.3 Comparison of methods	72
3.4 Perturbative results	73
3.4.1 Small-time expansion	74
3.4.2 Perturbation theory in the interaction picture	75
3.5 Numerical results	88

3.5.1	Crossover from adiabatic to anti-adiabatic regime	88
3.5.2	Crossover from weak to strong coupling in the adiabatic regime	89
3.5.3	Crossover from weak to strong coupling in the anti-adiabatic regime	93
3.6	Optimal phonon modes and local entanglement entropy	94
3.6.1	Optimal phonon modes and von Neumann entropy	95
3.6.2	Results	96
3.7	Summary	99
4	The single-site reduced density matrix in the Bose-Bose resonance model	101
4.1	The Bose-Bose resonance model	104
4.1.1	Numerical setup	105
4.1.2	Optimal modes	105
4.2	Ground-state properties	106
4.2.1	Molecular density and single-site von Neumann entropy	106
4.2.2	Properties of the local reduced density matrix	112
4.3	Non-Equilibrium properties	119
4.3.1	Molecular density and local von Neumann entropy	119
4.3.2	Post-quench eigenstate expectation values	121
4.3.3	Structure of optimal modes	124
4.4	Summary	126
5	Temporal decay of Néel order in the one-dimensional Fermi-Hubbard model	129
5.1	Time evolution and characteristic time scales	131
5.2	Time-averages of double occupancy	132
5.3	Connection to eigenstate thermalization hypothesis	133
5.4	Summary	136
6	Many-body localization in a one-dimensional system of spinless Fermions with attractive interactions	137
6.1	Implementation	141
6.2	Groundstate phase diagram	141
6.3	Summary and Outlook	146
	Conclusion	147
A	Tensor library	151
A.1	A blocky tensor class	151
A.1.1	The reshape operation	152
A.1.2	Tensor operations	153
A.2	The DMRG algorithm	154
	Bibliography	157
	Acknowledgements	175

Introduction

Non-interacting electrons in a periodic lattice occupy Bloch states [1]. Phonons – quantized vibrations of the lattice – are present in every solid and the coupling between electrons and phonons is at the heart of many exciting phenomena including the Peierls instability [2], conventional superconductivity [3,4], polaron formation [5,6] and relaxation in non-equilibrium dynamics [7,8]. The precise contribution of electron-phonon coupling to the very actively studied topic of high-temperature superconductivity is still under investigation [9].

Recently, ultrafast spectroscopy experiments have emerged which are able to resolve timescales of the order of a few femtoseconds [10]. This temporal resolution is comparable to the time-scales at which microscopic relaxation processes happen in solid-state systems which can thus be observed in real-time. Also, using strong laser pulses the sample can be brought far from equilibrium into a state that is not reachable by adiabatic evolution and thus allows to control a sample in a profound way [10,11]. For example, a strong perturbation of the sample can induce a phase transition and can enhance superconductivity or destroy it [12–14]. These experiments brought renewed interest into the study of electron-phonon physics because they enable scientists to directly study the relaxation dynamics of an excited electronic state back to equilibrium. For example, the femtosecond dynamics of polaron formation – a deformation of the lattice that is created by an electron moving through the system which gets localized by the potential it created itself – [15,16] was observed. Also, in the research of copper-oxide compounds (cuprates) which exhibit high-temperature superconductivity one still searches for the microscopic mechanism that is responsible for the attractive interaction between two electrons bound in a Cooper pair [11]. Two prominent candidates are bosonic excitations originating in electron-electron interactions, namely antiferromagnetic spin excitations, or electron-phonon interactions. Because in cuprates excitations due to those interactions live on comparable energy-scales [17], experiments probing equilibrium properties can not disentangle the two and non-equilibrium experiments are employed because relaxation due to different interactions happens on different time-scales [9].

A theoretical interpretation for the dynamics measured in experiments is desirable and would give insight into the fundamental processes happening in those systems. Real solids are very complicated and simplified models like the Holstein model [6] and the Hubbard-Holstein model [6,18] are used that are believed to capture relevant low-energy properties of strongly correlated electron-phonon systems. Analytical studies of those models in non-equilibrium are very difficult and reliable results are scarce even for equilibrium properties [19–21]. For example, analytical work on the equilibrium Holstein polaron (a single electron interacting with phonons) using perturbation theory provides reasonable results only for weakly- and strongly-coupled phonons but not in the physically most interesting crossover regime [19] where the characteristic electronic and phononic energy scales are not well separated.

Here, numerical methods enter the game. These are in principle able to fill in the gaps

both in equilibrium and non-equilibrium situations. For groundstate problems in one dimension these include exact diagonalization (ED) [22,23], and the density-matrix renormalization group (DMRG) method [24–27]. Numerical methods for the study of non-equilibrium dynamics include Krylov-space time evolution [28,29], the continuous-time quantum Monte-Carlo method [30,31], the time-evolving block decimation (TEBD) method [32,33] and the time-dependent density matrix renormalization group [34,35] method.

The Holstein model and the Hubbard-Holstein model, as examples of models with bosonic degrees of freedom – the phonons – do not conserve the number of phonons and, especially for stronger couplings between electrons and phonons, a large number of fluctuations in the number of bosons need to be taken into account [25]. Wavefunction-based methods such as ED, the DMRG method and the TEBD method need to set up a basis for the system of interest. As we will argue below, those methods scale unfavorably in the local Hilbert-space dimension which complicates numerical studies.

The main topic of this thesis is the improvement of wavefunction-based numerical methods for the efficient simulation of many-body systems with bosonic degrees of freedom in one dimension. For the calculation of groundstate properties we focus on the DMRG method. This algorithm scales with the third power of the local dimension $\mathcal{O}(d^3)$ where d is the local dimension which limits the number of states that can be kept in the local basis quite severely. Several improvements have been invented to deal with large local dimensions. The first one is the so-called pseudosite algorithm for electron-phonon problems [25] which maps a site containing $d = 2^N$ local boson states to N so-called pseudo-sites with a local dimension of $d = 2$. The trick of this mapping lies in the fact that DMRG scales roughly linear in the system size L and an increase of system size by a factor $\log_2(N)$ is thus cheap. A drawback of this method is that operators, even when local, now act on several pseudo sites and thought needs to be put into setting them up explicitly. Another improvement is the use of so-called optimal modes (OM) [36] which are a subset of the eigenstates $|\alpha\rangle$ of the local (one-site) reduced density matrix (RDM) instead of the phonon occupation number states

$$\rho^{(1)} = \text{tr}_{L-1}(|\psi\rangle\langle\psi|) = \sum_{\alpha} w_{\alpha} |\alpha\rangle\langle\alpha|, \quad (1)$$

where tr_{L-1} means a trace over all sites but one, $|\alpha\rangle$ are eigenstates of the local RDM and w_{α} are their weights. One can show that truncation by keeping the d_{O} highest weighted eigenstates of the RDM is optimal for a given global state [24]. While the mapping onto pseudo-sites is exact (up to a global cut-off in the phonon number) the optimal-mode basis is an approximation to the exact state and the number of states one needs to keep depends on how fast the weights w_{α} decay with the index α . While the original paper [36] introduced this local truncation scheme into a variant of ED to demonstrate it conceptually, it was first successfully incorporated into the DMRG method by Guo et al. [37] for the spin-boson model.

Independently, Hubig et al. [38] found a way of reducing the scaling of the DMRG algorithm itself to $\mathcal{O}(d)$ for strongly entangled states and to $\mathcal{O}(d^2)$ for weakly entangled states. The worse scaling of the standard DMRG algorithm of $\mathcal{O}(d^3)$ stems from the fact that it updates two sites simultaneously and can be pushed down to linear scaling using a scheme that updates a single site only at every iteration [38,39].

For the time-evolution of a quantum state we focus on Krylov-space time evolution [40] and the time-evolving block decimation method [32,33]. Krylov-space time evolution is a standard tool for the efficient simulation of dynamics in the ED framework. The time-evolving block decimation method scales with the third power of the local dimension $\mathcal{O}(d^3)$ just like standard

two-site DMRG. The local basis optimization [37] is, in principle, also possible during time-evolution, however, the question is how efficient this truncation can be as a function of time.

In this context we study the properties of the local reduced density matrix. Specifically, this thesis addresses the following questions: (i) Can we understand the structure of local OM states? (ii) How do the OM states and their weights behave in different phases and what happens in the vicinity of a phase transition? (iii) Can one distinguish phases or crossover regimes analyzing the OM? (iv) What can one learn about a state just knowing the OMs on a site? (v) How do the OM states and their weights respond to the time-evolution after a quench? (vi) Can we set up an efficient DMRG algorithm for electron-phonon problems in the groundstate and out-of-equilibrium using OMs?

References [36,41] show that the OM basis provides information about the physical state of a system on the example of the Holstein polaron. We continue along those lines and study the exact structure of the OM basis states in the Bose-Bose resonance model – a model describing two bosonic particle species interacting via a Feshbach interaction [42,43]. For our choice of parameters, this model features a rich phase diagram including a Mott insulating phase, a molecular quasi-condensate phase and a phase where atoms and molecules quasi condense [43,44]. For the three limiting cases deep inside those phases we approximate the local reduced density matrix using perturbation theory and the exact expression for a Bose-Hubbard model without interaction and thereby get an estimate for the optimal mode states and their weights which perfectly matches the numerically exact data obtained using the DMRG method. We find that the optimal mode states are different deep in the three phases of this specific model and we therefore conclude that they can be used to distinguish between states deep in the respective phases. Also, we use the DMRG method to calculate the weight spectrum and, derived from the weight spectrum, the local von Neumann entropy as well as the OMs as we cross two phase boundaries. This complements earlier works [45,46] where the local von Neumann entropy was used to detect phase transitions in spin- and fermionic models. Reference [46] showed that the local von Neumann entropy works as an indicator of phase transitions in some but not all cases and that the von Neumann entropy calculated from two sites is a better indicator. In this thesis we follow up with the study of the local reduced density matrix of a single site. Because we treat a model with bosonic degrees of freedom, the reduced density matrix has a much richer structure. We find that, for our model, the local von Neumann entropy (and thus the weight spectrum) as well as the OM states show features in the vicinity of the phase boundaries.

Also, we calculate the local von Neumann entropy as a function of the electron-phonon coupling strength of the Holstein polaron and find that it displays a maximum in the crossover regime between two distinct states in this model: the large and the small polaron states.

Performing time-evolution numerically is a costly operation. Methods based on ED need to set up the full accessible Hilbert space which scales unfavorably in the local dimension just as in the ground state problems. Matrix product state based methods like time-dependent DMRG [27,34,35] and TEBD suffer from time-dependent increase of entanglement in the system of interest [27] which inevitably increases the computational demand as time progresses. Also, those methods scale unfavorably with the size of the local Hilbert space and the use of an optimal mode basis to decrease the number of local degrees of freedom is thus very desirable. We thus study the behavior of the optimal mode basis and the weight spectra as a function of time after quenches for the Holstein polaron and in the Bose-Bose resonance model. We find for both models and all studied quenches that the time-dependence of local observables is encoded in the time-dependence of the eigenstates of the RDM. We conclude

from here that for a successful implementation of an optimal mode basis in a time-evolution algorithm like TEBD it is necessary to adapt the optimal modes as time progresses.

As explained above, two interesting improvements have been made recently: the single-site DMRG with subspace expansion (DMRG3S) [38] and the incorporation of optimal modes into the DMRG algorithm [37] which we term local basis optimization (LBO) [47]. In this thesis we combine these ingredients to create a new ground-state algorithm that scales linear in the optimized local basis dimension d_O for strongly entangled ground states instead of linear in the full local basis dimension d $\mathcal{O}(d_O) < \mathcal{O}(d)$. We test the method on the example of the Hubbard-Holstein model and for the Holstein polaron and find that it is an improvement compared to the bare DMRG3S method, first, because it is faster and, second, because it also reaches a higher precision using the same computational resources. We also adopt the diagonalization in a limited functional space (LFS) method [22,28], which was originally formulated for the treatment of infinitely large systems, and adapt it to work with periodic boundary conditions. Additionally, we discuss the so-called TEBD-LBO method which supplements the standard TEBD method with an additional LBO step in every time step to reduce the overall scaling [47] and is a first implementation of OM in a time-dependent DMRG method (see also Schröder et al. [48]). For this project, we carried out initial ED calculations in a bare and in an OM basis, while the implementation of the TEBD-LBO was done by C. Brockt [47].

For performing efficient ED calculations we wrote a library that automates the setup of bosonic and fermionic basis sets using an arbitrary number of commuting discrete symmetries. For DMRG calculations we wrote a full tensor library which includes dense tensor and blocky tensor classes necessary to exploit $U(1)$ symmetries in MPS calculations. In detail, the two-site DMRG, the strictly single-site DMRG, the single-site DMRG with local basis optimization and, recently, a time-evolving block decimation algorithm have been implemented using this library.

As noted above, the observation of polaron formation was reported by several pump-probe experiments [15,16]. Those triggered several theoretical studies [49,50] that revealed a complex interplay between a single electron and phonons under non-equilibrium conditions. The precise role of electron-phonon interactions in strongly correlated materials is an open problem [9]. In this thesis, we study the real-time relaxation of a single electron in the Holstein model and pose the following questions: (i) Which is the most efficient method for the study of non-equilibrium properties of the polaron problem? (ii) How efficient is the energy transfer from an electron to phonons? (iii) What is the time-scale for the relaxation of the kinetic energy? (iv) When is a semi-classical treatment of the problem justified?

A variety of methods have been used in the study of electron-phonon problems and we compare three of them – ED, diagonalization in a limited functional space [22] and the TEBD method [33] – in order to find out which one is superior for this specific problem. We find that diagonalization in a limited functional space is the best suited for this problem. As noted above, the interaction between the electron and phonons is quite complex and we perform an exhaustive study of the post-quench dynamics of three observables – the electronic kinetic energy, the phonon energy and the coupling energy – in all coupling regimes of the model. We find that the energy transfer is the most efficient in the weak-coupling adiabatic regime of the model where the electronic relaxation can be described by a Boltzmann approach. Using this, we analytically extract a relaxation time and discuss its dependence on the model parameters. Also, we show that the energy transfer is inefficient in the anti-adiabatic regime, where the phonon energy is larger than the bandwidth, a single phonon excitation costs too

much energy and almost no energy is transferred. In the strong-coupling adiabatic regime we find coherent oscillations and a corresponding energy transfer from electron to phonons and back. The success of the Boltzmann approach in predicting the numerical data shows that in the weak-coupling adiabatic case a semi-classical treatment is justified because phonons are treated like a bath. This project also complements earlier works [29, 49, 51].

In this thesis, we also consider the thermalization and relaxation in closed quantum many-body systems. Experiments with ultracold atoms allow the observation of quantum dynamics over long time intervals and enable the study of strongly correlated states from a new perspective [52, 53]. A simple initial state that is not an eigenstate of the system Hamiltonian can be prepared and the ensuing microscopic dynamics can then be investigated directly. This technique has been used in the study of non-equilibrium dynamics in Hubbard- and Heisenberg-type models [54–58]. The specific problem of the decay of Néel order has so far been addressed in the non-interacting case in one dimension [59] and for a two-dimensional system [60]. Also, the decay of a spin spiral has been studied in one and two dimensions [61].

We study the real-time decay of the Néel state in the one-dimensional Fermi-Hubbard model [62] (see also [63]). By that we extend previous studies [64] by the incorporation of charge dynamics additional to the spin dynamics present in the spin-1/2 XXZ-model. As a main result, we show that the relevant time scales for the relaxation of the double occupancy – a charge-related quantity – is set by the inverse of the hopping matrix element while for the staggered magnetization – a spin-related quantity – the dynamics is slower as the on-site repulsion U increases. This reflects the existence of two characteristic velocities in the low-energy, equilibrium physics of strongly interacting one-dimensional (1D) systems: spin and charge velocity related to spin-charge separation [65]. Also, we investigate if the steady-state value of the double occupancy is thermal in the framework of the eigenstate thermalization hypothesis (ETH) [66] for different choices of the on-site interaction U . The ETH gives an interpretation to the thermalization of a subsystem in closed quantum systems along with a few requirements on the Hamiltonian describing the system. One important requirement is ergodicity: the ability of the system to reach all states in the many-body Hilbert space of the system which have the same energy as the initial state in a finite time. We find that the steady-state value is close to the thermal one but different. This is not surprising since our system is integrable and thus not ergodic which is in line with Ref. [66]. We conclude from this that the double occupancy does not thermalize in our system.

The last topic we address in this thesis has recently received a lot of attention: many-body localization [67–70]. A one-dimensional system of non-interacting fermions in a disordered potential Anderson-localizes [71]. This means that all single-particle eigenstates of the Hamiltonian describing the system extend only over a finite length scale, the localization length. Because of that, the system is a perfect insulator and thermalization under the usual Gibbs ensemble does not happen. Many-body localization is an effect with similar properties in many-body eigenstates with finite energy density in a system where particles interact. The smallest disorder potential in a one-dimensional system of non-interacting particles leads to Anderson localization in all single-particle eigenstates. Most results suggest the existence of a many-body mobility edge, i.e. a transition from a localized phase into a delocalized phase as energy density increases at fixed disorder and interaction strength. This result, however, is still under intense debate [72]. An important difference between generic (i.e., thermalizing) and localized phases is the scaling of the entanglement entropy with the size of a subsystem.

In a generic many-body eigenstate it scales with the volume of the subsystem while for a localized state it scales with the size of the area that connects the subsystem with the rest of the system [68].

In this thesis we study the ground state of a system of attractively interacting fermions in a disordered potential. This problem was considered previously [73, 74] where the authors found a delocalized phase (a phase where electrons are delocalized over the whole length of the system) for a small region in the disorder-interaction plane [74]. We study the behavior of the difference in the eigenspectrum of the one-particle density matrix evaluated in many-body eigenstates [75] as well as the half-cut von Neumann entropy over the region where the delocalized phase exists. The reason for the existence of this delocalized regime is the competition of the three constituents of the model: the kinetic energy, the nearest-neighbor attraction between two electrons and the disorder potential. Phenomenologically, for small attractive interaction strength the disorder potential leads to localization. For intermediate attractive interaction, electrons can form pairs which enables them to quasi-condense in a delocalized state taking advantage of disorder induced density fluctuations and at strong attractive interaction electrons tend to form a domain-wall state pinned by the disorder potential [65]. We find that those two quantities, for weak disorder strengths, only indicate one phase boundary for our observed system sizes. For strong disorder we find the expected behavior of a purely localized phase over the full range of interaction strengths. The greater goal of this project is the investigation of the phase diagram at finite energy densities which is left for future work.

The structure of the thesis is as follows. Chapter 1 introduces all numerical methods used throughout the thesis. More specifically, the ED, the limited functional space basis setup, Krylov-space time evolution, single-site DMRG with local basis optimization and TEBD with local basis optimization methods are described in detail. Chapter 2 illustrates our tests of the single-site density matrix renormalization group method with local basis optimization (DMRG3S-LBO) on the example of the Holstein model with a single electron and the half-filled Hubbard-Holstein model. Chapter 3 illustrates the relaxation dynamics of a single electron coupling to Holstein phonons. Chapter 4 contains the study of the properties of the single-site reduced density matrix in a coupled system of bosons and composite molecules: the Bose-Bose resonance model. In Chapter 5 we study the problem of the temporal decay of Néel order in the Fermi-Hubbard model. The final Chapter 6 summarizes our current status in the investigation of the groundstate of a system consisting of attractively interacting fermions in a disordered potential. We conclude with a summary and an outlook.

Chapter 1

Numerical methods

The focus of this thesis is on the numerical computation of ground-state and dynamical properties of one-dimensional models with bosonic degrees of freedom. The one-dimensional Bose-Hubbard model is a canonical example. Because multiple bosons can reside on the same site one needs a local basis dimension equal to the number of bosons in the full system to treat this model exactly. Working with such models numerically using wave-function based methods has been a challenge ever since because of the huge local Hilbert space. The usual way out is a cutoff in the local Hilbert space [76] which, most of the time, is a good approximation when one is interested in ground states only. However, there are problems that necessitate a large number of local degrees of freedom where a small cutoff is just not physical.

We divide the classes of problems that we treat in this thesis into two main topics: (i) Systems in equilibrium and (ii) non-equilibrium dynamics. With equilibrium systems we mean either the computation of the ground state or the whole eigenspectrum of the Hamiltonian under study while non-equilibrium dynamics means time-evolution of a given initial state under some Hamiltonian.

Various numerical methods exist for the computation of ground states. The exact diagonalization method (ED) [40, 77] is the most straightforward and oldest one which solves the problem by setting up the Hamiltonian matrix explicitly. A widely used algorithm for the computation of ground states from large sparse matrices is the so-called Lanczos algorithm that approximates the Hamiltonian by a (comparatively) small matrix which captures the ground state to high precision [78]. Because one needs to set up the Hamiltonian in an explicit basis this method scales exponential with the length L of the system $N_{\text{st}} \propto \mathcal{O}(d^L)$ where N_{st} is the total number of states and d is the local dimension (for example, $d = 2$ for a spin-1/2 system where a site is either in an up- or down-spin state). Doubling the amount of local states is equivalent to multiplying the number of states N_{st} by a factor 2^L , exponential in L . Typically, this restricts the use of exact diagonalization to small systems of sizes $L \sim \mathcal{O}(10)$.

The density matrix renormalization group algorithm (DMRG) [24, 26, 27, 79] is a method designed to approximate lowly entangled ground states to high accuracy using a finite number of parameters for its description. The fact that the theoretical space of possible states scales exponentially with system size does not mean that the state of interest (a ground state) also exhausts this space. The entanglement entropy S is a measure for the amount of information that one part of the system has about another one or, in other words, how many states one needs in both subsystems to encode the information of the global state. The entanglement entropy in ground states of Hamiltonians with an excitation gap and short-range interactions

is known to obey a so-called *area law* [80,81] which states that the entanglement scales not with the volume L^D of the system but with its surface L^{D-1}

$$S \propto L^{D-1}. \quad (1.1)$$

In other words, the ground state of a system in a gapped phase can be described by a state space that is vanishingly small compared to the full Hilbert space. DMRG exploits this fact and finds the desired state in a set of basis states that optimally parameterize this small corner of the Hilbert space. For one-dimensional systems the algorithm scales roughly linearly in the system size with at most logarithmic corrections [82,83] and allows ground-state computations for system sizes up to $L \sim \mathcal{O}(10^3)$ for systems with a small local dimension. It achieves that by splitting the system into two parts - system and environment block - and optimizes the system block locally in an iterative fashion which constantly lowers the global energy while sweeping through the system. The standard algorithm is called two-site DMRG [24] which performs the local optimization by taking into account two sites of the system at a time. This algorithm has a complexity of $\mathcal{O}(d^3)$ with the local dimension d [27]. While much faster than the scaling of ED in d , this method is still limited in the number of local states that can be kept. The scaling to the third order stems from the optimization of two adjacent sites at the same time. It is easy (and in the so-called matrix product state language [84–86] even more natural) to write down a DMRG algorithm that optimizes by taking into account a single site at a time only (single-site DMRG [27]). However, DMRG relies on the fact that the optimizer has access to an enlarged state space which is only the case when optimizing at least on two sites. In 2005 White [39] introduced a procedure to enrich the state space with a set of states necessary for convergence of the method while sweeping through the system and was thereby able to improve convergence of both single- and two-site algorithms. Because the density matrix for the bond needs to be computed on every site this procedure again scales with $\mathcal{O}(d^3)$ even when using a single-site scheme. Very recently, Hubig et al. [38] came up with an algorithm that directly enriches the local state space without the detour over the density matrix. As we show below, this algorithm scales quadratically in the local dimension ($\mathcal{O}(d^2)$) for weakly entangled systems and linearly ($\mathcal{O}(d)$) for strongly entangled ones.

Zhang et al. [36,41] introduced a new idea to cope with systems that feature a large local dimension: the so-called optimal mode states. Those states are defined as a subset of the eigenstates of the local reduced density matrix

$$\rho^{(1)} = \text{tr}_{L-1}(|\psi\rangle\langle\psi|) = \sum_{\alpha} w_{\alpha} |\alpha\rangle\langle\alpha|, \quad (1.2)$$

where $|\alpha\rangle$ denote the eigenstates of the local reduced density matrix and w_{α} are their weights. Very similar to DMRG, their idea was to find a more efficient basis for a given subsystem, however, the subsystem is now a single site including the local degrees of freedom only. Analogous to the arguments leading to the truncation scheme in DMRG the eigenstates of the local reduced density matrix emerge as the natural basis to truncate in. Depending on the state to be described very few such optimal mode states are sufficient to describe it to high accuracy. The authors showed on the example of the one-dimensional Holstein model that making use of those states can lead to a significant reduction of the algorithmic effort for ground-state problems [36]. The natural basis for phonons is the occupation number basis or "bare" basis as we call it from here on. The authors found for the ground state of that model that keeping two optimal mode states yields the ground state energy to a precision that can

be found only when setting the system up in a bare phonon basis that keeps $\mathcal{O}(10)$ states which means a large reduction in the local basis dimension.

Guo et al. incorporated those optimal-mode states into the DMRG algorithm [37, 87]. They supplement the usual DMRG local update procedure by an additional step that updates the local degrees of freedom before the usual update of the bond degrees of freedom. They test the method on the example of the spin-boson model.

We introduce the density matrix renormalization group algorithm with local subspace expansion [38] as well as the local basis optimization procedure [37] in detail. Combining the two procedures we derive an algorithm that, depending on the studied model, scales better than linear in the local dimension – the DMRG3S-LBO algorithm. This algorithm theoretically achieves a speedup of $\mathcal{O}(d/d_{\text{O}})$ where d_{O} labels the number of optimal mode states used in the calculations. A test of the method is presented in Chapter 2.

In this chapter we also study methods for performing efficient time-evolution. Performing time-evolution of quantum states numerically is a hard problem both for methods based on exact diagonalization (Krylov-space time-evolution [88]) [23, 89–92] and DMRG (t-DMRG [27, 34, 35], tMPS [27], time-evolving block decimation (TEBD) [32–34]). ED-based methods are limited to small system sizes for large local dimensions because they suffer from the same scaling as the ground-state algorithm - exponential in the system’s size. Approximative methods like the time-evolving block decimation suffer from a time-dependent increase of entanglement [27] in a system. As mentioned above, the entanglement entropy in many ground states obeys an area law and is thus very low for one-dimensional systems. This does not hold during the time-evolution where the entanglement entropy can grow linearly with time (Lieb-Robinson bound [55, 93–95]).

For problems with a single charge carrier like the polaron problem [77, 96] an ED scheme exists which sets up an efficient basis set [23] in which the system Hamiltonian can then be diagonalized. Originally, it was introduced for the case of infinitely large systems. We adapt the scheme for systems with finite size and periodic boundary conditions [96] and show that it works well for time-evolution of a single electron interacting with phonons in a box of size L with periodic boundary conditions in Chapter 3.

Due to the volume-law scaling, MPS-based methods are usually restricted to small times depending on the number of states that can be kept during time-evolution. The TEBD method [32, 33] evolves the wavefunction over a time t by $t/\Delta t$ applications of an approximated time propagator that evolves the state over a time step Δt . The time propagator is approximated using the Trotter decomposition which gives an error that is proportional to a power of the time step that depends on the order o of the Trotter decomposition $\mathcal{O}((\Delta t)^{o+1})$ [33]. The resulting wavefunction, which has an increased dimension due to the application of the time propagator, is then truncated to a fixed precision by choosing the most important states from the reduced density matrix at the current cut through the system. The truncation finds the best approximation to the enlarged, time-evolved state and, thereby, adapts the state space as time progresses. This algorithm has two problems: First, the spreading of entanglement may still restrict the time-evolution to small times and second, the algorithm scales with the third power in the local dimension.

Brockt et al. [47] showed that, using an optimal mode basis that is adapted as time progresses, the computational effort for the time-evolution can in principle be reduced to $\mathcal{O}(m^3 d_{\text{O}}^3) + \mathcal{O}(m^2 d^3)$ where m denotes the number of states used during truncation which is directly linked to the entanglement in a state as we argue below. By combining the truncation in the optimal-mode basis with the TEBD algorithm it is possible to arrive at an algorithm

that still scales cubic with the local dimension d^3 but has a much smaller prefactor m^2 which makes a huge difference for strongly correlated systems [47].

The chapter is organized as follows. We start with a description of the exact-diagonalization methods used throughout this thesis for performing ground-state calculations as well as time-evolution in Sec. 1.1. We then introduce the DMRG method that is used here: the single-site DMRG with subspace expansion in Sec. 1.2. After that we derive how to include optimal modes into the DMRG with subspace expansion in Sec. 1.3.

1.1 Exact diagonalization methods

The phrase *exact diagonalization* is a broader term and generally refers to methods which construct the basis of a given system explicitly. While the actual form of this basis and also the goal can vary between methods the general scheme is to set up the Hamiltonian of the system under study explicitly and carry out calculations directly using this object.

In the context of equilibrium physics it is used to find exact eigenstates and compute observables in them. One distinguishes between two schemes which differ only in the eigenstates they target: Full diagonalization targets the whole spectrum of the system while ground-state ED targets the ground state of the system as the name implies. Equilibrium ED algorithms can be divided into three steps: (i) Setup of the basis, (ii) setup of the Hamiltonian matrix in that basis and (iii) calculation of eigenstates using the Hamiltonian matrix. The difference between full- and ground state ED algorithms is in the way the eigenproblem is solved. Full diagonalization uses a solver that is capable of diagonalizing the full matrix which mostly scales with the third power in the basis dimension $\mathcal{O}(N_{\text{st}}^3)$. A standard solver for groundstate ED is the Lanczos algorithm which approximates the full matrix and, thereby, finds an approximation to its ground state. For a sparse Hamiltonian this procedure scales linearly in the number of basis states $\mathcal{O}(N_{\text{st}})$.

For non-equilibrium problems the time-evolution of some initial state has to be computed

$$|\psi(t_0 + \Delta t)\rangle = e^{-iH\Delta t}|\psi(t_0)\rangle. \quad (1.3)$$

The fundamental problem involved with this operation is the need of constructing the exponential of an operator. For very small systems this operator can be constructed exactly. For larger systems, schemes exist that construct the operator in an approximate fashion which include the Lanczos algorithm [78] and the Jacobi-Davidson algorithm [97]. In this thesis we use the Lanczos algorithm.

At the heart of the applicability of all the ED methods - equilibrium and dynamical - lies the dimension of the basis N_{st} . Most Hamiltonians have symmetries which blockdiagonalize its matrix representation [40]. These symmetries can be used in numerics to reduce the dimension by restricting the numerically expensive operations to individual blocks instead of performing them on the whole matrix. Another idea is to explicitly exclude certain basis states. However, this procedure heavily depends on the choice of basis representation and also on the system under study.

1.1.1 Basics of exact diagonalization

A good manual of how to get ED up and running is given in Ref. [76]. Here, we summarize the essential parts.

During the setup of the Hamiltonian non-zero matrix elements are found by application of the Hamiltonian to each of the basis states in the Hilbert space

$$H|\psi_j\rangle = \sum_i h_{i,j}|\psi_i\rangle, \quad (1.4)$$

where $h_{i,j} = \langle\psi_i|H|\psi_j\rangle$ are matrix elements of the Hamiltonian. The application of H changes the state $|\psi_j\rangle$ into the set of states $|\psi_i\rangle$. To get the (row) index i it is necessary to search for the state $|\psi_i\rangle$ in the basis. Several schemes exist to make this step numerically efficient. A widely used one is the construction of a hashmap [76]: A hashtag is calculated for every single basis state and stored together with the index of the basis state. After that, the list is sorted by the value of the hashtag. The index of a state can now be retrieved by calculation of its hashtag and a search for the hashtag in the hashmap gives the index. Hamiltonians that involve only short-range interactions are very sparse and have of the order of $\mathcal{O}(N_{\text{st}})$ entries [40]. Finding the index of those states during setup of the Hamiltonian thus scales with $\mathcal{O}(N_{\text{st}} \log_2(N_{\text{st}}))$ where the logarithmic part is the cost of searching for a single hash. For a good review of this procedure see [76, 98].

To solve for the ground state the Lanczos algorithm is applied [40, 78, 98]. The most costly operation that has to be repeated several times is matrix-vector multiplication. For the sparse Hamiltonian this scales with $\mathcal{O}(N_{\text{st}})$. Because of this linearity large systems can often be treated even though the Hilbert-space scales exponentially in the system size. For the computation of the whole spectrum, dense matrix diagonalization needs to be performed which usually scales with the third power of the basis dimension $\mathcal{O}(N_{\text{st}}^3)$. Compared to ground-state computations, this scheme limits the applicable system sizes greatly. As an example, the full diagonalization of a dense matrix with dimension $N_{\text{st}} \approx 50000$ takes a time of order of a few hours exploiting the hermiticity of the matrix.

Symmetries

The only parameter that enters into the ED calculations is the number of states N_{st} . In other words, this is the only handle that we have in order to refine the algorithm. The first improvement is the implementation of global symmetries [98]. To ease the notation we will denote operators with a hat exclusively in this section. If the Hamiltonian is invariant under a symmetry transformation \hat{S} ($[\hat{H}, \hat{S}] = 0$), then the operator \hat{S} and the Hamiltonian \hat{H} have a common eigenbasis and application of \hat{H} onto a state can not change the quantum number s associated with \hat{S} . That means the Hamiltonian is blockdiagonal in the eigenstates of \hat{S} . If we know the eigenstates of \hat{S} we can set up the Hamiltonian in this basis and use the blockdiagonality to reduce the computational cost because the diagonalization of the full matrix can now be achieved by diagonalization of the blocks individually. For discrete symmetries one can easily construct eigenstates

$$|a(s)\rangle = \frac{1}{\sqrt{N_a}} \sum_{r=0}^{R-1} s^{-r} \hat{S}^r |a\rangle, \quad (1.5)$$

where $\hat{S}|a(s)\rangle = s|a(s)\rangle$ with $|s|^2 = 1$, R denotes the maximal reciprocity of the symmetry operator $\hat{S}^R|a\rangle = |a\rangle$ and $|a\rangle$ is a state called representative. An example for discrete symmetries are translation symmetry

$$\hat{T}|n_1 \dots n_L\rangle = |n_L n_1 \dots n_{L-1}\rangle,$$

reflection symmetry

$$\hat{P}|n_1 n_2 \dots n_{L-1} n_L\rangle = |n_L n_{L-1} \dots n_2 n_1\rangle$$

and spin-flip symmetry

$$\hat{F}(b_{\uparrow,i}^\dagger, b_{\downarrow,j}^\dagger |\emptyset\rangle) = b_{\downarrow,i}^\dagger b_{\uparrow,j}^\dagger |\emptyset\rangle.$$

For the application of an operator \hat{O} onto this symmetrized state, knowledge of its action on the representative is sufficient

$$\begin{aligned} \hat{O}|a(s)\rangle &= \frac{1}{\sqrt{N_a}} \sum_{r=0}^{R-1} s^{-r} \hat{S}^r \hat{O}|a\rangle \\ &= O_{b,a} \frac{1}{\sqrt{N_a}} \sum_{r=0}^{R-1} s^{-r} \hat{S}^r |b'\rangle \\ &= O_{b,a} \frac{1}{\sqrt{N_a}} \sum_{r=0}^{R-1} s^{-r} \hat{S}^{r-l} |b\rangle \\ &= O_{b,a} s^l \sqrt{\frac{N_b}{N_a}} |b(s)\rangle, \end{aligned} \tag{1.6}$$

where $O_{b,a}$ is the matrix element $\langle b' | \hat{O} | a \rangle$ and $|b\rangle = \hat{S}^{-l} |b'\rangle$. We note that $[\hat{O}, \hat{S}] = 0$ has to hold here. For many observables this is no problem because they can be symmetrized quite easily. As an example, take the electronic correlation operator in a translation symmetric system

$$\langle \hat{c}_l^\dagger \hat{c}_{l+x} \rangle = \frac{1}{L} \sum_j \langle \hat{c}_j^\dagger \hat{c}_{j+x} \rangle = \frac{\langle C_x \rangle}{L}, \tag{1.7}$$

where $\hat{C}_x = \sum_j \hat{c}_j^\dagger \hat{c}_{j+x}$ is the translation-invariant correlator. Clearly, the unsymmetrized operator correlator does not commute with the translation operator $[\hat{c}_l^\dagger \hat{c}_{l+x}, \hat{T}] \neq 0$ while the symmetrized version $[\hat{C}_x, \hat{T}] = 0$ has this property.

The matrix elements of the operator \hat{O} can be determined in the symmetry subspace s by knowledge of all norms N_a and representatives $|a\rangle$. A state is only defined for a given subspace if it is normalizable which is equivalent to the condition

$$f(R_a, R) = \sum_{n=0}^{R/R_a-1} s^{-nR_a} \neq 0, \tag{1.8}$$

where R_a defines the minimal reciprocity of the state $|a\rangle$, such that $\hat{S}^{R_a} |a\rangle = |a\rangle$. In cases where the Hamiltonian has multiple symmetries that also commute among each other the state naturally generalizes to

$$\begin{aligned} |a(s_1, s_2)\rangle &= \frac{1}{N_{a(s_2)}} \sum_{r=0}^{R-1} s_1^{-r} \hat{S}_1^r |a(s_2)\rangle \\ &= \frac{1}{N_{a(s_1)}} \sum_{r=0}^{R-1} s_2^{-r} \hat{S}_2^r |a(s_1)\rangle, \end{aligned} \tag{1.9}$$

where $|a(s_{1/2})\rangle$ is given by Eq. (1.5) and one now has to ensure Eq. (1.8) for each symmetry independently. The ED-code that was developed in this thesis is a numerical generalization of this scheme for an arbitrary number of discrete symmetries.

1.1.2 Krylov-space time-evolution

As mentioned above, we want to follow the time-evolution of a system in the state $|\psi(t_0)\rangle$. We start with a state at a given initial time and look at snapshots of the state after several applications of the time-propagator for time Δt which changes the state at a time t_0 into the state at a time $t_0 + \Delta t$

$$|\psi(t_0 + \Delta t)\rangle = e^{-iH\Delta t}|\psi(t_0)\rangle. \quad (1.10)$$

Despite the simple design of this equation it can be challenging to perform. The crux of the matter is the exponential operator $e^{-iH\Delta t}$. For small systems the Hamiltonian can be diagonalized completely and the time-evolution operator can be set up exactly

$$\begin{aligned} e^{-iH\Delta t} &= \sum_{n=0}^{\infty} \frac{(-iH\Delta t)^n}{n!} \\ &= \sum_{n=0}^{\infty} \frac{(-iU^\dagger \lambda U \Delta t)^n}{n!} \\ &= U^\dagger \left(\sum_{n=0}^{\infty} \frac{(-i\lambda \Delta t)^n}{n!} \right) U \\ &= U^\dagger e^{-i\lambda \Delta t} U, \end{aligned} \quad (1.11)$$

where $e^{-i\lambda \Delta t}$ is a diagonal matrix with the exponential of the eigenvalues of H on the diagonal and U^\dagger is a unitary basistransformation from eigenstates of the Hamiltonian to the original basis $H = U^\dagger \lambda U$.

For larger systems this is not possible [99]. For small Δt the exponential can be approximated by an expansion with finite order N

$$e^{-iH\Delta t} \approx \sum_{n=0}^N \frac{(-iH\Delta t)^n}{n!}, \quad (1.12)$$

which gives a theoretical error proportional to $\mathcal{O}((\Delta t)^{N+1})$. However, several convergence problems occur with this method because of the finite machine precision (for a review of this method and an overview over several other methods for the construction of matrix exponentials, see [100]).

Another way is to keep the exponential exact and approximate the Hamiltonian by a small tridiagonal matrix obtained via the Lanczos algorithm [78, 99]. The Hamiltonian is approximated by the tridiagonal matrix T_n and the time-evolution over one time-step Δt can be approximated by [100]

$$|\psi(t_0 + \Delta t)\rangle = e^{-iH\Delta t}|\psi(t_0)\rangle \approx V_n(t_0)e^{-iT_n(t_0)\Delta t}V_n^\dagger(t_0)|\psi(t_0)\rangle, \quad (1.13)$$

where the matrix $V_n(t_0)$ contains the n Lanczos vectors $|u_j\rangle$. The Lanczos vectors $|u_j\rangle$ span the Krylov space defined as

$$\mathcal{K}_n(H, |\psi\rangle) = \text{span}\{|\psi\rangle, H|\psi\rangle, \dots, H^{n-1}|\psi\rangle\}, \quad (1.14)$$

and the matrix $V_n(t)$ thus represents a transformation from the Krylov space to the original basis that $|\psi\rangle$ is set up in. Because the first Krylov vector equals the initial state $|u_1\rangle = |\psi(t_0)\rangle$, Eq. (1.13) becomes

$$|\psi(t_0 + \Delta t)\rangle \approx V_n(t_0)e^{-iT_n(t_0)\Delta t}\vec{e}_1, \quad (1.15)$$

where \vec{e}_1 is the first unit vector in the Krylov space basis. In other words, only the first row of $e^{-iT_n(t_0)\Delta t}$ contributes to the time-evolution. The error in this case is

$$\begin{aligned} \epsilon_n &= \|\psi(t_0 + \Delta t)\rangle - |\psi(t_0 + \Delta t)\rangle_{\text{approx}}\| \\ &\leq 12e^{-\frac{|E_{\max} - E_{\min}|\Delta t}{16n}} \left(\frac{e|E_{\max} - E_{\min}|\Delta t}{4n} \right), \end{aligned} \quad (1.16)$$

where $n \geq \frac{1}{2}|E_{\max} - E_{\min}|\Delta t$, E_{\max} denotes the highest eigenvalue of H and E_{\min} is the lowest one [99].

In Ref. [99] the error estimation Eq. (1.16) is used to get the optimal number of Krylov vectors to achieve the same error in every time-step. In this thesis we set the number of Krylov vectors to a fixed number (mostly to $n = 20$) and reduce the time-step until the full time-evolution converges over the whole time-domain of interest.

1.1.3 Exact diagonalization in a limited functional space

Bonča et al. [23,89] found another way of reducing the size of the Hilbert space for the Holstein model with a single electron coupled to quantum phonons on an infinite lattice

$$H = -t_0 \sum_j (c_j^\dagger c_{j+1} + \text{h.c.}) + \omega_0 \sum_j b_j^\dagger b_j - \gamma \sum_j (b_j^\dagger + b_j)n_j, \quad (1.17)$$

where c_j is a fermionic annihilator and b_j is a bosonic one acting on site j . The model parameters are the hopping t_0 , the phonon energy ω_0 and the electron-phonon interaction strength γ .

The basis setup algorithm for this system starts from a state without phonons and a single electron (product state)

$$|\psi_{\text{init}}\rangle = c_j^\dagger |\emptyset\rangle_e \otimes |\emptyset\rangle_p, \quad (1.18)$$

where the subscript p denotes the phonon state and e denotes the electron state. For the Holstein model the hopping- and interaction terms are off-diagonal operators

$$H_o = -t_0 \sum_j (c_j^\dagger c_{j+1} + \text{h.c.}) - \gamma \sum_j (b_j^\dagger + b_j)n_j. \quad (1.19)$$

The set of states that span the basis $\{|\psi\rangle\}$ is then built up from states created by the application of these off-diagonal terms up to N_h times onto the initial state

$$\{|\psi\rangle\} = \{|\psi\rangle : H^{n_h} |\psi_{\text{init}}\rangle \forall n_h \in [0, N_h]\}, \quad (1.20)$$

where N_h is the number of generations of basis states that are taken into account. So far, the procedure constructs all states that the system can connect to. For the case of $\gamma \approx t$ this is a good approximation as both terms are equally important and the resulting ground state is

an electron that is delocalized over the lattice [6]. However, in the case of $t \ll \gamma$ one knows that phonons exist only very close to the electron in the ground state. To account for that, the authors take into account a second parameter m in the generation of basis states

$$\{|\psi\rangle\} = \{|\psi\rangle : (H_{\text{kin}} + H_{\text{coup}}^m)^{n_h} |\psi_{\text{init}}\rangle \forall n_h \in [0, N_h], m \in [1, M]\}, \quad (1.21)$$

where M is the number of applications of the coupling term while the hopping term is applied once. In this way more phonon states are created locally which accounts for the stronger coupling strength. One needs to be aware, however, that the basis grows exponentially with the number of generations as every generation is used as the input to the construction of the next generation. A larger M also means that more states are created in every generation which leads to a much faster exponential growth with every generation.

In our work [96] we adapt this method and apply it to a translational invariant system with fixed size L . As before, the algorithm proceeds by taking some initial state $|\psi\rangle$ onto which the Hamiltonian is applied up to N_h times to create states that are included into the basis. Following this scheme, we construct states that are connected to the initial state by a finite number of applications of the Hamiltonian and only states which have a finite overlap with the initial state are included in the basis. Figure 1.1 shows the states that are created from

$$|\psi_{\text{init}}\rangle = c_0^\dagger |\emptyset\rangle_e \otimes |\emptyset\rangle_p. \quad (1.22)$$

The zero-generation state $n_h = 0$ is the initial state itself. The first generation $n_h = 1$ includes only the state created by the interaction term because the hopping term only creates the same state again (the Hamiltonian is translation symmetric). The second generation includes all three states created by hopping (top and bottom states) and interaction (middle state) terms. Each generation is computed from the states in the previous generation only. Of course, each state is kept only once even though the same state can emerge in multiple generations.

The implementation stores the newly generated basis states separately and searches the sorted list of states of all previous generations for the existence of each newly generated state. This step is crucial to the whole setup because basis states have to be unique. It scales with $\mathcal{O}(N_{\text{new}} \log_2(N_{\text{full}}))$ where N_{new} is the number of newly created states, N_{full} is the number of all states created previously and one has to keep in mind that N_{new} is of the order of $\mathcal{O}(N_{\text{full}})$ due to exponential growth. After that, the new and unique states are added to the full list of states which is then sorted (two copies exist of each state because we need them to create the next generation and thus also need two times as much memory) which scales with $\mathcal{O}(N_{\text{full}} \log_2(N_{\text{full}}))$. Since every next generation is exponentially larger than the last one, we can estimate the overall complexity of the basis setup to be $\mathcal{O}(N_{\text{full}}^{N_h} \log_2(N_{\text{full}}^{N_h}))$ where $N_{\text{full}}^{N_h}$ is the number of basis states in the last generation.

1.2 Density matrix renormalization group algorithm with local subspace expansion

In this section we describe the strictly single-site DMRG (DMRG3S) algorithm [38]. To this end we start by reviewing DMRG in the matrix product state (MPS) notation then talk about single-site DMRG and improvements to ensure convergence.

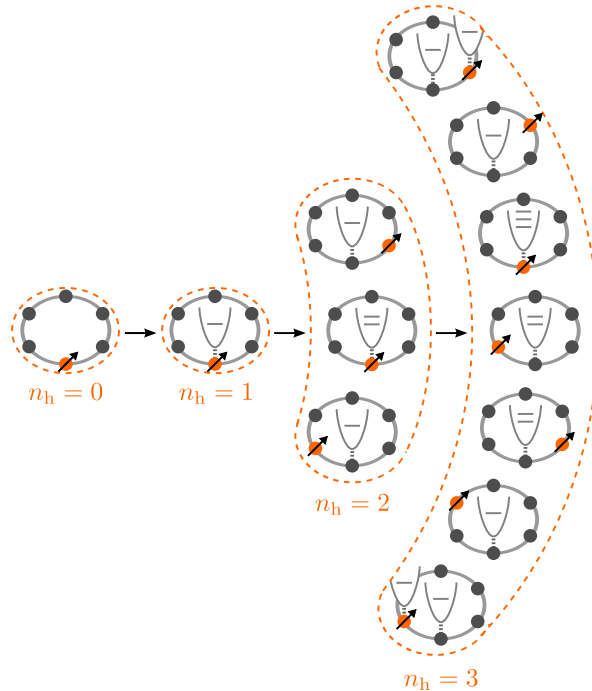


Figure 1.1: Sketch of the basis generation scheme of the limited functional space basis (adapted for periodic boundary conditions from Ref. [23]). The procedure starts from the initial state located in the zeroth generation $n_h = 0$ Eq. (1.18) and generates states for the next generation by application of the off-diagonal terms of the Hamiltonian Eq. (1.19) onto all states of the previously generated generation where each unique state is kept only once. Filled circles correspond to lattice sites and the ring structure indicates periodic boundary conditions. An arrow on a site is where the electron sits and the horizontal lines in the parabola-shaped symbols represent the phonon occupation number of the site it is attached to. The Hamiltonian Eq. (1.17) is translation-symmetric and the full basis set also includes all possible translations of the generated states.

1.2.1 Density matrix renormalization group

Historically, the DMRG algorithm is the successor of the numerical renormalization group (NRG) method which Wilson used in 1975 to solve the Kondo problem numerically [101]. This procedure was analyzed by White and Noack [102] to understand why it fails for low-energy properties of strongly correlated quantum many-body problems. They identified the problem in the implicit assumption of NRG that the low-energy eigenstates of the larger system can be constructed from the low-energy eigenstates of the smaller system which in general does not hold.

White developed a new algorithm [24, 79] which grows the system linearly by two sites at a time and chooses the best set of states for the whole system after it has been set up. Figure 1.2 illustrates the general steps involved in the algorithm. The system is split into two parts of the same size, the *system* block (A) and the *environment* block (B). A typical state

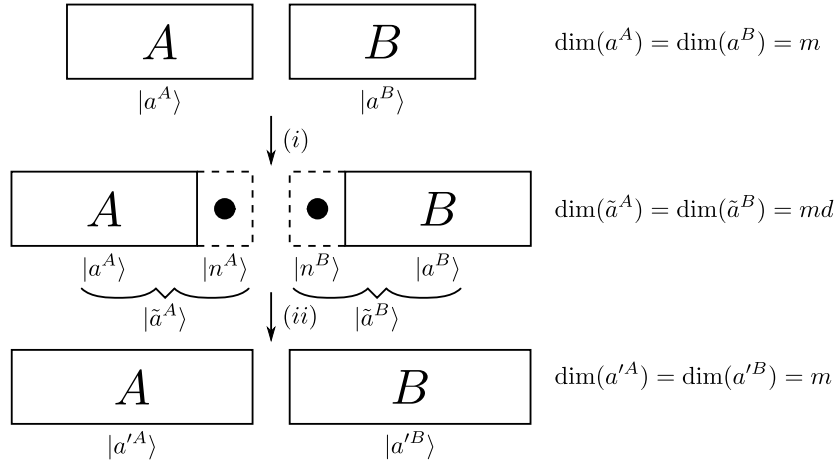


Figure 1.2: Sketch of the infinite-system DMRG procedure. The algorithm starts from a system is bipartitioned into the system block A and the environment block B . (i) The blocks are enlarged by two new sites which effectively enlarges the size of the system by two sites and enhances the total basis dimension of each block by a factor of the local dimension d . (ii) The full system is diagonalized to find the ground state and the basis of each block is truncated back to m states.

of this system is

$$|\psi\rangle = \sum_{a^A, a^B} \psi_{a^A, a^B} |a^A\rangle \otimes |a^B\rangle, \quad (1.23)$$

where a^A and a^B label the basis states of the two parts of the system which have dimension $\dim(a^A) = \dim(a^B) = m$. The next step ((i) in Fig. 1.2) consists of adding two sites at the middle of the system, one to the system block $|n^A\rangle$ and the other to the environment block $|n^B\rangle$. The ground state of the enlarged full system - called superblock - is then computed

$$\begin{aligned} |\psi_0\rangle &= \sum_{a^A, n^A, n^B, a^B} \psi_{a^A, n^A, n^B, a^B}^0 |a^A\rangle \otimes |n^A\rangle \otimes |n^B\rangle \otimes |a^B\rangle \\ &= \sum_{\tilde{a}^A, \tilde{a}^B} \psi_{\tilde{a}^A, \tilde{a}^B}^0 |\tilde{a}^A\rangle \otimes |\tilde{a}^B\rangle. \end{aligned} \quad (1.24)$$

Because the system just grew in size by two sites the basis-dimensions of the two blocks A and B grew by a factor of d to the new dimensions $\dim(\tilde{a}^A) = \dim(\tilde{a}^B) = md$ and a way of truncating the basis needs to be implemented to avoid exponential growth of the basis (step (ii) in Fig. 1.2). The crucial insight of White was that the best set of states for the system block A is found in the m highest weighted eigenstates of the reduced density matrix ρ_A for

the current half-cut of the system

$$\begin{aligned}
\rho_A &= \text{tr}_B(\rho) \\
&= \sum_{\tilde{a}''^B} \sum_{\substack{\tilde{a}'^A, \tilde{a}'^B \\ \tilde{a}^A, \tilde{a}^B}} \psi_{\tilde{a}'^A, \tilde{a}'^B}^* \psi_{\tilde{a}^A, \tilde{a}^B}^0 \langle \tilde{a}''^B | \tilde{a}'^B \rangle \langle \tilde{a}^B | \tilde{a}''^B \rangle | \tilde{a}'^A \rangle \langle \tilde{a}^A | \\
&= \sum_{\substack{\tilde{a}'^A, \tilde{a}^A \\ \tilde{a}^B}} \psi_{\tilde{a}'^A, \tilde{a}^B}^* \psi_{\tilde{a}^A, \tilde{a}^B}^0 | \tilde{a}'^A \rangle \langle \tilde{a}^A | \\
&\approx \sum_{\beta=0}^m \lambda_\beta | \beta \rangle \langle \beta |,
\end{aligned} \tag{1.25}$$

where the $|\beta\rangle$ denote the eigenstates of the reduced density matrix for block A and λ_β are their weights. In this way one constructs a state $|\tilde{\psi}\rangle$ that minimizes

$$\| |\psi\rangle - |\tilde{\psi}\rangle \|^2 = \langle \psi | \psi \rangle + \langle \tilde{\psi} | \tilde{\psi} \rangle - \langle \tilde{\psi} | \psi \rangle - \langle \psi | \tilde{\psi} \rangle, \tag{1.26}$$

where

$$\begin{aligned}
|\psi\rangle &= \sum_{i,j} \psi_{i,j} |i\rangle \otimes |j\rangle \\
&= \sum_{\beta,i,j} \psi_{i,j} u_{\beta,i}^* | \beta \rangle \otimes |j\rangle
\end{aligned} \tag{1.27}$$

is the full wavefunction and $|\beta\rangle = \sum_i u_{\beta,i} |i\rangle$ with $\sum_\beta u_{\beta,i}^* u_{\beta,i} = \delta_{i,i}$ a unitary basistransformation. The approximated wavefunction $|\tilde{\psi}\rangle$ is truncated in β

$$|\tilde{\psi}\rangle = \sum_{i,j} \sum_{\beta=0}^{m-1} \psi_{i,j} u_{\beta,i}^* | \beta \rangle \otimes |j\rangle, \tag{1.28}$$

where $m < \dim(j)$. We can write the overlap between truncated and full wavefunction

$$\begin{aligned}
\langle \tilde{\psi} | \psi \rangle &= \sum_{i,j} \sum_{\beta=0}^{m-1} \psi_{i',j'}^* u_{\beta,i'} u_{\beta,i} \psi_{i,j} u_{\beta,i}^* \langle \beta' | \beta \rangle \langle j' | j \rangle \\
&= \sum_{i',i} \sum_{\beta=0}^{m-1} u_{\beta,i'} \rho_{i',i} u_{\beta,i}^*,
\end{aligned} \tag{1.29}$$

where for the last line Eq. (1.25) was used. With the assumption that ψ and u are real Eq. (1.26) becomes

$$\| |\psi\rangle - |\tilde{\psi}\rangle \|^2 = 1 - \sum_{i',i} \sum_{\beta=0}^{m-1} u_{\beta,i'} \rho_{i',i} u_{\beta,i}. \tag{1.30}$$

Truncation in the eigenstates of the reduced density matrix emerges naturally from this form because the eigenvalues of this operator are all positive and sum up to one

$$\epsilon = \| |\psi\rangle - |\tilde{\psi}\rangle \|^2 = 1 - \sum_{\beta=0}^{m-1} \lambda_\beta. \tag{1.31}$$

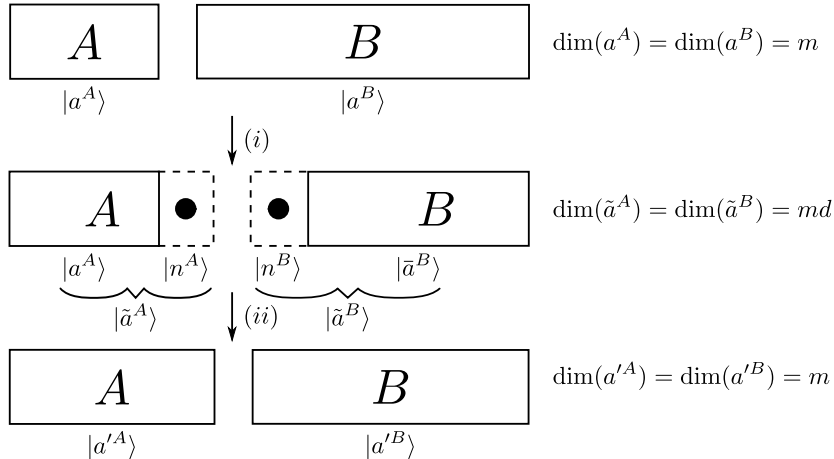


Figure 1.3: Sketch of the finite-system DMRG procedure. The algorithm starts from a system is bipartitioned into the system block A and the environment block B . (i) The system block A is enlarged by one site while the environment block B shrinks by one site. In this step, the state of the system is not altered but the two center sites include all local states which increases the overall basis dimension by a factor of the local dimension d . (ii) The full system is diagonalized to find the ground state and the basis of each block is truncated back to m states.

Equation (1.31) also defines the discarded weight ϵ that gives the truncation error and it is obvious from this form that at constant error the number of states to keep depends on the rate of decay of the weights λ_β . For one-dimensional solvable models one finds that the reduced density matrix [103] of a given subsystem has the form

$$\rho_A \propto e^{-\sum_l \epsilon_l n_l}, \quad (1.32)$$

where ϵ_l denotes the single-particle eigenvalues. The decay behavior of the weights thus depends on the spectrum of the single-particle eigenvalues. For one-dimensional free-particle models they can be calculated explicitly and the weight spectrum can be shown to decay very rapidly [103].

The resulting algorithm is called infinite-system DMRG. It performs better than the NRG algorithm but still has problems for a variety of systems because the full Hamiltonian is not known during intermediate steps. For example, the effect of an impurity at site j is not known to all sites to the left of site j and to all sites right of site $L - j$ because those sites have been constructed when the impurity was not there yet. Because of that, relevant fluctuations might not be included and never will be because the infinite-size algorithm never returns to those sites [26]. The infinite-system algorithm has thus been used mainly as a pre-processing step to set up a good initial state for a more powerful variant of DMRG which is also considered the state-of-the-art method for the computation of ground state properties in one-dimensional systems: the so-called *finite-system DMRG*. A sketch of the finite-system DMRG procedure is presented in Fig. 1.3. It proceeds like the infinite-system DMRG variant but, instead of keeping both system blocks A and B at the same size, finite-system DMRG grows one while shrinking the other. Figure 1.3 illustrates the left-to-right sweep: It starts from a bipartite system where the two blocks are not equally sized. After that (step (i) in Fig. 1.3), block B is

projected onto the full two-site basis for the left-most sites inside block B and an intermediate block that has shrunk by two sites

$$|n^A, n^B, \bar{a}^B\rangle = \sum_{a^B} \langle a^B | n^A, n^B, \bar{a}^B \rangle |a^B\rangle, \quad (1.33)$$

where \bar{a}^B labels the states of the intermediate block. The left site $|n^A\rangle$ is attached to block A and the right site stays with block B forming two new blocks with dimensions $\dim(\tilde{a}^A) = \dim(\bar{a}^B) = md$. From here on the finite-size algorithm runs analogous to the infinite-size algorithm. By iteratively sweeping through the system the algorithm visits each site multiple times (by introducing "new" two sites in the middle of the system).

We have seen so far that DMRG was a great success due to its ability to find the ground state of a given system in an optimal set of basis states without having to span the whole Hilbert space of the system. In some sense DMRG finds the needle in the haystack while considering only a small fraction of the whole Hilbertspace at a time. The success of the procedure rests on the fact that during truncation the eigenvalues of the reduced density matrix ordered in descending magnitude decay very fast and ideally exponentially with increasing index β

$$\lambda_\beta \propto e^{-c\beta}. \quad (1.34)$$

We now relate this spectrum to the notion of entanglement for which the scaling in ground states is known. Using the bipartite form of the wavefunction

$$|\psi\rangle = \sum_{i,j} \psi_{i,j} |i\rangle \otimes |j\rangle \quad (1.35)$$

we can always bring it into the form of a Schmidt decomposition (for example by performing singular value decomposition on $\psi_{i,j}$)

$$\begin{aligned} |\psi\rangle &= \sum_a c_a \left(\sum_i U_{i,a} |i\rangle \right) \otimes \left(\sum_j V_{a,j}^* |j\rangle \right) \\ &= \sum_a c_a |a\rangle_A \otimes |a\rangle_B, \end{aligned} \quad (1.36)$$

where $U^\dagger U = \mathbb{1}$ and $V^\dagger V = \mathbb{1}$ are left- and right-canonical matrices and $\psi_{i,j} = \sum_a U_{i,a} c_a V_{a,j}^*$.

We can convince ourselves that the Schmidt coefficients c_a are directly related to the entanglement between the subsystems A and B : Assume that the two subsystems are completely independent. Hence, the system is in a product state of the two parts of the system and c_a will have a single entry that is equal to one while the remaining ones are equal to zero. In the other extreme case of a maximally entangled state $c_a = 1/N_{\text{st}}^{(A)} \forall a$ where $N_{\text{st}}^{(A)}$ is the dimension of the basis of half of the system. Building the half-cut reduced density matrix using this state we can identify the eigenvalues λ_β and eigenstates $|\beta\rangle$ of the reduced density matrix Eq. (1.25) with the quantities $|c_a|^2$ and $|a\rangle_A$

$$\rho_A = \sum_a |c_a|^2 |a\rangle_A \langle a|_A, \quad (1.37)$$

$$\lambda_\beta = |c_a|^2, \quad (1.38)$$

$$|\beta\rangle = |a\rangle_A. \quad (1.39)$$

From this we see that the weights used to truncate the block basis during DMRG updates are related to the entanglement between the two subsystems A and B . One way of quantifying the entanglement is the so-called von Neumann entropy

$$S_{\text{vN}} = - \sum_a |c_a|^2 \log(|c_a|^2). \quad (1.40)$$

One knows that the entanglement entropy for a subsystem of a system in a generic many-body eigenstate scales with the volume of the subsystem [81]

$$S \propto l^D, \quad (1.41)$$

where l is the size of the subsystem and D is the considered dimension. Non-degenerate ground states of systems with an excitation gap are special because one can prove that the entanglement entropy scales proportional to the boundary region of the subsystem under study [80] instead of with the volume

$$S \propto l^{D-1}. \quad (1.42)$$

Using the definition of the von Neumann entropy we can relate the entanglement to the number of non-zero Schmidt-coefficients in the system. We assume the worst case in which, for the accurate description of a system of size L , we need m Schmidt-coefficients where all of them have the same weight $|c_a|^2 = 1/m$

$$\begin{aligned} S &= \log(m), \\ m &= e^S \propto e^{l^{D-1}}, \end{aligned} \quad (1.43)$$

where the last line follows from the scaling of entropy in the ground state Eq. (1.42). For one-dimensional systems and assuming that the system size is large enough to support the full correlation length $l \gg \xi$ we conclude that the number of states is roughly independent of the size of the system

$$m(l) \propto \text{const}. \quad (1.44)$$

For the case of gapless (critical) one-dimensional systems ($D = 1$) the area law is violated, however, the corrections are small and can be inferred using conformal field theory [82, 83]

$$S = \frac{c}{6} \log \left(\frac{2L}{\pi a} \sin \left(\frac{\pi l}{L} \right) \right) + C, \quad (1.45)$$

where l is the size of the subsystem, a is the lattice spacing, c is called the conformal charge and C is some positive constant. This has been verified numerically and also proven rigorously for a variety of models [32, 104–107]. The scaling of the entanglement entropy with the system size is the reason why DMRG works so well. While the Hilbert space of the system grows exponentially d^L the entanglement only grows logarithmically at worst and we can assume that for a general one-dimensional system we need only a finite number of states to approximate it to a good precision.

We continue by introducing the DMRG method in matrix-product state (MPS) formulation for one-dimensional systems. A very good review of the topic is presented in Ref. [27]. Here, we summarize the necessary aspects to make this thesis self-contained.

Matrix product states

Any quantum state can be brought into matrix product state [84–86] form when its weights with respect to the physical basis are interpreted as a rank- L tensor

$$|\psi\rangle = \sum_{\vec{n}} c_{n_1, \dots, n_L} |\vec{n}\rangle, \quad (1.46)$$

where \vec{n} is a shorthand for (n_1, \dots, n_L) and n_j is a label for the local state site j is in. We now introduce two dummy indices a_0 and a_L to the left and right of the physical indices to make the following decomposition more consistent. The first two indices (a_0, n_1) and all the other indices (n_2, \dots, n_L, a_L) are grouped together to bring $c_{\vec{n}}$ into the form of a matrix

$$|\psi\rangle = \sum_{\vec{n}} c_{(a_0, n_1), (n_2, \dots, n_L, a_L)} |\vec{n}\rangle. \quad (1.47)$$

This matrix is then decomposed by singular value decomposition

$$c_{(a_0, n_1), (n_2, \dots, n_L, a_L)} = U_{(a_0, n_1), a_1} \lambda_{a_1} V_{a_1, (n_2, \dots, n_L, a_L)}^*. \quad (1.48)$$

Afterwards, the U -tensor is reshaped to a rank-3 tensor $A_{a_0, a_1}^{n_1} = U_{(a_0, n_1), a_1}$ and the singular values λ are multiplied into V^\dagger to form a new c -tensor

$$\begin{aligned} |\psi\rangle &= \sum_{\vec{n} a_1} A_{a_0, a_1}^{n_1} c_{a_1, (n_2 \dots n_L, a_L)} |\vec{n}\rangle \\ &= \sum_{\vec{n} \vec{a}} A_{a_0, a_1}^{n_1} \cdots A_{a_{L-2}, a_{L-1}}^{n_{L-1}} c_{a_{L-1}, (n_L, a_L)} |\vec{n}\rangle \\ &= \sum_{\vec{n} \vec{a}} A_{a_0, a_1}^{n_1} \cdots A_{a_{L-2}, a_{L-1}}^{n_{L-1}} M_{a_{L-1}, a_L}^{n_L} |\vec{n}\rangle, \end{aligned} \quad (1.49)$$

where we arrive at the last line by repeating steps (1.47) and (1.48) $L - 1$ times and reshaping the matrix $c_{a_{L-1}, (n_L, a_L)}$ to the rank-3 tensor $M_{a_{L-1}, a_L}^{n_L}$. The A -tensors fulfill

$$\sum_{a_{j-1}, n_j} A_{a_{j-1}, a'_j}^{*n_j} A_{a_{j-1}, a_j}^{n_j} = \delta_{a'_j, a_j}, \quad (1.50)$$

which is a consequence of the singular value decomposition. MPS tensors which fulfill this equation are called "left-canonical". The decomposition can also be carried out starting from the right

$$\begin{aligned} |\psi\rangle &= \sum_{\vec{n}} c_{n_1, \dots, n_L} |\vec{n}\rangle \\ &= \sum_{\vec{n}} c_{(a_0, n_1, \dots, n_{L-1}), (n_L, a_L)} |\vec{n}\rangle \\ &= \sum_{\vec{n} a_{L-1}} c_{(a_1, n_1 \dots n_{L-1}), a_{L-1}} B_{a_{L-1}, a_L}^{n_L} |\vec{n}\rangle \\ &= \sum_{\vec{n} \vec{a}} M_{a_0, a_1}^{n_1} B_{a_1, a_2}^{n_2} \cdots B_{a_{L-1}, a_L}^{n_L} |\vec{n}\rangle, \end{aligned} \quad (1.51)$$

where now after an SVD the V^\dagger -tensors are reshaped to rank-3 tensors $B_{a_{j-1}, a_j}^{n_j} = V_{a_{j-1}, (n_j, a_j)}^*$. The B -tensors are called "right-canonical"

$$\sum_{a_j, n_j} B_{a'_{j-1}, a_j}^{n_j} B_{a_{j-1}, a_j}^{*n_j} = \delta_{a'_{j-1}, a_{j-1}}, \quad (1.52)$$

which results from the properties of the V^\dagger -tensors. Mixing the two procedures we can also obtain a "mixed canonical" representation of the state

$$|\psi\rangle = \sum_{\vec{n}\vec{a}} A_{a_0, a_1}^{n_1} \cdots A_{a_{j-2}, a_{j-1}}^{n_{j-1}} M_{a_{j-1}, a_j}^{n_j} B_{a_j, a_{j+1}}^{n_{j+1}} \cdots B_{a_{L-1}, a_L}^{n_L} |\vec{n}\rangle. \quad (1.53)$$

This is the form we will mostly deal with during DMRG sweeps. The index a_i that is introduced by SVD between two local tensors is called the bond index. In general, it is of dimension $m_j = m_{j-1}d$ up to the center of the system where m_{j-1} is the dimension of the bond index to the left and d is the dimension of the local physical degrees of freedom. Starting from the left, the dimension is thus given by $m_j = d^j$ on site j up to its maximal dimension $m_{L/2} = d^{L/2}$ for the center bond. From Eqs. (1.50) and (1.52) we know that a_{j-1} and a_j label an orthonormal set of basis states for the left

$$|a_{j-1}\rangle_A = \sum_{\substack{a_0 \cdots a_{j-2} \\ n_1 \cdots n_{j-1}}} A_{a_0, a_1}^{n_1} \cdots A_{a_{j-2}, a_{j-1}}^{n_{j-1}} |n_1 \cdots n_{j-1}\rangle, \quad (1.54)$$

and right ($\{n_{j+1}, \dots, L\}$) part of the system

$$|a_j\rangle_B = \sum_{\substack{a_{j+1} \cdots a_L \\ n_{j+1} \cdots n_L}} B_{a_j, a_{j+1}}^{n_{j+1}} \cdots B_{a_{L-1}, a_L}^{n_L} |n_{j+1} \cdots n_L\rangle. \quad (1.55)$$

With those definitions we can write Eq. (1.53)

$$|\psi\rangle = \sum_{a_{j-1}, n_j, a_j} M_{a_{j-1}, a_j}^{n_j} |a_{j-1}\rangle_A \otimes |n_j\rangle \otimes |a_j\rangle_B. \quad (1.56)$$

The bipartition of the system can now be reached by singular value decomposition of the M -tensor

$$\begin{aligned} |\psi\rangle &= \sum_{a_{j-1}, n_j, a_j, \bar{a}_j} A_{a_{j-1}, \bar{a}_j}^{n_j} \lambda_{\bar{a}_j} V_{\bar{a}_j, a_j}^* |a_{j-1}\rangle_A \otimes |n_j\rangle \otimes |a_j\rangle_B \\ &= \sum_{\bar{a}_j} \lambda_{\bar{a}_j} |\bar{a}_j\rangle_A \otimes |\bar{a}_j\rangle_B, \end{aligned} \quad (1.57)$$

where $|\bar{a}_j\rangle_A = \sum_{a_{j-1}, n_j} A_{a_{j-1}, \bar{a}_j}^{n_j} |a_{j-1}\rangle_A \otimes |n_j\rangle$ is the enlarged left environment state and $|\bar{a}_j\rangle_B = \sum_{a_j} V_{\bar{a}_j, a_j}^* |a_j\rangle_B$ transforms the right basis to the eigenstates of the reduced density matrix at this half-cut. Note that this form is only possible for a state where all sites left of site j are left-canonical and all sites to the right are right canonical because only then the

left and right states are orthonormal sets

$$\begin{aligned}
\langle \bar{a}'_j | \bar{a}_j \rangle_A &= \sum_{a'_{j-1}, n_j, a_{j-1}} A_{a'_{j-1}, \bar{a}'_j}^{*n_j} A_{a_{j-1}, \bar{a}_j}^{n_j} \langle a'_{j-1} | a_{j-1} \rangle_A \\
&= \sum_{a_{j-1}, n_j} A_{a_{j-1}, \bar{a}'_j}^{*n_j} A_{a_{j-1}, \bar{a}_j}^{n_j} \\
&= \delta_{\bar{a}'_j, \bar{a}_j}, \tag{1.58}
\end{aligned}$$

$$\begin{aligned}
\langle \bar{a}'_j | \bar{a}_j \rangle_B &= \sum_{a'_j, a_j} V_{\bar{a}'_j, a'_j} V_{\bar{a}_j, a_j} \langle a'_j | a_j \rangle_B \\
&= \sum_{a_j} V_{\bar{a}'_j, a_j} V_{\bar{a}_j, a_j} \\
&= \delta_{\bar{a}'_j, \bar{a}_j}. \tag{1.59}
\end{aligned}$$

We have seen that any state can be formulated as an MPS by using a single tool from linear algebra: the singular value decomposition. We now want to see how quantum numbers fit into this picture.

In the above formulation the physical indices n_j specify the local state. This can be simply the number of particles that occupy the site or it is a number that maps to a more complicated set of local degrees of freedom (like a state consisting of electronic and bosonic degrees of freedom $|n_j\rangle = |n_j^e\rangle \otimes |n_j^p\rangle$). Equation (1.56) allows a similar identification of the bond index with an actual physical state: each of the a_{j-1} (a_j) labels a particular superposition of the physical state of a smaller part of the system including sites $i_A = 1, \dots, j-1$ ($i_B = j+1, \dots, L$). In DMRG we are interested in the ground state of a given Hamiltonian. Assuming this Hamiltonian has a $U(1)$ -symmetry (e.g. conservation of particle number) all of its eigenstates have a well-defined global quantum number. All subdivisions of the system have well-defined quantum numbers as well because otherwise states with a different global quantum number can emerge. We can always group physical and bond indices according to their quantum number

$$|\psi\rangle = \sum_{\vec{N}, \vec{n}} A_{N_0, N_1}^{n_1} \cdots A_{N_{j-2}, N_{j-1}}^{n_{j-1}} M_{N_{j-1}, N_j}^{n_j} B_{N_j, N_{j+1}}^{n_{j+1}} \cdots B_{N_{L-1}, N_L}^{n_L} |\vec{n}\rangle, \tag{1.60}$$

where each $M_{N_{i-1}, N_i}^{n_i}$ is now a tensor instead of a single number and $N_i = \{a_{i_1}, a_{i_2}, \dots\}$. It is clear from the above form that only certain combinations of the three indices N_{j-1}, n_j, N_j are allowed which makes the tensors blockdiagonal. The choice of the actual quantum number for each bond is arbitrary in the sense that one can also label them starting from the right side of the system or choose some kind of mixed labeling. We choose a labeling starting at the left side of the system

$$N_j = N_{j-1} + n_j. \tag{1.61}$$

A sketch of such a state is shown in Fig. 1.4. Eq. (1.60) together with this labeling can be used numerically to exploit additive quantum numbers. The main benefits of this representation are, on the one hand, the ability to do DMRG in a Hilbert space with a fixed quantum number and, on the other hand, exploiting the blockstructure of the MPS during linear algebra operations.

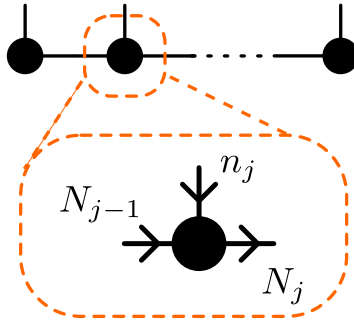


Figure 1.4: Sketch of an MPS. A filled circle is the symbol for a tensor and the legs coming out of it visualize the indices of the tensor. An MPS-tensor is a rank-3 tensor and has thus 3 legs: N_{j-1} the left leg representing the left bond index, N_j the right leg representing the right bond index and n_j the upper leg representing the physical index. The labeling is chosen to be left-to-right directional Eq. (1.61).

Matrix product operators

Now that we have decomposed arbitrary states into an MPS we need a way to operate on them, for example, during the calculation of an expectation value $\langle \psi | \hat{O} | \psi \rangle$. This is done by a similar object: the matrix product operator (MPO). Every operator can be written as an MPO by the same reasoning as above

$$\begin{aligned} \hat{O} &= \sum_{\vec{n}', \vec{n}} O^{\vec{n}', \vec{n}} |\vec{n}'\rangle \langle \vec{n}| \\ &= \sum_{\substack{\vec{n}', \vec{n} \\ \vec{b}}} W_{b_0, b_1}^{n'_1, n_1} \dots W_{b_{L-1}, b_L}^{n'_L, n_L} |\vec{n}'\rangle \langle \vec{n}|, \end{aligned} \quad (1.62)$$

where b_0 and b_L have been inserted so all tensors can be treated on equal footing.

To understand those objects we set up a Bose-Hubbard Hamiltonian without on-site interaction

$$\begin{aligned} H &= -t \sum_j (d_j^\dagger d_{j+1} + \text{h.c.}) \\ &= \sum_j (\mathbb{1} \otimes \dots \otimes \mathbb{1} \otimes d_j^\dagger \otimes d_{j+1} \otimes \mathbb{1} \otimes \dots \otimes \mathbb{1} \\ &\quad + \mathbb{1} \otimes \dots \otimes \mathbb{1} \otimes d_j \otimes d_{j+1}^\dagger \otimes \mathbb{1} \otimes \dots \otimes \mathbb{1}), \end{aligned} \quad (1.63)$$

where d_j (d_j^\dagger) are bosonic annihilation (creation) operators on site j . To bring this into MPO form we introduce four intermediate states: (i) No term to the right, (ii) Complete term to the right, (iii) d operator to the right and (iv) d^\dagger operator to the right. In this "basis" the MPO tensor is set up by setting the matrix elements so we get exactly the operator strings from Eq. (1.63). The final MPO tensor for the bulk of the system is shown in Fig. 1.5. The identity operator is applied if there is a complete or no term at all to the right. A complete term for the operator above is either a $d_j^\dagger d_{j+1}$ or a $d_{j+1}^\dagger d_j$ term to the right. The (iii)-state is connected to the (i)-state by setting the d operator on a site j . On the next site the (iii)-state is connected to the (ii)-state by completing the d_j operator with a $-td_{j-1}^\dagger$ operator and we

$$W[j] = \begin{array}{c} \begin{array}{ccc} \Delta N_j = 0 & \Delta N_j = -1 & \Delta N_j = 1 \end{array} \\ \left(\begin{array}{cc|cc} \mathbb{1} & 0 & 0 & 0 \\ 0 & \mathbb{1} & -td_j^\dagger & -td_j \\ \hline d_j & 0 & 0 & 0 \\ \hline d_j^\dagger & 0 & 0 & 0 \end{array} \right) \begin{array}{l} \Delta N_{j-1} = 0 \\ \Delta N_{j-1} = -1 \\ \Delta N_{j-1} = 1 \end{array} \end{array}$$

Figure 1.5: MPO tensor representation of the Hubbard Hamiltonian for the bulk of the system.

end up with a complete term to the right. An easy check for correctness is performed by contracting those operators out for a small system. The row and column indices in Fig. 1.5 correspond to the d_{j-1} and d_j indices in Eq. (1.62) while the n'_j and n_j indices are hidden inside the local operators $0, \mathbb{1}, d$ and d^\dagger .

We want to assign quantum numbers to the bond indices of the MPO. An operator maps from one state to another. The term $d_j^\dagger d_{j+1}$ increases the number of particles at site j by one and decreases the number of particles on site $j+1$ by one at the same time. In other words, a particle hops from site $j+1$ to site j . We use this fact to label our MPO bond: While the physical quantum numbers n'_j and n_j determine the change of the local state $\Delta n_j = n'_j - n_j$, the quantum numbers assigned to the MPO bonds need to represent the change in the quantum number of the bond of the MPS when applying the MPO

$$\hat{O} = \sum_{\substack{\vec{n}', \vec{n} \\ \Delta \vec{N}}} W_{\Delta N_0, \Delta N_1}^{n'_1, n_1} \cdots W_{\Delta N_{L-1}, \Delta N_L}^{n'_L, n_L} |\vec{n}'\rangle \langle \vec{n}|. \quad (1.64)$$

Because there is a directionality in the labeling of the MPS bond which we fixed to be left-to-right we do the same thing for the MPO. This is illustrated in Fig. 1.6. For an operator that conserves the $U(1)$ -symmetry the relation

$$\Delta N_{j-1} + n_j = n'_j + \Delta N_j \quad (1.65)$$

has to hold. For the case of particle number conservation it means that particles are not created or destroyed. With this we can now assign the quantum numbers to the bonds in Fig. 1.5. The Hubbard Hamiltonian (Eq. 1.63) allows hopping of a single particle only, therefore we have three different quantum numbers $\Delta N = 0, -1$ and 1 which correspond to the identity, hopping from right to left and hopping from left to right, respectively.

DMRG optimization

We can now formulate the typical DMRG procedure. For the ground state we know

$$\langle \psi_0 | H | \psi_0 \rangle = E_0 \langle \psi_0 | \psi_0 \rangle, \quad (1.66)$$

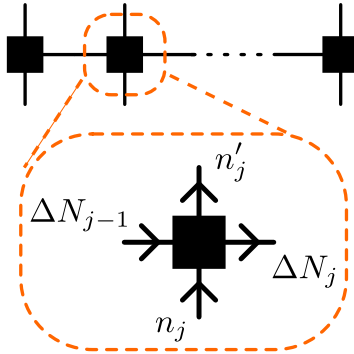


Figure 1.6: Sketch of an MPO. A filled rectangle symbolizes a single tensor. An MPO-tensor is a rank-4 tensor and thus has four legs indicating the four indices: ΔN_{j-1} at the left side representing the left bond index, ΔN_j at the right side representing the right bond index, n_j the lower leg representing the incoming physical index and n'_j at the upper leg which represents the outgoing physical index. The labeling is chosen to be left-to-right directional Eq. (1.65). Bond indices are labeled by the change in the bond indices of an MPS when the MPO is applied onto it: $N'_{j-1} = N_{j-1} + \Delta N_{j-1}$ and $N'_j = N_j - \Delta N_j$.

where $E_0 < E_i \forall i > 0$. In general, the task of finding the ground state can be formulated as a minimization problem in the parameter λ over the variational space of all possible states $|\psi\rangle$

$$\langle \psi | H | \psi \rangle - \lambda \langle \psi | \psi \rangle = 0. \quad (1.67)$$

Because the full system has d^L degrees of freedom this procedure would scale exponential in the system size. As stated earlier, the idea of White [24] was to optimize the state locally and sweep through the system multiple times in the course of the finite-system method. For the standard version - the two-site DMRG scheme - the algorithm optimizes two sites at a time. In MPS formulation the optimization scheme for position j in the system reads

$$\min_{M^{[j,j+1]}} \left[\sum (M_{N'_0, N'_1}^{*n'_1} W_{\Delta N_0, \Delta N_1}^{n'_1, n_1} M_{N_0, N_1}^{n_1}) \right. \\ \dots (M_{N'_{j-1}, N'_{j+1}}^{*n'_j, n'_{j+1}} W_{\Delta N_{j-1}, \Delta N_{j+1}}^{n'_j, n'_{j+1}, n_j, n_{j+1}} M_{N_{j-1}, N_{j+1}}^{n_j, n_{j+1}}) \dots \\ \left. (M_{N'_{L-1}, N'_L}^{*n'_L} W_{\Delta N_{L-1}, \Delta N_L}^{n'_L, n_L} M_{N_{L-1}, N_L}^{n_L}) \right], \quad (1.68)$$

where the sum goes over indices that occur twice in the above equation and $M_{N_{j-1}, N_{j+1}}^{n_j, n_{j+1}} = \sum_{N_j} M_{N_{j-1}, N_j}^{n_j} M_{N_j, N_{j+1}}^{n_{j+1}}$ is the rank-4 tensor describing sites j and $j+1$ and $W_{\Delta N_{j-1}, \Delta N_{j+1}}^{n'_j, n'_{j+1}, n_j, n_{j+1}} = \sum_{\Delta N_j} W_{\Delta N_{j-1}, \Delta N_j}^{n'_j, n_j} W_{\Delta N_j, \Delta N_{j+1}}^{n'_{j+1}, n_{j+1}}$ is the two-site MPO-tensor for these two sites. In words, the equation minimizes the global energy $\langle \psi | H | \psi \rangle$ by variation of the two-site tensor $M_{N_{j-1}, N_{j+1}}^{n_j, n_{j+1}}$

only. To make this equation a bit more handy we introduce the L - and R -tensors

$$\begin{aligned} L_{\Delta N_{j-1}}^{N'_{j-1}, N_{j-1}} &= \sum (M_{N'_0, N'_1}^{*n'_1} W_{\Delta N_0, \Delta N_1}^{n'_1, n_1} M_{N_0, N_1}^{n_1}) \\ &\quad \cdots (M_{N'_{j-2}, N'_{j-1}}^{*n'_{j-1}} W_{\Delta N_{j-2}, \Delta N_{j-1}}^{n'_{j-1}, n_{j-1}} M_{N_{j-2}, N_{j-1}}^{n_{j-1}}) \\ &= \sum M_{N'_{j-2}, N'_{j-1}}^{*n'_{j-1}} W_{\Delta N_{j-2}, \Delta N_{j-1}}^{n'_{j-1}, n_{j-1}} L_{\Delta N_{j-2}}^{N'_{j-2}, N_{j-2}} M_{N_{j-2}, N_{j-1}}^{n_{j-1}}, \end{aligned} \quad (1.69)$$

$$R_{\Delta N_{j+1}}^{N'_{j+1}, N_{j+1}} = \sum M_{N'_{j+1}, N'_{j+2}}^{*n'_{j+2}} W_{\Delta N_{j+1}, \Delta N_{j+2}}^{n'_{j+2}, n_{j+2}} R_{\Delta N_{j+2}}^{N'_{j+2}, N_{j+2}} M_{N_{j+1}, N_{j+2}}^{n_{j+2}}, \quad (1.70)$$

where again the sums run over all indices that occur two times in the equation. Those tensors include all sites that are kept constant at a single optimization step. With this we can write Eq. (1.68)

$$\min_{M^{[j, j+1]}} \left[\sum L_{\Delta N_{j-1}}^{N'_{j-1}, N_{j-1}} (M_{N'_{j-1}, N'_{j+1}}^{*n'_j, n'_{j+1}} W_{\Delta N_{j-1}, \Delta N_{j+1}}^{n'_j, n'_{j+1}, n_j, n_{j+1}} M_{N_{j-1}, N_{j+1}}^{n_j, n_{j+1}} R_{\Delta N_{j+1}}^{N'_{j+1}, N_{j+1}}) \right], \quad (1.71)$$

where again the sum goes over indices that occur twice in the equation and by $M^{[j, j+1]}$ we mean the MPS-tensor describing sites j and $j+1$. The optimization is usually carried out by the Lanczos procedure which treats the M -tensor as a vector $M_{(N_{j-1}, n_j, n_{j+1}, N_{j+1})}$ and the effective Hamiltonian as a matrix

$$\begin{aligned} H_{(N'_{j-1}, n'_j, n'_{j+1}, N'_{j+1}), (N_{j-1}, n_j, n_{j+1}, N_{j+1})} &= \\ L_{\Delta N_{j-1}}^{N'_{j-1}, N_{j-1}} W_{\Delta N_{j-1}, \Delta N_{j+1}}^{n'_j, n'_{j+1}, n_j, n_{j+1}} R_{\Delta N_{j+1}}^{N'_{j+1}, N_{j+1}}. \end{aligned} \quad (1.72)$$

The Lanczos procedure sets up a tridiagonal matrix which, after full diagonalization, yields the eigenstate of the effective Hamiltonian with lowest energy to arbitrary precision. In practice, the Lanczos method constructs an optimal local tensor $\bar{M}_{N_{j-1}, N_{j+1}}^{n_j, n_{j+1}}$ which minimizes the global energy. To return to the MPS-representation of the state the two-site tensor is now split up by use of SVD

$$\bar{M}_{N_{j-1}, N_{j+1}}^{n_j, n_{j+1}} = A_{N_{j-1}, \tilde{N}_j}^{n_j} \lambda_{\tilde{N}_j} B_{\tilde{N}_j, N_{j+1}}^{n_{j+1}}, \quad (1.73)$$

where the bond index \tilde{N}_j is now enhanced to a dimension of md (which is a property of SVD). The key idea of White [24] was to truncate in the basis of the eigenstates of the reduced density matrix of the current half of the system. The density matrix of the system is defined as

$$\begin{aligned} \rho &= |\psi\rangle\langle\psi| \\ &= \sum_{\substack{\vec{n}', \vec{N}' \\ \vec{n}, \vec{N}}} (A_{N'_0, N'_1}^{n'_1} \cdots A_{N'_{j-1}, \tilde{N}'_j}^{n'_j} \lambda_{\tilde{N}'_j} B_{\tilde{N}'_j, N'_{j+1}}^{n'_{j+1}} \cdots B_{N'_{L-1}, N'_L}^{n'_L}) \\ &\quad (A_{N_0, N_1}^{*n_1} \cdots A_{N_{j-1}, \tilde{N}_j}^{*n_j} \lambda_{\tilde{N}_j}^* B_{\tilde{N}_j, N_{j+1}}^{*n_{j+1}} \cdots B_{N_{L-1}, N_L}^{*n_L}) |\vec{n}'\rangle\langle\vec{n}|, \end{aligned} \quad (1.74)$$

where we use the wavefunction after optimization and SVD and \vec{N} includes \tilde{N}_j . The half-cut reduced density matrix then reads

$$\begin{aligned}
\rho_A &= \text{tr}_B(\rho) \\
&= \sum_{\vec{n}_B} \langle \vec{n}_B | \rho | \vec{n}_B \rangle \\
&= \sum (A_{N'_0, N'_1}^{n'_1} \cdots A_{N'_{j-1}, \tilde{N}_j}^{n'_j} \lambda_{\tilde{N}_j} B_{\tilde{N}_j, N'_{j+1}}^{n_{j+1}} \cdots B_{N'_{L-1}, N'_L}^{n_L}) \\
&\quad (A_{N_0, N_1}^{*n_1} \cdots A_{N_{j-1}, \tilde{N}_j}^{*n_j} \lambda_{\tilde{N}_j}^* B_{\tilde{N}_j, N_{j+1}}^{*n_{j+1}} \cdots B_{N_{L-1}, N_L}^{*n_L}) |\vec{n}'_A\rangle \langle \vec{n}_A| \\
&= \sum (A_{N'_0, N'_1}^{n'_1} \cdots A_{N'_{j-1}, \tilde{N}_j}^{n'_j} \lambda_{\tilde{N}_j}) (A_{N_0, N_1}^{*n_1} \cdots A_{N_{j-1}, \tilde{N}_j}^{*n_j} \lambda_{\tilde{N}_j}^*) |\vec{n}'_A\rangle \langle \vec{n}_A| \\
&= \sum |\lambda_{\tilde{N}_j}|^2 |\tilde{N}_j\rangle \langle \tilde{N}_j|.
\end{aligned} \tag{1.75}$$

From this analysis we see that the singular value decomposition of the two-site tensor does provide the optimal set of basis states in the sense that it minimizes the discarded weight Eq. (1.31) and that the square of the singular values gives the importance of those states. The bond can now be truncated by keeping m of the states $|\tilde{N}_j\rangle$ which correspond to the m singular values with the largest magnitudes. After truncation the singular values are rescaled so their squares sum up to one and contracted into $B^{[j+1]}$ during a left-to-right sweep or into $A^{[j]}$ during a right-to-left sweep. The steps are then repeated for the site $j+1$ or $j-1$. The singular value decomposition for an $(m \times n)$ -matrix scales with $\mathcal{O}(\max(m, n) \min(m, n)^2)$ and the two-site DMRG thus scales with $\mathcal{O}(m^3 d^3)$.

Above we described the general DMRG procedure in MPS formulation at the example of the two-site algorithm. It is straightforward to perform optimization over as many sites as one desires.

1.2.2 DMRG with subspace expansion

The standard two-site DMRG algorithm as introduced above is quite stable for one-dimensional models with short-range interactions [26]. This is due to the presence of the second center site which gives the algorithm access to a larger number of states [108]. This will become clear below. However, in comparison to single-site DMRG [39] which optimizes the tensor of a single site at a time and thus scales with $\mathcal{O}(m^3 dw)$ only it also increases the complexity of a single update by a factor of d^2 . The problem with bare single-site DMRG lies in the fact that the state space available during optimization is fixed by the environment and the algorithm can thus get stuck or converge very slowly [39]. We illustrate the argument with the following example.

We consider a product state of a system containing two particles

$$\begin{aligned}
|\psi\rangle &= |1010\rangle \\
&= |1\rangle_A \otimes |0\rangle_S \otimes |10\rangle_B,
\end{aligned} \tag{1.76}$$

where the second line illustrates the system divided into its three parts: Left and right environment blocks ($|1\rangle_A, |10\rangle_B$) and the active site ($|0\rangle_S$) in the middle. If the Hamiltonian that acts on this state conserves the particle number ($U(1)$ symmetry) the $A(B)$ -Block would have a particle quantum number of $N_A = 1$ ($N_B = 1$) which leaves only $N_S = 0$ for the

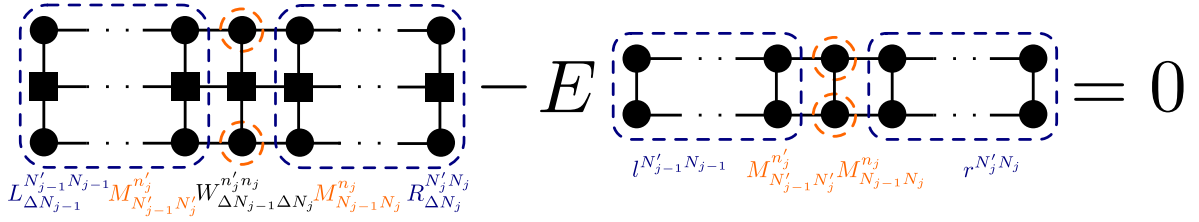


Figure 1.7: Optimization of the wavefunction by variation of a single local tensor only. The environment of the active site j is expressed via the left and right tensors.

system site. An algorithm that is able to change only a single site is pinned for this particular choice of starting state.

In MPS formulation the same state reads

$$|\psi\rangle = A_{0,1}^{[1]1} M_{1,1}^{[2]0} B_{1,2}^{[3]1} B_{2,2}^{[4]0} |1010\rangle, \quad (1.77)$$

where for the tensors chosen above $M_{N_{j-1}, N_j}^{[j]n_j} = 1$ (and $M_{N_{j-1}, N_j}^{[j]n_j} = 0$ for all tensor blocks not shown above) and N_{j-1} denotes the number of particles of the chain left of site j and $N_j = n_j + N_{j-1}$. Starting with a left-to-right sweep at site $j = 2$ we optimize by application of the Hamiltonian on the chain (Eq. 1.68)

$$M_{N'_{L-1}, N'_L}^{n'_L} = \sum (L_{\Delta N_{L-1}}^{N'_{L-1}, N_{L-1}} W_{\Delta N_{L-1}, \Delta N_L}^{n'_L, n_L} R_{\Delta N_L}^{N'_L, N_L}) M_{N_{L-1}, N_L}^{n_L}. \quad (1.78)$$

In the MPS language the information about the environment is encoded in the L and R tensors (Fig. 1.7). Possible fluctuations emerge as nonzero entries in these tensors. For the product state Eq. (1.76) the in- and outgoing bond indices in the left and also in the right tensors need to be identical. Figure 1.7 illustrates this fact: The left and right tensors are built up while keeping the in- and outgoing states fixed. Because the state is a product state only one nonzero value contributes to the left tensor $L_{\Delta N_{j-1}=0}^{N'_{j-1}=1, N_{j-1}=1} = f(\vec{n}_L)$ and the right tensor $R_{\Delta N_j=0}^{N'_j=1, N_j=1} = f(\vec{n}_R)$. In other words, we can sweep as long as we want, this initial state will never transform into the ground state of the Hamiltonian we choose for our system. The advantage of the two-site scheme is that, during optimization, the algorithm has access to the physical state of two adjacent sites and can thus include every fluctuation that is necessary in between the two sites that are compatible with the rest of the system (sites $j - 1$ and $j + 2$).

A strategy to overcome this problem is to work in the so-called centermatrix wavefunction formalism of an MPS [38, 108]

$$\begin{aligned} |\psi\rangle &= \sum_{\vec{a}, \vec{n}} A_{a_0, a_1}^{n_1} \cdots A_{a_{j-2}, a_{j-1}}^{n_{j-1}} M_{a_{j-1}, a_j}^{n_j} B_{a_j, a_{j+1}}^{n_{j+1}} \cdots B_{a_{L-1}, a_L}^{n_L} |\vec{n}\rangle \\ &= \sum_{\vec{a}, \vec{n}} \cdots A_{a_{j-2}, a_{j-1}}^{n_{j-1}} (\tilde{A}_{a_{j-1}, x}^{n_j} C_{x, a_j}) B_{a_j, a_{j+1}}^{n_{j+1}} \cdots |\vec{n}\rangle. \end{aligned} \quad (1.79)$$

The tensor at site j has been replaced by a new local tensor times the centermatrix $M_{a_{j-1}, a_j}^{n_j} = \tilde{A}_{a_{j-1}, x}^{n_j} C_{x, a_j}$, where $C_{x, a_j} = M_{(a_{j-1}, n_j), a_j}$ and $\tilde{A}_{a_{j-1}, x}^{n_j} = \delta_{a_{j-1}d + n_j, x}$ with $x = a_{j-1}d + n_j$. With this substitution two things have happened: the relevant part of the wavefunction is now in C_{x, a_j} and we have increased the bond dimension of the bond a_j by a factor of d . In principle,

this bond does now support all possible fluctuations. To see this in the MPS formulation we can now contract the \tilde{A} -tensor into the L -tensor and thereby enlarge the L -Block by one site

$$L_{b_j}^{x',x} = \tilde{A}_{a'_{j-1},x'}^{*n'_j} W_{b_{j-1},b_j}^{n'_j,n_j} L_{b_{j-1}}^{a'_{j-1},a_{j-1}} \tilde{A}_{a_{j-1},x}^{n_j}. \quad (1.80)$$

The resulting L -tensor will have all possible fluctuations. At this point we see that the contractions above involve operations of $\mathcal{O}(m^3 d^3 w)$. In other words, all advantages of the single-site DMRG in terms of scaling with the local dimension are lost already at that stage. Optimization is now performed on the centermatrix using L and R

$$\bar{C}_{x',a'_j} = L_{b_j}^{x',x} R_{b_j}^{a'_j,a_j} C_{x,a_j}. \quad (1.81)$$

Because R depends on the right bond index a_j , it has not been enhanced and, therefore, does not include fluctuations and the optimization is the same as without the enhanced bond. After this local optimization the C -matrix is contracted into $B_{a_j,a_{j+1}}^{n_{j+1}}$

$$|\psi\rangle = \sum_{\vec{a}, \vec{n}} \cdots A_{a_{j-2},a_{j-1}}^{n_{j-1}} \tilde{A}_{a_{j-1},x}^{n_j} \tilde{B}_{x,a_{j+1}}^{n_{j+1}} B_{a_{j+1},a_{j+2}}^{n_{j+2}} \cdots |\vec{n}\rangle, \quad (1.82)$$

and the algorithm continues in the same way at site $j+1$. Because the $\tilde{A}^{[j]}$ -tensor has been enlarged, fluctuations are now taken fully into account. We see that this procedure is indeed able to include fluctuations into the state and will therefore enable the algorithm to improve the state. However, the scaling with the local dimension is the same as in two-site DMRG.

So far, we did not talk about truncation of the enhanced bond. This is necessary since otherwise, after some sweeps, we will have an MPS with the maximal bond dimension on every site $\mathcal{O}(d^L)$. In general, the bond can be truncated by performing an SVD on the centermatrix after it has been optimized. However, even after optimization the centermatrix is rectangular with the lower dimension being on the right side which sets the maximal number of non-zero singular values to the lower dimension and, therefore, the bond dimension can never grow. Also, even after optimization the centermatrix is zero for all states that have been included artificially on the current bond because of the aforementioned limitation that the right bond does not necessarily support important fluctuations. Because of that, truncation by SVD will choose the same states that have been in the bond prior to expansion which renders the whole procedure meaningless. To overcome this limitation one needs to find out which states will be important during the optimization on the next bond and preserve them during truncation. In 2005 S. White [39] introduced a procedure to perturb the density matrix of the system which does just that. A simple argument is the following. Consider the power method which iteratively projects a random starting state onto the ground state to a given Hamiltonian by successive application of the operator $\exp(-\epsilon H)$ onto the state in every iteration

$$|\psi_{n+1}\rangle = e^{-\epsilon H} |\psi_n\rangle \approx (1 - \epsilon H) |\psi_n\rangle. \quad (1.83)$$

The point is that for ϵ small enough (smaller than the inverse of the highest eigenvalue of the Hamiltonian $\epsilon |E_{\max}| < 1$) and a non-vanishing overlap between initial state and ground state the power method is guaranteed to converge to the ground state $|\psi_{n \rightarrow \infty}\rangle = |\psi_0\rangle$ provided that in every step $|\psi_n\rangle$ and $H|\psi_n\rangle$ are supported by the basis (in other words: the basis has to be able to represent this state). To ensure that the state $H|\psi_n\rangle$ is included into the basis, we first decompose H into two parts: one that acts on the system block (the left part of

the system during a left-to-right sweep and the right part during a right-to-left sweep, see Fig. 1.3) and another that acts on the environment block (the rest of the system)

$$\begin{aligned}
H &= \sum_{\vec{b}\vec{n}\vec{n}'} W_{b_0 b_1}^{n'_1 n_1} \cdots W_{b_{j-1} b_j}^{n'_j n_j} W_{b_j b_{j+1}}^{n'_{j+1} n_{j+1}} \cdots W_{b_{L-1} b_L}^{n'_L n_L} |\vec{n}'\rangle \langle \vec{n}| \\
&= \sum_{b_j} \left(\sum_{\vec{n}'_A \vec{n}_A} X_{b_j}^{\vec{n}'_A \vec{n}_A} |\vec{n}'_A\rangle \langle \vec{n}_A| \right) \otimes \left(\sum_{\vec{n}'_B \vec{n}_B} Y_{b_j}^{\vec{n}'_B \vec{n}_B} |\vec{n}'_B\rangle \langle \vec{n}_B| \right) \\
&= \sum_{\alpha} \hat{A}^{\alpha} \otimes \hat{B}^{\alpha}
\end{aligned} \tag{1.84}$$

where $A^{\alpha} \otimes B^{\alpha}$ include all terms that work on the system only $X_A \otimes \mathbb{1}_B$, environment only $\mathbb{1}_A \otimes Y_B$ and both $Z_A \otimes Z_B$. Using Eq. (1.84) we can now get the contribution of $H|\psi\rangle$ on the system block

$$\begin{aligned}
A^{\alpha}|\psi\rangle &= \sum (W_{b_0 b_1}^{n'_1 n_1} A_{a_0, a_1}^{n_1} \cdots (W_{b_{j-1} b_j}^{n'_j n_j} M_{a_{j-1}, a_j}^{n_j} B_{a_j, a_{j+1}}^{n_{j+1}} \cdots |\vec{n}'_A\rangle \otimes |\vec{n}_B\rangle) \\
&= \sum \cdots (W_{b_{j-1} \alpha}^{n'_j n_j} \tilde{M}_{a_{j-1}, x}^{n_j} C_{x, a_j} B_{a_j, a_{j+1}}^{n_{j+1}} \cdots |\vec{n}'_A\rangle \otimes |\vec{n}_B\rangle),
\end{aligned} \tag{1.85}$$

where the sum is over indices that occur two times. To get an idea of the importance of the bond states that are introduced by $A^{\alpha}|\psi\rangle$ we trace over block B and fix the state on sites $i = 1, \dots, j$. The latter is necessary since we can not change other sites but the currently active one and are thus only interested in the weights for the states we can reach. With this we set up the change in the reduced density matrix for our respective bond

$$\begin{aligned}
\Delta\rho^{\alpha} &= a_{\alpha} \langle \psi_A | \text{tr}_B (A^{\alpha} |\psi\rangle \langle \psi| A^{\dagger \alpha}) | \psi_A \rangle \\
&= a_{\alpha} \sum_{\substack{x, x' \\ x'', x''' \\ a_j}} (L_{\alpha}^{x'', x} C_{x, a_j}) (C_{x', a_j}^* L_{\alpha}^{x''', x'}) \\
&= a_{\alpha} \sum_{\substack{x, x' \\ x'', x'''}} L_{\alpha}^{x'', x} \rho_{x, x'} L_{\alpha}^{x''', x'},
\end{aligned} \tag{1.86}$$

where $\rho_{x, x'} = \sum_{a_j} C_{x, a_j} C_{x', a_j}^*$ is the reduced density matrix for block A (see Fig. 1.3).

To see that this actually works we can employ the example from before again. We again take the left part of the system including site $j = 2$ as block A and the rest of the system as block B and expand the bond between sites $j = 2$ and $j = 3$.

$$\begin{aligned}
|\psi\rangle &= A_{0,1}^{[1]1} M_{1,1}^{[2]0} B_{1,2}^{[3]1} B_{2,2}^{[4]0} |1010\rangle \\
&= A_{0,1}^{[1]1} (\tilde{A}_{1,1}^{[2]0}, \tilde{A}_{1,2}^{[2]1}) \begin{pmatrix} C_{1,1} \\ C_{2,2} \end{pmatrix} B_{1,2}^{[3]1} B_{2,2}^{[4]0} |1010\rangle.
\end{aligned} \tag{1.87}$$

We assume that the Hamiltonian we want to apply to this system contains nonzero terms that let a particle hop from one site to the next: $W_{1,0}^{0,-1}, W_{0,1}^{0,1}$. From the centermatrix we can

directly set up the reduced density matrix for the bond

$$\begin{aligned}
\rho &= \sum_{x,x'} \rho_{x,x'} \\
&= \rho_{1,1} \\
&= \begin{pmatrix} 0 & 0 & 0 \\ 0 & \rho_{1,1} & 0 \\ 0 & 0 & 0 \end{pmatrix}.
\end{aligned} \tag{1.88}$$

For the left tensor we find

$$L = (L_{-1}^{2,1}, L_1^{1,2}). \tag{1.89}$$

Insertion of those objects in Eq. (1.86) yields the perturbation

$$\Delta\rho^{-1} = a_{-1}\Delta\rho_{2,2} \tag{1.90}$$

We see that the term suggests to enlarge the bond state space by the $N = 2$ state

$$\begin{aligned}
\rho' &= \rho + \Delta\rho \\
&= \begin{pmatrix} 0 & 0 & 0 \\ 0 & \rho_{1,1} & 0 \\ 0 & 0 & a_{-1}\Delta\rho_{2,2} \end{pmatrix}.
\end{aligned} \tag{1.91}$$

The centermatrix wavefunction formalism enlarges the active bond to include all states reachable by application of the Hamiltonian while keeping the bonds to the left and right fixed. To truncate, it is necessary to perform $\mathcal{O}(m^3d^3)$ operations which is no improvement over two-site DMRG.

In 2015 Hubig et al. [38] introduced a new way of enriching the local state space which scales linearly in the local dimension. Above, we argue that it is crucial to include both $|\psi\rangle$ and $H|\psi\rangle$ in the basis to achieve convergence. The left part of the Hamiltonian was applied to the full reduced density matrix in the basis including *all* fluctuations to be able to cherry-pick the important states from the huge mass of all the states. Even though we enlarge the state space by all possible fluctuations d , a single application of the Hamiltonian can only create w fluctuations at a single bond

$$\begin{aligned}
W_{b_{j-1}, b_j}^{n'_j, n_j} M_{a_{j-1}, a_j}^{n_j} &= \tilde{M}_{(a_{j-1}b_{j-1}), (a_j b_j)}^{n'_j} \\
&= \tilde{M}_{\tilde{a}_{j-1}, \tilde{a}_j}^{n'_j},
\end{aligned} \tag{1.92}$$

where \tilde{M} is a $(mw \times d \times mw)$ -tensor (and not $(md \times d \times md)$). In other words, even though we enhance the space by d states only w can be reached by the procedure outlined above. The idea of Hubig et al. [38] was to expand the local tensor only by the states that can be reached by a single application of the Hamiltonian. In fact, we can pretend to know the states we need and set up the centermatrix state in this smaller statespace. This leads to an enhanced local tensor $\tilde{A}_{a_{j-1}, x}^{n_j}$ and centermatrix C_{x, a_j} where \tilde{A} is now a $(m \times d \times mw)$ -tensor and C is a $(mw \times m)$ -matrix. Following the procedure above we find that it now scales with $\mathcal{O}(m^3dw^3)$. To enhance the bond dimension the authors make use of the so-called subspace expansion.

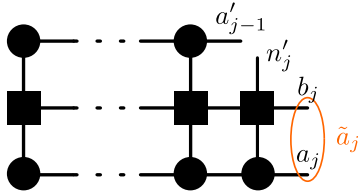


Figure 1.8: Graphical representation of the expansion tensor Eq. (1.95).

This idea originates in the so-called tensor train community [38, 109]. Here, the local state space is enhanced by directly expanding the local state tensors on two adjacent sites by an expansion term P

$$\begin{aligned}
|\psi\rangle &= \sum_{\vec{a}, \vec{n}} A_{a_0, a_1}^{n_1} \cdots A_{a_{j-2}, a_{j-1}}^{n_{j-1}} M_{a_{j-1}, a_j}^{n_j} B_{a_j, a_{j+1}}^{n_{j+1}} \cdots B_{a_{L-1}, a_L}^{n_L} |\vec{n}\rangle \\
&= \sum_{\vec{a}, \vec{n}} \cdots A_{a_{j-2}, a_{j-1}}^{n_{j-1}} \tilde{M}_{a_{j-1}, x}^{n_j} \tilde{B}_{x, a_{j+1}}^{n_{j+1}} B_{a_{j+1}, a_{j+2}}^{n_{j+2}} \cdots |\vec{n}\rangle,
\end{aligned} \tag{1.93}$$

where

$$\tilde{M}^{[j]} = (M^{[j]}, P^{[j]}), \quad \tilde{B}^{[j+1]} = \begin{pmatrix} B^{[j+1]} \\ 0 \end{pmatrix}. \tag{1.94}$$

The tensor $P^{[j]}$ is built by first applying the left part of the Hamiltonian A to the left part of the wavefunction and then projecting it onto the current state one site left of the current site $j - 1$

$$P_{a'_{j-1}, \tilde{a}_j}^{n'_j} = a L_{b_{j-1}}^{a'_{j-1}, a_{j-1}} W_{b_{j-1}, b_j}^{n'_j, n_j} M_{a_{j-1}, a_j}^{n_j}, \tag{1.95}$$

where $\tilde{a}_j = (a_j b_j)$ and a is a constant parameter. This is sketched in Fig. 1.8. In fact, this is very similar to Eq. (1.86) with the difference that, here, we enhance the bond a_j by b_j while before we enhanced prior to this step in "all possible ways" and by doing this step found the importance of the "unknown" states. The actual subspace expansion is now performed by putting both $M^{[j]}$ and $P^{[j]}$ into one tensor. Without the use of quantum numbers one actually just "copies them together". The tensor one site to the right $B^{[j+1]}$ is enhanced by zeros to match the dimension. Because of the zero-padding the global state did not change at all. Note also that we are now able to truncate by SVD because the bond dimension is not bounded by just a single bond index but by the combined index of local and left bond index which has dimension $md > mw$ where we assume $d \gg w$ (as is mostly the case). The construction of $P^{[j]}$ scales with $\mathcal{O}(m^3 dw) + \mathcal{O}(m^2 d^2 w^2)$ and the truncation of the resulting tensor by SVD scales with $\mathcal{O}(m^3 dw^2)$. Taking everything together the single-site DMRG with subspace expansion (DMRG3S) scales with $\mathcal{O}(m^3 dw^2) + \mathcal{O}(m^2 d^2 w^2)$.

1.3 Local optimal mode states in DMRG with subspace expansion

As described above the great advantage of the DMRG3S algorithm is the reduction of the scaling with the local degrees of freedom from $\mathcal{O}(d^3)$ to $\mathcal{O}(d)$ for a dominating bond index

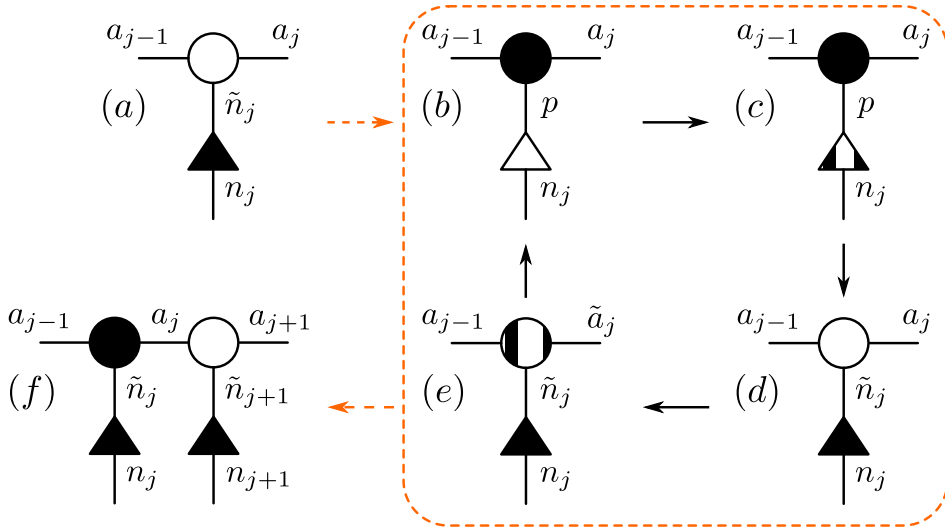


Figure 1.9: Flow diagram of the variational MPS algorithm with local basis optimization [37].

dimension $m \gg d \gg w$ or to $\mathcal{O}(d^2)$ for dominating local dimension $d \gg m \gg w$. In bosonic systems which feature potentially large local dimensions this reduction has a huge impact. Guo et al. [37] incorporate the truncation in the optimal mode basis into the DMRG algorithm. In this section we describe the crucial steps of this algorithm and show how to combine it with the DMRG3S method. The resulting algorithm updates the bonds in the same way as the DMRG3S algorithm but additionally carries out a truncation in the local degrees of freedom which has the potential to further reduce the computational effort.

A test of the method described here is presented in Chapter 2.

1.3.1 The OBB-VMPS optimization procedure

The DMRG algorithm sweeps through the system and tries to find the optimal basis for the current bond while the local state space remains unchanged. Guo et al. [37] alter the update of the bond: They substitute it by an iterative self-consistent update of both, the local and the bond degrees of freedom. The update scheme is presented in Fig. 1.9. Starting point for the algorithm is shifting the focus from the bond degrees of freedom to the local degrees of freedom (step (a) to (b) in Fig. 1.9). The site update starts with an optimization of the local basis for the current environment (c). After that, the focus is shifted back to the bond degrees of freedom (d). During a left-to-right sweep the bond is then optimized using one of the above described variants of DMRG in (e). To be self-consistent, the steps (b)-(e) are repeated until the local basis has converged. After that, the sweeping proceeds to the next site in the chain (f) and the algorithm starts from (a).

Local state transformations

The procedure relies on a decomposition of each MPS-tensor into a part encoding the transformation from the optimized local basis to the original occupation number states and another part which approximates the original tensor. We start from a standard left-normalized

matrix-product state

$$|\psi\rangle = \sum_{\vec{a}, \vec{n}} A_{a_0, a_1}^{n_1} \cdots A_{a_{L-1}, a_L}^{n_L} |\vec{n}\rangle, \quad (1.96)$$

where \vec{a} is a shorthand for the bond indices and $|\vec{n}\rangle$ is a shorthand for the physical degrees of freedom. Another way of representing the same state is

$$|\psi\rangle = \sum_{\vec{a}, \vec{n}, \vec{\tilde{n}}} (\tilde{A}_{a_0, a_1}^{\tilde{n}_1} V^{\tilde{n}_1, n_1}) \cdots (\tilde{A}_{a_{L-1}, a_L}^{\tilde{n}_L} V^{\tilde{n}_L, n_L}) |\vec{n}\rangle, \quad (1.97)$$

at which we arrive by performing an SVD on each site which splits the bond indices from the physical index

$$A_{a_{j-1}, a_j}^{n_j} \rightarrow A_{(a_{j-1}, a_j), \tilde{n}_j} \quad (1.98)$$

$$A_{(a_{j-1}, a_j), \tilde{n}_j} = \sum_{\tilde{n}_j} U_{(a_{j-1}, a_j), \tilde{n}_j} S_{\tilde{n}_j, \tilde{n}_j} V_{\tilde{n}_j, n_j}^\dagger \quad (1.99)$$

$$A_{a_{j-1}, a_j}^{n_j} = \tilde{A}_{a_{j-1}, a_j}^{\tilde{n}_j} V^{\tilde{n}_j, n_j}, \quad (1.100)$$

where $\tilde{A}_{a_{j-1}, a_j}^{\tilde{n}_j} = U_{a_{j-1}, a_j}^{\tilde{n}_j} S_{\tilde{n}_j, \tilde{n}_j}$. Because in this form the $V^{\tilde{n}_j, n_j}$ operators are only a basis transformation we can also express the state in the $|\vec{\tilde{n}}\rangle$ basis

$$|\psi\rangle = \sum_{\vec{a}, \vec{\tilde{n}}} \tilde{A}_{a_0, a_1}^{\tilde{n}_1} \cdots \tilde{A}_{a_{L-1}, a_L}^{\tilde{n}_L} |\vec{\tilde{n}}\rangle. \quad (1.101)$$

Both of those forms Eqs. (1.97) and (1.101) will be of importance later. Note that, at this point, we have not truncated in any way and the two basis sets $|\vec{n}\rangle$ and $|\vec{\tilde{n}}\rangle$ are exact representations of the same state while the V -tensors transform between the two representations.

Relation between local basis transformation and local reduced density matrix

We want to see what those local basis transformations are and start from a mixed-canonical state

$$|\psi\rangle = \sum_{\vec{a}, \vec{n}} A_{a_0, a_1}^{n_1} \cdots A_{a_{j-2}, a_{j-1}}^{n_{j-1}} M_{a_{j-1}, a_j}^{n_j} B_{a_j, a_{j+1}}^{n_{j+1}} \cdots B_{a_{L-1}, a_L}^{n_L} |\vec{n}\rangle, \quad (1.102)$$

where we can say that the current "focus" (the norm of the state) is on site j . We want to calculate the density matrix for this state

$$\begin{aligned} \rho &= |\psi\rangle\langle\psi| \\ &= \sum_{\vec{a}, \vec{n}, \vec{a}', \vec{n}'} (\cdots A_{a_{j-2}, a_{j-1}}^{n_{j-1}} M_{a_{j-1}, a_j}^{n_j} B_{a_j, a_{j+1}}^{n_{j+1}} \cdots) \\ &\quad \times (\cdots A_{a'_{j-2}, a'_{j-1}}^{n'_{j-1}} M_{a'_{j-1}, a'_j}^{n'_j} B_{a'_j, a'_{j+1}}^{n'_{j+1}} \cdots) \\ &= \sum_{a_{j-1} a_j n_j, a'_{j-1} a'_j n'_j} (M_{a_{j-1}, a_j}^{n_j} |a_{j-1}\rangle_A \otimes |a_j\rangle_B \otimes |n_j\rangle) \\ &\quad \times (M_{a'_{j-1}, a'_j}^{n'_j} \langle a'_{j-1}|_A \otimes \langle a'_j|_B \otimes \langle n'_j|), \end{aligned} \quad (1.103)$$

where

$$|a_{j-1}\rangle_A = \sum_{\{a_i\}_{i<j}} A_{a_0,a_1}^{n_1} \cdots A_{a_{j-2},a_{j-1}}^{n_{j-1}} |n_1 \cdots n_{j-1}\rangle$$

and

$$|a_j\rangle_B = \sum_{\{a_i\}_{i>j}} B_{a_j,a_{j+1}}^{n_{j+1}} \cdots B_{a_{L-1},a_L}^{n_L} |n_{j+1} \cdots n_L\rangle$$

The local reduced density matrix is given by

$$\begin{aligned} \rho^{(1)} &= \text{tr}_{AB}(\rho) \\ &= \sum_{a''_{j-1}, a''_j} \sum_{a'_{j-1}, a'_j} M_{a_{j-1}, a_j}^{n_j} M_{a'_{j-1}, a'_j}^{*n'_j} \langle a'_{j-1} | a''_{j-1} \rangle_A \langle a'_j | a''_j \rangle_B \\ &\quad \langle a''_{j-1} | a_{j-1} \rangle_A \langle a''_j | a_j \rangle_B \\ &\quad |n_j\rangle \langle n'_j| \\ &= \sum_{\substack{a_{j-1}, a_j \\ n_j, n'_j}} M_{a_{j-1}, a_j}^{n_j} M_{a_{j-1}, a_j}^{*n'_j} |n_j\rangle \langle n'_j|. \end{aligned} \tag{1.104}$$

To advance, we perform singular value decomposition on $M_{a_{j-1}, a_j}^{n_j}$ after grouping the two bond indices together

$$\begin{aligned} \rho^{(1)} &= \sum_{\substack{a_{j-1}, a_j \\ n_j, n'_j}} \sum_{p, p'} (\tilde{M}_{a_{j-1}, a_j}^p \lambda_p V_{p, n_j}) (\tilde{M}_{a_{j-1}, a_j}^{*p'} \lambda_{p'}^* V_{p', n'_j}^*) |n_j\rangle \langle n'_j| \\ &= \sum_{\substack{a_{j-1}, a_j \\ n_j, n'_j}} \sum_{p, p'} \tilde{M}_{a_{j-1}, a_j}^p \tilde{V}_{p, n_j} \tilde{M}_{a_{j-1}, a_j}^{*p'} \tilde{V}_{p', n'_j}^* |n_j\rangle \langle n'_j| \\ &= \sum_{n_j, n'_j, p} \tilde{V}_{p, n_j} \tilde{V}_{p, n'_j}^* |n_j\rangle \langle n'_j|, \end{aligned} \tag{1.105}$$

where in the second line $\tilde{V}_{p, n_j} = \sum_p \lambda_p V_{p, n_j}$ and in the last line

$$\sum_{a_{j-1}, a_j} \tilde{M}_{a_{j-1}, a_j}^p \tilde{M}_{a_{j-1}, a_j}^{*p'} = \delta_{pp'}$$

is used. The identity of the last line is possible because of the property $U^\dagger U = \mathbb{1}$ of the left matrix after singular value decomposition. From this derivation we see that indeed the local transformation tensor \tilde{V}_{p, n_j} is related to the local reduced density matrix by $\sum_p \tilde{V}_{p, n_j} \tilde{V}_{p, n'_j}^*$. Also, we can see from line three that the singular values of the preceding singular value decomposition are the squareroot of the eigenvalues of the local reduced density matrix:

$$\begin{aligned} \rho^{(1)} &= \sum_{n_j, n'_j} \sum_p \lambda_p \lambda_p^* (V_{p, n_j} |n_j\rangle) (\langle n'_j | V_{p, n'_j}^*) \\ &= \sum_p |\lambda_p|^2 |p\rangle \langle p|, \end{aligned} \tag{1.106}$$

where we have used $|p\rangle = \sum_{n_j, n'_j} V_{p, n_j} |n_j\rangle$. Comparing to Eq. (1.2) we see that the optimization of the local Hilbert space is indeed equivalent to a truncation in the optimal mode basis [36, 37, 41].

Local Hilbertspace optimization

In this section we describe the step in which the local Hilbertspace is optimized (steps (a) to (d) in Fig. 1.9). To get started we consider a state in the middle of a DMRG sweep where we assume we already have an optimal basis on every site (this might also be a trivial cutoff at the start of the algorithm)

$$\begin{aligned} |\psi\rangle &= \sum_{\substack{\vec{n}_j, n_j \\ \vec{a}}} \cdots A_{a_{j-2}, a_{j-1}}^{n_{j-1}} (\tilde{M}_{a_{j-1}, a_j}^{\vec{n}_j} V_{\vec{n}_j, n_j}) B_{a_j, a_{j+1}}^{n_{j+1}} \cdots |\vec{n}_j\rangle \otimes |n_j\rangle \\ &= \sum_{\substack{\vec{n}_j, n_j \\ a_{j-1}, a_j}} \tilde{M}_{a_{j-1}, a_j}^{\vec{n}_j} V_{\vec{n}_j, n_j} |a_{j-1}\rangle_A \otimes |n_j\rangle \otimes |a_j\rangle_B \end{aligned} \quad (1.107)$$

where $|\vec{n}_j\rangle$ denotes the local state on all sites except the j -th site and $M_{a_{j-1}, a_j}^{n_j} = \tilde{M}_{a_{j-1}, a_j}^{\vec{n}_j} V_{\vec{n}_j, n_j}$. We want to shift the focus to the V tensor so we perform an SVD on the \tilde{M} tensor (step (a) to (b) in Fig. 1.9)

$$\begin{aligned} |\psi\rangle &= \sum_{\substack{\vec{n}_j, n_j \\ a_{j-1}, a_j}} \tilde{M}_{(a_{j-1}, a_j), \vec{n}_j} V_{\vec{n}_j, n_j} |a_{j-1}\rangle_A \otimes |n_j\rangle \otimes |a_j\rangle_B \\ &= \sum_p X_{a_{j-1}, a_j}^p \lambda_p Y_{p, \vec{n}_j} V_{\vec{n}_j, n_j} |a_{j-1}\rangle_A \otimes |n_j\rangle \otimes |a_j\rangle_B \\ &= \sum_{\substack{\vec{n}_j, n_j \\ p}} \lambda_p Y_{p, \vec{n}_j} V_{\vec{n}_j, n_j} |p\rangle \otimes |n_j\rangle \\ &= \sum_{n_j, p} \tilde{V}_{p, n_j} |p\rangle \otimes |n_j\rangle, \end{aligned} \quad (1.108)$$

where the last line emerges by contraction of $\lambda_p Y_{p, \vec{n}_j}$ into $\tilde{V}_{\vec{n}_j, n_j}$. At this point we see the analogy to Eq. (1.105) (where the environment has been traced out). This form can now be used to optimize the local physical Hilbertspace.

The former paragraph shows how to shift the focus from the bond indices ("vertical" cut through system) to the local Hilbertspace ("horizontal" cut through system). Now we will use this form to optimize in the local space. We optimize the \tilde{V}_{p, n_j} -tensor using a Lanczos procedure. The expensive operation during this procedure is the application of the Hamiltonian on the local state tensor

$$\tilde{V}'_{(p', n'_j)} = H_{(p', n'_j), (p, n_j)} \tilde{V}_{(p, n_j)}. \quad (1.109)$$

To see how this operation scales we write down the full expression

$$\tilde{V}'_{p', n'_j} = X_{a'_{j-1}, a'_j}^{*p'} \left(L_{b_{j-1}}^{a'_{j-1}, a_{j-1}} W_{b_{j-1}, b_j}^{n'_j, n_j} R_{b_j}^{a'_j, a_j} \right) X_{a_{j-1}, a_j}^p \tilde{V}_{p, n_j}, \quad (1.110)$$

where the X_{a_{j-1},a_j}^p represent a basis transformation

$$|p\rangle = \sum_{a_{j-1},a_j} X_{a_{j-1},a_j}^p |a_{j-1}\rangle \otimes |a_j\rangle.$$

Leaving out the $X_{a'_{j-1},a'_j}^{*p'}$ on the left side of the equation we recover the usual local optimization scheme since $X_{a_{j-1},a_j}^p \tilde{V}_{p,n_j} = M_{a_{j-1},a_j}^{n_j}$. To achieve optimal ordering we perform Eq. (1.110) in the following way

$$\sum_{a'_{j-1}} X_{a'_{j-1},a'_j}^{*p'} L_{b_{j-1}}^{a'_{j-1},a_{j-1}} = \alpha_{a'_j,b_{j-1}}^{p',a_{j-1}} \rightarrow \mathcal{O}(m^3 d_O w) \quad (1.111)$$

$$\sum_{a_j} R_{b_j}^{a'_j,a_j} X_{a_{j-1},a_j}^p = \beta_{b_j,a_{j-1}}^{a'_j,p} \rightarrow \mathcal{O}(m^3 d_O w) \quad (1.112)$$

$$\sum_{n_j} W_{b_{j-1},b_j}^{n'_j,n_j} \tilde{V}_{p,n_j} = \gamma_{b_{j-1},b_j}^{n'_j,p} \rightarrow \mathcal{O}(d^2 d_O w^2) \quad (1.113)$$

$$\sum_{b_j,p} \gamma_{b_{j-1},b_j}^{n'_j,p} \beta_{b_j,a_{j-1}}^{a'_j,p} = \delta_{b_{j-1},a_{j-1}}^{n'_j,a'_j} \rightarrow \mathcal{O}(m^2 d d_O w^2) \quad (1.114)$$

$$\sum_{\substack{a'_j,a_{j-1} \\ b_{j-1}}} \alpha_{a'_j,b_{j-1}}^{p',a_{j-1}} \delta_{b_{j-1},a_{j-1}}^{n'_j,a'_j} = \tilde{V}^{p',n'_j} \rightarrow \mathcal{O}(m^2 d d_O w), \quad (1.115)$$

where we see that a single multiplication scales with $\mathcal{O}(m^3 d_O w) + \mathcal{O}(m^2 d d_O w^2)$.

After this update procedure, the focus of the state is shifted back to the bond by performing an SVD on \tilde{V}^{p,n_j} and contraction of the left-canonical part and the singular values into X_{a_{j-1},a_j}^p . Note, that no truncation is needed at this step because the dimension of p has not grown.

The problem of multiple subspaces

In the above formulation the algorithm works well when no $U(1)$ symmetries are used. In this case, the local update procedure can distribute the states over local subspaces as it pleases. We want to see what happens for a model describing spinless electrons coupled to phonons like the Holstein model which also conserves the global particle number. Then, at every site we have two local particle subspaces $n = 0, 1$ which both have a substructure due to the fact that phonons are not globally conserved. The problem is that a certain choice of d_O can not be changed by the algorithm and the first choice of optimal modes fixes this number for each subspace. This can be inferred by inspection of the local update Eq. (1.109): the dimension of p' and p is fixed by the number of optimal modes in each subspace individually because this is the smallest dimension when shifting the focus from the bond to the local degrees of freedom. Afterwards, the focus is shifted back to the bond and again an SVD is performed with p having smallest dimension. The point is, that we can never increase the number of optimal modes in a given subspace as soon as it is chosen once.

There are multiple ways of circumventing this problem and we describe three of them. In

general, we can use subspace expansion in order to change the number of states

$$\bar{X} = (X, 0), \quad (1.116)$$

$$\bar{V} = \begin{pmatrix} \tilde{V} \\ \alpha Q \end{pmatrix}, \quad (1.117)$$

where Q is some expansion term that mixes in new states and α is its weight. The difference in schemes is now the difference in possible expansion terms Q . Afterwards, the space is truncated back to either the global d_O highest weighted optimal modes or to a fixed local number of states d_O .

The first and simplest one is the expansion of each subspace by a zero matrix $Q = 0$ with dimension d_O . Remember that the sole purpose of the subspace expansion is to enable all subspaces to choose the same number of optimal modes and this is what the zero matrix does. After this expansion the space is truncated down to $\dim(p) = d_O$ in all subspaces. Due to the SVD the V -tensor includes d_O states. In order to perform a global truncation we keep all states up to the point where the first subspace chooses the d_O mode. This is necessary because keeping the same number of optimal modes in all subspaces might introduce an inconsistency (there might be optimal modes that are not included in the chosen space).

Another scheme is to expand using an identity matrix $Q = \mathbb{1}$ with dimension d . This includes all possible bare states and is the optimal expansion term. However, one needs to keep track of the α parameter which needs to be updated dynamically just as in the usual subspace expansion.

The last scheme is to expand by all possible states that the local Hamiltonian can construct

$$\begin{aligned} Q_{\bar{p}_j, n_j} &= W_{\Delta N_{j-1}, \Delta N_j}^{n'_j, n_j} \tilde{V}_{p_j, n_j} \\ &= Q_{(\Delta N_{j-1}, \Delta N_j, p_j), n_j}, \end{aligned} \quad (1.118)$$

where $\bar{p}_j = (\Delta N_{j-1}, \Delta N_j, p_j)$. This term is analogous to the P -tensor during the usual subspace expansion Eq. (1.95).

In our work, we use the simplest variant which keeps the same number of states in all subspaces. For a test of this method on the example of the Hubbard-Holstein model, see Chap. 2.

1.3.2 DMRG3S-LBO bond update

The remaining step in the algorithm is the update of the bond dimension. This step corresponds to parts (e) and (f) in Fig. 1.9. As described, we want to use the DMRG3S algorithm because of its linear scaling in the local dimension. This algorithm is described in Sec. 1.2.2. The most expensive steps are the application of the effective Hamiltonian onto the local tensor, the calculation of the subspace expansion tensor $P_{a_{j-1}, (a_j w_j)}^{n_j}$ and the subsequent singular value decomposition.

We start with the application of the effective Hamiltonian

$$\tilde{M}_{a'_{j-1}, a'_j}^{\tilde{n}'_j} = H_{(a'_{j-1}, \tilde{n}'_j, a'_j), (a_{j-1}, \tilde{n}_j, a'_j)} M_{a_{j-1}, a_j}^{\tilde{n}_j}. \quad (1.119)$$

We write down the full operation to infer the scaling

$$\tilde{M}_{a'_{j-1}, a'_j}^{\tilde{n}'_j} = \tilde{V}_{\tilde{n}'_j, n'_j}^* \left(L_{b_{j-1}}^{a'_{j-1}, a_{j-1}} W_{b_{j-1}, b_j}^{n'_j, n_j} R_{b_j}^{a'_j, a_j} \right) \tilde{V}_{\tilde{n}_j, n_j} M_{a_{j-1}, a_j}^{\tilde{n}_j}, \quad (1.120)$$

where now the $\tilde{V}_{\tilde{n}_j, n_j}$ is a basis transformation

$$|\tilde{n}_j\rangle = \sum_{n_j} \tilde{V}_{\tilde{n}_j, n_j} |n_j\rangle.$$

We can leave out the $\tilde{V}_{\tilde{n}_j, n_j}$ on the left side of Eq. (1.120) and arrive at the usual bond update of the local tensor. We achieve optimal ordering when performing the multiplications in the following order

$$\sum_{n_j} W_{b_{j-1}, b_j}^{n'_j, n_j} \tilde{V}_{\tilde{n}_j, n_j} = \alpha_{b_{j-1}, b_j}^{n'_j, \tilde{n}_j} \rightarrow \mathcal{O}(d^2 d_O w^2) \quad (1.121)$$

$$\sum_{n'_j} \tilde{V}_{\tilde{n}_j, n'_j} \alpha_{b_{j-1}, b_j}^{n'_j, \tilde{n}_j} = \beta_{b_{j-1}, b_j}^{\tilde{n}'_j, \tilde{n}_j} \rightarrow \mathcal{O}(d d_O^2 w^2) \quad (1.122)$$

$$\sum_{a_j} R_{b_j}^{a'_j, a_j} \tilde{M}_{a_{j-1}, a_j}^{\tilde{n}_j} = \gamma_{b_j, a_{j-1}}^{a'_j, \tilde{n}_j} \rightarrow \mathcal{O}(m^3 d_O w) \quad (1.123)$$

$$\sum_{\tilde{n}_j, b_j} \beta_{b_{j-1}, b_j}^{\tilde{n}'_j, \tilde{n}_j} \gamma_{b_j, a_{j-1}}^{a'_j, \tilde{n}_j} = \delta_{b_{j-1}, a_{j-1}}^{\tilde{n}'_j, a'_j} \rightarrow \mathcal{O}(m^2 d_O^2 w^2) \quad (1.124)$$

$$\sum_{a_{j-1}, b_{j-1}} L_{b_{j-1}}^{a'_{j-1}, a_{j-1}} \delta_{b_{j-1}, a_{j-1}}^{\tilde{n}'_j, a'_j} = \tilde{M}_{a'_{j-1}, a'_j}^{\tilde{n}'_j} \rightarrow \mathcal{O}(m^3 d_O w), \quad (1.125)$$

where we see a scaling with $\mathcal{O}(m^2 d_O^2 w^2)$ which is slightly better than the scaling of the update of the local degrees of freedom $\mathcal{O}(m^2 d d_O w^2)$ where the full local dimension enters linearly.

The next operation is the calculation of the subspace expansion tensor which we demonstrate for a left-to-right sweep

$$P_{a_{j-1}, (a_j b_j)}^{\tilde{n}_j} = L_{b_{j-1}}^{a'_{j-1}, a_{j-1}} V^{* \tilde{n}'_j, n'_j} W_{b_{j-1}, b_j}^{n'_j, n_j} V^{\tilde{n}_j, n_j} M_{a_{j-1}, a_j}^{\tilde{n}_j}, \quad (1.126)$$

where $V^{\tilde{n}_j, n_j}$ is inserted to transform the MPO-tensor to the optimal mode basis. This operation is optimally performed in the order

$$\sum_{n_j} W_{b_{j-1}, b_j}^{n'_j, n_j} \tilde{V}_{\tilde{n}_j, n_j} = \alpha_{b_{j-1}, b_j}^{n'_j, \tilde{n}_j} \rightarrow \mathcal{O}(d^2 d_O w^2) \quad (1.127)$$

$$\sum_{n'_j} \tilde{V}_{\tilde{n}'_j, n'_j} \alpha_{b_{j-1}, b_j}^{n'_j, \tilde{n}_j} = \beta_{b_{j-1}, b_j}^{\tilde{n}'_j, \tilde{n}_j} \rightarrow \mathcal{O}(d d_O^2 w^2) \quad (1.128)$$

$$\sum_{a_j} \beta_{b_{j-1}, b_j}^{\tilde{n}'_j, \tilde{n}_j} M_{a_{j-1}, a_j}^{\tilde{n}_j} = \gamma_{b_{j-1}, b_j, a_{j-1}, a_j}^{\tilde{n}'_j} \rightarrow \mathcal{O}(m^2 d_O^2 w^2) \quad (1.129)$$

$$\sum_{\tilde{n}_j, b_j} L_{b_{j-1}}^{a'_{j-1}, a_{j-1}} \gamma_{b_{j-1}, b_j, a_{j-1}, a_j}^{\tilde{n}'_j} = P_{a_{j-1}, (a_j b_j)}^{\tilde{n}_j} \rightarrow \mathcal{O}(m^3 d_O w^2). \quad (1.130)$$

We see that the scaling is the same as in the original DMRG3s algorithm but with reduced local dimension d_O instead of the bare basis size d .

The subspace-expanded local tensor $\tilde{M}_{a_{j-1}, (b_j a_j)}^{\tilde{n}_j}$ needs to be truncated and we perform an SVD which scales as $\mathcal{O}(m^3 d w^2)$ (remember that SVD scales linear in the large matrix dimension and quadratic in the small matrix dimension).

We can now compare the DMRG3S with local basis optimization to the bare DMRG3S algorithm which scales with $\mathcal{O}(m^3 dw^2) + \mathcal{O}(m^2 d^2 w^2)$. For dominating bond dimension $m \gg d \gg w$ we find a theoretical speedup of $\mathcal{O}(d/d_O)$. For dominating local dimension $d \gg m \gg w$ we distinguish two cases: (i) $d_O \gtrsim m$ and (ii) $d_O < m$. In case (i) we find a theoretical speedup of $\mathcal{O}((d/d_O)^2)$. In case (ii) we find a theoretical speedup of $\mathcal{O}(d^2/d_O m)$. Of course one needs to be careful with this speedup as instead of performing one bond update per site we now perform at least one local and one bond update per site. Because of that the ratio d/d_O should be a large number.

1.4 Time-evolving block decimation with dynamic local basis optimization

In this section we introduce the TEBD algorithm [47] with local basis optimization in MPS notation. The algorithm differs from the original TEBD algorithm [33, 34] by a shift to the local optimal mode basis before carrying out the most expensive step of the procedure: the singular value decomposition. Depending on the value of the ratio d/d_O the method achieves a theoretical speedup of a factor m compared to the original TEBD which is huge for states with a large bond dimension.

1.4.1 Time-evolving block decimation

We begin with the description of the TEBD algorithm. The TEBD method directly applies the time-propagator onto the wavefunction to time-evolve the state for an infinitesimal time-step Δt

$$|\psi(t + \Delta t)\rangle = e^{-iH\Delta t}|\psi(t)\rangle. \quad (1.131)$$

As we have seen in Sec. 1.2.1 any state can be represented by an MPS. Also, the actual representation is quite arbitrary which we noted earlier with the equivalence between left- and right-canonical decompositions. There exists another representation which is beneficial for the TEBD algorithm [33]

$$|\psi\rangle = \sum_{\vec{n}, \vec{N}} \Gamma_{N_0, N_1}^{n_1} \lambda_{N_1} \Gamma_{N_1, N_2}^{n_2} \lambda_{N_2} \cdots \lambda_{N_{L-1}} \Gamma_{N_{L-1}, N_L}^{n_L} |\vec{n}\rangle, \quad (1.132)$$

where the relations $A_{N_{j-1}, N_j}^{n_j} = \lambda_{N_{j-1}} \Gamma_{N_{j-1}, N_j}^{n_j}$ and $B_{N_{j-1}, N_j}^{n_j} = \Gamma_{N_{j-1}, N_j}^{n_j} \lambda_{N_j}$ hold and N_j again label additive quantum numbers. This form is called canonical and allows direct access to the bipartition of the state at every site. When starting the state decomposition at the left one arrives at this decomposition by subsequent SVDs

$$\begin{aligned} |\psi\rangle &= \sum_{\vec{n}} c_{n_1, \dots, n_L} |\vec{n}\rangle \\ &= \sum_{\vec{n}, N_1} U_{N_0, N_1}^{n_1} \lambda_{N_1} \lambda_{N_1}^{-1} c_{n_2, \dots, n_L} |\vec{n}\rangle \\ &= \sum_{\vec{n}, N_1} \lambda_{N_0} \Gamma_{N_0, N_1}^{n_1} \lambda_{N_1} \lambda_{N_1}^{-1} c_{n_2, \dots, n_L} |\vec{n}\rangle \\ &= \sum_{\vec{n}, \vec{N}} \lambda_{N_0} \Gamma_{N_0, N_1}^{n_1} \lambda_{N_1} \Gamma_{N_1, N_2}^{n_2} \cdots \lambda_{N_{L-1}} \Gamma_{N_{L-1}, N_L}^{n_L} \lambda_{N_L} |\vec{n}\rangle, \end{aligned} \quad (1.133)$$

where every $\Gamma_{N_{j-1}, N_j}^{n_j} = \lambda_{N_{j-1}}^{-1} U_{N_{j-1}, N_j}^{n_j}$ and the third line is obtained by insertion of $\lambda_{N_0} \lambda_{N_0}^{-1}$ to the left of the first tensor and $\lambda_{N_0} = \mathbb{1}$. A valid bipartition of the system is available at every bond since the state can be contracted at both sides of the λ_{N_j} to arrive at the form

$$|\psi\rangle = \sum_{N_j} \lambda_{N_j} |N_j\rangle_A \otimes |N_j\rangle_B, \quad (1.134)$$

where

$$|N_j\rangle_A = \sum_{\vec{n}_A, \vec{N}} \lambda_{N_0} \Gamma_{N_0, N_1}^{n_1} \cdots \lambda_{N_{j-1}} \Gamma_{N_{j-1}, N_j}^{n_j} |\vec{n}_A\rangle$$

is the left part of the wavefunction and

$$|N_j\rangle_B = \sum_{\vec{n}_B, \vec{N}} \Gamma_{N_j, N_{j+1}}^{n_{j+1}} \lambda_{N_{j+1}} \cdots \Gamma_{N_{L-1}, N_L}^{n_L} \lambda_{N_L} |\vec{n}_B\rangle$$

is the right part.

We assume that the Hamiltonian involves nearest-neighbor interactions only and use the Trotter-Suzuki decomposition to split the time-evolution operator $U = e^{-iH\Delta t}$ into two parts involving only odd or even terms

$$\begin{aligned} U &= e^{-i(H_{\text{even}} + H_{\text{odd}})\Delta t} \\ &\approx e^{-iH_{\text{even}}\Delta t} e^{-iH_{\text{odd}}\Delta t}. \end{aligned} \quad (1.135)$$

For a system with an even number of sites

$$\begin{aligned} e^{-iH_{\text{even}}\Delta t} &= e^{-iH_2\Delta t} e^{-iH_4\Delta t} \cdots e^{-iH_{L-2}\Delta t} \\ &= U_2 \otimes \cdots \otimes U_{L-2}, \end{aligned} \quad (1.136)$$

$$\begin{aligned} e^{-iH_{\text{odd}}\Delta t} &= e^{-iH_1\Delta t} e^{-iH_3\Delta t} \cdots e^{-iH_{L-1}\Delta t} \\ &= U_1 \otimes \cdots \otimes U_{L-1}, \end{aligned} \quad (1.137)$$

where H_j means a part of the Hamiltonian that involves sites j and $j+1$ and the exponential can be written as a multiplication because all two-site terms commute $[H_i, H_j] = 0$. For example, consider the Hamiltonian with open boundary conditions and two-site terms $A_{j,j+1}$ and single-site terms B_j

$$H = \sum_j A_{j,j+1} + \sum_j B_j = \sum_j H_j, \quad (1.138)$$

where $H_j = A_{j,j+1} + \frac{1}{2}(B_j + B_{j+1})$ in the bulk, $H_1 = A_{1,2} + B_1 + 1/2B_2$ on the left side and $H_{L-1} = A_{L-1,L} + 1/2B_{L-1} + B_2$. Those gate operators can be brought into the form of a two-site MPO-tensor

$$U_j = \sum_{\substack{n'_j, n'_{j+1} \\ n_j, n_{j+1} \\ \Delta N_{j-1}, \Delta N_{j+1}}} U_{\Delta N_{j-1}, \Delta N_{j+1}}^{n'_j, n'_{j+1}; n_j, n_{j+1}} |n'_j, n'_{j+1}\rangle \langle n_j, n_{j+1}|, \quad (1.139)$$

where $\Delta N_{j-1} = \Delta N_{j+1} = 0$ for a Hamiltonian with nearest-neighbor interaction. The full MPOs for odd and even updates read

$$U_{\text{odd}} = U_1 \cdots U_{L-1} \quad (1.140)$$

$$U_{\text{even}} = \mathbb{1}_1 U_2 \cdots U_{L-2} \mathbb{1}_L. \quad (1.141)$$

The application of the full time-evolution operator is now performed in two steps: first the even update is performed onto the wavefunction Eq. (1.132) which forms a new MPS and afterwards the odd update is performed on this intermediate state

$$\begin{aligned} |\psi(t + \Delta t)\rangle &= U |\psi(t)\rangle \\ &= U_{\text{odd}}(U_{\text{even}}|\psi(t)\rangle). \end{aligned} \quad (1.142)$$

The applications of the gate operators inside of the even and odd operators can be performed completely independently

$$\begin{aligned} U_{\text{even}}|\psi(t)\rangle &= \sum_{\substack{\vec{n}', \vec{n} \\ \vec{N}, \Delta \vec{N}}} \lambda_{N_0} \lambda_{N_0}^{-1} (\mathbb{1}_{0,0}^{n'_1, n_1} M_{N_0, N_1}^{n_1}) \lambda_{N_1}^{-1} \\ &\quad \lambda_{N_1} \lambda_{N_1}^{-1} (U_{\Delta N_1, \Delta N_3}^{n'_2, n'_3, n_2, n_3} M_{N_1, N_3}^{n_2, n_3}) \lambda_{N_3}^{-1} \\ &\quad \vdots \\ &\quad \lambda_{N_{L-3}} \lambda_{N_{L-3}}^{-1} (U_{\Delta N_{L-3}, \Delta N_{L-1}}^{n'_{L-2}, n'_{L-1}, n_{L-2}, n_{L-1}} M_{N_{L-3}, N_{L-1}}^{n_{L-2}, n_{L-1}}) \lambda_{N_{L-1}}^{-1} \\ &\quad \lambda_{N_{L-1}} \lambda_{N_{L-1}}^{-1} (\mathbb{1}_{0,0}^{n'_L, n_L} M_{N_{L-1}, N_L}^{n_L}) \lambda_{N_L}^{-1} \lambda_{N_L}, \end{aligned} \quad (1.143)$$

where the bulk tensors $M_{N_{j-1}, N_{j+1}}^{n_j, n_{j+1}} = \lambda_{N_{j-1}} \Gamma_{N_{j-1}, N_j}^{n_j} \lambda_{N_j} \Gamma_{N_j, N_{j+1}}^{n_{j+1}} \lambda_{N_{j+1}}$ and on the first and last sites $M_{N_{j-1}, N_j}^{n_j} = \lambda_{N_{j-1}} \Gamma_{N_{j-1}, N_j}^{n_j} \lambda_{N_j}$ to make the notation consistent. The combinations of lambda matrices and their inverse in front and after each operation ensure that the state after the contraction has the same MPS form. After the even-site contractions the state reads

$$\begin{aligned} U_{\text{even}}|\psi(t)\rangle &= \sum \lambda_{N_0} (\lambda_{N_0}^{-1} M_{N'_0, N'_1}^{n'_1} \lambda_{N_1}^{-1}) \\ &\quad \lambda_{N_1} (\lambda_{N_1}^{-1} M_{N'_1, N'_3}^{n'_2, n'_3} \lambda_{N_3}^{-1}) \\ &\quad \vdots \\ &\quad \lambda_{N_{L-3}} (\lambda_{N_{L-3}}^{-1} M_{N'_{L-3}, N'_{L-1}}^{n'_{L-2}, n'_{L-1}} \lambda_{N_{L-1}}^{-1}) \\ &\quad \lambda_{N_{L-1}} (\lambda_{N_{L-1}}^{-1} M_{N'_{L-1}, N'_L}^{n'_L} \lambda_{N_L}^{-1}) \lambda_{N_L} |\vec{n}'\rangle, \end{aligned} \quad (1.144)$$

where $N'_j = (\Delta N_j N_j) = N_j$ since $\Delta N_j = 0$. To regain the original one-site tensor form an SVD is performed on the two-site tensors

$$M_{N_{j-1}, N_{j+1}}^{n_j, n_{j+1}} = U_{(N_{j-1} n_j), \tilde{N}_j} \lambda_{\tilde{N}_j} V_{\tilde{N}_j, (n_{j+1} N_{j+1})}^* \quad (1.145)$$

The quantum numbers N'_j are fixed by two of the other four quantum numbers $\tilde{N}_j = N_{j-1} + n_j = N_{j+1} - n_{j+1}$. The dimension of N'_j is $\mathcal{O}(md)$ and needs to be truncated. Because of

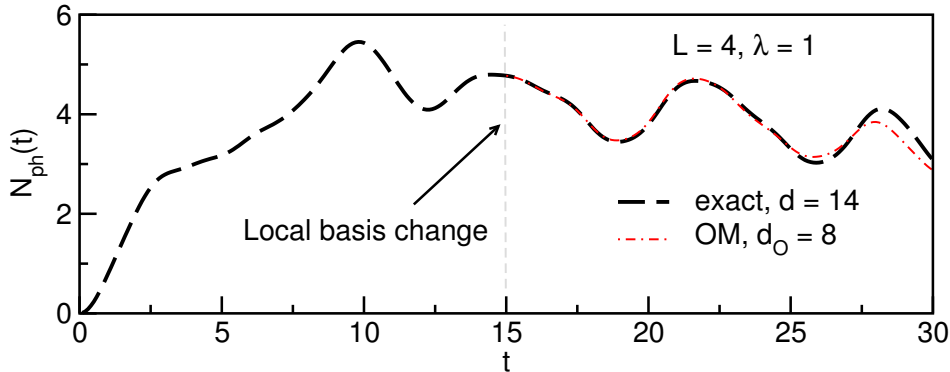


Figure 1.10: Time evolution of the phonon number in a Holstein polaron system with parameters $L = 4, \omega_0 = t_0 = 1, \lambda = 1$ starting from a free electron with momentum $k = \pi$ (for the full discussion of this quench, see Ch. 3). At time $t = 15t_0$ the local basis is changed to a smaller bare basis $d = 8$ and to a smaller optimal basis $d_O = 8$.

the canonical form of the MPS the system is bipartite and the singular values can directly be used for truncation

$$\begin{aligned}
 |\psi\rangle &= \sum_{N_{j-1}, N_{j+1}} M_{N_{j-1}, N_{j+1}}^{n_j, n_{j+1}} |N_{j-1}\rangle_A \otimes |N_{j+1}\rangle_B \\
 &= \sum_{N_j} \lambda_{\tilde{N}_j} |\tilde{N}_j\rangle_A \otimes |\tilde{N}_j\rangle_B,
 \end{aligned} \tag{1.146}$$

where $|\tilde{N}_j\rangle_A = \sum_{N_{j-1}, n_j} U_{(N_{j-1}n_j), \tilde{N}_j} |N_{j-1}\rangle_A$ for the left part of the system and $|\tilde{N}_j\rangle_B = \sum_{N_{j+1}, n_{j+1}} V_{\tilde{N}_j, (N_{j+1}n_{j+1})}^* |N_{j+1}\rangle_B$ for the right side of the system by the usual argument of orthonormality in the right index of U and left index of V^\dagger (Eqs. (1.50) and (1.52)). After a truncation has been performed the canonical form of the wavefunction is restored by the identifications

$$\Gamma_{N_{j-1}, N_j}^{n_j} = \sum_{N_{j-1}} \lambda_{N_{j-1}}^{-1} U_{(N_{j-1}n_j), N_j} \tag{1.147}$$

$$\Gamma_{N_j, N_{j+1}}^{n_{j+1}} = \sum_{N_{j+1}} V_{N_j, (n_{j+1}N_{j+1})}^* \lambda_{N_{j+1}}^{-1}. \tag{1.148}$$

The great advantage of the TEBD method is that the local updates during an odd or even global update can be performed completely in parallel because one has access to the bipartition of the wavefunction on every bond. Neglecting algorithmic instabilities due to the multiplication with the inverse singular values the algorithm scales with $\mathcal{O}(m^3 d^2)$ for the setup of a single two-site M -tensor, $\mathcal{O}(m^2 d^4 w^2)$ for each local contraction of U with M ($w = 1$) and with $\mathcal{O}(m^3 d^3)$ for the SVD of the updated two-site tensor to get back the canonical form. As before in the ground state section, operations on two sites at the same time lead to a bad scaling with the local dimension d .

1.4.2 Local basis optimization in TEBD

The study of the Holstein polaron (see Chapter 3) shows that the optimal mode basis varies as time progresses. This suggests that the optimal basis states need to be adapted in every time

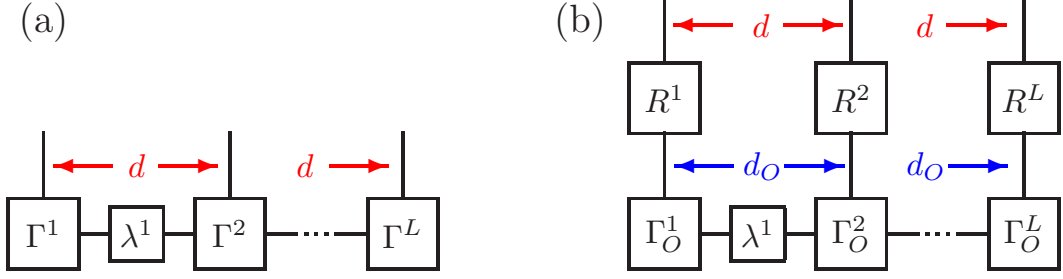


Figure 1.11: Tensor structure of a wavefunction (a) before and (b) after transformation into an optimal mode basis using the R -tensors. Because $d_O < d$ after transformation the wavefunction is an approximation to its former form.

step. Figure 1.10 demonstrates this fact: The time evolution of the phonon number operator is shown in a local basis of size $d = 14$ computed using standard Krylov-space time evolution. At time $t = 15t_0$ the state is projected onto a state that lives in a smaller optimal mode basis $d_O = 8$ which is then used during time-evolution. We observe a small kink together with a subsequent time evolution that is very close to the exact result for some time. After that, however, the evolution starts to deviate which suggests that the optimal modes need to be changed as time progresses.

To improve the scaling of the TEBD method Brockt et al. [47] introduce an intermediate optimal basis computed in every time-step that effectively reduces the local dimension ($d_O \ll d$) during the singular value decomposition of the system. The improved algorithm proceeds in the same way up to the point of application of the two-site gate operator onto the local two-site tensor Eq. (1.143). The complexity of the applications can be reduced to $\mathcal{O}(m^2 d^2 w^2)$ because of the sparseness of the time-evolution operator when the time-step Δt is small: in this case one can approximate $e^{-iH_j t}$ to finite order

$$e^{-iH_j t} = 1 - itH + \frac{t^2}{2} H^2 - \dots \quad (1.149)$$

To proceed, the local density matrix is computed

$$\begin{aligned} \rho^{(1)} &= \text{tr}_E(\rho) \\ &= \sum \langle N''_{j-1} | \otimes \langle n''_{j+1} | \otimes \langle N''_{j+1} | \\ &\quad \left(M_{N'_{j-1}, N'_{j+1}}^{n'_j, n'_{j+1}} |N'_{j-1}\rangle \otimes |n'_j n'_{j+1}\rangle \otimes |N'_{j+1}\rangle \right) \\ &\quad \left(\langle N_{j-1} | \otimes \langle n_j n_{j+1} | \otimes \langle N_{j+1} | M_{N_{j-1}, N_{j+1}}^{*n_j, n_{j+1}} \right) \\ &\quad |N''_{j-1}\rangle \otimes |n''_{j+1}\rangle \otimes |N''_{j+1}\rangle \\ &= \sum_{\substack{n_j, n'_j \\ n_{j+1} \\ N_{j-1}, N_{j+1}}} M_{N_{j-1}, N_{j+1}}^{n'_j, n_{j+1}} M_{N_{j-1}, N_{j+1}}^{*n_j, n_{j+1}} |n'_j\rangle \langle n_j|, \end{aligned} \quad (1.150)$$

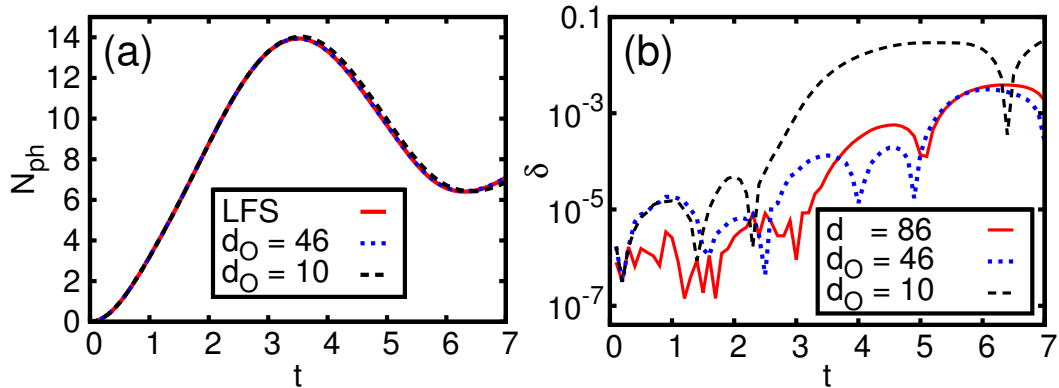


Figure 1.12: Test of the TEBD-LBO algorithm. (a) The phonon number as a function of time computed by Krylov-space time evolution (exact) and by the TEBD-LBO algorithm for an optimal basis dimension of $d_O = 10, 48$. (b) The error with respect to the exact evolution of the bare TEBD algorithm compared to the TEBD-LBO algorithm.

which scales with $\mathcal{O}(m^2 d^3)$. Diagonalization of this matrix yields the optimal mode basis

$$\rho^{(1)} = \sum_{\tilde{n}} w_{\tilde{n}} |\tilde{n}\rangle \langle \tilde{n}|, \quad (1.151)$$

where the w_α are used to decide on the d_O most important modes to keep. The unitary transformation $R_{n_j, \tilde{n}_j} = \langle n_j | \tilde{n}_j \rangle$ is used to project the two-site tensor into the optimal mode basis

$$M_{N_{j-1}, N_{j+1}}^{\tilde{n}_j, \tilde{n}_{j+1}} = \sum_{n_j, n_{j+1}} R_{n_j, \tilde{n}_j} R_{n_{j+1}, \tilde{n}_{j+1}} M_{N_{j-1}, N_{j+1}}^{n_j, n_{j+1}}, \quad (1.152)$$

which has a complexity of $\mathcal{O}(m^2 d^2 d_O)$. The tensor structure after this step is shown in Fig. 1.11. The SVD can now be performed on the transformed two-site tensor at a cost of $\mathcal{O}(m^3 d_O^3)$

$$M_{N_{j-1}, N_{j+1}}^{\tilde{n}_j, \tilde{n}_{j+1}} = \sum U_{N_{j-1}, \tilde{N}_j}^{\tilde{n}_j} \lambda_{\tilde{N}_j} V_{\tilde{N}_j, N_{j+1}}^*{}^{\tilde{n}_{j+1}}. \quad (1.153)$$

The truncation is performed using the bipartition of the system just as in the bare algorithm Eq. (1.146). The canonical form is now restored by the identifications Eq. (1.148) and the tensors are transformed back into the bare basis

$$\Gamma_{N_{j-1}, N_j}^{n_j} = R_{n_j, \tilde{n}_j}^* \Gamma_{N_{j-1}, N_j}^{\tilde{n}_j}. \quad (1.154)$$

The overall scaling is dominated by either the setup of the single-site reduced density matrix $\mathcal{O}(m^2 d^3)$ or by the SVD $\mathcal{O}(m^3 d_O^3)$ which amounts to a reduction of complexity by a factor $1/m$ or a factor d^3/d_O^3 whichever is worse. This method does not suffer from the problem of how to predict the optimal mode states necessary to represent the state at the next time-step because it performs the time-evolution in the full bare basis.

Figure 1.12(a) compares the time evolution of the phonon number operator N_{ph} using the TEBD-LBO algorithm to the one using Krylov-space time evolution in a limited functional

space in a Holstein polaron system of size $L = 6$ and parameters $\omega_0 = t_0 = 1, \gamma = 2t_0$ (see Ch. 3 for an exhaustive discussion of this problem). The bare basis in this case has size $d = 86$. For d_O the TEBD-LBO algorithm deviates from the LFS solution. With increasing d_O the deviation gets smaller. Figure 1.12(b) compares the deviation of the phonon number computed by the TEBD-LBO algorithm and the TEBD algorithm with respect to the solution computed by the LFS algorithm. With increasing d_O the error of the optimized algorithm approaches the TEBD error as is expected.

Chapter 2

Optimal modes in the one-dimensional Hubbard-Holstein model

The optimal mode basis [36, 41] is defined as the subset of the eigenstates of the reduced density matrix of a single site with the highest weights

$$\rho^{(1)} = \text{tr}_{L-1}(\rho) = \sum_{\alpha} w_{\alpha} |\alpha\rangle \langle \alpha|, \quad (2.1)$$

where $|\alpha\rangle$ denotes the α -th eigenstate with weight w_{α} . This basis is optimal for truncation in the local (as opposed to bond) degrees of freedom during a DMRG sweep [37] and was used so far for the simulation of the spin-boson model both in equilibrium [37, 87] and non-equilibrium studies [48]. Also, it was implemented into the TEBD method for the study of the Holstein model in non-equilibrium [47] (for a description of the method, see Chap. 1).

In this chapter we study the behavior of the local weight spectrum w_{α} with different filling and parameter regimes in the ground state of the Hubbard-Holstein model

$$\begin{aligned} H = & -t_0 \sum_{j,\sigma} (c_{j,\sigma}^{\dagger} c_{j+1,\sigma} + \text{h.c.}) + U \sum_j n_{j,\uparrow} n_{j,\downarrow} \\ & - \gamma \sum_j (b_j^{\dagger} + b_j) n_j + \omega_0 \sum_j b_j^{\dagger} b_j, \end{aligned} \quad (2.2)$$

where $c_{\sigma,j}$ annihilates an electron with spin σ at site j , $n_{j,\sigma} = c_{j,\sigma}^{\dagger} c_{j,\sigma}$ measures the local density of electrons with spin σ , $n_j = n_{j,\uparrow} + n_{j,\downarrow}$ is the local electronic density and b_j annihilates a phonon at site j . This model has been studied vigorously because in addition to a metal-insulator transition it also features an insulator-insulator transition between a Mott insulating phase (driven by U) and a Peierls phase (driven by the electron-phonon interaction strength γ) [110–112]. Phonon-number is not conserved in this model and it has been shown that, depending on the choice of parameters, one needs a huge number of local states even in the ground state [77]. The decay of the weight spectrum is crucial to the efficiency of the truncation in the optimal mode basis and we want to describe how it depends on filling and different choices of parameters for this model. More precisely, we show results for the single-electron and half-filled case for three choices of electron-phonon interaction strength: weak

$$W_j = \begin{array}{c} \begin{array}{ccccc} (0,0) & (-1,0) & (1,0) & (0,-1) & (0,1) \end{array} \\ \begin{array}{c} \left(\begin{array}{c|c|c|c|c} \mathbb{1} & 0 & 0 & 0 & 0 \\ x_j & \mathbb{1} & -t_0 c_{\uparrow,j}^\dagger & -t_0 c_{\uparrow,j} & -t_0 c_{\downarrow,j}^\dagger & -t_0 c_{\downarrow,j} \\ \hline c_{\uparrow,j}^\dagger & 0 & 0 & 0 & 0 \\ c_{\uparrow,j} & 0 & 0 & 0 & 0 \\ \hline c_{\downarrow,j}^\dagger & 0 & 0 & 0 & 0 \\ c_{\downarrow,j} & 0 & 0 & 0 & 0 \end{array} \right) \end{array} \\ \begin{array}{c} (\Delta N_\uparrow, \Delta N_\downarrow) \\ (0,0) \\ (-1,0) \\ (1,0) \\ (0,-1) \\ (0,1) \end{array} \end{array}$$

Figure 2.1: MPO representation of the Hubbard-Holstein Hamiltonian Eq. (2.2). The numbers in brackets at the top and right sides of the matrix show the quantum numbers of the respective blocks. The maximal block-bond dimension of this MPO is $w_{(0,0)} = 2$.

coupling $\gamma/t_0 = 0.5$, intermediate coupling $\gamma/t_0 = 1.5$ and strong coupling $\gamma/t_0 = 2.5$. We find that the optimal mode weights decay very fast compared to the bare weights (the weights of the bare phonon occupation number states) and that this decay is not strongly affected by the choice of the interaction strength while the decay of the bare weights is strongly influenced by the choices of those parameters. Consequently, a local basis consisting of very few optimal modes should suffice to approximate the full wavefunction to sufficient accuracy in all observed parameter regimes.

We also test our DMRG3S-LBO method (Chap. 1.3) on the example of this model. Contrary to what is done in Ref. [37], where a local update is implemented in addition to the sweeping over the lattice sites, we perform only a single local iteration at every site during sweeping by first updating the local Hilbert space followed by an update of the bond before sweeping to the next site. To demonstrate the usefulness of the method and we compare to the bare DMRG3S method as introduced in Ref. [38] for the single-electron and half-filled cases. We perform calculations for two choices of the interaction strength γ : the weak-coupling regime where $\gamma/t_0 < 1$ and the strong-coupling regime where $\gamma/t_0 > 1$. We find that the method generally needs more iterations for convergence than its bare counterpart (DMRG3S) which we attribute to the missing local sweeping. However, in the time-domain it converges much faster than the bare DMRG3S algorithm and usually finds a lower ground-state energy for the same bond dimension m . The speedup of the calculation correlates nicely with the ratio of bare local dimension and optimized local dimension d/d_O .

2.1 Implementation of the Hubbard-Holstein model

Our model Eq. (2.2) describes two fermionic species – up- and down-electrons – interacting with local phonon degrees of freedom. An arbitrary state thus can be written in the form

$$|\psi\rangle = \sum_{\substack{n_{j,\uparrow}, n_{j,\downarrow} \\ n_{j,p}}} c_{(n_{1,\uparrow}, n_{1,\downarrow}, n_{1,p}), \dots, (n_{L,\uparrow}, n_{L,\downarrow}, n_{L,p})} |(n_{1,\uparrow}, n_{1,\downarrow}, n_{1,p}), \dots, (n_{L,\uparrow}, n_{L,\downarrow}, n_{L,p})\rangle, \quad (2.3)$$

where $n_{j,\sigma}$ labels the electronic degrees of freedom with spin σ and $n_{j,p}$ labels the phononic degrees of freedom. The number of electrons is individually conserved (conservation of mag-

netization and total particle number) while the number of phonons is not conserved as is obvious from the interaction term. This means that the physical index of blocks in our MPSs and MPOs are labeled by the tuple $(n_\uparrow, n_\downarrow)$ where $n_\sigma \in 0, 1$ and each label has an internal dimension $d_{(n_\uparrow, n_\downarrow)} = N_{\text{ph}}^{\text{cutoff}}$ due to the phonon degrees of freedom which are not conserved. A typical MPS-tensor has the following structure

$$\left(M_{(N_\uparrow, N_\downarrow)_{j-1}, (N_\uparrow, N_\downarrow)_j}^{(n_\uparrow, n_\downarrow)_j} \right)_{a_{j-1}, a_j}^{n_{j,p}}, \quad (2.4)$$

where a_{j-1} and a_j label the bond index and $n_{j,p}$ labels the phonon degrees of freedom inside the block described by quantum numbers $(N_\uparrow, N_\downarrow)_{j-1}, (N_\uparrow, N_\downarrow)_j$ and $(n_\uparrow, n_\downarrow)_j$.

For our numerical setup we need the Hamiltonian in MPO form. Naturally, the MPO-bond indices also have an internal structure now

$$\left(M_{(\Delta N_\uparrow, \Delta N_\downarrow)_{j-1}, (\Delta N_\uparrow, \Delta N_\downarrow)_j}^{(n'_\uparrow, n'_\downarrow)_j, (n_\uparrow, n_\downarrow)_j} \right)_{b_{j-1}, b_j}^{n'_{j,p}, n_{j,p}}, \quad (2.5)$$

where the b_j label the bond index inside a block fixed by all of the quantum numbers. In order to set up the Hamiltonian MPO, we consider the six basis states (i) no term to the right, (ii) full term to the right, (iii) $c_{j,\uparrow}$ to the right, (iv) $c_{j,\uparrow}^\dagger$ to the right, (v) $c_{j,\downarrow}$ to the right and (vi) $c_{j,\downarrow}^\dagger$ to the right. This results in the MPO depicted in Fig. 2.1. We note the second row of this matrix: all fermionic operators are preceded by $-t_0$. The attentive reader might find that this term does not account for possible minus sign changes due to the presence of the other fermionic species. An example for a sign change is the following: We consider a two-site system only since, no matter how many sites are in front or at the back of the two sites involved in the hopping process, only those two local states contribute to the overall sign of the operation. We perform the following hopping operation

$$\begin{aligned} c_{1,\uparrow}^\dagger c_{2,\uparrow} | \downarrow, \uparrow \rangle &= -c_{1,\uparrow}^\dagger c_{1,\downarrow}^\dagger c_{2,\uparrow} c_{2,\uparrow} | \emptyset \rangle \\ &= -| \uparrow \downarrow, 0 \rangle, \end{aligned} \quad (2.6)$$

where we pick up a minus sign when the operator $c_{2,\uparrow}$ switches place with the operator $c_{1,\downarrow}^\dagger$. This minus sign can only exist when there are two species in the system and we account for this by exploiting the fact that hopping operators in our model always come in pairs located on adjacent sites. The MPO-operators are purely local and, thus, have no idea what is going on to the left of them and over how many operators they needed to hop in order to end up at the desired position. So, we account for the minus sign in the operator that is on the site of the particle that the other operator has to hop over. As an example, the MPO has the following entry

$$(W_{(0,0),(-1,0)}^j)_{1,0} = \tilde{c}_{j,\uparrow}^\dagger = \begin{pmatrix} 0 & 0 & 0 & 0 \\ 1 & 0 & 0 & 0 \\ 0 & 0 & 0 & 0 \\ 0 & 0 & -1 & 0 \end{pmatrix}, \quad (2.7)$$

where the local fermionic basis is labeled in the following way: $|0\rangle = |(0,0)\rangle$, $|1\rangle = |(1,0)\rangle$, $|2\rangle = |(0,1)\rangle$ and $|3\rangle = |(1,1)\rangle$ and where the matrix can be seen as blockdiagonal consisting of two copies of the creation operator c_j^\dagger , once when there is no spin-down electron present

and once when there is one present. The minus sign in the (3, 2)-entry of this matrix accounts for the fact that there is a down-particle on this site. This has to be done for all sign changes. In this model there are four which correspond, additionally to the one described above, to the operations

$$c_{2,\uparrow}^\dagger c_{1,\uparrow} |\downarrow, \uparrow\rangle, c_{1,\downarrow}^\dagger c_{2,\downarrow} |0, \uparrow\downarrow\rangle, c_{2,\downarrow}^\dagger c_{1,\downarrow} |\downarrow, \uparrow\rangle. \quad (2.8)$$

Note that the sign change is implemented in the first operator (at site j , not $j + 1$) for up-operators and on the second operator for down-operators because we chose the order in which creation operators act on the state to be ordered first by site and second by spin with up-spin operators to the left of down-spin operators:

$$|\uparrow\downarrow, \uparrow\downarrow\rangle = c_{1,\uparrow}^\dagger c_{1,\downarrow}^\dagger c_{2,\uparrow}^\dagger c_{2,\downarrow}^\dagger |\emptyset\rangle. \quad (2.9)$$

2.2 One electron

The Hubbard-Holstein model reduces to the Holstein polaron model when one fixes the number of electrons to one

$$H = -t_0 \sum_j (c_j^\dagger c_{j+1} + \text{h.c.}) + \omega_0 \sum_j b_j^\dagger b_j - \gamma \sum_j (b_j^\dagger + b_j) n_j. \quad (2.10)$$

For a strong interaction one gets the well known fully localized electron solution with a coherent state distribution of phonons on the site of the electron while for weak interaction the electron is delocalized over the length of the system [96].

2.2.1 Weight spectrum

Here, we report the weight spectrum for the three choices of electron-phonon interaction strength $\gamma = 0.5, 1.5$ and 2.5 , which roughly correspond to the weak, intermediate and strong coupling regimes, in Fig. 2.2. Figure 2.2(a) shows the bare weight spectrum, the diagonal entries of the local reduced density matrix $\rho^{(1)}$ in the phonon occupation number basis n_p , sorted by magnitude. Figure 2.2(b) shows the optimal weight spectrum w_α . With increasing interaction strength the weights decay slower in their respective index. This behavior holds for both, bare and optimal mode weights, however, the optimal mode spectrum at a given value of γ decays much quicker than the respective bare spectrum. Also, comparing the bare and optimal mode weights as a function of interaction strength we find that the reduction is larger for stronger interaction.

2.2.2 Tests of the DMRG3S-LBO method

We test the DMRG3S-LBO method in the Holstein model with a single electron (polaron problem). The initial state is chosen to be a translation symmetric superposition of all single electron states without phonons

$$|\psi_{\text{init}}\rangle = \frac{1}{\sqrt{L}} (|1, 0, 0, 0, \dots\rangle + |0, 1, 0, 0, \dots\rangle), \quad (2.11)$$

where L denotes the size of the system.

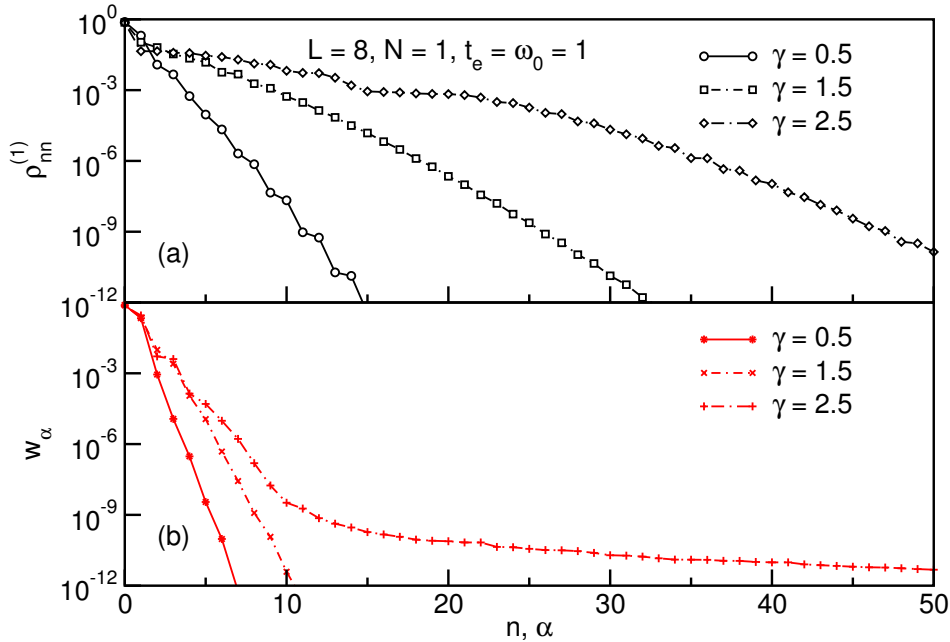


Figure 2.2: Weight spectrum of the (a) phonon occupation number states $\rho_{nn}^{(1)}$ and (b) optimal modes w_α for a system of size $L = 8$ and parameters $t_0 = \omega_0 = 1$ and different values of electron-phonon coupling strength $\gamma = 0.5, 1.5$ and 2.5 for the Holstein model with filling $n_\uparrow = 1/L$. Simulations are performed using the DMRG3S method keeping $m = 400$ bond states and $d = 40$ local states.

Weak coupling regime

We first test the method in the case of a weak electron-phonon coupling. In this case, it is known for the ground state of the Holstein model that the electron is very delocalized and only very few phonons exist (see [25] and references therein). Thus, one should generally get away with very few local degrees of freedom. Figure 2.3 compares the convergence behavior of the DMRG3S method to the DMRG3S-LBO method. We take up to twenty local phonon states $d = 20$ and a bond dimension of $m = 200$ which is enough to fully converge the ground state energy up to $\mathcal{O}(10^{-14})$ which is the internal threshold for the truncation in the bond dimension. Figure 2.3(a) shows the convergence to the ground-state energy E_0 which we obtain to high precision using the DMRG3S-LBO method keeping up to $m = 2000$ bond states and a local optimal cutoff of $d_O = 6$ states. We find that the DMRG3S method converges very fast in the first few iterations. However, for a large number of iterations it converges to a precision that is worse than what we get using the DMRG3S-LBO method for both choices of the optimal local dimension $d_O = 4$ and 6 . The best precision is obtained for an optimal cutoff of $d_O = 6$. We want to note that we get the exact same behavior for increased bond dimension which means that $m = 200$ is sufficient for this problem. Figure 2.3(b) illustrates the convergence of the energy versus the computation time. We see that, while taking more iterations to converge, the DMRG3S-LBO method converges after less time than the DMRG3S method because of the smaller local dimension.

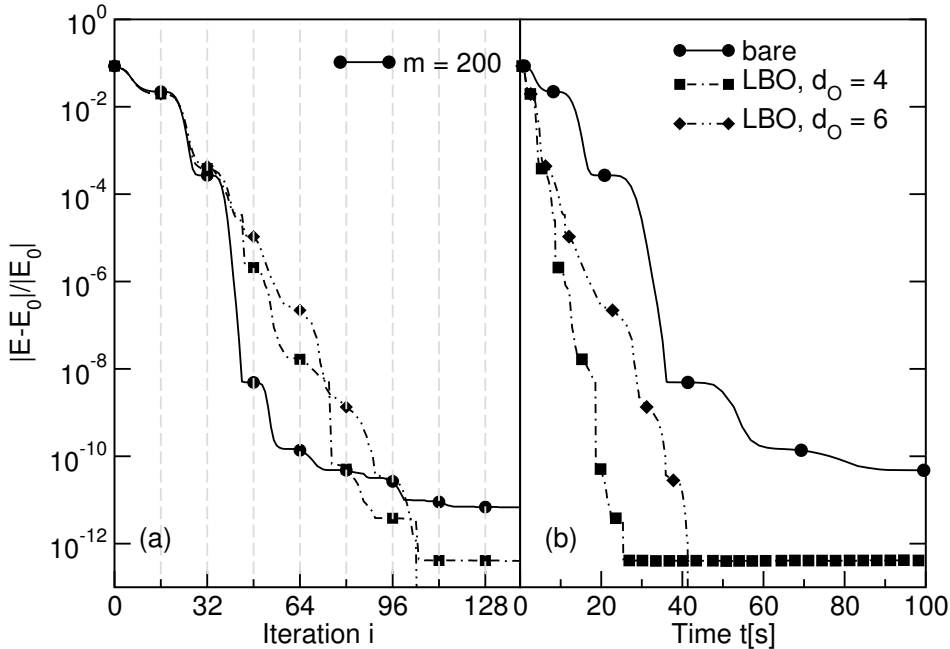


Figure 2.3: Convergence of the DMRG3S-LBO method compared to the DMRG3S algorithm for the Holstein model with a single particle and weak electron-phonon coupling strength $t_0 = \omega_0 = 1, \gamma = 0.5t_0$ in a system of size $L = 16$ and up to $d = 20$ phonons at every site. The ground-state energy $E_0 = -0.133006964216993t$ is computed using the DMRG3S-LBO algorithm keeping up to $m = 2000$ bond states and an optimal local cutoff of $d_O = 6$. The relative energy difference $|E - E_0|/|E_0|$ is illustrated (a) as a function of the iteration and (b) as a function of the computation time in seconds.

Strong coupling regime

The second test we perform is in the strongly coupled regime where $\gamma = 2.5$. It is known for the ground state in this regime that the electron is strongly localized and that a vast amount of phonons has to be kept in the local basis [25]. Our results are shown in Fig. 2.4. Figure 2.4(a) shows the relative difference between the ground-state energy at iteration i computed using the DMRG3S and DMRG3S-LBO methods and the ground state energy computed using DMRG3S-LBO using $m = 2000$ and $d_O = 10$. Like in the weak-coupling case the bare DMRG3S method converges in fewer iterations. The overall convergence, however, is different: a very steep descent of the energy in the first few iterations followed by a much slower convergence that looks exponential for the DMRG3S-LBO method (constant slope for $i > 1000$). Also, this slope seems to be less steep with increasing local optimal dimension d_O . In the observed number of iterations the DMRG3S-LBO method does not reach the precision of the DMRG3S method, however, the slope suggests a lower overall energy at a later iteration. We note that the energy we compare to was computed using $N_{\text{sweeps}} = 2500$ sweeps. For comparison, here we only show iterations up to $N_{\text{sweeps}} = 100$ sweeps.

Figure 2.4(b) shows the convergence versus the computation time. We find that in this specific case there is no great difference between the two versions of the method in terms of computation time.

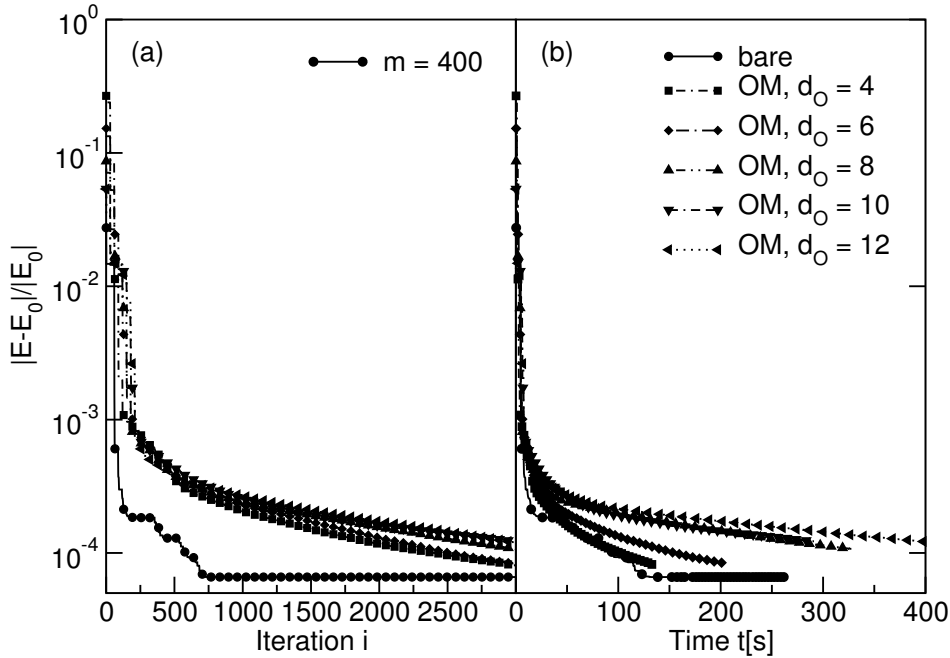


Figure 2.4: Convergence of the DMRG3S-LBO method compared to the DMRG3S algorithm for the Holstein model with a single electron and strong electron-phonon coupling strength $t = \omega_0 = 1, \gamma = 2.5$ in a system of size $L = 16$ and up to $d = 60$ phonon modes at every site. The ground-state energy $E_0 = -0.4020868504726t$ is computed using the DMRG3S-LBO algorithm keeping up to $m = 2000$ bond states and an optimal local cutoff of $d_O = 10$. To get full convergence $N_{\text{sweeps}} = 2500$ sweeps were performed. The relative energy difference $|E - E_0|/|E_0|$ is illustrated (a) as a function of the iteration and (b) as a function of the computation time in seconds.

2.3 Half filling

We now treat the full Hubbard-Holstein model at half filling $N_\uparrow = N_\downarrow = L/2$. In this case we need to fix an additional parameter: the on-site repulsive interaction strength U . Again, we compute the weight spectrum and compare it to the one-electron case. Also, we test the DMRG3S-LBO method for this more complicated model. The initial state is now given by

$$|\psi_{\text{init}}\rangle = \frac{1}{\sqrt{2}}(|1, 0, 1, 0, \dots\rangle + |0, 1, 0, 1, \dots\rangle). \quad (2.12)$$

2.3.1 Weight spectrum

In this section we study the weight spectrum for the half-filled case for two choices of the repulsive interaction strength $U = t_0, 10t_0$. Figure 2.5 shows the weight spectrum for the electron-phonon interaction strengths $\gamma = 0.5t_0, 1.5t_0$ and $2.5t_0$ and a repulsive interaction strength of $U = 1t_0$. The weights decay exponentially just like in the one-electron case and also the behavior with electron-phonon interaction strength is quite similar: with increasing γ the bare weights decay slower. Again, the optimal mode weights are not influenced as much. The optimal mode weights in the $\gamma = 2.5t_0$ case do even decay faster than in the weak interacting case.

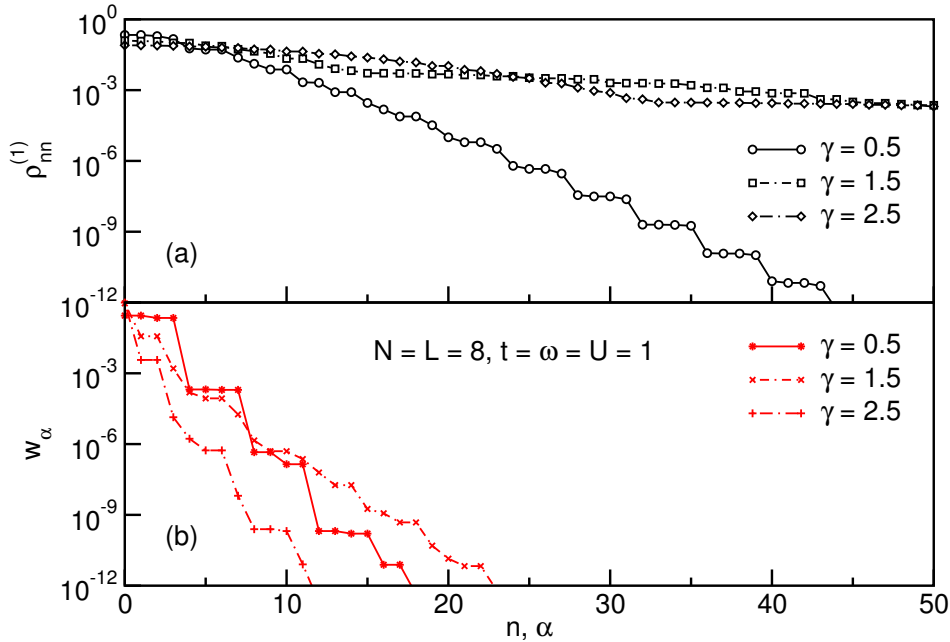


Figure 2.5: Weight spectrum of the (a) phonon occupation number states $\rho_{nn}^{(1)}$ and (b) optimal modes w_α for a system of size $L = 8$ and parameters $\omega_0 = U = t_0$ and different values of electron-phonon coupling strength $\gamma = 0.5t_0, 1.5t_0$ and $2.5t_0$ for the half-filled Hubbard-Holstein model $n_\uparrow = n_\downarrow = 1/2$. Numerics are performed using the DMRG3S method keeping $m = 600$ bond states and $d = 100$ local states.

Figure 2.6 shows the case of strong electron-electron repulsion $U = 10t_0$. Compared to Fig. 2.5 the effect of a stronger repulsion is a faster decay of the weight spectrum. Also, the optimal mode weights are now decaying slower with increasing interaction. However, we still expect to gain a lot when using an optimal basis.

2.3.2 Tests of the DMRG3S-LBO method

We here discuss the efficiency of the DMRG3S-LBO method (see Chapter 1 for a description of the method) on the example of the half-filled one-dimensional Hubbard-Holstein model. To this end we compare the DMRG3S-LBO method to the DMRG3S method for two sets of parameters in the weak and strong electron-phonon coupling regime $\gamma = 0.4t_0$ and $1.6t_0$.

Weak coupling regime

We first demonstrate that the setup of the Hamiltonian is correct by direct comparison to ED in a system of size $L = 4$ keeping up to $n = 40$ global phonons (the ground state energy is converged up to machine precision). This is illustrated in Fig. 2.7(a) and (b). Figure 2.7(a) presents the relative energy difference to the ED ground state energy as a function of iteration i . All algorithms converge in the first two half sweeps (one full sweep) through the system which is, no doubt, due to the small size of the system. The DMRG2 and DMRG3S methods converge fastest, basically to the same energy. Oscillations and a growing energy after convergence are due to the fixed precision of $\epsilon = 10^{-14}$ when updating the bond.

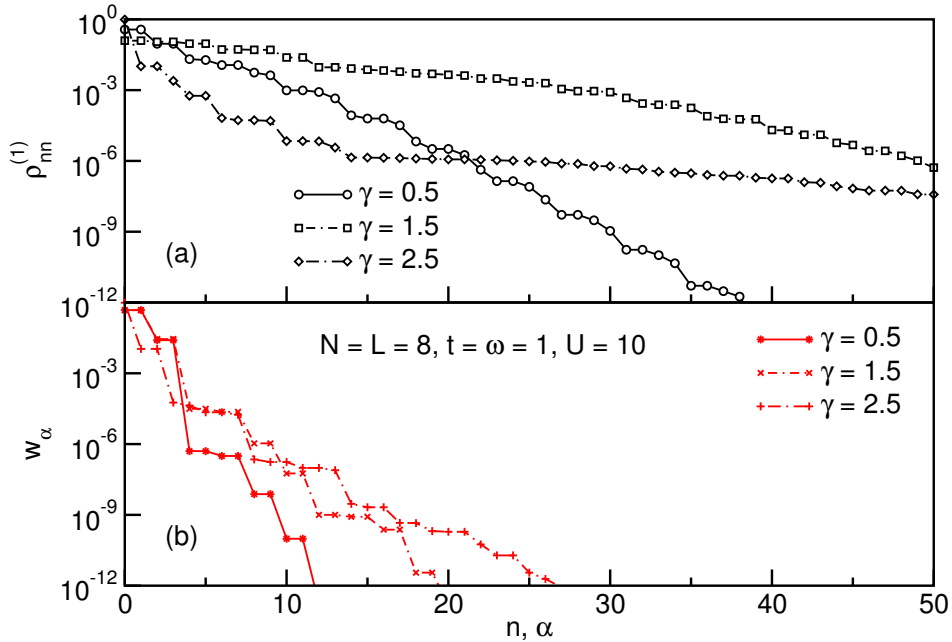


Figure 2.6: Weight spectrum of the (a) phonon occupation number states $\rho_{nn}^{(1)}$ and (b) optimal modes w_α for a system of size $L = 8$ and parameters $t_0 = \omega_0 = 1, U = 10t_0$ and different values of electron-phonon coupling strength $\gamma = 0.5t_0, 1.5t_0$ and $2.5t_0$ for the half-filled Hubbard-Holstein model $n_\uparrow = n_\downarrow = 1/2$. Numerics are performed using the DMRG3S method keeping $m = 600$ bond states and $d = 100$ local states.

Thus, the bond dimension of $m = 400$ is not the bottleneck in this case. The DMRG3S-LBO method also nicely converges to the exact ground-state energy. This algorithm converges to the ground state energy found by the DMRG2 and DMRG3S algorithms with increasing local dimension d_O . After the DMRG3S-LBO method has converged we note no oscillatory behavior of the energy which suggests that here the bottleneck is the fixed number of kept modes instead of the error during truncation. Figure 2.7(b) illustrates the energy difference as a function of simulation time. Here, even for such a small system, we find that the DMRG3S-LBO method converges much faster than the other two methods.

We now turn to larger systems where we can not compare to ED anymore, however, we see that the implementation is generally correct. Figure 2.8 illustrates the relative difference between the approximative ground state energy obtained by the DMRG3S and DMRG3S-LBO methods for the two bond dimensions $m = 200, 400$ and local dimension $d = 20$ and the exact ground state energy obtained by DMRG3S-LBO for $m = 2000$ and $d_O = 6$. Also, we show the convergence of the DMRG2 method as a reference. We note, that the energy goes further down by increasing the local dimension d , however, the DMRG2 algorithm takes a lot of time then.

Figure 2.8(a) shows the relative energy difference as a function of the iteration (one iteration is the update of a single site, L iterations is a half-sweep and $2L$ iterations is a full sweep). For the first few iterations the data of DMRG3S and DMRG3S-LBO methods are on top of each other and the algorithms perform the same. Later on, the DMRG3S-LBO data is below the DMRG3S data for both bond dimensions. We therefore conclude that the algorithm works and, for this case, is an improvement over the bare state algorithm. For

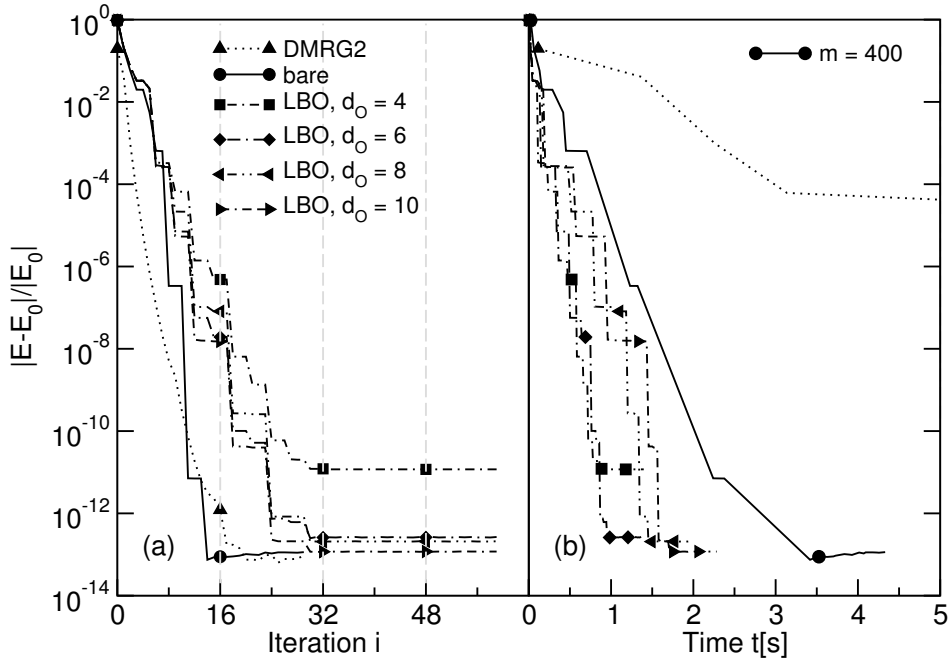


Figure 2.7: Convergence of the DMRG3S-LBO method compared to the DMRG3S and DMRG2 algorithms for the half-filled Hubbard-Holstein model and weak electron-phonon coupling strength $\omega_0 = U = t_0, \gamma = 0.4t_0$ in a system of size $L = 4$ and up to $d = 40$ phonon modes at each site. The ground state energy $E_0 = -1.0726057155685598t_0$ is computed using exact diagonalization keeping up to $N_p = 40$ phonons globally in a system of size $L = 4$. The relative energy difference $|E - E_0|/|E_0|$ is illustrated (a) as a function of the iteration and (b) as a function of the computation time in seconds.

$m = 200$ the $d_O = 6$ algorithm performs worse than the $d_O = 4$ algorithm. With increasing bond dimension, however, this difference goes down. This is to be expected since it has to perform like the bare algorithm when setting $d_O = d$. The DMRG2 algorithm performs very good in the iteration picture and shows the fastest convergence. As expected, it reaches a better precision than the DMRG3S and DMRG3S-LBO algorithms for $m = 200$.

Figure 2.8(b) shows the relative difference between exact and approximative ground-state energies as a function of time. We see that the DMRG3S-LBO variant has a great advantage in terms of runtime compared to the bare algorithm: the optimal algorithm scales favorably because, even though we are in the weak-coupling regime, a very small number of optimal modes is sufficient to get good precision. Comparison to the DMRG2 result shows that one can get a much better precision using a larger bond dimension of $m = 400$ states in a much shorter time. Direct comparison shows that all other algorithms are fully converged by the time the DMRG2 finishes its second sweep.

We conclude that the DMRG3S-LBO method has a huge advantage over the bare DMRG3S algorithm in the weak coupling regime.

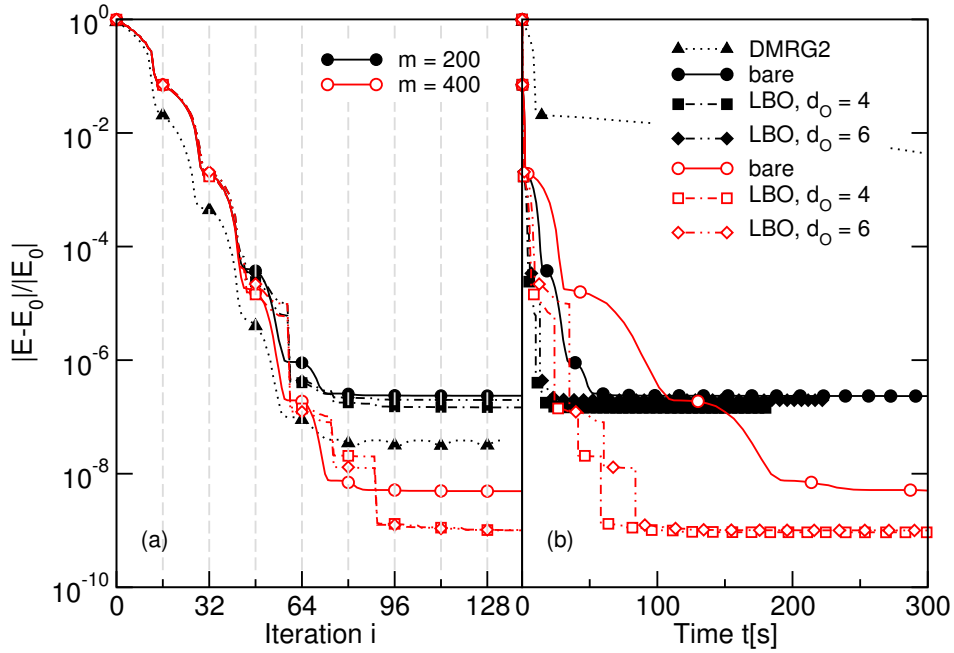


Figure 2.8: Convergence of the DMRG3S-LBO method compared to the DMRG3S and DMRG2 algorithms for the half-filled Holstein model and weak electron-phonon coupling strength $\omega_0 = U = t_0, \gamma = 0.4t_0$ in a system of size $L = 16$ and up to $d = 20$ local phonons. The ground state energy $E_0 = -1.179039494252t_0$ is computed using the DMRG3S-LBO algorithm keeping up to $m = 2000$ bond states and an optimal local cutoff of $d_O = 6$. The relative energy difference $|E - E_0|/|E_0|$ is illustrated (a) as a function of the iteration and (b) as a function of the computation time in seconds.

Strong coupling regime

Figure 2.9 shows the energy convergence for a strong electron-phonon coupling strength $\gamma = 1.6$.

As in the weak case, Figure 2.9(a) shows the relative energy difference as a function of the iteration. We see that the bare algorithm approaches the numerically exact ground state energy in an exponential fashion with a slight slope. This convergence behavior seems to be typical for the strong-coupling regime of the Hubbard-Holstein model which suggests that it is related to self-trapping. The DMRG3S-LBO algorithm performs equally well in the beginning but gets caught in a local minimum along the way for many iterations up to a point where it suddenly converges to the global minimum. As the number of kept optimal modes is increased, the algorithm gets stuck for less many iterations. For the highest shown optimal mode cutoff $d_O = 12$ the DMRG3S-LBO again reaches a lower energy than the bare algorithm in the observed number of iterations. Keeping a larger bond dimension $m = 600$ has the effect of trapping the algorithm in the intermediate state for more iterations, however, the convergence afterwards is increased and it reaches a lower energy for high enough cutoff d_O .

Figure 2.9(b) shows the relative energy difference as a function of simulation time. We see a clear advantage in the usage of the optimized algorithm: Even though the optimized approach gets stuck in an intermediate state, it is much faster and even reaches a lower ground-

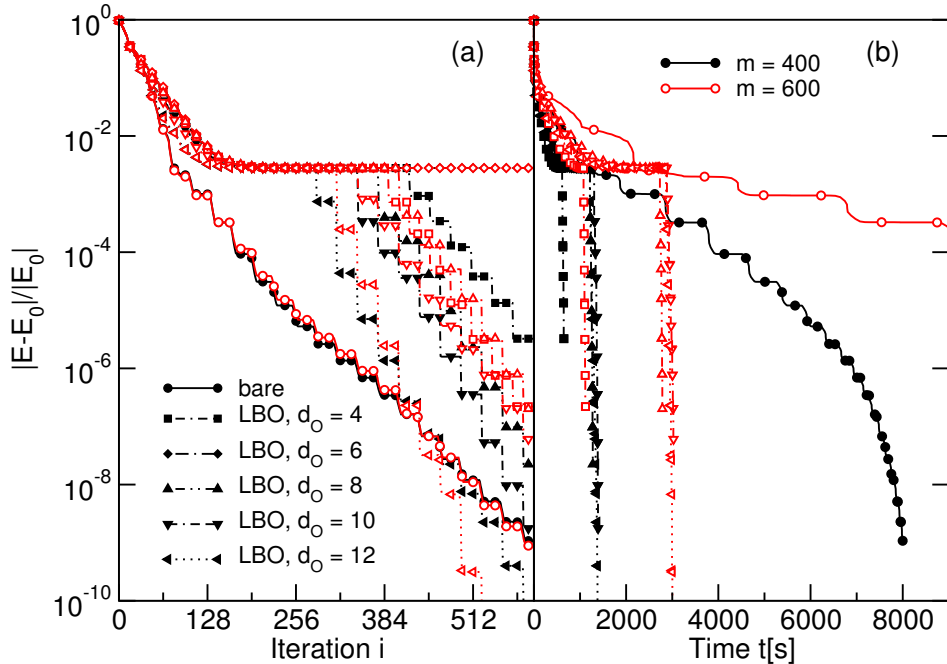


Figure 2.9: Convergence of the DMRG3S-LBO method compared to the DMRG3S algorithm for the half-filled Hubbard-Holstein model and strong electron-phonon coupling strength $t_0 = \omega_0 = U = 1, \gamma = 1.6$ in a system with size $L = 16$ and up to $d = 60$ local phonon states. The ground state energy $E_0 = -4.8333654559835t_0$ is computed using the DMRG3S-LBO algorithm keeping up to $m = 2000$ bond states and an optimal local cutoff of $d_O = 10$. The relative energy difference $|E - E_0|/|E_0|$ is illustrated (a) as a function of the iteration and (b) as a function of the computation time in seconds. Please note that the DMRG3S-LBO data for $d_O = 6, m = 400$ and $m = 600$ are on top of each other.

state energy. The impact of increasing the bond dimension is of course a longer simulation time as the bond dimension contributes with the third power. We want to emphasize here, that using the optimized method while keeping 20% (12 modes out of 60) of the maximal local dimension we reach a higher precision than the bare method in 18% of the time the bare method takes.

We also want to note that one needs to be careful in the choice of the local cutoff: for $d_O = 6$ we find that the optimized algorithm does not get out of the local minimum in the observed number of iterations.

2.4 Conclusion

We here studied the DMRG3S-LBO method on the example of the Hubbard-Holstein model at the two choices for filling $n_\uparrow = 1/L, n_\downarrow = 0$ and $n_\uparrow = n_\downarrow = L/2$. We compare this method to the bare DMRG3S method in different coupling regimes and find that for constant bond dimension DMRG3S-LBO reaches a lower ground state energy for all studied cases. While the bare method converges faster in terms of actual number of iterations, the DMRG3S-LBO method reaches convergence in less computation time in almost all cases. Even though we perform a second update at every site (the optimization in the local basis) the speedup

correlates nicely with the ratio d/d_0 especially in the half-filled case. We note that in the first implementation of LBO in a DMRG algorithm [37] (there for the spin-boson model) a local sweeping scheme was used where a local update and following bond update is performed in a loop locally until the local basis converges for the current environment. In this chapter we did not use local sweeping and the local basis is updated only once before the local bond is updated. We expect the effect of the local sweeping to be a convergence that closely follows the bare algorithm at the cost of additional local iterations.

Chapter 3

Real-time decay of a highly excited charge carrier in the one-dimensional Holstein model

The advent of ultrafast spectroscopy experiments enabled researchers to observe dynamical electronic processes in materials in real-time [10, 11]. So-called pump and probe experiments are able to resolve timescales as small as $\mathcal{O}(10)$ femtoseconds [10]. The bottleneck in experiments have long been the detectors which were not able to resolve time scales faster than 10^5 fs. Pump and probe experiments shift the resolution problem from the detectors to the duration of a single pulse of the laser which is used in the experiment. These experiments consist of two steps: First, they create a non-equilibrium state in the sample of interest by application of a so-called pump beam. The pump beam has a very short pulse duration and has the effect of exciting the charge carriers in the sample to a selection of states which is defined by the energy spectrum of the beam in a very short time. Very shortly after the arrival of the pump beam, before the sample relaxes, a subsequent measurement of the reflectivity of the sample is performed by a second pulse - the probe beam. For example, in high-temperature superconductors the change in reflectivity is related to the non-equilibrium quasiparticle density $\Delta n(t)$ which gives information about the kinetic processes happening in the sample [10]. A laser pulse interacts with the sample for a time proportional to the pulse duration. Therefore, the pulse duration of the two beams determines the resolution of the measurement because whatever signal hits the detector has to be related to what has happened in the sample while it was interacting with the pulse. In this way the relaxation dynamics of the sample can be studied in real-time with an outstanding temporal resolution from the early stage up to the thermalized system [9, 113, 114].

This development in experimental techniques brought about a renewed interest in the study of nonequilibrium systems with strong correlations. A strong pump pulse can take a system very far from equilibrium and, therefore, change the physical properties of the sample [10, 11]. Examples include photo-induced phase transitions [115–117], ultrafast optical switching [118, 119] (metal-insulator transition) and photo-enhancement [12] or photo-induced weakening of superconductivity [13, 14]. It is thus possible to manipulate materials in a profound way. On the other hand, the observation of the relaxation dynamics of a system after a weak perturbation of the equilibrium state where only a small redistribution of energy among the different degrees of freedom happens can give information about the basic inter-

actions which determine the equilibrium properties of the material [11]. In principle, degrees of freedom that are not discernible in the frequency domain can be disentangled in the time domain by monitoring thermalization processes characterized by different time scales. For example, in so-called cuprate (copper-oxide compound) systems which exhibit superconductivity at – compared to conventional superconductors – extremely high temperatures one tries to understand the mechanism leading to the phenomenon of high temperature superconductivity using ultrafast spectroscopy experiments [9, 17, 113, 120–123]. The excitation by a pump pulse can be considered an injection of quasiparticles into the system [10, 11] and the relaxation dynamics depend on the coupling of the quasiparticles to other degrees of freedom. Two candidates are antiferromagnetic spin fluctuations [124] and phonon excitations [113] whose separation is impeded by their partial coexistence on the same energy scale [17]. In conventional superconductors the crucial ingredient that leads to Cooper pairing is the electron-phonon interaction and one still tries to find its precise contribution to high-temperature superconductivity [1, 3, 9].

For systems featuring strong enough electron-phonon coupling, optically excited charge carriers relax to a state where they become dressed by phonons and form a quasiparticle with a renormalized mass - the polaron [50]. This so-called self-trapping of a charge carrier [15, 16, 125–130] and also polaron transport [131–133] have been studied experimentally. Also, the relaxation dynamics of photo-excited charge carriers in semi-conductors where phonons are believed to be a key ingredient have been examined [134]. Electronic correlations influence the many-body spectrum strongly and provide relaxation channels but phonons may still provide the dominant (fastest) relaxation channel. This has been conjectured for one-dimensional Mott insulators [7, 8, 135] where the relaxation via spin degrees of freedom is not efficient and also in the context of the mechanism of ultrafast demagnetization of ferromagnets [136, 137]. Contrary results were found for two-dimensional systems with antiferromagnetic correlations where relaxation due to coupling to antiferromagnetic spin excitations can be very fast [138–141] and on short time-scales can absorb more energy than phonons [89]. Very recently, it was also shown that in relaxation due to the coupling to hard-core bosons (magnetic excitations) the relaxation time depends on the excitation energy or the density of excited carriers while this is not the case in relaxation due to coupling to usual bosonic degrees of freedom (like phonons) [142].

Before the era of high-precision time-resolved experiments most of the numerical tools were developed to address transport properties within semiclassical approaches [143, 144]. However, in strongly interacting systems electron- and lattice dynamics live on comparable timescales [29, 145] and it can be necessary to treat the charge carriers and the lattice degrees of freedom on equal footing [22, 28]. A variety of methods are available that treat isolated charge carriers coupled to quantum phonons [22, 28, 29, 49, 50, 146–149]. Also, methods exist that are able to treat many-electron systems beyond mean-field [150] and Boltzmann approaches [151, 152]. The dynamics of electrons coupled to phonons has been studied in the Holstein model using dynamical mean-field theory [141], continuous-time quantum Monte Carlo [153] and Keldysh Green functions within the Migdal approximation [154, 155]. In addition, the Holstein-Hubbard and t-J Holstein models have been studied using methods based on exact diagonalization [89–92], density matrix renormalization group [7] and dynamical mean-field theory [145, 156].

In this project, we apply wavefunction-based methods to study the non-equilibrium dynamics of a coupled electron-phonon system. More specifically, we study a system which consists of a single electron coupled to quantum phonons, described by the one-dimensional

Holstein model [6]

$$\begin{aligned}
 H = & -t_0 \sum_j (c_j^\dagger c_{j+1} + \text{h.c.}) + \omega_0 \sum_j b_j^\dagger b_j \\
 & - \gamma \sum_j (b_j^\dagger + b_j) n_j,
 \end{aligned}
 \tag{3.1}$$

where c_j (b_j) annihilates an electron (phonon) at site j and $n_j = c_j^\dagger c_j$ is the local electron density at site j . The initial state is given by a single electron and no phonons in an eigenstate of the Holstein Hamiltonian with vanishing coupling strength $\gamma = 0$ labeled by the quasimomentum K

$$|\psi_0\rangle = c_K^\dagger |\emptyset\rangle. \tag{3.2}$$

We choose the electron to start from a highly excited state and, unless stated otherwise, set $K = \pi$ which also fixes the total quasimomentum of the full system. Physically, the motivation for this setup is to model the dynamics of a free electron wave-packet that emerges after a sudden external perturbation as, for example, a pump pulse during ultrafast spectroscopy experiments [49, 50, 147]. We use a state with a sharp momentum rather than a wave-packet to simplify the analysis of the dynamics.

As stressed in Chap. 1, the dynamics of systems with bosonic degrees of freedom are hard to simulate numerically using wavefunction based methods because of the possibly high cutoff in the number of bosonic states. For the Holstein model this problem is, depending on the actual choice of model parameters, especially severe and even ground state calculations can be very demanding. As discussed in Chap. 1, exact diagonalization and the density matrix renormalization group algorithm methods scale unfavorably in the number of local degrees of freedom d (for references see [157, 158] for the Holstein model and [51, 159–161] for the Hubbard-Holstein model). It has been shown that the rapid growth of the Hilbert space can be countered by truncation of the bosonic subspace in the so-called optimal mode basis for the case of the Holstein model [36, 41] and also for the case of a bipolaron in the Hubbard-Holstein model [162].

For our system we first compare three wavefunction-based methods - exact diagonalization (ED), diagonalization in a limited functional space (LFS) [23] and the standard time-evolving block decimation (TEBD) [33] methods to find out which one is best suited for the non-equilibrium study. The most powerful method is found to be diagonalization in a limited functional space (for an introduction to the method, see Chap. 1). We construct the limited functional space basis on a finite lattice with periodic boundary conditions and show that it allows for the efficient simulation of the non-equilibrium dynamics in all parameter regimes up to times including the relaxation and steady-state domains. This complements a previous work which uses the same method to study the relaxation regime on an infinite lattice [29].

We then analytically and numerically describe the non-equilibrium dynamics in limiting cases and in the two crossover regimes – from the non-adiabatic to the adiabatic regime and from the weak coupling to the strong coupling regime. We use perturbation theory in the interaction picture to analytically treat the cases of the weak coupling anti-adiabatic and adiabatic limits as well as the strong-coupling anti-adiabatic limit. For the anti-adiabatic limit we find an inefficient energy transport from electron to phonons and coherent oscillations in the steady-state regime while in the adiabatic regime relaxation dynamics can be observed. Setting up a set of Boltzmann equations for the description of the relaxation dynamics and

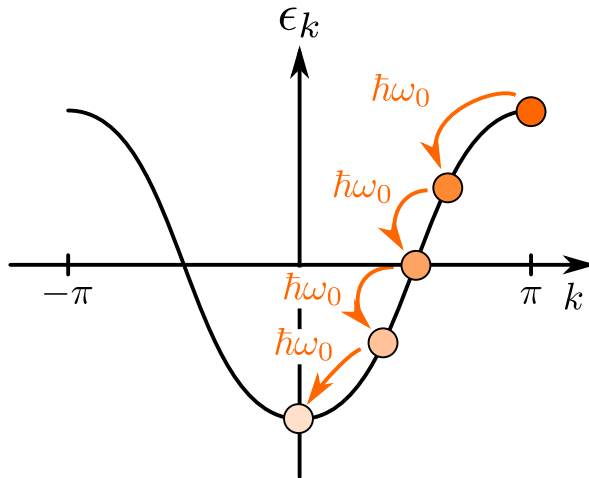


Figure 3.1: Sketch of the electronic relaxation: The electron starts with an energy $E_{\text{kin}}(t=0) = 2t_0$ and momentum $k(t=0) = \pi$. As time progresses it excites phonons that cost an energy of $\Delta E = \hbar\omega_0$ until all energy is transferred from the electron to the phonon subsystem and the electron comes to rest at the bottom of the band.

comparison to numerical data obtained using the LFS method we find good agreement between the two approaches. Making the assumption of a constant density of states we extract the relaxation time τ for this system $\tau\omega_0 = (16/\pi)(\gamma/t_0)^{-2}$. We find that it reasonably well describes the relaxation time also for our model even though it has a tight-binding dispersion. The agreement of the data obtained from the Boltzmann equations and the numerical data for the Holstein model gives a nice physical interpretation of the relaxation in the weak-coupling adiabatic regime: The electron moves through the lattice and emits phonons. Each emission leaves the electron with less energy and momentum until it hits the bottom of the electron band. A sketch of this cascade of phonon emissions is given in Fig. 3.1.

We numerically compute the dynamics of the Holstein model to study the crossover from adiabatic to anti-adiabatic as well as from weak-coupling to the strong-coupling regime. In the adiabatic regime, the dynamics of the momentum distribution function is consistent with the sketch Fig. 3.1: Initially, all the weight is located at $k = \pi$ while at later times a maximum forms at $k = 0$ which is accompanied by a reduction of the kinetic energy of the electron. In the stationary regime the maximum remains at $k = 0$ for most of the time but coherent oscillations of observables are visible for all coupling strengths. For the weak-coupling adiabatic regime we show that the amplitude of oscillations vanishes with increasing system size while it approaches a constant in the strong coupling adiabatic regime. We also provide an estimate for the phonon energy in the steady-state regime which is given by the initial kinetic energy minus the kinetic energy and coupling energy in the ground state of the system in the quasimomentum subspace $k = \pi$. An explanation of why this estimate works remains to be found, however, it is supported by the numerical data. This suggests that the time-evolution can be viewed as the energy transfer from the subsystem containing both, electronic and electron-phonon coupling energy, to the phonon subsystem.

Finally, we study the local reduced density matrix as a function of time. Zhang et al. [36, 41] showed that the eigenbasis of the single-site reduced density matrix ρ can be used to truncate in the local degrees of freedom and thereby ease ground state calculations

significantly. This quantity is obtained by tracing the system of size L over $L - 1$ sites

$$\rho = \text{tr}_{L-1}(|\psi\rangle\langle\psi|) = \sum_{\alpha} w_{\alpha} |\alpha\rangle\langle\alpha|, \quad (3.3)$$

where $|\psi\rangle$ is a pure state describing the full system, $|\alpha\rangle$ are the eigenstates of the local reduced density matrix and w_{α} are the so-called weights which give the importance of the local eigenstate $|\alpha\rangle$ for the global state $|\psi\rangle$. The eigenstates of the local reduced density matrix are called optimal modes.

Here, we compute the four highest weighted optimal modes, their weights and the local von Neumann entropy as a function of time in the weak- and strong-coupling adiabatic regimes. For the weak-coupling regime, the highest weighted optimal mode in the steady-state regime is a slightly broadened version of the bare phonon vacuum which does not change significantly in time. In the strong coupling regime the form of the highest weighted optimal mode depends strongly on time: It oscillates between the bare phonon vacuum as in the initial state and another state that strongly resembles a coherent state as in the strongly coupled anti-adiabatic limit. This suggests that the single-site coherent oscillations govern the dynamics even when the hopping t_0 is not vanishingly small. For the local von Neumann entropy we find no strong time-dependence in the steady-state regime. After a short relaxation time which correlates with the relaxation of the kinetic energy the entropy is effectively constant with a value that grows slightly with increasing coupling strength.

We also compare the weight distributions in the steady-state to the ground state distributions for the same choice of coupling strengths and quasi-momentum subspace. All of the distributions decay roughly exponentially, however, the steady-state distributions decay much slower than their respective ground state equivalents. As explained above, local observables exhibit coherent oscillations in the strongly coupled limit. Since all information about the local state of the system is encoded in the local reduced density matrix

$$\langle\hat{O}_j\rangle(t) = \text{tr}(\rho_j^{(1)}\hat{O}_j), \quad (3.4)$$

oscillations have to be resembled by either the weights (and therefore the local von Neumann entropy) or the optimal modes. We find that the oscillations are reflected in the optimal modes of the system which is intuitive because the von Neumann entropy is the same for both, the single site and its environment.

The results of this chapter excluding the dependence of the local von Neumann entropy in the groundstate on the coupling strength (Fig. 3.2) have been published in Ref. [96].

3.1 The one-dimensional Holstein model

The Holstein model describes spinless electrons coupled to local optical phonons with frequency ω_0 [6]. The Hamiltonian consists of three terms

$$H = H_{\text{kin}} + H_{\text{ph}} + H_{\text{coup}}, \quad (3.5)$$

where H_{kin} is the kinetic energy of electrons, H_{ph} is the energy stored in the local phonon oscillators and H_{coup} describes the interaction between electrons and phonons. The three

terms in real and momentum space read

$$H_{\text{kin}} = -t_0 \sum_j (c_j^\dagger c_{j+1} + c_{j+1}^\dagger c_j) = \sum_k \epsilon_k c_k^\dagger c_k, \quad (3.6)$$

$$H_{\text{ph}} = \omega_0 \sum_j b_j^\dagger b_j = \omega_0 \sum_q b_q^\dagger b_q, \quad (3.7)$$

$$\begin{aligned} H_{\text{coup}} &= -\gamma \sum_j (b_j^\dagger + b_j) n_j \\ &= -\frac{\gamma}{\sqrt{L}} \sum_{k,q} (b_q^\dagger c_{k-q}^\dagger c_k + \text{h.c.}), \end{aligned} \quad (3.8)$$

where c_j (c_j^\dagger) are fermionic annihilation (creation) operators, b_j (b_j^\dagger) are bosonic annihilation (creation) operators and $n_j = c_j^\dagger c_j$ is the local fermionic number operator at site j . The momentum space operators

$$c_k = 1/\sqrt{L} \sum_j e^{ikj} c_j, \quad (3.9)$$

$$b_q = 1/\sqrt{L} \sum_j e^{iqj} b_j, \quad (3.10)$$

are defined via discrete Fourier transformation of the real-space operators. The electrons obey the usual tight-binding dispersion

$$\epsilon_k = -2t_0 \cos(k). \quad (3.11)$$

Here, we treat a single electron only which fixes the electronic filling to $n = 1/L$.

The limits of the Holstein model are characterized by two ratios: the ratio between the phonon energy ω_0 and the hopping integral t_0 and the ratio between the coupling strength γ and the hopping integral t_0 . Phenomenologically, this ratio specifies which one of the two particle species - electrons and phonons - is faster. The system is in the so-called *adiabatic* regime for the choice of parameters $\omega_0 \ll 2t_0(1 - \cos(K))$ where $2t_0(1 - \cos(K))$ is the electronic bandwidth for an initial electron with momentum K (the total energy in the system). The lower bound of $-2t_0 \cos(K) \geq -2t_0$ holds because of the conservation of total quasi-momentum in the system. In this limit, the energy in the system is higher than the energy-cost of a single phonon and one expects an efficient energy transfer from the electron to phononic excitations. The *anti-adiabatic* regime is characterized by $\omega_0 \gg 2t_0(1 - \cos(K))$. In this case the energy of a single quantum phonon exceeds the maximal electronic energy-difference. Thus, one expects that the energy transfer is inefficient in this regime. The second ratio distinguishes the regime in terms of the coupling strength between electrons and phonons. The *weak coupling* regime is characterized by $t_0 \gg \gamma$ while in the *strong coupling* regime $t_0 \ll \gamma$. We can now distinguish the four limiting cases of this model: the weak-coupling anti-adiabatic limit, the strong-coupling anti-adiabatic limit, the weak-coupling adiabatic limit and the strong-coupling adiabatic limit.

In the ground state at non-zero coupling γ the electron and a cloud of phonons form a composite particle with renormalized mass - the polaron (for previous studies, see [23, 25] and references therein). In the weak-coupling regime (both adiabatic and non-adiabatic)

the ground state features a highly mobile electron and very few phonons. Because electron-phonon correlations decay very slowly with the distance this is called the *large-polaron* limit. The anti-adiabatic strong-coupling limit is called *small polaron* because correlations decay very fast in this limit. In this case the polaron has a strongly renormalized mass [5, 163].

3.2 Ground-state properties

As discussed in the introduction, we are interested in the properties of the three contributions to the total energy, the kinetic energy, the coupling energy and the phonon energy as well as the local von Neumann entropy and the optimal mode spectrum as a function of the model parameters. We start with the description of the limiting cases in the ground state of the Holstein model. We can find an exact expression for the quantities of interest in the two limiting cases of the large and small polaron in the quasimomentum subspace K .

In the limit of weak interactions $\gamma \ll t_0, \omega_0$ the Hamiltonian can be approximated by

$$H = -t_0 \sum_j (c_j^\dagger c_{j+1} + \text{h.c.}) + \omega_0 \sum_j b_j^\dagger b_j, \quad (3.12)$$

and the ground state will be very close to the fully delocalized $k = K$ state

$$|\psi_0\rangle = \frac{1}{i\sqrt{L}} \sum_j e^{-iKj} c_j^\dagger |\emptyset\rangle. \quad (3.13)$$

The ground state energy is then

$$E_K = E_{\text{kin}} = -2t_0 \cos(K). \quad (3.14)$$

The Holstein Hamiltonian conserves the number of electrons which blockdiagonalizes the local reduced density matrix in the local number of electrons

$$[\text{tr}_{L-1}(|\psi\rangle\langle\psi|), n] = 0. \quad (3.15)$$

A simple proof can be given for an arbitrary system divided into two parts: system block S and environment block E. If the global system is in an eigenstate of the electron number operator $[\rho_{\text{T}}, N_e] = 0$ the number of particles in the environment uniquely fixes the number of particles in the system block since $N_e = N_e^{\text{S}} + N_e^{\text{E}}$. Therefore,

$$\text{tr}_{\text{E}}([\rho, N_e]) = [\text{tr}_{\text{E}}(\rho), n_{\text{S}}] = 0 \quad (3.16)$$

has to hold, where $N_e^{\text{S}} = n_{\text{S}} \otimes \mathbf{1}$ which gives the identity $\text{tr}_{\text{E}}(\rho N_e^{\text{S}}) = \text{tr}_{\text{E}}(\rho) n_{\text{S}}$. For the case of a system subpart of only a single site the blocks are $n_{\text{S}} = n_e = 0$ and $n_{\text{S}} = n_e = 1$ where each block has dimension $N_{\text{max}} + 1$ where N_{max} is the maximal phonon occupation. So, the optimal modes have a well-defined number of electrons. In the weak coupling limit they will be very close to the bare phonon states for both, an unoccupied and an occupied site. We can also estimate the local entanglement entropy because in this limit only the $|e = 0\rangle \otimes |p = 0\rangle$ and $|e = 1\rangle \otimes |p = 0\rangle$ states will contribute significantly. Generally, the sum over the weights of the optimal modes can be grouped according to the electronic occupation number

$$1 = \sum_{\alpha'=0}^{N_{\text{max}}} w_{\alpha'}^{n_e=0} + \sum_{\alpha''=0}^{N_{\text{max}}} w_{\alpha''}^{n_e=1}, \quad (3.17)$$

where α' labels states in the $n_e = 0$ block and α'' labels states in the $n_e = 1$ block. Because there is just a single electron in the system the sum rules for those two parts are

$$\sum_{\alpha'=0}^{N_{\max}} w_{\alpha'} = \frac{L-1}{L}, \quad \sum_{\alpha''=0}^{N_{\max}} w_{\alpha''} = \frac{1}{L}, \quad (3.18)$$

which represent the probability of finding no and one electron in the system. In other words, the local reduced density matrix is diagonal in the bare basis and the weights are just given by the probabilities to have zero or one electron on a site. Therefore, the local reduced density matrix is given by

$$\begin{aligned} \rho &= P(e=0)|e=0\rangle\langle e=0| + P(e=1)|e=1\rangle\langle e=1| \\ &= \frac{(L-1)}{L}|0\rangle\langle 0| + \frac{1}{L}|1\rangle\langle 1|. \end{aligned} \quad (3.19)$$

Thus, in this case the smallest possible entropy is

$$S_{\text{vN}} = \ln(L) - \frac{L-1}{L} \ln(L-1), \quad (3.20)$$

which approaches zero as the chain length L is increased.

In the opposite limit of strong interactions $\gamma, \omega_0 \gg t_0$ the model can be approximated by a fully local one consisting of electron-phonon coupling and phonon energy terms only

$$H = \gamma \sum_j (b_j^\dagger + b_j) n_j + \omega_0 \sum_j b_j^\dagger b_j. \quad (3.21)$$

The single electron in the system is completely immobile and on the site it occupies the Hamiltonian takes the form

$$H = \gamma(b^\dagger + b) + \omega_0 b^\dagger b. \quad (3.22)$$

This Hamiltonian has the form of a shifted harmonic oscillator and can be diagonalized introducing shifted operators

$$b = a + g, \quad (3.23)$$

where $g = \gamma/\omega_0$. Putting those in Eq. (3.22) we get

$$H = \omega_0 a^\dagger a - \epsilon_b, \quad (3.24)$$

where $\epsilon_b = g\omega_0$ is called the polaron binding energy. The ground state on this site is defined by $a|\tilde{n} = 0\rangle = 0$ where $\tilde{n} = a^\dagger a$. We can insert the definition of the a -operator and find the action of the unshifted operator b on the ground state

$$b|\tilde{n} = 0\rangle = g|\tilde{n} = 0\rangle. \quad (3.25)$$

The shifted basis can be expressed in terms of the unshifted basis

$$\begin{aligned} |\tilde{n}\rangle &= \sum_n c_n |n\rangle, \\ \sum_n c_n b|n\rangle &= g \sum_n c_n |n\rangle \\ \Rightarrow c_n &= g \frac{1}{\sqrt{n}} c_{n-1} \\ &= g^n \frac{1}{\sqrt{n!}} c_0, \end{aligned}$$

where the third line follows by application of the annihilation operator on the phonon number state and substitution of $n' = n - 1$. The constant c_0 can be fixed by the requirement that the final state has norm $\langle \tilde{n} | \tilde{n} \rangle = 1$

$$c_0 = e^{-\frac{g^2}{2}}, \quad (3.26)$$

where the definition of the exponential function $\exp(x) = \sum_n x^n/n!$ is used. The final form is

$$|\tilde{n}\rangle = e^{-\frac{g^2}{2}} e^{gb^\dagger} |n = 0\rangle. \quad (3.27)$$

This is the definition of a coherent state which has the properties $\langle n \rangle = \langle n \rangle^2 = g^2$. The translation invariant ground state of the the full system reads

$$|\psi_0\rangle = \frac{e^{-g^2/2}}{\sqrt{L}} \sum_j c_j^\dagger e^{gb_j^\dagger} |\emptyset\rangle. \quad (3.28)$$

In other words, the optimal modes in the strong coupling anti-adiabatic ground state are coherent states with average phonon number n . As in the case above we have two local states that are relevant for the ground state: the zero phonon state on an empty site $|e = 0\rangle \otimes |n = 0\rangle$ and a coherent state in the phonon subspace on a site with an electron $|e = 1\rangle \otimes |\tilde{n} = 0\rangle$. Therefore, the entropy has the same lower limit as in the weak coupling case Eq. (3.20). Thus, the ground state energy is the polaron binding energy $\epsilon_b = \gamma^2/\omega_0$. In this state the phonon and coupling energies are

$$E_{\text{ph}} = \epsilon_b, \quad E_{\text{coup}} = -2\epsilon_b. \quad (3.29)$$

Between those two limiting cases a crossover happens from the large to the small polaron case with increasing coupling strength γ . To distinguish between the two one introduces the dimensionless electron-phonon coupling parameter

$$\lambda = \frac{\gamma^2}{2t_0\omega_0} \quad (3.30)$$

which is the ratio between the ground state energy of the strong coupling limit $E_0^s = -\gamma^2/\omega_0^2$ and the ground state energy of the weak coupling limit $E_0^w = -2t_0$. Hence the crossover happens in the vicinity of $\lambda^* \approx 1$.

One also defines another dimensionless parameter called the adiabaticity parameter

$$\alpha = \frac{\omega_0}{t_0} \quad (3.31)$$

which distinguishes the adiabatic $\alpha \ll 1$ from the anti-adiabatic limit $\alpha \gg 1$.

Figure 3.2 illustrates the behavior of the local von Neumann entropy S_{vN} as a function of the coupling strength λ . Interestingly, the local entanglement shows a peak in the vicinity of the crossover from large $\lambda < 1$ to small polaron $\lambda \gg 1$. Intuitively this behavior is clear because, as derived above, in both limits Eq. (3.20) has to hold (open symbols). As system size is increased the magnitude of $S_{\text{vN}}^{(1)}(\lambda)$ decreases, however, plotting the relative von Neumann entropy $S_{\text{vN}}(\lambda) - S_{\text{vN}}(\infty)/S_{\text{vN}}(\lambda_{\text{max}}) - S_{\text{vN}}(\infty)$ shows that the signal does not vanish as system size increases. Hence, the position of the maximum can be used to define the crossover scale.

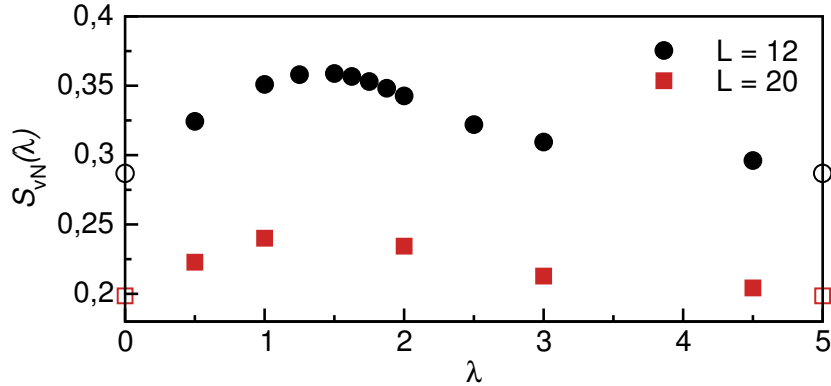


Figure 3.2: Local von Neumann entropy in the ground state as a function of the coupling strength λ for systems of sizes $L = 12, 20$ and parameters $t_0 = \omega_0 = 1$. Data for finite coupling strengths (closed symbols) were computed using exact diagonalization in a limited functional space. The data for $\lambda = 0$ and $\lambda = \infty$ (open symbols) are obtained from Eq. (3.20).

3.3 Comparison of methods

The main topic of this project is the non-equilibrium physics of the Holstein polaron and also the study of the optimal mode basis as a function of time. We need a method that is capable of reaching long enough simulation times in order to get to a steady state with the available computational resources. We compared exact diagonalization, diagonalization in a limited functional space and the time-evolving block decimation methods in order to find the most efficient one for this special problem (for an introduction in all of those methods see Sec. 1). While the TEBD computations were done in Hannover by C. Brockt and E. Jeckelmann we performed ED and LFS computations.

As discussed before (Sec. 3.2), in the ground state of the weak coupling limit Hamiltonian the electron is smeared out over the system but very few phonons are created. For the large polaron case the electron is delocalized over a large area and one needs a system size that is large enough to support the full polaron state. In the limit of the small polaron the ground state features a completely localized electron that is surrounded by a large number of phonons. As discussed in Sec. 1, exact diagonalization scales exponentially with the system size and with d^L with the local dimension. Time-evolving block decimation scales roughly linear with the system size but with the third power in the local dimension. Finally, the diagonalization in a limited functional space method uses the finite size of the polaron and constructs basis states only in a fixed vicinity of the electron. Therefore, it constructs the optimal set of states for each regime.

Figure 3.3(a) compares time-evolution in a LFS with time-evolution in the full ED basis for a system of size $L = 8$ and parameters $t_0 = \omega_0, \lambda = 0.5$. LFS correctly simulates the dynamics of an $L = 8$ system in a basis whose size is smaller by a factor $D^{\text{LFS}}/D^{\text{ED}} = 0.7$. We use this comparison for a demonstration of correctness only rather than as a proof of the efficiency of the LFS method due to the inefficiency of the ED method for larger system sizes and local dimension. Figure 3.3(b) illustrates the convergence behavior of the LFS method. For a system of size $L = 12$ (not reachable by ED) the phonon energy is plotted versus time for various choices of basis size D . With increasing basis size (generations N_h) the system reaches a steady state with an increasing number of phonons until it converges for $N_h = 20$.

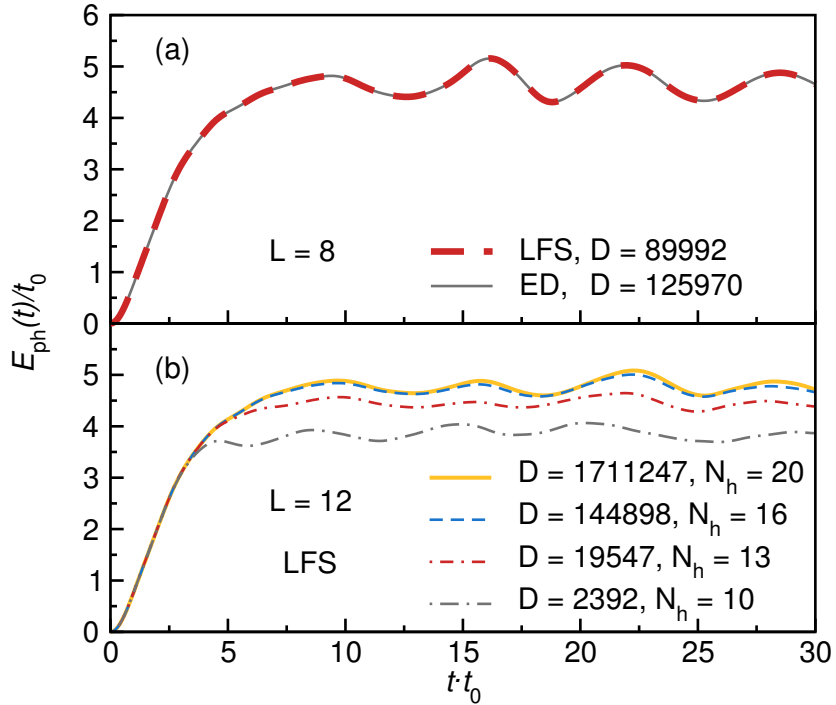


Figure 3.3: (a) Comparison of LFS with ED for a system with weak interactions $\lambda = 0.5$. (b) Convergence of LFS method to exact value with increasing basis dimension D . In both cases we set $\omega_0 = t_0$.

Figure 3.4 shows the comparison between LFS and TEBD methods for a system of size $L = 12$ in the weak coupling regime $\lambda = 0.5$. The dynamics of the phonon energy in both methods agrees perfectly over the time-window studied.

In summary, ED scales unfavorably with both system size and local dimension and, therefore, is strongly limited in the choice of simulable model parameters. TEBD is better suited for the dynamics in the weak coupling regime where a large lattice is required but a small number of local phonons is sufficient. LFS is best suited for this problem in the strong- and intermediate coupling regime because it adapts the size of the phonon cloud: for the intermediate coupling regime one needs a small amount of polaronic states and also just a moderately sized system to reach the steady state. In the strong coupling regime one needs to include a huge amount of bosonic fluctuations in the basis but, because the polaron is quite localized, small system sizes are sufficient for the dynamics up to the steady state.

3.4 Perturbative results

We start the analysis of dynamics of the Holstein polaron by employing perturbation theory to get intuition for the various limiting cases of our model. The first step is an expansion in time which allows us to infer the relevant mechanism that lowers the kinetic energy during the first few time steps. After that, we use time-dependent perturbation theory in the interaction picture to get an expansion of the expectation values of observables in ηt where η is one of the prefactors of the three terms of our model that is taken to be small compared to the

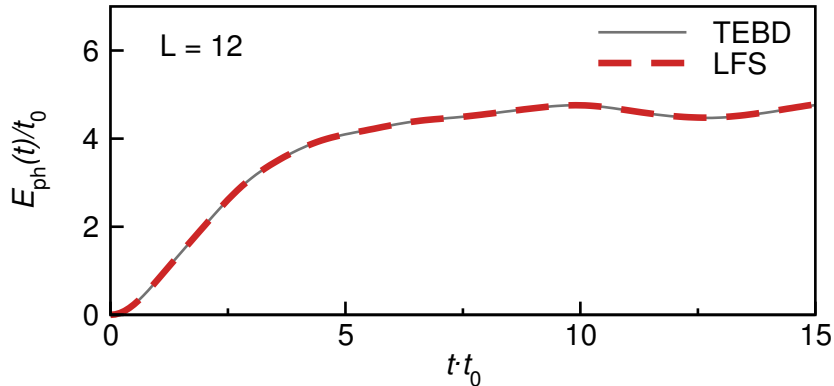


Figure 3.4: Comparison of the phonon energy $E_{\text{ph}}(t)$ obtained by diagonalization in LFS and the TEBD method. We set $\lambda = 0.5$, $\omega_0 = t_0$ and $L = 12$. Open boundary conditions are used in this figure (we use the free-electron eigenstate with the highest energy as the initial state).

others. This expansion allows the time-evolution up to longer times compared to the small-time expansion as long as ηt is small. We use this method to infer the dynamics in the limits of weak electron-phonon coupling $\eta = \gamma \ll t_0, \omega_0$ and weak hopping integral $\eta = t_0 \ll \omega_0, \gamma$ (anti-adiabatic limit). The equations found for the kinetic energy in the weak coupling limit are then used in a Boltzmann equation to find a description of the dynamics of the system.

3.4.1 Small-time expansion

To get insight into what happens during time-evolution at short times we start with an expansion of the time-evolution of an operator in time. To this end we employ the Baker-Campbell-Hausdorff formula

$$e^X O e^{-X} = O + [X, O] + \frac{1}{2!}[X, [X, O]] + \dots, \quad (3.32)$$

where $X = iHt$ and the n -th order expansion yields results up to $\mathcal{O}(t^n)$

$$\langle O \rangle(t) = \langle \psi_0 | O + it[H, O] + \frac{t^2}{2}[H, [H, O]] + \dots | \psi_0 \rangle. \quad (3.33)$$

A small-time expansion only keeps terms up to the first non-vanishing order.

We first derive the small-time expansion of the phonon energy operator $H_{\text{ph}} = \omega_0 \sum_j b_j^\dagger b_j$. Using Eq. (3.33) we need terms up to second order

$$\begin{aligned} [H, b_j^\dagger b_j] &= \gamma(b_j^\dagger - b_j)n_j, \\ [H, [H, b_j^\dagger b_j]] &= \gamma\omega_0(b_j^\dagger + b_j)n_j - 2\gamma^2 n_j n_j \\ &\quad - \gamma t_0(b_j^\dagger - b_j)(c_j^\dagger(c_{j+1} + c_{j-1}) - (c_{j+1}^\dagger + c_{j-1}^\dagger)c_j) \end{aligned}$$

because the first order terms vanish in the given initial state $|\psi(t=0)\rangle$. The phonon energy is then given by

$$E_{\text{ph}} = \omega_0(\gamma t)^2 + \mathcal{O}(t^3). \quad (3.34)$$

The kinetic energy operator $H_{\text{kin}} = -t_0 \sum_j (c_j^\dagger c_{j+1} + \text{h.c.})$ can be expanded in the same way up to second order

$$\begin{aligned}
[H, H_{\text{kin}}] &= \gamma t_0 \sum_j (b_j^\dagger + b_j - b_{j+1}^\dagger - b_{j+1}) (c_j^\dagger c_{j+1} - c_{j+1}^\dagger c_j), \\
[H, [H, H_{\text{kin}}]] &= -\gamma^2 t_0 \sum_j (b_j^\dagger + b_j - b_{j+1}^\dagger - b_{j+1})^2 (c_j^\dagger c_{j+1} - c_{j+1}^\dagger c_j) \\
&\quad - \gamma t_0^2 \sum_j (b_j^\dagger + b_j - b_{j+1}^\dagger - b_{j+1}) \\
&\quad \quad [(1 - 2n_j)(c_{j-1}^\dagger c_{j+1} + c_{j+1}^\dagger c_{j-1}) \\
&\quad \quad - (1 - 2n_{j+1})(c_j^\dagger c_{j+2} + c_{j+2}^\dagger c_j) \\
&\quad \quad - 2(n_j - n_{j+1})] \\
&\quad + \omega_0 \gamma t_0 \sum_j (b_j^\dagger - b_j - b_{j+1}^\dagger + b_{j+1}) (c_j^\dagger c_{j+1} - c_{j+1}^\dagger c_j).
\end{aligned}$$

For our initial state Eq. (3.2) we find

$$E_{\text{kin}}(t) = E_{\text{kin}}(t=0)(1 - (\gamma t)^2) + \mathcal{O}(t^3), \quad (3.35)$$

where $E_{\text{kin}}(t=0) = 2t_0$.

The last part we are interested in is the coupling energy operator $H_{\text{coup}} = -\gamma \sum_j (b_j^\dagger + b_j)n_j$. Because the total energy is conserved in our system $E_{\text{tot}} = E_{\text{kin}}(t=0)$ we can infer the short-time expansion of the coupling energy by requiring $E_{\text{kin}}(t=0) = E_{\text{kin}}(t) + E_{\text{ph}}(t) + E_{\text{coup}}(t)$ resulting in

$$E_{\text{coup}}(t) = (E_{\text{kin}}(0) - \omega_0)(\gamma t)^2 + \mathcal{O}(t^3). \quad (3.36)$$

The short-time dynamics of the system is thus controlled by the time scale set by the coupling to the phonons $1/\gamma$. This is expected because the initial state is an eigenstate of the kinetic energy operator H_{kin} . Figure 3.5 compares results for the phonon energy E_{ph} as a function of $t\gamma$ computed in either numerical simulation, or short-time expansion. The short-time expansion describes the results well for $t\gamma \lesssim 0.5$ and works longer for stronger coupling strength.

3.4.2 Perturbation theory in the interaction picture

The small-time expansion expands only in time. If one parameter of the model η is much smaller than all other ones perturbation theory in the interaction picture can be used to get a different expansion of the time-evolution of expectation values. We split the Hamiltonian into two parts

$$H = H_0 + \eta V. \quad (3.37)$$

The wavefunction in the interaction picture is defined as

$$|\psi(t)\rangle_I = e^{iH_0 t} |\psi(t)\rangle_S, \quad (3.38)$$

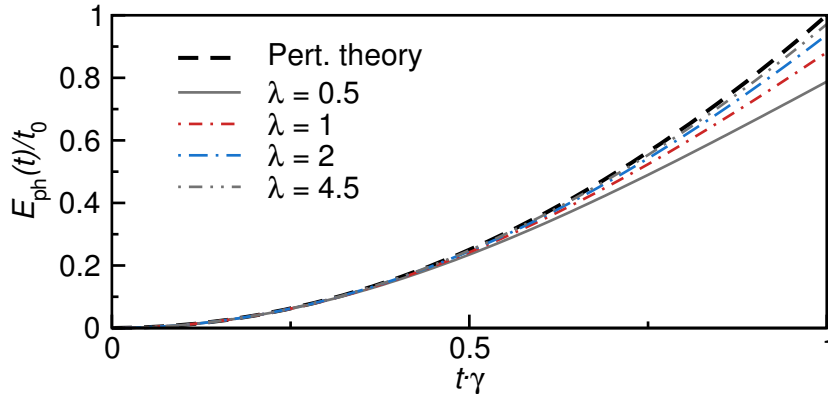


Figure 3.5: Phonon energy E_{ph} as a function of time for various interaction strengths λ . The time axis is rescaled by γ and results are compared to the approximation from the small-time expansion (dashed line). With increasing interaction strength the small-time approximation works for a longer time. For all choices of coupling strength we set $\omega_0 = t_0$.

where $|\psi(t)\rangle_S$ is the wavefunction in the Schrödinger picture. Similarly we arrive at an operator in the interaction picture

$$O_I = e^{iH_0 t} O_S e^{-iH_0 t}, \quad (3.39)$$

where O_S is the operator in the Schrödinger picture. The time-evolution of the wavefunction is then

$$i \frac{\partial}{\partial t} |\psi(t)\rangle_I = \eta V_I |\psi(t)\rangle_I, \quad (3.40)$$

where we plugged in Eq. (3.38). The time propagator is defined as an operator that transforms the wavefunction at a time t_0 to a time $t_1 = t_0 + t$

$$|\psi(t_1)\rangle_I = U_I(t) |\psi(t_0)\rangle_I, \quad (3.41)$$

$$U_S(t) |\psi(t_0)\rangle_S = e^{-iH_0 t} U_I(t) |\psi(t_0)\rangle_I, \quad (3.42)$$

where we operate with $e^{-iH_0 t}$ from the left on both sides on the equation and insert $|\psi(t_1)\rangle_S = U_S(t) |\psi(t_0)\rangle_S$ to arrive at the second line. Because for the initial state $|\psi(t_0)\rangle_I = |\psi(t_0)\rangle_S$ we can relate the time propagators of both pictures to each other

$$U_S(t) = e^{-iH_0 t} U_I(t). \quad (3.43)$$

We now have the relevant parts to find an approximation to the time propagator in the Schrödinger picture. First, we express Eq. (3.40) via the time propagator Eq. (3.41)

$$i \frac{\partial}{\partial t} U_I(t) = \eta V_I(t) U_I(t). \quad (3.44)$$

We can integrate this equation on both sides to get an equation for $U_I(t)$

$$U_I(t) = U_I(t_0) - i\eta \int_{t_0}^t dt' V_I(t') U_I(t') \quad (3.45)$$

This equation can be solved by inserting $U_I(t')$ on the right hand side

$$\begin{aligned}
U_I(t) &= 1 - (i\eta) \int_{t_0}^t dt' e^{iH_0 t'} V(t') e^{-iH_0 t'} \\
&+ (i\eta^2) \int_{t_0}^t dt' \int_{t_0}^{t'} dt'' e^{iH_0 t'} V(t'') e^{-iH_0(t'-t'')} V(t') e^{-iH_0 t'} \\
&+ \mathcal{O}((\eta t)^3),
\end{aligned} \tag{3.46}$$

where we used Eq. (3.39) to relate the equation to the interaction part in the Schrödinger picture. We can finally use Eq. (3.43) to find an approximation in ηt for the time propagator in the Schrödinger picture

$$\begin{aligned}
U_S(t) &= e^{-iH_0 t} - i\eta \int_0^{t-t_0} dt_1 e^{-iH_0 t_1} V(t-t_1) e^{-iH_0(t-t_1)} \\
&- \eta^2 \int_0^{t-t_0} dt_1 \int_0^{t-t_1-t_0} dt_2 e^{-iH_0 t_1} V(t-t_1) e^{-iH_0 t_2} \\
&\quad \times V(t-t_1-t_2) e^{-iH_0(t-t_1-t_2)} \\
&+ \mathcal{O}((\eta t)^3),
\end{aligned} \tag{3.47}$$

where $t_1 = t - t'$ and $t_2 = t' - t''$ was used to reparametrize the intermediate timesteps. With the definition of the time propagator the expectation value of an operator at some point in time reads

$$\begin{aligned}
\langle \mathcal{O} \rangle(t) &= \langle U_0^\dagger \mathcal{O} U_0 \rangle + \eta \langle U_0^\dagger \mathcal{O} U_1 + U_1^\dagger \mathcal{O} U_0 \rangle \\
&+ \eta^2 \langle U_1^\dagger \mathcal{O} U_1 + U_0^\dagger \mathcal{O} U_2 + U_2^\dagger \mathcal{O} U_0 \rangle + \mathcal{O}(\eta^3),
\end{aligned} \tag{3.48}$$

where

$$U_0(t) = e^{-iH_0 t}, \tag{3.49}$$

$$U_1(t) = -i \int_0^{t-t_0} dt_1 e^{-iH_0 t_1} V e^{-iH_0(t-t_1)}, \tag{3.50}$$

and

$$\begin{aligned}
U_2(t) &= - \int_0^{t-t_0} dt_1 \int_0^{t-t_1-t_0} dt_2 e^{-iH_0 t_1} V e^{-iH_0 t_2} \\
&\quad \times V e^{-iH_0(t-t_1-t_2)}.
\end{aligned} \tag{3.51}$$

In this last step we omit the time-dependence of the interaction term V because in our problem the Hamiltonian is time-independent. The advantage compared to the small-time expansion is that for a small prefactor η a low order expansion captures longer times.

Weak electron-phonon coupling

We derive $\langle O \rangle(t)$ from Eq. (3.48) explicitly for $\eta = \gamma \ll t_0, \omega_0$ and $V = H_{\text{coup}}/\gamma$ for the initial state Eq. (3.2). Because the initial state has a well-defined momentum we use the momentum-space representation of the Hamiltonian.

We start with the first order terms

$$\langle O^{(1)} \rangle(t) = \langle U_0^\dagger O U_1 \rangle + \langle U_0^\dagger O U_1 \rangle^*, \quad (3.52)$$

$$\begin{aligned} \langle U_0^\dagger O U_1 \rangle &= \langle \psi_0^K | e^{iH_0 t} O(-i) \int_0^t d\tau e^{-iH_0 \tau} V e^{-iH_0(t-\tau)} | \psi_0^K \rangle \\ &= (-i) \int_0^t d\tau e^{i\epsilon_K \tau} \langle \psi_0^K | O e^{-iH_0 \tau} V | \psi_0^K \rangle, \end{aligned} \quad (3.53)$$

where $\epsilon_K = \langle \psi_0^K | H_0 | \psi_0^K \rangle$. We can explicitly calculate $e^{-iH_0 \tau} V | \psi_0^K \rangle$

$$e^{-iH_0 \tau} V | \psi_0^K \rangle = -\frac{e^{-i\omega_0 \tau}}{\sqrt{L}} \sum_q e^{-i\epsilon_{K-q} \tau} b_q^\dagger | \psi_0^{K-q} \rangle. \quad (3.54)$$

With this we find

$$\begin{aligned} \langle U_0^\dagger O U_1 \rangle &= \frac{i}{\sqrt{L}} \sum_q \langle \psi_0^K | O b_q^\dagger | \psi_0^{K-q} \rangle \int_0^t d\tau e^{-i(\epsilon_{K-q} + \omega_0 - \epsilon_K) \tau} \\ &= -\frac{1}{\sqrt{L}} \sum_q \langle \psi_0^K | O b_q^\dagger | \psi_0^{K-q} \rangle \frac{1 - e^{-i(\delta E_{K,q}) t}}{\delta E_{K,q}}, \end{aligned} \quad (3.55)$$

where $\delta E_{K,q} = \epsilon_{K-q} + \omega_0 - \epsilon_K$. The full first order term is then

$$\langle O^{(1)} \rangle(t) = \frac{2}{\sqrt{L}} \sum_q R_{K,q}^{(1)} \frac{1 - \cos(\delta E_{K,q} t)}{\delta E_{K,q}}, \quad (3.56)$$

where $R_{K,q}^{(1)} = \langle \psi_0^K | O b_q^\dagger | \psi_0^{K-q} \rangle$.

The second order term can be calculated in the same fashion

$$\langle O^{(2)} \rangle(t) = \langle U_1^\dagger O U_1 \rangle + \langle U_0^\dagger O U_2 \rangle + \langle U_0^\dagger O U_2 \rangle^*. \quad (3.57)$$

We start with the term involving the second order time propagator

$$\begin{aligned} \langle U_0^\dagger O U_2 \rangle &= \langle \psi_0^K | e^{iH_0 t} O(-1) \int_0^t dt_1 \int_0^{t-t_1} dt_2 e^{-iH_0 t_1} V e^{-iH_0 t_2} \\ &\quad \times V e^{-iH_0(t-t_1-t_2)} | \psi_0^K \rangle \\ &= (-1) \int_0^t dt_1 \int_0^{t-t_1} dt_2 e^{i\epsilon_K(t_1+t_2)} \langle \psi_0^K | O e^{-iH_0 t_1} V e^{-iH_0 t_2} V | \psi_0^K \rangle. \end{aligned} \quad (3.58)$$

By insertion of Eq. (3.54)

$$\begin{aligned} \langle U_0^\dagger O U_2 \rangle &= \frac{1}{\sqrt{L}} \sum_q \int_0^t dt_1 e^{i\epsilon_K t_1} \langle \psi_0^K | O e^{-iH_0 t_1} V b_q^\dagger | \psi_0^{K-q} \rangle \\ &\quad \times \int_0^{t-t_1} dt_2 e^{i(\epsilon_K - \omega_0 - \epsilon_{K-q}) t_2}. \end{aligned} \quad (3.59)$$

We can explicitly perform the operation $e^{-iH_0 t_1} V b_q^\dagger | \psi_0^{K-q} \rangle$

$$\begin{aligned} e^{-iH_0 t_1} V b_q^\dagger | \psi_0^{K-q} \rangle &= -\frac{1}{\sqrt{L}} \left(\sum_{q'} e^{-i(2\omega_0 + \epsilon_{K-q-q'}) t_1} b_{q'}^\dagger b_q^\dagger c_{K-q-q'}^\dagger \right. \\ &\quad \left. + e^{-i\epsilon_K t_1} c_K^\dagger \right) | \emptyset \rangle. \end{aligned} \quad (3.60)$$

Inserted back into Eq. (3.59) we get

$$\begin{aligned} \langle U_0^\dagger O U_2 \rangle &= -\frac{1}{L} \sum_q \int_0^t dt_1 [\langle \psi_0^K | O | \psi_0^K \rangle \\ &\quad + e^{-i(2\omega_0 + \epsilon_{K-q-q'}) t_1} \langle \psi_0^K | O b_{q'}^\dagger b_q^\dagger | \psi_0^{K-q-q'} \rangle] \\ &\quad \times \int_0^{t-t_1} dt_2 e^{i(\epsilon_K - \omega_0 - \epsilon_{K-q}) t_2}. \end{aligned} \quad (3.61)$$

The second term proportional to $(b_q^\dagger)^2$ is only relevant for operators which include terms $(b_q)^2$. We are only interested in measuring the three contributions to the energy that the Hamiltonian consists of (H_{kin} , H_{ph} and H_{coup}) and therefore neglect this part in the further discussion

$$\begin{aligned} \langle U_0^\dagger O U_2 \rangle &= -\frac{1}{L} \langle \psi_0^K | O | \psi_0^K \rangle \sum_q \int_0^t dt_1 \int_0^{t-t_1} dt_2 e^{i(\epsilon_K - \omega_0 - \epsilon_{K-q}) t_2} \\ &= -\frac{1}{L} \langle \psi_0^K | O | \psi_0^K \rangle \sum_q \left(\frac{1 - e^{-i\delta E_{K,q} t}}{\delta E_{K,q}^2} - \frac{it}{\delta E_{K,q}} \right). \end{aligned} \quad (3.62)$$

The sum together with the hermitian conjugate of this term finally gives

$$\langle U_0^\dagger O U_2 + U_2^\dagger O U_0 \rangle = -\frac{2}{L} \sum_q R_K^{(2a)} \frac{1 - \cos(\delta E_{K,q} t)}{(\delta E_{K,q})^2}, \quad (3.63)$$

where $R_K^{(2a)} = \langle \psi_0^K | O | \psi_0^K \rangle$. We continue with the derivation of the term involving two first

order propagators

$$\begin{aligned}
\langle U_1^\dagger O U_1 \rangle &= \langle \psi_0^K | (i) \int_0^t d\tau e^{iH_0(t-\tau)} V^\dagger e^{iH_0\tau} \\
&\quad \times (-i) \int_0^t d\tau' e^{-iH_0\tau'} V e^{-iH_0(t-\tau')} | \psi_0^K \rangle \\
&= \frac{1}{L} \sum_{q,q'} \langle \psi_0^{K-q} | b_q O b_{q'}^\dagger | \psi_0^{K-q'} \rangle \frac{e^{i\delta E_{K,q}t} - 1}{i\delta E_{K,q}} \frac{e^{-i\delta E_{K,q'}t} - 1}{-i\delta E_{K,q'}}.
\end{aligned} \tag{3.64}$$

Under the assumption that for operators of interest $O = O' \delta_{q,q'}$ we can simplify this result to

$$\langle U_1^\dagger O U_1 \rangle = \frac{2}{L} \sum_q R_{K,q}^{(2b)} \frac{1 - \cos(\delta E_{K,q}t)}{(\delta E_{K,q})^2}, \tag{3.65}$$

where $R_{K,q}^{(2b)} = \langle \psi_0^{K-q} | b_q O b_{q'}^\dagger | \psi_0^{K-q'} \rangle$.

We are now in the position to find an approximation to the operators we are interested in up to second order time-dependent perturbation theory. To this end we only need to evaluate $R_{K,q}^{(1)}$, $R_K^{(2a)}$ and $R_{K,q}^{(2b)}$ for the respective observable. For the Hamiltonian operators we find

$$\begin{aligned}
E_{\text{kin}} &= \epsilon_K \left[1 - \frac{2\gamma^2}{L} \sum_q \frac{1 - \cos(\delta E_{K,q}t)}{(\delta E_{K,q})^2} \right] \\
&\quad + \frac{2\gamma^2}{L} \sum_q \epsilon_{K-q} \frac{1 - \cos(\delta E_{K,q}t)}{(\delta E_{K,q})^2},
\end{aligned} \tag{3.66}$$

$$E_{\text{ph}} = \frac{2\omega_0\gamma^2}{L} \sum_q \frac{1 - \cos(\delta E_{K,q}t)}{(\delta E_{K,q})^2}, \tag{3.67}$$

$$E_{\text{coup}} = -\frac{2\gamma^2}{L} \sum_q \frac{1 - \cos(\delta E_{K,q}t)}{(\delta E_{K,q})^2}. \tag{3.68}$$

An expansion in t of these equations up to second order yields the small-time expansion results Eqs. (3.34), (3.35) and (3.36).

The first case we analyze in this framework is the anti-adiabatic regime $\omega_0 > 2t_0(1 - \cos(K))$. As pointed out above, the energy transfer in this case is expected to be inefficient because a single phonon costs more energy than there is in the system. To understand the relevant energy scales in this regime we consider the limiting case $\omega_0 \gg t_0$ which allows the substitution of $\delta E_{K,q}$ by ω_0 in Eqs. (3.66)-(3.68). For the phonon energy this yields

$$\begin{aligned}
E_{\text{ph}}(t) &= \omega_0 N_{\text{ph}}(t) \\
&= 2\omega_0 \left(\frac{\gamma}{\omega_0} \right)^2 (1 - \cos(\omega_0 t)).
\end{aligned} \tag{3.69}$$

Clearly the time-evolution is governed by oscillations with frequency ω_0 : The system starts from the initial state without phonons. As time progresses the number of phonons increases

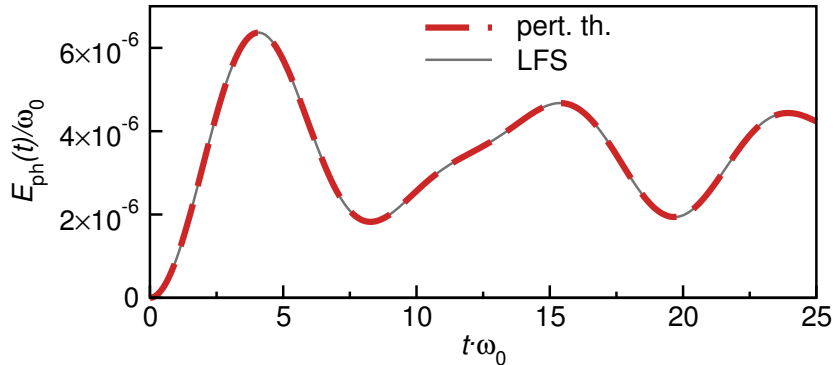


Figure 3.6: Time evolution of the phonon energy $E_{\text{ph}}(t)$ in the weak-coupling anti-adiabatic limit for $L = 12$. The parameters are set to $t_0/\omega_0 = 0.1$ and $\gamma/\omega_0 = 0.01$ which corresponds to $\lambda = 0.5 \times 10^{-3}$. Data from numerical simulations using the LFS method (solid line) are compared to Eq. (3.67) from perturbation theory.

up to a maximum of $N_{\text{ph}}^{\text{max}} = 4(\gamma/\omega_0)^2$. Afterwards the number of phonons goes back to zero. We will recover a similar behavior in the strong coupling limiting case.

When $1 < \omega_0/t_0 \ll \infty$, Eq. (3.69) is a very bad approximation. However, the sum over q in Eqs. (3.66)-(3.68) can be performed exactly then. This is shown in Fig. 3.6. The direct comparison to numerical data shows that for this choice of parameters this formula perfectly describes the physics. Since Eq. (3.69) was derived taking processes into account where at most a single phonon is created this implies that higher-order processes are unimportant in this parameter regime.

We now turn to the adiabatic regime $\omega_0 < 2t_0(1 - \cos(K))$. A main interest in the project is the study of the relaxation dynamics of the electron. We study the electronic relaxation by measuring the decrease of the kinetic energy. Equation (3.66) can be brought into the form

$$E_{\text{kin}}(t) = \epsilon_K - \frac{4\gamma^2}{L} \sum_q (\epsilon_K - \epsilon_{K-q}) \frac{\sin^2(\frac{\delta E_{K,q} t}{2})}{(\delta E_{K,q})^2}, \quad (3.70)$$

where we used $1 - \cos(x) = 2 \sin^2(x/2)$. The energy that the electron loses as time progresses is given by

$$\begin{aligned} \Delta E_{\text{kin}}(t) &= \frac{4\gamma^2}{L} \sum_q (\epsilon_{K-q} - \epsilon_K) \frac{\sin^2(\frac{\delta E_{K,q} t}{2})}{(\delta E_{K,q})^2} \\ &= \sum_q (\epsilon_{K-q} - \epsilon_K) n_{K-q}(t), \end{aligned} \quad (3.71)$$

where $n_{K-q}(t) = \frac{4\gamma^2}{L} \frac{\sin^2(\frac{\delta E_{K,q} t}{2})}{(\delta E_{K,q})^2}$. All information about the relaxation is thus encoded in the time-evolution of the momentum distribution function $n_k(t)$. The system at time t is in a state

$$|\psi(t)\rangle = c_K(t)|\psi^K\rangle + \sum_{q \neq 0} c_{K-q}(t)|\psi^{K-q}\rangle. \quad (3.72)$$

The occupation of a state with momentum $K - q$ is thus

$$n_{K-q}(t) = \langle \psi(t) | n_{K-q} | \psi(t) \rangle = |c_{K-q}(t)|^2. \quad (3.73)$$

The density matrix for the state $|\psi(t)\rangle$ is defined as

$$\begin{aligned}\rho(t) &= |\psi(t)\rangle\langle\psi(t)| \\ &= |c_K(t)|^2 |\psi^K\rangle\langle\psi^K| + \sum_{\substack{q \neq 0 \\ q' < q}} c_{K-q}(t) c_{K-q'}^*(t) |\psi^{K-q}\rangle\langle\psi^{K-q'}|,\end{aligned}\quad (3.74)$$

and encodes the probability of finding the system in a state $|\psi^{K-q}\rangle$ at time t in the diagonal entries $|c_{K-q}(t)|^2$. The probability to find the electron in a state with momentum different from $k = K$ is then

$$\begin{aligned}P_{k \neq K}(t) &= \sum_{q \neq 0} \langle\psi^{K-q}|\rho(t)|\psi^{K-q}\rangle \\ &= \sum_{q \neq 0} |c_{K-q}(t)|^2 \\ &= \sum_{q \neq 0} n_{K-q}(t),\end{aligned}\quad (3.75)$$

where the last line follows from Eq. (3.73). We define the transition rate for the electron which is the probability per time interval Δt for a transition of the electron to states different from its initial state

$$\begin{aligned}W(\Delta t) &= \frac{1}{\Delta t} \sum_{k \neq K} n_k(\Delta t) \\ &= \frac{4\gamma^2}{L} \sum_{q \neq 0} \frac{1}{\Delta t} \frac{\sin^2\left(\frac{\delta E_{K,q} t}{2}\right)}{(\delta E_{K,q})^2}.\end{aligned}\quad (3.76)$$

For a large system $L \gg 1$ the quasi-momentum space is continuous and the sum over momenta can be replaced by an integral over energies including the density of states

$$\begin{aligned}D_{\text{ele}}(E + \epsilon_0 - \omega_0) &= 2t_0 \frac{\partial q}{\partial \epsilon_{K-q}} \\ &= \frac{1}{\sqrt{1 - \left(\frac{E + \epsilon_0 - \omega_0}{2t_0}\right)^2}},\end{aligned}\quad (3.77)$$

where $\epsilon_{K-q} = -2t_0 \cos(K - q)$, $E + \epsilon_0 - \omega_0$ is the energy of the electron after transition and ϵ_0 is the energy of the electron before the transition. The transition rate is then

$$W(\Delta t) = \frac{\gamma^2}{t_0} \int_{-2t_0 - (\epsilon_0 - \omega_0)}^{2t_0 - (\epsilon_0 - \omega_0)} dE D_{\text{ele}}(E + \epsilon_0 - \omega_0) \frac{2}{\pi} \frac{1}{\Delta t} \frac{\sin^2\left(\frac{E \Delta t}{2}\right)}{E^2}.\quad (3.78)$$

For large enough times Δt

$$\delta(E) = \frac{2}{\pi} \frac{1}{\Delta t} \frac{\sin^2\left(\frac{E \Delta t}{2}\right)}{E^2},\quad (3.79)$$

and the transition rate is time-independent. Insertion into Eq. (3.78) recovers Fermi's golden rule [164]

$$W = \frac{\gamma^2}{t_0} D_{\text{ele}}(\epsilon_0 - \omega_0) = 2\lambda\omega_0 D_{\text{ele}}(\epsilon_0 - \omega_0).\quad (3.80)$$

In the adiabatic limit $\omega_0 \rightarrow 0$ the transition rate can be approximated to leading order

$$W_K = \frac{\gamma^2}{t_0 |\sin(K)|}, \quad (3.81)$$

where K denotes the initial momentum of the electron. This result agrees up to a factor of two with the exact rate that was obtained for a 1D polaron model with linear electronic dispersion [148]. The two models give the same result only in this limit because for the two models to be equivalent one has to require a small momentum transfer which is only given for small ω_0 . From Eq. (3.71) we see that $\delta E_{K,q} = 0$ is required to reach the largest transition rate. Both requirements are fulfilled simultaneously in the adiabatic limit $\omega_0 \ll t_0$.

Because the electronic dispersion diverges at the band edges for transitions that touch the band edge the integral Eq. (3.78) needs to be evaluated explicitly. In the case of $\epsilon_0 - \omega_0 \approx -2t_0$ the electronic density of states $D_{\text{ele}}(E - 2t_0)$ can be expanded around $E = 0$. Taking the limit of $4t_0\Delta t \gg 1$ one obtains the asymptotic behavior

$$W(\Delta t) \approx \frac{\gamma^2}{\sqrt{t_0}} \frac{2\sqrt{2}}{3\sqrt{\pi}} \sqrt{\Delta t}, \quad (3.82)$$

which shows that the transition rate to the lowest electronic state is not time-independent. For the case where $\epsilon_0 = \epsilon_K$ and $\omega_0 = 2t_0(1 - \cos(K))$ we find a power law behavior of ΔE_{kin} .

The crucial insight of Lev Vidmar was to use the results for the transition rate of the electron together with the Boltzmann equation to find a semiclassical approximation to the time-evolution of the electron in a system in the thermodynamic limit. The Boltzmann equation for the electron-phonon system is

$$\dot{n}_k = \sum_q W_{k,q} [f_{k,q}^{\text{in}} - f_{k,q}^{\text{out}}], \quad (3.83)$$

where

$$\begin{aligned} f_{k,q}^{\text{in}} &= n_{k-q}(1 - n_k)N_q\delta(\epsilon_k - \epsilon_{k-q} - \hbar\omega_0) \\ &+ n_{k+q}(1 - n_k)(N_q + 1)\delta(\epsilon_k - \epsilon_{k+q} + \hbar\omega_0), \end{aligned} \quad (3.84)$$

describes the process where an electron gets scattered into the state with momentum k and

$$\begin{aligned} f_{k,q}^{\text{out}} &= n_k(1 - n_{k-q})(N_q + 1)\delta(\epsilon_k - \epsilon_{k-q} - \hbar\omega_0) \\ &+ n_k(1 - n_{k+q})N_q\delta(\epsilon_k - \epsilon_{k+q} + \hbar\omega_0), \end{aligned} \quad (3.85)$$

describes the reverse process where an electron gets scattered out of the state with momentum k either by emitting or absorbing a single phonon. We first reformulate Eq. (3.83) in terms of densities in the energy space instead of momentum space

$$\dot{n}_{\epsilon_i} = -W_{i+1}n_{\epsilon_i}(1 - n_{\epsilon_{i+1}}/2) + W_i n_{\epsilon_{i-1}}(1 - n_{\epsilon_i}/2), \quad (3.86)$$

where $\omega_q = \omega_0$ since we have dispersionless phonons and the factor of 1/2 comes from the fact that for every energy there are two momenta. Also, we set $N_q = 0$ at all times which means that the electron never encounters a phonon that it excited previously in time. For a very large system with dispersionless phonons this assumption is reasonable. In total there

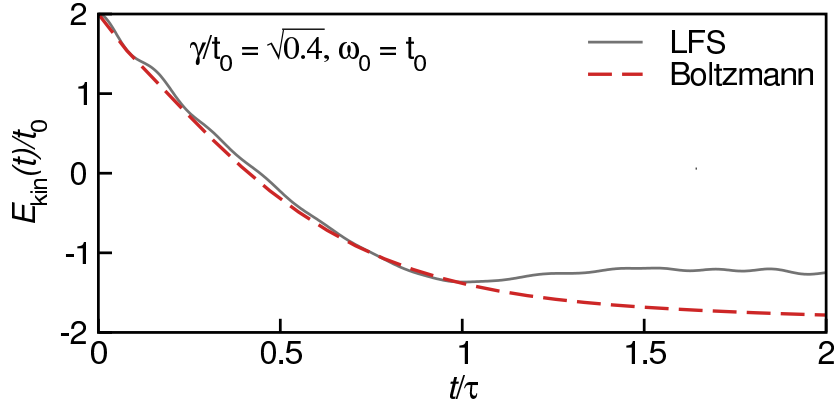


Figure 3.7: Time evolution of the kinetic energy $E_{\text{kin}}(t)$ in the weak-coupling adiabatic limit for $L = 12$, $\gamma/t_0 = 0.4$, $\omega_0 = t_0$ compared to the numerical solution of the Boltzmann Eqs. (3.87). The time axis is rescaled by the relaxation time Eq. (3.92).

are $s = 2t_0(1 - \cos(K))/\omega_0$ transitions until the electron has given all of its energy to the phonon subsystem. The full relaxation is then described by the cascade of transitions

$$\begin{aligned}
\dot{n}_{\epsilon_0} &= -W_1 n_{\epsilon_0} (1 - n_{\epsilon_1}/2), \\
\dot{n}_{\epsilon_1} &= -W_2 n_{\epsilon_1} (1 - n_{\epsilon_2}/2) + W_1 n_{\epsilon_0} (1 - n_{\epsilon_1}/2), \\
&\dots \\
\dot{n}_{\epsilon_{s-1}} &= -W_s n_{\epsilon_{s-1}} (1 - n_{\epsilon_s}/2) + W_{s-1} n_{\epsilon_{s-2}} (1 - n_{\epsilon_{s-1}}/2), \\
\dot{n}_{\epsilon_s} &= W_s n_{\epsilon_{s-1}} (1 - n_{\epsilon_s}/2),
\end{aligned} \tag{3.87}$$

where $\epsilon_i = \epsilon_{i-1} - \omega_0$. A sketch of this cascade is presented in Fig. 3.1. For all $1 \leq i < s$ the transition rate is given by Eq. (3.80) and for the last transition it is given by the time-dependent Eq. (3.82). Figure 3.7 shows the solution of Eqs. (3.87) compared to the numerical solution for a system of size $L = 12$. For this choice of parameters the data show perfect agreement in the whole relaxation regime $t/\tau \leq 1$ which indicates that for sufficiently small γ the processes Eq. (3.87) are most relevant for the dynamics of the system. The deviations after relaxation can be attributed to the finite system size of the numerically simulated system where the electron will at some point encounter previously excited phonons.

We can get an analytical expression for the relaxation time in this system for a constant density of states $D_{\text{ele}} = \pi/4$ which is exact for the case of a linear dispersion ([148, 149]). From Eq. (3.80)

$$\Gamma = \frac{\pi}{2} \lambda \omega_0, \tag{3.88}$$

and Eqs. (3.87) become

$$\begin{aligned}
\dot{n}_{\epsilon_0} &= -\Gamma n_{\epsilon_0} (1 - n_{\epsilon_1}/2), \\
\dot{n}_{\epsilon_1} &= -\Gamma n_{\epsilon_1} (1 - n_{\epsilon_2}/2) + \Gamma n_{\epsilon_0} (1 - n_{\epsilon_1}/2), \\
&\dots \\
\dot{n}_{\epsilon_{s-1}} &= -\Gamma n_{\epsilon_{s-1}} (1 - n_{\epsilon_s}/2) + \Gamma n_{\epsilon_{s-2}} (1 - n_{\epsilon_{s-1}}/2), \\
\dot{n}_{\epsilon_s} &= \Gamma n_{\epsilon_{s-1}} (1 - n_{\epsilon_s}/2),
\end{aligned} \tag{3.89}$$

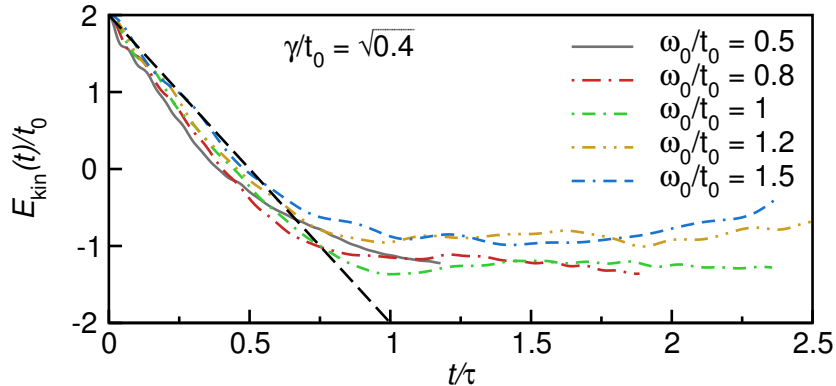


Figure 3.8: Relaxation dynamics of the kinetic energy $E_{\text{kin}}(t)$ in the weak-coupling regime. For all shown data, hopping integral t_0 and electron-phonon interaction γ are kept fixed at $(\gamma/t_0)^2 = 0.4$ while the adiabaticity takes the values $\alpha = \omega_0/t_0 = 0.5, 0.8, 1, 1.2, 1.5$ which correspond to $\lambda = 0.4, 0.25, 0.2, 0.17$ and 0.13 . The data is calculated numerically using the LFS method for a system with size $L = 12$. The dashed line is the function $E_{\text{kin}}(t)/t_0 = 2(1 - 2(t/\tau))$ with the relaxation time τ defined by Eq. (3.92).

which can be solved analytically for $1 \leq m < s$

$$n_{\epsilon_m}(t) = \frac{(\Gamma t)^m}{m!} e^{-\Gamma t}. \quad (3.90)$$

This is a Poissonian distribution with maximum at $m \approx \Gamma t$. As an estimate for the relaxation time we take the time it takes until the maximum of the distribution is at position $m = s$

$$\tau = \frac{s}{\Gamma}, \quad (3.91)$$

which leads to

$$\tau \omega_0 = \frac{16}{\pi} \left(\frac{\gamma}{t_0} \right)^{-2} = \frac{8}{\pi} \left(\frac{\lambda \omega_0}{t_0} \right)^{-2}. \quad (3.92)$$

An important insight from this relation is that the relaxation depends on all three model parameters.

We compare Eq. (3.92) to numerics in Fig. 3.8 for different values of ω_0 . With time measured in units of τ the curves collapse fairly well in the relaxation regime. We attribute this agreement to the fact that the relaxation dynamics is dominated by the slowest transitions W_m in the Boltzmann equations (3.87). Following Eq. (3.80) this is the case when the electron is away from the band edges.

Small hopping amplitude

In this section we cover the strong coupling anti-adiabatic case $t_0 \ll \gamma, \omega_0$.

In the extreme case of $t_0 = 0$ the electron is completely immobile and no net transfer of energy from electron to phonons is expected. The unperturbed Hamiltonian is given by Eq. (3.24) and because all sites are decoupled it can be diagonalized by a rotation in the phonon basis to the coherent states as shown in Sec. 3.2. Since the previously derived

perturbative solutions work for operators we want to transform the Hamiltonian instead of the basis. Every operator can be rotated by a unitary Lang-Firsov transformation [165]

$$\tilde{O} = e^{iS} O e^{-iS}, \quad (3.93)$$

with the hermitian operator

$$\begin{aligned} S &= g \sum_j p_j n_j \\ &= ig \sum_j (b_j^\dagger - b_j) n_j, \end{aligned} \quad (3.94)$$

where again $g = \gamma/\omega_0$. We can recover the shifted operators Eq. (3.23) by transforming the annihilation and creation operators explicitly

$$\begin{aligned} \tilde{b}_j &= e^{iS} b_j e^{-iS} \\ &= e^{-g(b_j^\dagger - b_j)n_j} b_j e^{g(b_j^\dagger - b_j)n_j} \\ &= b_j + g n_j, \end{aligned} \quad (3.95)$$

where the transformation is non-trivial only on a site with a non-vanishing electron density. The transformed Hamiltonian is then

$$\begin{aligned} \tilde{H}_0 &= \gamma \sum_j (\tilde{b}_j^\dagger + \tilde{b}_j) \tilde{n}_j + \omega_0 \sum_j \tilde{b}_j^\dagger \tilde{b}_j \\ &= \omega_0 \sum_j b_j^\dagger b_j - \epsilon_b, \end{aligned} \quad (3.96)$$

where the Hamiltonian is diagonalized using Eq. (3.95). The initial state becomes

$$\begin{aligned} |\tilde{\psi}_0\rangle &= e^{iS} |\psi_0\rangle \\ &= \frac{e^{-g^2/2}}{\sqrt{L}} \sum_j e^{iKj} [e^{-g b_j^\dagger} c_j^\dagger |\emptyset\rangle]. \end{aligned} \quad (3.97)$$

The time-evolution for this state can be calculated exactly

$$\begin{aligned} |\tilde{\psi}_0(t)\rangle &= e^{-i\tilde{H}_0 t} |\tilde{\psi}_0\rangle \\ &= e^{-i(\omega_0 \sum_j b_j^\dagger b_j - \epsilon_b)t} |\tilde{\psi}_0\rangle \\ &= e^{i\epsilon_b t} \frac{e^{-g^2/2}}{\sqrt{L}} \sum_j e^{iKj} [e^{-g(t) b_j^\dagger} c_j^\dagger |\emptyset\rangle], \end{aligned} \quad (3.98)$$

where $g(t) = g e^{-i\omega_0 t}$. This wavefunction is similar to the one found for the ground state in the small polaron case Eq. (3.28) but the phonon cloud does now fluctuate in time. To gain insight into this state we can evaluate operator expectation values directly in this representation

$$O(t) = \langle \tilde{\psi}_0(t) | \tilde{O} | \tilde{\psi}_0(t) \rangle. \quad (3.99)$$

We first evaluate the phonon displacement \tilde{x}_j and phonon momentum \tilde{p}_j operators

$$\begin{aligned}\tilde{x}_j &= \tilde{b}_j^\dagger + \tilde{b}_j \\ &= b_j^\dagger + b_j + 2gn_j,\end{aligned}\tag{3.100}$$

$$\begin{aligned}\tilde{p}_j &= i(\tilde{b}_j^\dagger - \tilde{b}_j) \\ &= i(b_j^\dagger - b_j).\end{aligned}\tag{3.101}$$

Because the time-evolved state $|\tilde{\psi}(t)\rangle$ is an eigenstate of the annihilation operator

$$b_j|\tilde{\psi}(t)\rangle = g(t)|\tilde{\psi}(t)\rangle,\tag{3.102}$$

we can easily write down their expectation values

$$x_j(t) = \frac{2g}{L}(1 - \cos(\omega_0 t)),\tag{3.103}$$

$$p_j(t) = \frac{2g}{L}\sin(\omega_0 t).\tag{3.104}$$

These expectation values allow a physical interpretation of what happens in the system as time progresses. The prefactor $1/L$ stems from the delocalized nature of the electron: the probability to find the electron on site j is $1/L$. On the site where the electron sits the boson degrees of freedom behave like a harmonic oscillator with frequency ω_0 and an equilibrium position of $\langle x_{\text{eq}} \rangle = 2g$. The initial state fixes $\langle x_j(t=0) \rangle = \langle p_j(t=0) \rangle = 0$ which is the minimal position of the oscillator. Thus, the oscillator swings between $\langle x_j \rangle = 0$ and $\langle x_j \rangle = 4g$.

The same steps can be repeated for phonon energy

$$E_{\text{ph}}(t) = 2g^2\omega_0(1 - \cos(\omega_0 t)),\tag{3.105}$$

which is the same result as in the weak coupling anti-adiabatic case. A necessary condition for oscillatory behavior seems to be that the system is in the anti-adiabatic regime.

Equation (3.99) can be seen as a zero-order expansion in $\eta = t_0$ (Eq. (3.48)). We can also find the zero-order expansion of the kinetic energy

$$\langle \tilde{\psi}(t) | \tilde{H}_{\text{kin}} | \tilde{\psi}(t) \rangle = \sum_k \epsilon_k \langle \tilde{\psi}(t) | \tilde{n}_k | \tilde{\psi}(t) \rangle.\tag{3.106}$$

We find

$$n_k(t) = \frac{1}{L} + e^{2g^2(\cos(\omega_0 t) - 1)}(\delta_{k,K} - \frac{1}{L}),\tag{3.107}$$

where $\tilde{n}_k = \frac{1}{L} \sum_{l,m} e^{ik(l-m)} e^{ig(p_l - p_m)} c_l^\dagger c_m$ was used. The kinetic energy is then

$$E_{\text{kin}}(t) = -2t_0 \cos(K) e^{2g^2(\cos(\omega_0 t) - 1)}.\tag{3.108}$$

This result shows that in the limit of small hopping amplitude the system oscillates without relaxation between the initial state with energy $E_{\text{kin}} = -2t_0 \cos(K)$ and an exponentially reduced value $E_{\text{kin}} = -\exp(-4g^2)2t_0 \cos(K)$ with period $2\pi/\omega_0$. Figure 3.9 compares this analytic function to TEBD data for $t_0/\omega_0 = 0.1, 0.001$ and $\gamma/\omega_0 = 1$.

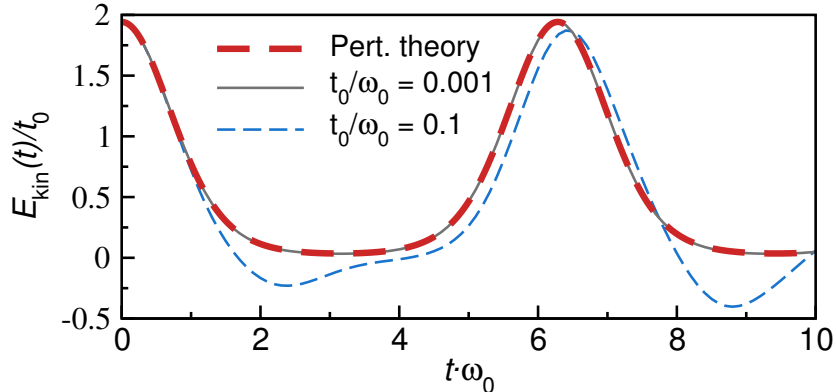


Figure 3.9: Time evolution of the kinetic energy $E_{\text{kin}}(t)$ in the strong-coupling anti-adiabatic regime for $\gamma/\omega_0 = 1$ and $L = 12$. The bold dashed line represents the result from perturbation theory Eq. (3.108), while the solid and thin dashed lines give results from TEBD for a system with parameters $t_0/\omega_0 = 10^{-3}$ and 10^{-1} which correspond to $\lambda = 500$ and 5 , respectively.

3.5 Numerical results

Perturbation theory works fine for a few limiting cases. However, it is not able to make predictions in the intermediate parameter regime. We use time-evolution in an LFS to study the dynamics in this regime. Also, we perform diagonalization in an LFS to get ground state expectation values and compare the steady-state expectations to them.

3.5.1 Crossover from adiabatic to anti-adiabatic regime

We have seen in Sec. 3.4.2 that second-order perturbation expansion in the weak-coupling anti-adiabatic regime yields oscillatory behavior of all parts of the Hamiltonian. Relaxation does not take place in this case. In the weak-coupling adiabatic case the relaxation is nicely described by the Boltzmann equation and almost all of the kinetic energy is transferred to the phonon subsystem. In this section we study how the relaxation dynamics evolve from the one case to the other by varying the ratio ω_0/t_0 . We choose a system in the weak-coupling regime where $\gamma < \omega_0, 4t_0$ which has the advantage that the reduction in kinetic energy is mostly compensated by an increase in the phonon energy in the adiabatic case (the coupling energy is negligible in this regime and total energy is conserved).

Figure 3.10 shows the time-evolution of phonon energy rescaled by the electronic bandwidth $E_{\text{ph}}/4t_0$ (Fig. 3.10(a)) and kinetic energy E_{kin}/t_0 (Fig. 3.10(b)) in a system with $\lambda = 0.2$. In the adiabatic regime for $\omega_0 = t_0$ we observe $E_{\text{ph}}/4t_0 \approx 1$ and a strong reduction of the kinetic energy for long times. Clearly, this regime is dominated by the relaxation of the kinetic energy. The fact that $E_{\text{kin}} + E_{\text{ph}} \approx E_{\text{kin}}(t = 0)$ holds shows that the Boltzmann picture is a good approximation: electron and phonons coexist but do not interact much. For the anti-adiabatic case $\omega_0 \gg t_0$ we observe $E_{\text{ph}}/4t_0 < 1$ for all times. Also, most of the system's excess energy remains in the electron. In this regime we find a completely different type of behavior which is characterized by coherent oscillations and a weak energy transfer between electrons and phonons. Figure 3.10 suggests a continuous crossover between the two regimes.

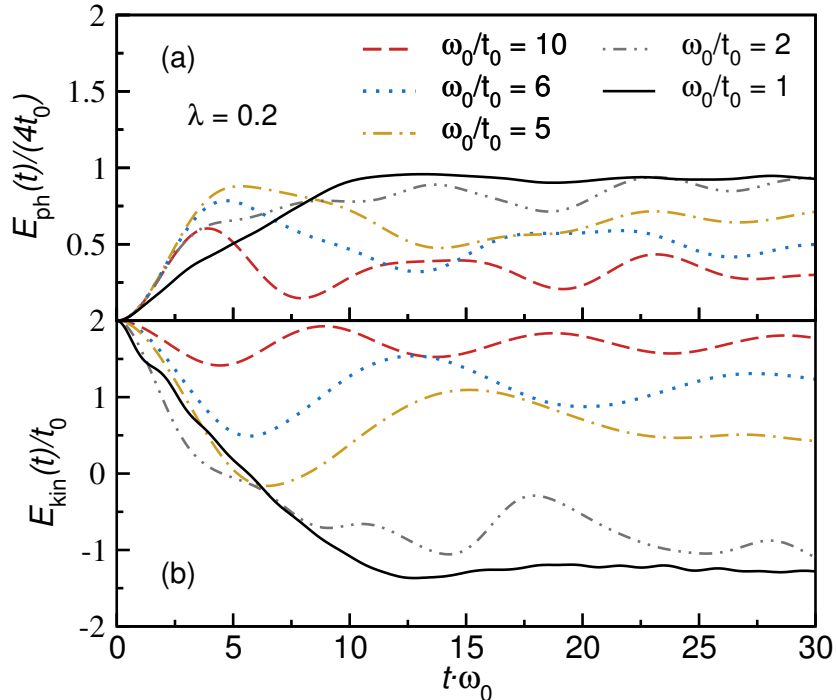


Figure 3.10: Time evolution of (a) the phonon energy $E_{\text{ph}}(t)$ and (b) the kinetic energy $E_{\text{kin}}(t)$ for fixed coupling strength $\lambda = 0.2$ and various values of the adiabaticity parameter $\alpha = 10, 6, 5, 2, 1$ spanning the spectrum from anti-adiabatic regime ($\alpha = 10$) to the adiabatic regime ($\alpha = 1$). Numerical data was computed using LFS in a system with size $L = 12$.

3.5.2 Crossover from weak to strong coupling in the adiabatic regime

In this section we study the change of the dynamics when the system parameters are tuned from the weak- to the strong-coupling adiabatic regime. To this end, we divide the dynamics into two time-domains: the relaxation regime and the steady-state regime. The relaxation regime is characterized by a net energy flow from the electron to the phononic subsystem while on the average no energy flow happens in the stationary regime.

Relaxation regime

We define the relaxation regime as the time in which excess energy is transferred from the electron to the phonon degrees of freedom, roughly given by Eq. (3.92). Perturbation theory allowed us to distinguish the limiting cases where a relaxation can be expected and where it can not be expected: The most important condition is that the phonon energy is much smaller than the electronic bandwidth. Because the kinetic energy and the momentum distribution function are intimately related in this model a decrease of kinetic energy also means a redistribution of electronic momenta in the momentum distribution function of the electron. The picture that the Boltzmann approach suggested was that the electron moves through the lattice, scatters at the lattice sites which creates a phonon and, thereby, the electron transfers momentum and energy to the phonon degrees of freedom (see Fig. 3.1). In Fig. 3.11 we plot the momentum distribution function as a function of time for (a) weak and (b) strong coupling. At time $t_0 t = 0$ the electron has momentum $k = \pi$ defined by the initial state Eq. 3.2. The

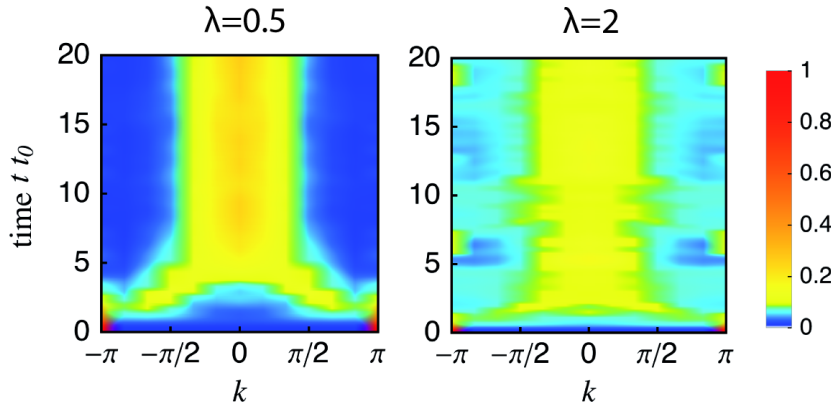


Figure 3.11: Time evolution of the momentum distribution function $n_k(t)$ in the (a) weak- and (b) strong-coupling case in a system with parameters $L = 12, \omega_0 = t_0$.

redistribution of momentum begins immediately afterwards and can be seen in Fig. 3.11(a) as an expansion of the bright region in the direction of $k = 0$. The system has reached its steady state when the maximum of $n_k(t)$ has reached $k = 0$ (at time $t_0 t \approx 5$). Note, that this is how we defined the characteristic relaxation time in Sec. 3.4.2. Also, the maximum in $n_k(t)$ approaches $k = 0$ roughly linearly which is in accordance with Eq. (3.90). The redistribution of momenta is initially faster for the strongly-coupled case and the maximum reaches the zero momentum state faster than in the weak-coupling case.

We also plot the expectation values of the three parts of the Hamiltonian as a function of time in Fig. 3.12: $E_{\text{ph}}(t)$, $E_{\text{coup}}(t)$ and $E_{\text{kin}}(t)$. In terms of the crossover at $\lambda^* \approx 1$ no exciting features emerge in the relaxation regime. The phonon energy grows more rapidly with increasing coupling and the coupling energy grows strongly. While for weak coupling the kinetic energy is transferred directly to the phonons in the strong-coupling regime the excess energy stored in the phonons is accounted for by the coupling term. The relaxation of the kinetic energy proceeds more rapidly with increasing λ consistent with our analytic result from the Boltzmann equation Eq. (3.92).

Oscillations in the stationary regime

In Figs. 3.11(b) and 3.12 we see a regime that we could not treat using perturbation theory: the strong-coupling adiabatic case $\omega_0 \lesssim 4t_0 \ll \gamma$. Here, the observables E_{ph} and E_{coup} exhibit oscillations after a short relaxation time while the kinetic energy is close to zero after relaxation. The same is true for the momentum distribution Fig. 3.11(b) where the maximum remains at $k = 0$ for most of the observed time but strong oscillations are visible. We defined the stationary regime as the regime where no net energy transfer from electrons to phonons happens anymore. To account for the oscillations we take the average over the oscillation period $2\pi/\omega_0$ as the steady state value of the respective observable.

The first question we want to address is whether the oscillations in the static regime persist when we increase the size of the system $L \rightarrow \infty$. To quantify the deviation of the amplitude from its average we use the variance of temporal fluctuations of an observable $A(t)$ about the

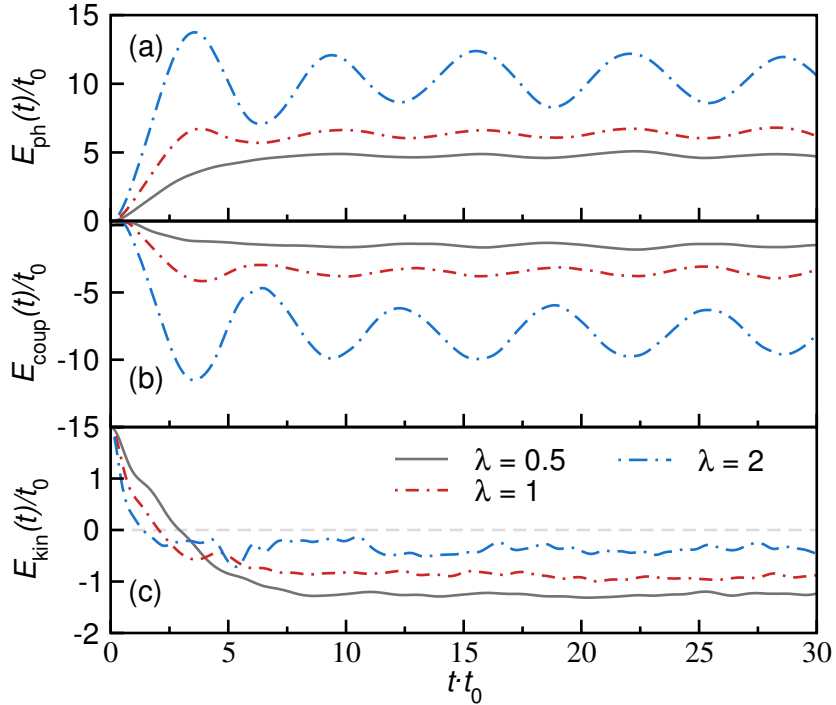


Figure 3.12: Time evolution of the expectation values of the three parts of the Hamiltonian: (a) $E_{\text{ph}}(t)$, (b) $E_{\text{coup}}(t)$ and (c) $E_{\text{kin}}(t)$ for three different choices of coupling strength $\lambda = 0.5, 1$ and 2 and $\omega_0 = t_0$. Data for $\lambda = 0.5$ and 1 were computed in a system of size $L = 12$ and $L = 8$ for $\lambda = 2$.

average in the stationary regime

$$\sigma_{\Delta A}^2 = \frac{1}{t_2 - t_1} \int_{t_1}^{t_2} (A(t) - \bar{A})^2 dt, \quad (3.109)$$

where t_1 and t_2 are chosen to be at the minimum and maximum of the oscillations and \bar{A} represents the time average. This is shown in Fig. 3.13: For $\lambda = 0.5$ (the weak-coupling case Fig. 3.13(a)) the oscillations decay to zero in the limit of large system sizes. This is the limit where the electron is smeared out over the lattice and this explains why the two points for the smallest system sizes show a different decay with $1/L$. For $\lambda = 2$ (the strong-coupling case Fig. 3.13(b)) the oscillations seem to persist to arbitrary lattice size. It is instructive to compare the phonon energy in Fig. 3.12 to the perturbative solution in the strong-coupling anti-adiabatic limit Eq. (3.105). This is illustrated in Fig. 3.14 for the cases of $\lambda = 2$ and $\lambda = 4.5$ which correspond to $\gamma = 2$ and $\gamma = 3$. Because the kinetic energy approaches zero for this case the remaining energy has to be in the phonon and coupling parts of the Hamiltonian $E_{\text{kin}}(t = 0) = E_{\text{ph}}(t) + E_{\text{coup}}(t)$ which is similar to a system where $t_0 = 0$. Clearly, the oscillation period is very close to $2\pi/\omega_0$ and with increasing coupling strength λ the oscillation amplitude grows and approaches the single-site dynamics Eq. (3.105). We will come back to the oscillations in Sec. 3.6 where we will analyze the so-called optimal modes which play the role a kind of generalized local observable.

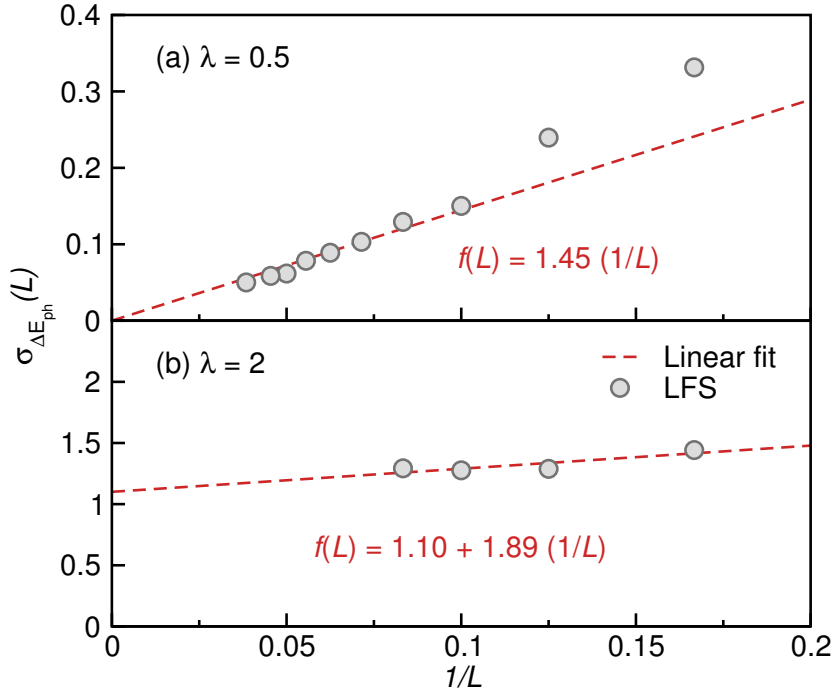


Figure 3.13: Standard deviation of the variation in the phonon energy in the steady-state regime $\sigma_{\Delta E_{\text{ph}}}(L)$ as a function of inverse system size $1/L$ for coupling strengths $\lambda = 0.5$ (weak-coupling adiabatic case, $L = 12$) and $\lambda = 2$ (strong-coupling adiabatic case, $L = 8$) where $\omega_0 = t_0$. In the weak-coupling case the standard deviation goes to zero as system size is increased. For the strong-coupling case we find that coherent oscillations persist for large system sizes.

The steady state

We analyze the steady-state expectation values of the three observables E_{ph} , E_{coup} and E_{kin} as a function of the coupling strength λ . For oscillating observables we define the averaged value over a sufficiently long time interval as the steady-state value. We compare those values to their respective ground state expectation and show that one can find an estimate for the steady-state value of the phonon number $N_{\text{ph}} = E_{\text{ph}}/\omega_0$. This is summarized in Figure 3.15. Figure 3.15(a) shows three quantities: the kinetic- and coupling-energy in the steady state versus their expectation values for the ground state in the quasi-momentum $k = \pi$ subspace for the same choice of model parameters in the two insets and the sum of those two quantities in the main panel. The steady-state coupling energy follows the ground state expectation value very closely over the whole observed parameter region. The kinetic energy expectation values deviate strongly in the regime of small coupling $\lambda \lesssim 1$. For larger coupling strengths the steady-state value approaches the ground state expectation value. For the combined quantity $E_{\text{coup}} + E_{\text{kin}}$ we find that ground state and steady-state values resemble each other very strongly. Fig. 3.15(b) contrasts the steady-state expectation value of the phonon energy with the ground state expectation value. For all observed values of the coupling strength there is a slightly varying offset between the ground state and steady-state values. The quantity $E_{\text{kin}}(t=0) - E_{\text{coup}}^0(\lambda) - E_{\text{kin}}^0(\lambda)$ closely reproduces the steady-state curve where $E_{\text{coup}}^0(\lambda)$ and $E_{\text{kin}}^0(\lambda)$ are the ground state expectation values of the coupling and kinetic energies at

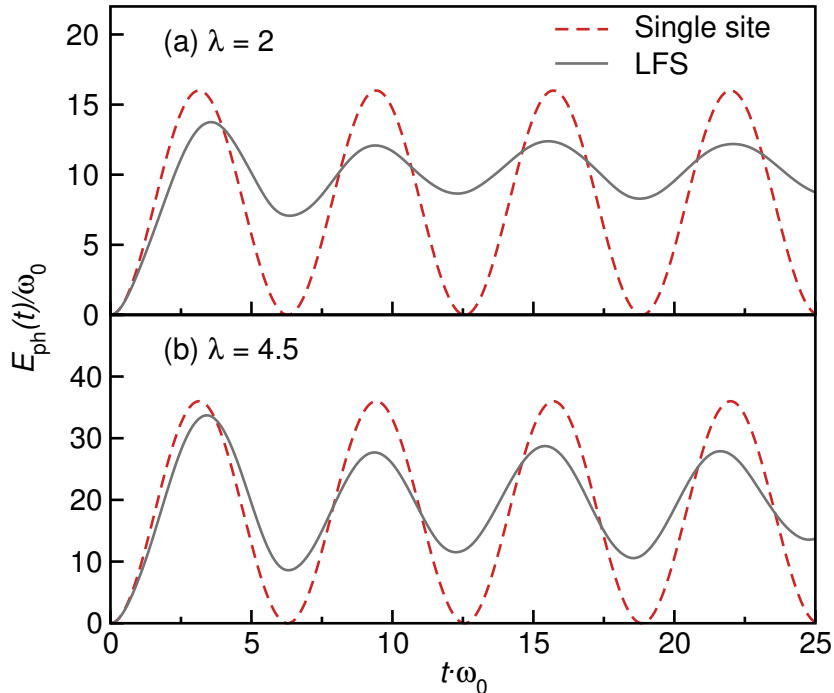


Figure 3.14: Time evolution of the phonon energy $E_{\text{ph}}(t)$ for two coupling strengths in the strong-coupling adiabatic regime: (a) $\lambda = 2$ and (b) $\lambda = 4.5$ compared to the expectation from time-dependent perturbation theory in the strong-coupling anti-adiabatic regime Eq. (3.105). With increasing coupling strength the numerical data approaches the perturbative approximation. The numerical simulation was done using the LFS method with $L = 8$ and $t_0 = \omega_0 = 1$.

coupling strength λ . This has to be the case because the total energy is conserved in the system $E = E_{\text{kin}} + E_{\text{coup}} + E_{\text{ph}} = E_{\text{kin}}(t = 0)$. While the kinetic and coupling energy relax to a steady-state value that is very close to their ground state expectation value all excess energy is stored in the form of excess phonons in the stationary state. We can use this fact to give an estimate of the number of phonons in the system in the steady state without performing the time-evolution

$$\bar{N}_{\text{ph}} = \frac{E - (E_{\text{kin}}^0 + E_{\text{coup}}^0)}{\omega_0}. \quad (3.110)$$

For the weak-coupling case we found that energy was transferred from electron to excess phonons directly. For the strong-coupling case a considerable amount of energy is stored in the coupling energy and for the correct number of excess phonons one needs to take into account kinetic and coupling energy.

3.5.3 Crossover from weak to strong coupling in the anti-adiabatic regime

In this section we study the remaining transition from weak to strong coupling in the anti-adiabatic regime at $\omega_0/t_0 = 10$. Figures 3.6, 3.10(a) and 3.16 show results for the kinetic (E_{kin}) and phonon energy (E_{ph}) as a function of time in the weak-coupling anti-adiabatic

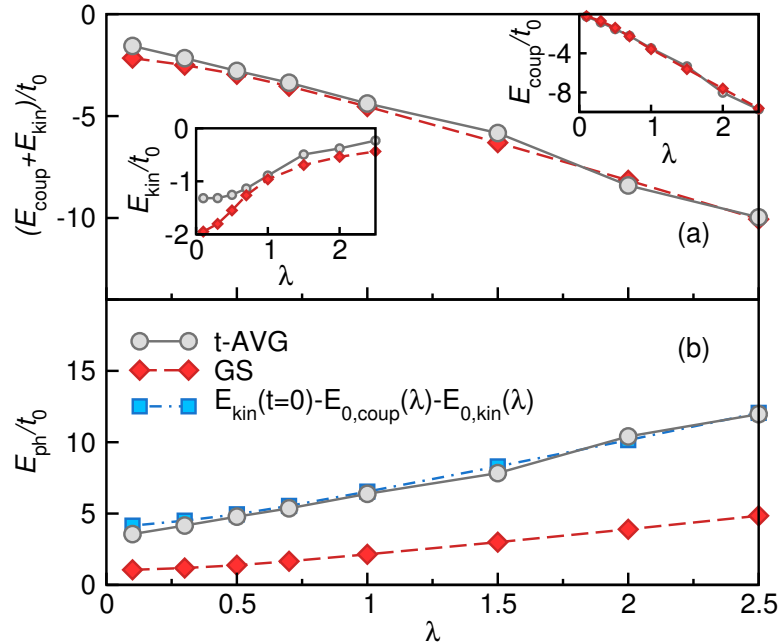


Figure 3.15: Time-averaged steady-state expectation values for the three competing parts of the Hamiltonian as a function of electron-phonon coupling strength λ calculated using the LFS method in a system of size $L = 12$ and $t_0 = \omega_0$. The data are compared to the polaron ground-state (GS) expectation values in the $K = \pi$ quasi-momentum subspace. The upper panel (a) shows the kinetic energy E_{kin} and coupling energy E_{coup} along with the sum of the two contributions $E_{\text{kin}} + E_{\text{coup}}$ compared to their respective ground-state expectation values. The lower panel (b) shows the phonon energy E_{ph} compared to its ground-state expectation and the quantity $E_{\text{kin}}(t=0) - E_{0,\text{coup}}(\lambda) - E_{0,\text{kin}}(\lambda)$ where $E_{0,\text{coup}}(\lambda)$ and $E_{0,\text{kin}}(\lambda)$ are the ground-state expectation values for coupling and kinetic energy at coupling strength λ .

regime. This regime is characterized by an inefficient energy transfer from electron to phonons and coherent oscillations. Figure 3.16 shows that the behavior is different in the strong-coupling regime: The kinetic energy shows oscillations between its initial value $E_{\text{kin}} = 2t_0$ and $E_{\text{kin}} \approx 0$. The initial state revives at integer multiples of the phonon period $2\pi/\omega_0$. This is consistent with the results from weak-coupling perturbation theory Eq. (3.108). In between these two regimes a third intermediate regime can be distinguished: The amplitude of oscillations decreases with increasing time and the reduction of E_{kin} is of the order of the hopping integral t_0 . Comparison of the dynamics in this regime for different applicable system sizes does not indicate that the oscillation amplitude vanishes completely as the system size is increased.

3.6 Optimal phonon modes and local entanglement entropy

This section illustrates the behavior of the eigenstates and eigenvalues of the reduced density matrix as a function of time. For ground state computations it has been shown that truncation in the basis of these eigenstates - called optimal modes - can significantly reduce the computational cost necessary for the simulation of the Holstein model [36, 41]. Here, we are

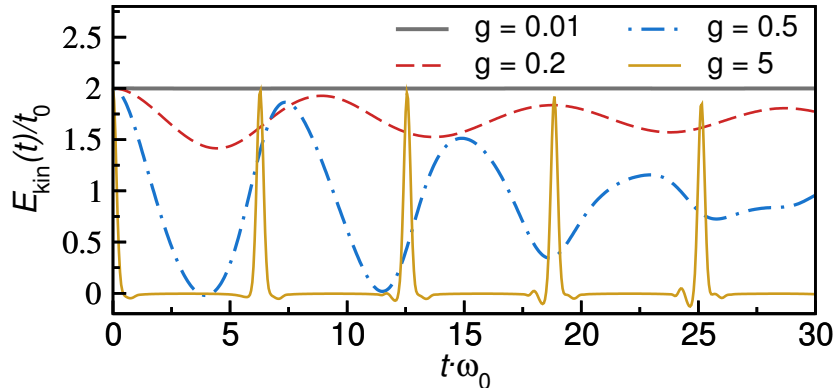


Figure 3.16: Time-evolution of the kinetic energy $E_{\text{kin}}(t)$ at $\omega_0/t_0 = 10$ (anti-adiabatic regime) for several values of the electron-phonon coupling $g = \gamma/\omega_0$. Numerical data was obtained using LFS in a system of size $L = 12$.

interested in the question, if one can also use those modes to reduce the computational cost during time-evolution. Three quantities are studied in this context: the local von Neumann entropy S_{vN} , the weight spectrum w_α and the optimal modes projected onto the phonon occupation number states $|\langle \alpha | n \rangle|^2$. The local von Neumann entropy is related to the decay behavior of the weight spectrum and thus is a good measure for the general behavior of the weight spectrum as function of time. The actual weight spectrum determines how efficient a truncation scheme can be and the optimal mode states can be viewed as a generalized local observable giving information about the state of a local subsystem

$$\langle \hat{O} \rangle(t) = \text{tr}(\rho^{(1)} \hat{O}). \quad (3.111)$$

3.6.1 Optimal phonon modes and von Neumann entropy

As discussed in the introduction [36, 41], the number of local basis states that are necessary to describe the phonon subsystem crucially depends on the basis in which they are set up. In the phonon occupation number basis, which we will denote *bare basis* from here on, we have seen that already in the ground state a large number of states can be necessary for the efficient description of the system (Sec. 3.2). We showed for the strong-coupling limit that the eigenstates of the local reduced density matrix have the form of a Poissonian distribution

$$|\beta\rangle = \sum_n \langle n | \beta \rangle |n\rangle, \quad (3.112)$$

where the probability to find the n -th bare state is given by

$$P(n; |\beta|^2) = |\langle n | \beta \rangle|^2 = \frac{|\beta|^{2n} e^{-|\beta|^2}}{n!}. \quad (3.113)$$

This means that the average number and variance of bare states is given by

$$n_j = \langle b_j^\dagger b_j \rangle = \text{Var}[P(n; |\beta|^2)] = |\beta|^2. \quad (3.114)$$

For our system we have $\beta = \gamma/\omega$ and thus $\langle n_j \rangle = (\gamma/\omega)^2$. We will thus need of the order $\mathcal{O}(g^2)$ bare states for the description of the ground state. Setting the state up in the optimal

mode basis, however, reduces the number of necessary basis states to two: the state with zero electrons and no phonons $|0\rangle_e \otimes |0\rangle_{\text{ph}}$ and the one-electron state with a coherent state in the phonon occupation number basis $|1\rangle_e \otimes |\beta = 0\rangle$.

The same holds for the time-evolved state given in Eq. (3.97) where $\beta(t) = ge^{-i\omega_0 t}$ and the average phonon number is thus given by $n_j(t) = 2g^2(1 - \cos(\omega_0 t))$.

To extract those modes from an arbitrary system-state one splits the basis into two parts - system and environment - like in DMRG (see, e.g. [25–27]) and sets up the reduced density matrix for the system part (S) by tracing the full density matrix over the environment part (E)

$$\rho_S = \text{tr}_E(|\psi\rangle\langle\psi|) = \sum_{\alpha} w_{\alpha} |\alpha\rangle\langle\alpha|, \quad (3.115)$$

where α labels the eigenstates of the reduced density matrix. An optimal basis is obtained by selection of the d_O highest weighted eigenstates. If the weights w_{α} decay fast with increasing index α the dimension of the optimized basis can be very small compared to the size of the bare basis - just like in DMRG. We call those states optimal modes if the system part (S) of the state is a single site only.

As discussed in Sec. 3.2 the local reduced density matrix is blockdiagonal in the number of electrons. Thus, the eigenstates of the reduced density matrix can be grouped into two sets of $N_{\text{max}} + 1$ states.

The local von Neumann entropy S_{vN} can be computed from the weights of these states in both blocks

$$S_{vN} = - \sum_{\alpha=0}^{2N_{\text{max}}+2} w_{\alpha} \ln(w_{\alpha}). \quad (3.116)$$

This quantity has the property that its value depends on how fast the weights w_{α} decay with index α . It takes its minimal value $S_{vN} = 0$ for $w_0 = 1, w_{\alpha} = 0 \forall \alpha \neq 0$ and its maximal value $S_{vN} = \ln(2N_{\text{max}} + 2)$ for $w_{\alpha} = 1/(2N_{\text{max}} + 2)$. In other words, the more entangled a site is with the rest of the system the larger the entanglement entropy.

The initial state Eq. (3.2) can be described by two local states: the zero-electron $|0\rangle_e \otimes |0\rangle_{\text{ph}}$ and the one-electron state $|1\rangle_e \otimes |0\rangle_{\text{ph}}$ with no phonons. With the same reasoning as in Sec. 3.2

$$S_{vN}(t=0) = \frac{1}{L} \ln(L) + \frac{L-1}{L} \ln\left(\frac{L}{L-1}\right). \quad (3.117)$$

3.6.2 Results

This section illustrates the optimal modes and their weights in the time-dependent state of the system. The first quantity we study is the von Neumann entropy for different values of the coupling strength λ . This is illustrated in Fig. 3.17 for the values $\lambda = 0.5, 2$ and 4.5 . Comparing to Fig. 3.12 we can divide the evolution into relaxation and steady-state regimes. In the relaxation regime the entropy grows in correlation with the decrease of kinetic energy. The larger the coupling strength the steeper the slope. Interestingly, the value of the von Neumann entropy in the steady-state regime is not strongly dependent on the coupling strength even though the time-evolution does not reach long enough times to decide if the entropy is close to a steady-state. Figure 3.12 shows strong coherent oscillations in the steady-state regime. The von Neumann entropy, however, shows no such feature at

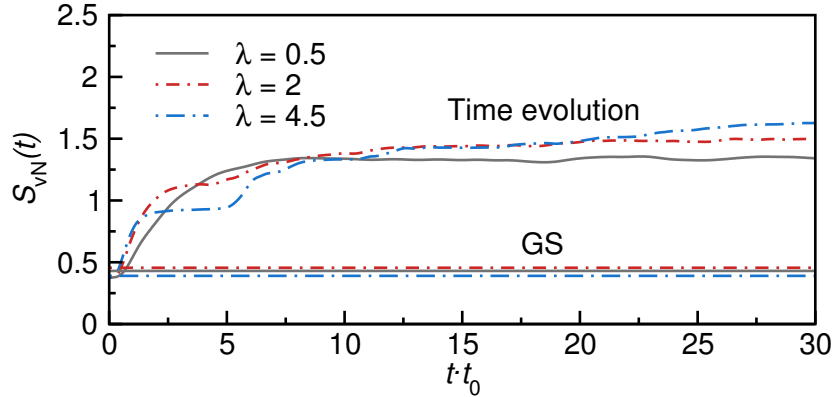


Figure 3.17: Time-evolution of the local von Neumann entropy $S_{\text{vN}}(t)$ for $\omega_0 = t_0 = 1$ and three different values of the coupling strength $\lambda = 0.5, 2$ and 4.5 . The time-dependent data compared to the ground state expectation (GS) of the local von Neumann entropy at the same coupling parameters. The values at $t = 0$ are captured by Eq. (3.20).

all. Since it measures the entanglement between the local site and the rest of the system this behavior supports the assumption that the oscillations stem from the single-site dynamics. The fact that the entropy is still increasing at $tt_0 \approx 30$ for very strong coupling $\lambda = 4.5$ can be heuristically explained by the very small effective hopping amplitude of the polaron. Even though the electron is very slow it is still mobile and will move through the lattice which means that the correlation with the environment can still grow even at longer times. Figure 3.17 also shows the local von Neumann entropy in the ground state for the three chosen coupling strengths. Compared to the steady-state value they are much lower, comparable to the entropy in the initial state.

Next we study the weights and optimal modes in the steady-state regime. More specifically, we are interested in those quantities on a site occupied by an electron. Global observables like the phonon and coupling energy display oscillations. We define two points in time: $t = t_{\text{min}}$ which is the time when the phonon energy is at a minimum and $t = t_{\text{max}}$ which is the time when the phonon energy exhibits a maximum. Since the eigenvalues of the one-electron block sum up to $1/L$ we rescale them by a factor L to be independent of system size

$$\tilde{w}_\alpha = Lw_{\alpha''}, |\alpha\rangle = |\alpha''\rangle_{N_e=1}. \quad (3.118)$$

Figure 3.18 shows the rescaled weights at the times $t = t_{\text{max}}$. We plot only data for $t = t_{\text{max}}$ because the weight spectrum does not vary significantly throughout the steady-state regime and therefore $w_\alpha(t_{\text{min}}) \approx w_\alpha(t_{\text{max}}) \forall \alpha$. This is also visible in the local von Neumann entropy $S_{\text{vN}}(t)$ (Fig. 3.17) which is derived from the weight spectrum and shows no oscillations in time. All of the shown curves decay roughly exponentially with the index α . However, the steady-state weights decay much slower than the weights in the ground state. For the efficient truncation in the optimal mode basis a faster decay of the weights means that one needs to retain a lower number of states to reach a given precision in the approximation. Comparing the spectra for ground state and steady-states we see that a lower number of states is required to get a designated precision [36, 41] in the ground state than in the steady-state. This is consistent with the behavior of the von Neumann entropy Fig. 3.17.

We now take a look at the optimal mode states $|\alpha\rangle$ in the stationary regime. The local

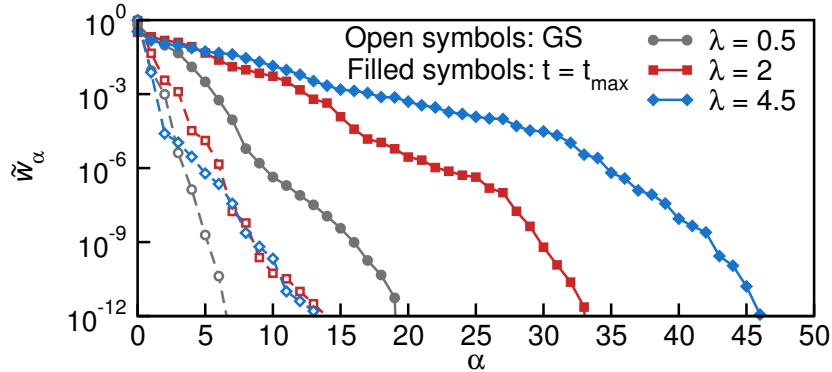


Figure 3.18: Rescaled weights \tilde{w}_α of the optimal modes in descending order for $t_0 = \omega_0 = 1$ and different values of the coupling strength λ both from ground state (open symbols) and steady-state (filled symbols) calculations. The point in time $t = t_{\max}$ is defined as the time where the phonon energy has a maximum (see Fig. 3.12). For $\lambda = 0.5$ we choose $t_{\max}t_0 = 15.8$ and for $\lambda = 2$ and 4.5 we choose $t_{\max}t_0 = 9.3$.

reduced density matrix encodes the dynamics of local observables

$$\langle O_{\text{loc}} \rangle(t) = \text{tr}(\rho_{\text{S}}(t)O_{\text{loc}}). \quad (3.119)$$

We have seen that the coupling- and phonon energies $E_{\text{coup}}, E_{\text{ph}}$ both exhibit coherent oscillations and both of them are local observables. That means that somehow those oscillations need to be reflected in the optimal mode states since the weights exhibit almost no time-dependence in the steady-state regime.

We first study the weak-coupling regime $\lambda = 0.5, \omega_0 = t_0 = 1$ in Figs. 3.19(a)-(d) where the highest weighted optimal mode is shown in Fig. 3.19(a) and the fourth-lowest weighted one is shown in Fig. 3.19(d). First, the difference between the modes at t_{\min} and t_{\max} is small which can be related to the small amplitude of oscillations which even vanishes in this regime as system size increases (see. Fig. 3.13). Second, the optimal mode states are slightly broadened versions of bare states. This is expected as in the weak-coupling regime only few phonons are emitted and in the weak-coupling limit optimal modes are equal to the bare modes. As the coupling term adds fluctuations in the phonon number it makes sense that the modes in the weak-coupling regime are broadened bare modes. As expected, the highest weighted mode is the one with its peak at $n = 0$ phonons. Quite counterintuitively, the next two highest weighted modes have their peaks at the $n = 2$ and $n = 1$ bare phonon modes. Perturbation theory up to second order of an initial state with no phonons and the coupling term as perturbation would suggest the $n = 1$ mode with a prefactor of γ/ω_0 and the $n = 2$ mode with a prefactor $\gamma^2/(\sqrt{2}\omega_0^2)$ which is far smaller than the first-order term.

The four highest weighted optimal mode states for the case of strong coupling $\lambda = 4.5$ are shown in Figs. 3.20(a)-(d). Contrary to the results in the weak coupling regime the difference in the modes at times $t = t_{\min}$ and $t = t_{\max}$ is so huge that they are not even resembling each other. The largest difference can be observed in the $\alpha = 0$ optimal mode Fig. 3.20(a). At $t = t_{\min}$ it is strongly peaked at the $n = 0$ bare mode while at $t = t_{\max}$ it resembles a Poissonian distribution $P(n; |\beta|^2)$ with a width set by the actual phonon number $|\beta|^2 = N_{\text{ph}}(t_{\max}) = E_{\text{ph}}(t_{\max})/\omega_0$. While this value of $|\beta|^2$ disagrees strongly with the estimate from perturbation theory $|\beta|^2 = 4g^2$ in the limit of $t_0 = 0$ (see Fig. 3.14) this result

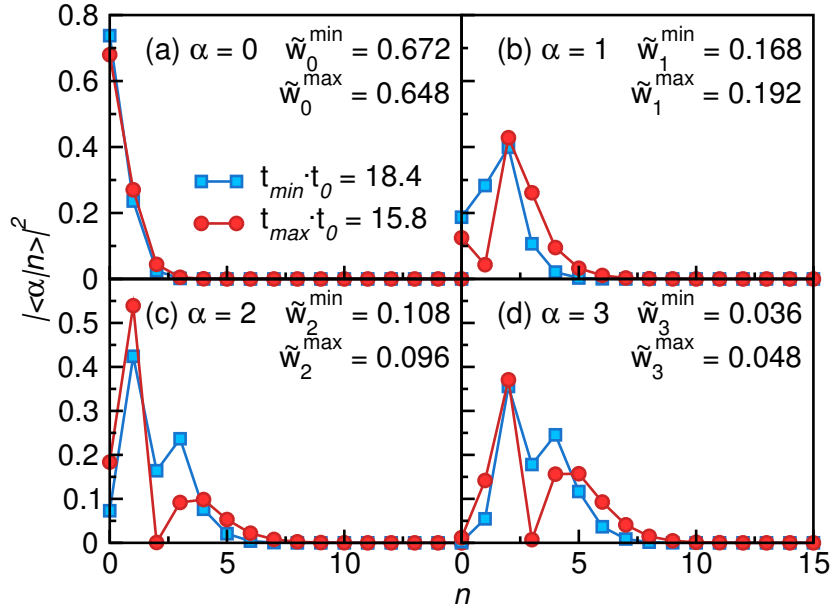


Figure 3.19: Four highest weighted optimal mode states expressed in terms of bare states $|\langle\alpha|n\rangle|^2$ at $\lambda = 0.5$ (weak-coupling regime), $t_0 = \omega_0$ and $L = 12$ (LFS). We consider two points in time: the point in time where the phonon energy (see Fig. 3.12) has a maximum $t = t_{\max}$ (circles) and the point in time where it has a minimum $t = t_{\min}$ (squares). \tilde{w}_{\max} and \tilde{w}_{\min} denote the optimal mode weights at the two given times.

agrees qualitatively with a coherent phonon state obtained in the $t_0 = 0$ limit Eq. (3.97). The second highest weighted optimal mode state shown in Fig. 3.20(b) at $t = t_{\max}$ resembles a Poisson distribution in the bare modes that has its peak at $|\beta|^2 = g^2$ which is the same as in the ground state for this coupling strength $\lambda = 4.5$ (indicated by the dashed line in Fig. 3.20(b)). This suggests that at $t = t_{\max}$ the state is characterized by a coexistence of distinct coherent states. The lower-weighted optimal modes shown in Figs. 3.20(c) and (d), however, do not have a simple structure.

3.7 Summary

In this chapter, we analyzed the relaxation dynamics in the Holstein model. We considered an initial state where a single electron is highly excited while the phonon energy is zero and monitor the dynamics of this state via the observables of the phonon energy, the coupling energy and the kinetic energy.

For a weak electron-phonon coupling and a phonon energy that is smaller than the electronic bandwidth, we observe that the electron dissipates energy in the relaxation regime and then enters a stationary regime with vanishing temporal fluctuations about the average value in the thermodynamic limit. The relaxation is characterized by a redistribution of the electron momentum from the top of the band $k = \pi$ to the bottom of the band $k = 0$. In this regime we compare the relaxation dynamics from the Boltzmann equation with numerical data and find good agreement. Assuming a constant density of states we find an analytical expression for the relaxation time from the Boltzmann ansatz $\tau\omega_0 = (16/\pi)(t_0^2/\gamma^2)$ which is

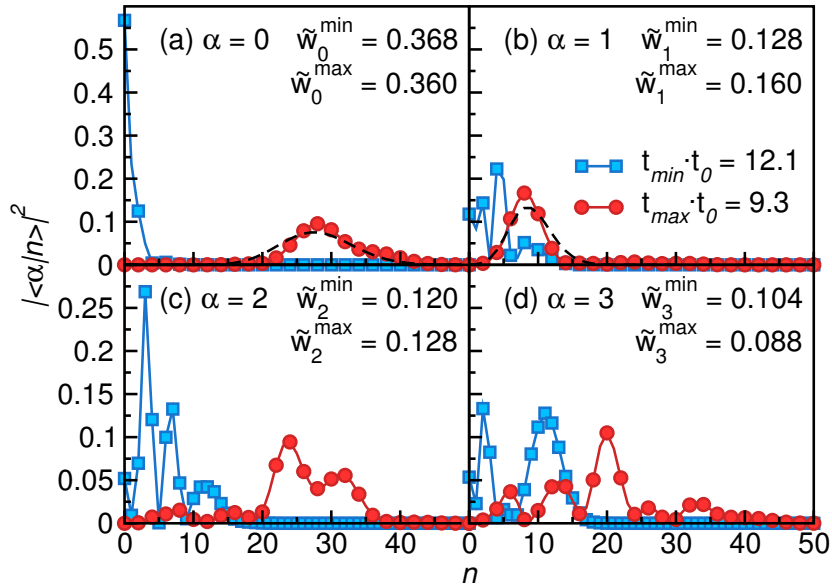


Figure 3.20: Four highest weighted optimal mode states expressed in terms of bare states $|\langle\alpha|n\rangle|^2$ at $\lambda = 4.5$ (strong-coupling regime), $t_0 = \omega_0$ and $L = 12$ (LFS). We consider two points in time: the point in time where the phonon energy (see Fig. 3.12) has a maximum $t = t_{\max}$ (circles) and the point in time where it has a minimum $t = t_{\min}$ (squares). \tilde{w}_{\max} and \tilde{w}_{\min} denote the optimal mode weights at the two given times.

curiously consistent with the numerical data from our 1D tight-binding system. For a system where the electron-phonon coupling is large or the phonon energy is larger than the electronic bandwidth the dynamics are governed by coherent oscillations and it gets harder to disentangle relaxation and stationary regime. We find that the dynamics in those cases are described by a single-site Holstein model ($t_0 = 0$) which reveals two important scales: the period of oscillations $2\pi/\omega_0$ and the amplitude of oscillations γ/ω_0 . For our initial state the single-site dynamics is particularly simple: the phonon state of an occupied site is a coherent state with the time-dependent eigenvalue $\beta = g(1 - e^{-i\omega_0 t})$. This allows to extract an upper bound for the number of phonons on this site during time-evolution: four times the value found in the ground state for the same model parameters.

We also study the behavior of the local reduced density matrix during time-evolution. We find that, after a fast relaxation, the weight spectrum stays roughly constant during time-evolution while, in the strong-coupling case, the optimal modes change in an oscillatory fashion as time progresses. Also, the optimal-mode structure contains information about the dynamics of the system: in the strong-coupling case the highest weighted optimal mode has the same structure as in the $t_0 = 0$ limit. This is consistent with the numerical observation that single-site coherent oscillations (calculated in the $t_0 = 0$ limit) persist to finite values of t_0 .

Finally, we benchmark the time-evolving block decimation method and diagonalization in a limited functional space (LFS) and find that, given that the initial increase in phonon number can be captured, the LFS method is very efficient in describing the dynamics for very long times on relatively large lattices and in different parameter regimes.

Chapter 4

The single-site reduced density matrix in the Bose-Bose resonance model

Numerical work has suggested that the local (single-site) entanglement entropy is sensitive to quantum phase transitions in interacting fermionic systems in one dimension such as the extended Hubbard model [45], Hubbard dimer [166], spin systems [46, 166] and the Bose-Hubbard model [167]. In those models the local entanglement entropy works as an indicator because it combines quantities such as the local density that are important to determining the physical properties of the system. However, it was also found that it is not sensitive to all phase transitions [46] and that the two-site entropy is a better indicator in some cases. The local von Neumann entropy $S_{\text{vN}}^{(1)}$ is a measure of entanglement between two parts of a system and is defined via the reduced density matrix

$$\rho^{(1)} = \text{tr}_{L-1}(\rho) = \sum_{\alpha} w_{\alpha} |\alpha\rangle, \quad (4.1)$$

$$S_{\text{vN}}^{(1)} = - \sum_{\alpha} w_{\alpha} \ln(w_{\alpha}), \quad (4.2)$$

where $|\alpha\rangle$ are the eigenstates of the reduced density matrix which we will call optimal modes from here on, w_{α} are their weights and tr_{L-1} denotes tracing over all but one site of the system. Because the number of spin-up and down particles is conserved in the Hubbard model and the local Hilbert space has only two or four degrees of freedom for spin-1/2 and Hubbard models, respectively, the local reduced density matrix has very few free parameters. For example, for a spin-1/2 system with spin-inversion symmetry the local reduced density matrix is independent of the actual state due to the block diagonal structure

$$\rho^{(1)} = \begin{pmatrix} \rho_{\uparrow\uparrow}^{(1)} & 0 \\ 0 & \rho_{\downarrow\downarrow}^{(1)} \end{pmatrix}, \quad (4.3)$$

where $\rho_{\uparrow\uparrow}^{(1)} = \rho_{\downarrow\downarrow}^{(1)} = 1/2$ denote the diagonal elements of the local reduced density matrix which also represent the probability of finding a particle with the respective spin on a site. The local von Neumann entropy is then fixed to

$$S_{\text{vN}}^{(1)} = \ln(2), \quad (4.4)$$

which is independent of the details of the actual state the system is in. For the Fermi-Hubbard model at half filling and vanishing magnetization there is only one free parameter [45].

We are interested in systems with a large local bosonic Hilbert space. Because of the large local Hilbert space, the reduced density matrix in those systems has a lot more degrees of freedom, especially when the bosonic particle number is not conserved, which means that the eigenstates of the local reduced density matrix need not be eigenstates of the local bosonic particle number operator. In this project we study how the local reduced density matrix behaves at a phase transition by monitoring the weights and the optimal modes as a function of system parameters. For systems with phononic degrees of freedom, such as the Holstein model [6], the local Hilbert space can be very large (see Sec. 3). As discussed in Chap. 1, Zhang et al. [36] introduced the term optimal modes for the eigenstates of the local reduced density matrix, which they use to truncate a given state in the local degrees of freedom to gain a computational advantage depending on how fast the weight spectrum decays. Thus, the study of the local reduced density matrix also gives information about the efficiency of local Hilbert space optimization techniques.

In this work, we consider the so-called Bose-Bose resonance model which describes two species of particles – atoms and molecules (labeled $s = a, m$) – in a one-dimensional lattice. This model has a global $U(1)$ symmetry while the individual particle numbers are not conserved ($[H, N_a] \neq 0, [H, N_m] \neq 0$ but $[H, N_a + 2N_m] = 0$). Thus, this system's local reduced density matrix possesses non-trivial optimal modes which are mixtures of bare atomic and molecular occupation number states with the same total local number of particles $N_T^{(1)} = N_a^{(1)} + 2N_m^{(1)}$. The Hamiltonian reads

$$H = H_{\text{BH},a} + H_{\text{BH},m} + H_{\text{int}} + H_{\text{F}} + H_{\text{D}}, \quad (4.5)$$

where

$$H_{\text{BH},s} = -t_s \sum_j (s_j^\dagger s_{j+1} + \text{h.c.}) + \frac{U_s}{2} \sum_j n_{j,s} (n_{j,s} - 1), \quad (4.6)$$

$$H_{\text{int}} = U_{\text{am}} \sum_j n_{j,a} n_{j,m}, \quad (4.7)$$

$$H_{\text{F}} = g \sum_j (m_j^\dagger a_j a_j + m_j a_j^\dagger a_j^\dagger), \quad (4.8)$$

$$H_{\text{D}} = \epsilon_m \sum_j n_{j,m}. \quad (4.9)$$

Each species is described by a Bose-Hubbard term $H_{\text{BH},s}$ which allows the particles to hop and also includes a local repulsion with particles of the same species. Furthermore, H_{int} denotes the inter-species repulsion term. The so-called Feshbach term H_{F} allows the transformation of two atoms into one molecule and vice versa and the detuning term H_{D} regulates which of the two species is energetically favorable. For this project we set $t_m = t_a/2, U_a/2 = U_m/2 = U_{\text{am}} = g = U$ for which the ground state phase diagram is known from Ref. [43]. Also, we consider a fixed filling $N_T/L = 2$ where L denotes the number of lattice sites and we measure energy in units of the hopping parameter $t_a = 1$. Figure 4.1 shows the ground state phase diagram for this model schematically. For our choice of parameters the model features three phases: the Mott insulating phase (MI), the molecular quasicondensate phase (MC) and a phase where both species form a quasicondensate (AC+MC) [43].

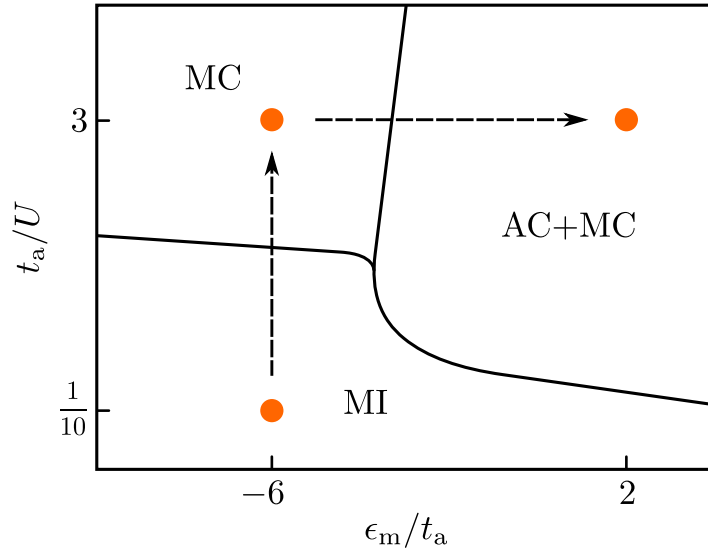


Figure 4.1: Sketch of the phase diagram for the Bose-Bose resonance model [43]. The labels denote the three phases: Mott insulating phase (MI), molecular quasi-condensate phase (MC) and atomic and molecular quasicondensate phase (AC+MC). Each one of the three points is deep in its respective phase. The horizontal and vertical dashed lines between those points mark trajectories through the phase diagram along which we compute entanglement properties and optimal modes, both in equilibrium and in quantum quenches.

We start with the study of the ground-state properties of our system where we tune the parameters along the two trajectories shown in Fig. 4.1. The horizontal trajectory starts deep in the MC phase and ends deep in the AC+MC phase, so that we cross a phase boundary in between. Note that only the detuning ϵ_m/t_a varies along the whole line. The vertical trajectory connects the MI phase with the MC phase by variation of the inverse interaction strength t_a/U . For both trajectories we measure the molecular density and the local von Neumann entropy as a function of the system parameter that drives the transition. We find that, for the horizontal trajectory, the first derivative with respect to the detuning of the local von Neumann entropy displays a peak at the location of the phase boundary that gets sharper with increasing system size. For the vertical trajectory we find that the local von Neumann entropy is an increasing function of the system size in the MI phase and a decreasing function of the system size in the MC phase. The reason for this behavior in the MI phase is explained by the finite correlation length: in the MI phase the correlation length decays exponentially and thereby the entanglement in this phase will grow with system size until it saturates when the system is large enough to support the full correlation length. In the MC phase we use the exact formula for a free condensate to show that in this case the local von Neumann entropy goes with $1/L$ to a finite value. This system-size behavior leads to features in the vicinity of the phase boundary as our numerical data suggest: the local von Neumann entropy is sensitive to both phase transitions. Next, we study the weights and optimal modes at points deep in the three phases (circles in Fig. 4.1) and explain their structure by comparison to a Bose-Hubbard model and first-order perturbation theory. We find that the structure of the optimal modes can be used to distinguish the three phases. The structure of the optimal modes is then illustrated as a continuous function of the detuning along the horizontal trajectory and

of the interaction strength along the lower trajectory. Since the optimal modes are different in all three phases, they need to change along the respective trajectory and we find that those changes happen in the vicinity of the phase transition.

We also perform quantum quenches along the two trajectories: We start in the MI (MC) phase and quench the system parameters to a point deep in the MC (AC+MC) phase. This procedure can be seen as a different limit compared to the ground-state scheme: Here, the system parameters can be considered as being changed adiabatically so the system stays in the ground state. The quantum quench is the other limit where the system parameters are changed immediately which leads to a non-equilibrium situation. This is also relevant to ultra-cold quantum gas physics where such quenches play an important role [168–170]. For recent studies of non-equilibrium properties in fermionic and bosonic systems coupled to bound states via Feshbach interactions we refer to Refs. [171–176].

In our system we discuss the time-evolution of the $k = 0$ component of the atomic and molecular momentum distribution function, the molecular density and the local von Neumann entropy. Also, we study the behavior of the optimal mode structure for the four most important optimal modes as a function of time. Because the local dimension is large in this system it makes sense to ask for thermalization also on a single site. By comparison to expectation values in the canonical ensemble we find that the single-site reduced density matrix is thermal in the steady state.

4.1 The Bose-Bose resonance model

As noted above, the BBRM has a rich phase diagram (cf. Fig. 4.1). The phase boundaries correspond to the vanishing of one or both of the one-particle and two-particle excitation gaps [43, 177]

$$E_{1,g} = E_0(L, N_T + 1) + E_0(L, N_T - 1) - 2E_0(L, N_T), \quad (4.10)$$

$$E_{2,g} = E_0(L, N_T + 2) + E_0(L, N_T - 2) - 2E_0(L, N_T), \quad (4.11)$$

where $E_0(L, N)$ denotes the ground state energy for a system of size L hosting N particles. The MI phase is characterized by a non-vanishing one- and two-particle excitation gap $E_{1,g}^{\text{MI}} \neq 0, E_{2,g}^{\text{MI}} \neq 0$ while at the phase boundary to the MC phase the two-particle excitation gap closes $E_{1,g}^{\text{MC}} \neq 0, E_{2,g}^{\text{MC}} = 0$ and molecules condense. When traversing the phase boundary between the MC and AC+MC phases also the one-particle excitation gap closes $E_{1,g}^{\text{AC+MC}} = 0, E_{2,g}^{\text{AC+MC}} = 0$ which means that both species – atoms and molecules – condense in this phase.

The Bose-Hubbard model, as one of the simplest bosonic models, features only a single particle species. Due to particle conservation the number of particles in the environment uniquely fixes the local state and thus, the local reduced density matrix is diagonal at all times. The BBRM features two species described by a Bose-Hubbard model and has non-trivial optimal modes due to the fact that the Feshbach term mixes particle species. Thus, only the total particle number is conserved and the optimal modes can mix local states with the same total particle number. With this background, the BBRM is a perfect model to study the influence of the presence of a phase transition on the structure of the optimal modes.

In this section we derive the Hamiltonian Eq. (4.5) in matrix-product operator form and discuss the general form of the optimal modes that are possible in this model.

$N_T^{(1)}$	$n: N_a^{(1)}, N_m^{(1)}\rangle$									
0	0:	$ 0; 0\rangle$								
1	1:	$ 1; 0\rangle$								
2	2:	$ 2; 0\rangle$	3:	$ 0; 1\rangle$						
3	4:	$ 3; 0\rangle$	5:	$ 1; 1\rangle$						
4	6:	$ 4; 0\rangle$	7:	$ 2; 1\rangle$	8:	$ 0; 2\rangle$				
5	9:	$ 5; 0\rangle$	10:	$ 3; 1\rangle$	11:	$ 1; 2\rangle$				
6	12:	$ 6; 0\rangle$	13:	$ 4; 1\rangle$	14:	$ 2; 2\rangle$	15:	$ 0; 3\rangle$		
7	16:	$ 7; 0\rangle$	17:	$ 5; 1\rangle$	18:	$ 3; 2\rangle$	19:	$ 1; 3\rangle$		
8	20:	$ 8; 0\rangle$	21:	$ 6; 1\rangle$	22:	$ 4; 2\rangle$	23:	$ 2; 3\rangle$	24:	$ 0; 4\rangle$
\vdots										

Table 4.1: Bare local basis sets for a fixed number of total particles $N_T^{(1)}$ on a site. The number n left of the respective state is its position in the full local basis. As $N_T^{(1)}$ increases, a growing number of states can mix due to the Feshbach term.

4.1.1 Numerical setup

To simulate this system numerically it is necessary to label the local states

$$|n\rangle = |N_a^{(1)}; N_m^{(1)}\rangle, \quad (4.12)$$

where we order first by the total local particle number $N_T^{(1)} = N_a^{(1)} + 2N_m^{(1)}$ and then by the number of local molecules $N_m^{(1)}$ in ascending order. This local basis is shown in Tab. 4.1. The $N_T^{(1)}$ -subspace includes $d_{N_T^{(1)}} = \lfloor (N_T^{(1)} + 2)/2 \rfloor$ states.

We can now set up the MPO in block form. By inspection of the Hamiltonian we see that we have MPO bond quantum numbers of $\Delta N = 0$ for the diagonal operators

$$x_j = \frac{U_a}{2} n_{j,a} (n_{j,a} - 1) + \frac{U_m}{2} n_{j,m} (n_{j,m} - 1) + U_{am} n_{j,a} n_{j,m} + g(m_j^\dagger a_j a_j + m_j a_j^\dagger a_j^\dagger) + \epsilon_m n_{j,m}, \quad (4.13)$$

$\Delta N = -1, 1$ for the atomic hopping terms and $\Delta N = -2, 2$ for the molecular hopping terms. For the actual representation we choose the following abstract basis states: (i) no term to the right, (ii) full term to the right, (iii) a_j to the right, (iv) a_j^\dagger to the right, (v) m_j to the right, (vi) m_j^\dagger to the right. This translates to the structure depicted in Fig. 4.2. Please note the very low maximal block-bond dimension of $w = 2$.

4.1.2 Optimal modes

Since the global particle number N_T is conserved by the Hamiltonian Eq. (4.5) the reduced density matrix is block-diagonal in the local total particle number $N_T^{(1)}$ (for a proof, see Eq. (3.16)). From the previous section we see that an $N_T^{(1)}$ -block has dimension $d_{N_T^{(1)}} = \lfloor (N_T^{(1)} + 2)/2 \rfloor$ and this is thus the maximal number of states that an optimal mode can mix.

$$W_j = \begin{array}{c} \begin{array}{cccccc} & 0 & -1 & 1 & -2 & 2 & \Delta N \\ \left(\begin{array}{c|c|c|c|c|c} \mathbb{1} & 0 & 0 & 0 & 0 & 0 \\ x_j & \mathbb{1} & -t_a a_j^\dagger & -t_a a_j & -t_m m_j^\dagger & -t_m m_j \\ \hline a_j & 0 & 0 & 0 & 0 & 0 \\ a_j^\dagger & 0 & 0 & 0 & 0 & 0 \\ \hline m_j & 0 & 0 & 0 & 0 & 0 \\ m_j^\dagger & 0 & 0 & 0 & 0 & 0 \end{array} \right) & \begin{array}{c} 0 \\ -1 \\ 1 \\ -2 \\ 2 \end{array} \end{array} \end{array}$$

Figure 4.2: MPO representation of the BBRM Hamiltonian (Eq. (4.5)). The bond labels ΔN divide the full object into blocks of maximal bond dimension $w = 2$.

4.2 Ground-state properties

In this section we analyze the molecular density, the local von Neumann entropy and the structure of the optimal modes in the three phases of the model - the Mott insulating phase (MI), the molecular condensate phase (MC) and the phase where both species form a condensate (AC+MC).

4.2.1 Molecular density and single-site von Neumann entropy

We study the molecular density and local von Neumann entropy as a continuous function of the system parameters ϵ_m/t_a and t_a/U which drive the phase transitions. For this purpose we choose two trajectories in the phase diagram where each crosses a single phase boundary. The two trajectories are depicted in Fig. 4.1 by the horizontal and vertical arrows.

Contour connecting MC and AC+MC phase

We start with the contour connecting the MC to the AC+MC phase by variation of the detuning ϵ_m and fixed interaction strength $t_a/U = 3$ (the horizontal arrow in Fig. 4.1). The results for this case are shown in Fig. 4.3. Figure 4.3(a) shows the density of molecules as a function of the detuning ϵ_m/t_a . At the left edge $\epsilon_m = -6t_a$ almost all atoms in the system are bound in molecules. This is the effect of a negative detuning which makes the molecular state energetically preferable

$$\lim_{\epsilon_m \rightarrow -\infty} N_m(\epsilon_m) = \frac{N_T}{2}. \quad (4.14)$$

The opposite holds in the limit of large detuning

$$\lim_{\epsilon_m \rightarrow \infty} N_m(\epsilon_m) = 0, \quad (4.15)$$

which is also reflected by the data. The local von Neumann entropy is plotted in Fig. 4.3(b) as a function of the detuning parameter ϵ_m/t_a . For large positive and negative values of ϵ_m/t_a , $S_{vN}^{(1)}$ saturates at finite values with a maximum slightly to the right of the phase boundary

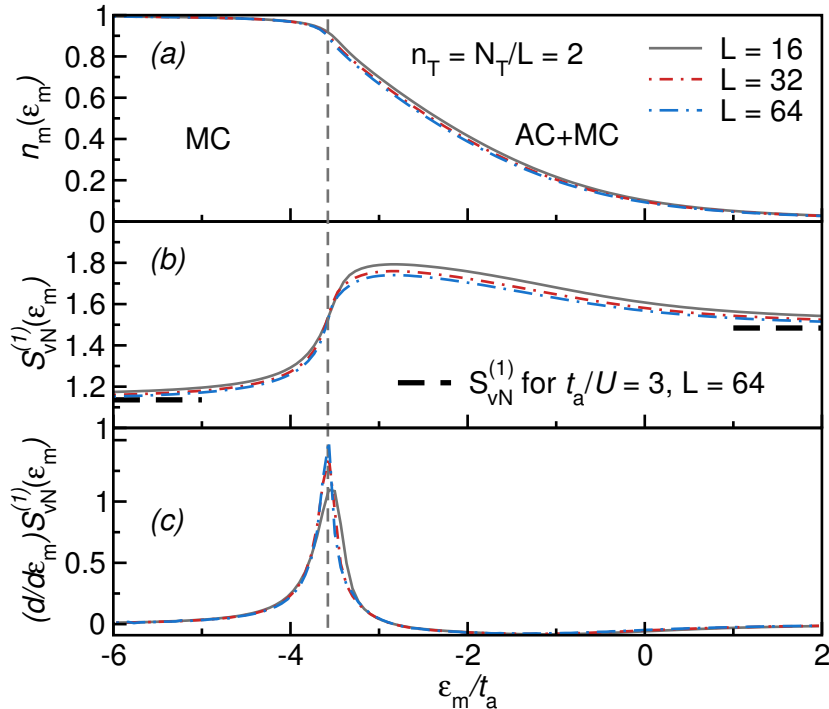


Figure 4.3: Density of molecules (a), single-site von Neumann entropy (b) and first derivative with respect to the detuning ϵ_m for the groundstate along the horizontal trajectory between the MC ($\epsilon_m = -6t_a, t_a/U = 3$) and AC+MC ($\epsilon_m = 2t_a, t_a/U = 3$) phases. The vertical dashed line indicates the position of the phase transition [43]. The horizontal dashed lines in (b) show the values calculated for a Bose-Hubbard model at unit filling and $U/t = 20$ in the MC limit and at double filling and $U/t = 10$ in the AC+MC limit. The data is calculated using DMRG with a local cutoff $N_T^{(1)} = 30$ and a bond dimension $m = 200$.

(indicated by the dashed vertical line in Fig. 4.3). We estimate the value of $S_{vN}^{(1)}$ at the left and right edges of the plot by a Bose-Hubbard model describing $N_m = N_T/2$ molecules at the left and $N_a = N_T$ atoms at the right border

$$H = -t_s \sum_j (s_j^\dagger s_{j+1} + \text{h.c.}) + U \sum_j s_j^\dagger s_j, \quad (4.16)$$

where, as before, $s = a, m$ labels the actual species used. The value of the interaction strength $U/t_a = 1/3$ is small and we first give an estimate for the local von Neumann entropy for vanishing interaction strength. For this case, the von Neumann entropy for a bipartition of the system into parts A and B with lengths $L_A = 1, L_B = L - 1$ and N particles can be calculated exactly [178]

$$S_{vN}^{(1)} = - \sum_{\alpha=0}^N w_\alpha \ln(w_\alpha), \quad (4.17)$$

where

$$w_\alpha = L^{-N} \binom{N}{\alpha} (L-1)^{(N-\alpha)}. \quad (4.18)$$

For our system we find

$$\lim_{\epsilon_m \rightarrow -\infty} S_{\text{vN}}(\epsilon_m) \approx 1.27, \quad (4.19)$$

$$\lim_{\epsilon_m \rightarrow \infty} S_{\text{vN}}(\epsilon_m) \approx 1.66, \quad (4.20)$$

which is slightly higher than what we find numerically. The reason for that is the non-zero repulsive interaction $U/t_a > 0$ which leads to a depletion of the condensate. Therefore, we compare the BBRM data to the von Neumann entropy of a Bose-Hubbard model with parameters $N = 128, t = 1, U/2 = t/3$ at the side of the AC+MC phase and $N = 64, t = 0.5, U/2 = t/3$ at the side of the MC phase which give a lower limit to the data for the BBRM system (dashed lines in Fig. 4.3(b)). The difference in the local von Neumann entropy in the two limits of $\epsilon_m \ll -t_a$ and $\epsilon_m \gg t_a$ arises from the difference in particle numbers in these two limits.

Figure 4.3(c) shows the first derivative of the local von Neumann entropy with respect to the detuning ϵ_m/t_a . It shows a pronounced maximum in the vicinity of the phase boundary from the MC to the AC+MC phase ϵ_m^c/t_a (vertical dashed line in Fig. 4.3). As the system size is increased the maximum gets sharper and approaches a delta function with a finite maximum value at the transition (from finite-size scaling). This behavior suggests that $S_{\text{vN}}^{(1)}$ is sensitive to this transition. The behavior of the local von Neumann entropy can be qualitatively understood in the limit of vanishing interactions $U/t_a \rightarrow 0$. In this limit the system is described by the Hamiltonian

$$\begin{aligned} H &= -t_a \sum_j (a_j^\dagger a_{j+1} + \text{h.c.}) \\ &= -t_m \sum_j (m_j^\dagger m_{j+1} + \text{h.c.}) \\ &= \epsilon_m \sum_j n_j^m. \end{aligned} \quad (4.21)$$

The ground state is either a condensate of molecules or atoms only depending on the exact value of ϵ_m because the two species cannot mix. The ground state energy is thus given by either $E_0^a = -2t_a N_T$ on the AC + MC side or $E_0^m = -2t_m N_T/2 + \epsilon_m N_T/2$ on the MC side. The transition happens abruptly when both energies are equal and we get a critical detuning of $\tilde{\epsilon}_m = -3t_a$. As discussed above, the von Neumann entropy is different for the two cases due to a different particle number and it will thus display a sudden jump at $\tilde{\epsilon}_m/t_a$. For the first derivative in ϵ_m/t_a this means a singularity at that point. The effect of a finite interaction is to smoothen this jump and, thus, leads to a finite value of the maximum in the derivative. Also, we observe a shift of the maximum to a value smaller than $\tilde{\epsilon}_m = -3t_a > \epsilon_m^c$.

Contour connecting MI and MC phase

The next transition is the one following the vertical arrow in Fig. 4.1 which connects the MI and MC phases. Figure 4.4 shows the molecular density and the local von Neumann entropy as a function of the inverse interaction t_a/U . Both are monotonically increasing functions of the inverse interaction.

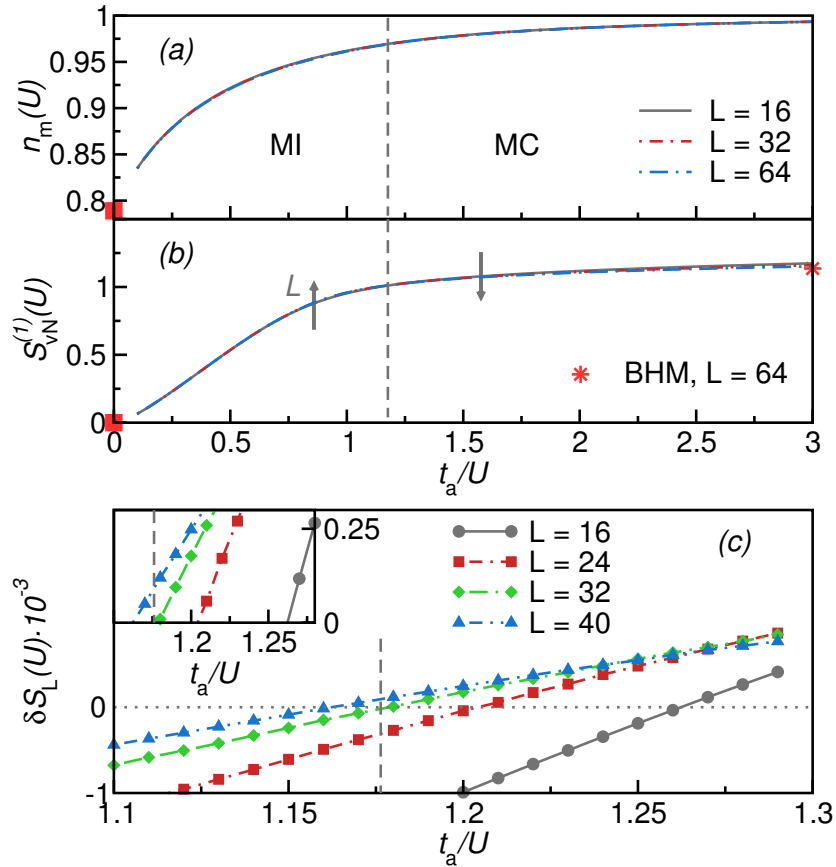


Figure 4.4: Density of molecules (a) and single-site von Neumann entropy (b) for the groundstate along the vertical trajectory between the MI ($\epsilon_m = -6t_a, t_a/U = 0.1$) and MC ($\epsilon_m = -6t_a, t_a/U = 3$) phases. The vertical dashed line indicates the position of the phase transition [43]. The squares show the value calculated for a fully local Hamiltonian in the MI limit and the stars for a Bose-Hubbard model at unit filling and appropriately chosen parameters in the MC limit. The arrows in (b) indicate the change in the local von Neumann entropy as system size is increased. (c) Difference of local von Neumann entropy between systems of size L and $2L$ (Eq. (4.41)). The data is calculated using DMRG with a local cutoff $N_T^{(1)} = 30$ and a bond dimension $m = 400$.

In the limit of infinite interaction strength $t_a/U = 0$ the Hamiltonian Eq. 4.5 reduces to

$$\begin{aligned}
 H = U \sum_j [n_{j,a}(n_{j,a} - 1) + n_{j,m}(n_{j,m} - 1) \\
 + n_{j,a}n_{j,m} + m_j^\dagger a_j a_j + m_j a_j^\dagger a_j^\dagger].
 \end{aligned}
 \tag{4.22}$$

At exactly $t_a/U = 0$ the molecular density takes a finite value while the local von Neumann entropy vanishes. We can diagonalize the Hamiltonian (Eq. (4.22)) analytically. Because it is fully local and blockdiagonal in the local occupation number $N_T^{(1)}$, the ground state in the $N_T^{(1)} = 2$ subspace and $g = 0$ is a product state where each site is occupied by a single

molecule

$$|\psi_0^{\text{MI},g=0}\rangle = \prod_j |\phi_0^{\text{MI},g=0}\rangle, \quad (4.23)$$

$$|\phi_0^{\text{MI},g=0}\rangle = |0; 1\rangle, \quad (4.24)$$

where $|\phi_0^{\text{MI},g=0}\rangle$ denotes the local ground state for vanishing Feshbach interaction and $|0; 1\rangle$ is the local state occupied by one molecule (see Tab. 4.1). A nonzero Feshbach interaction g can only couple states in the $N_{\text{T}}^{(1)} = 2$ subspace and the local state will thus be a superposition of the one-molecule state and the two-atom state

$$|\phi_0^{\text{MI},g\neq 0}\rangle = c_1|2; 0\rangle + c_2|0; 1\rangle, \quad (4.25)$$

where c_1 and c_2 are determined by diagonalization of the Hamiltonian matrix

$$H_j^{N_{\text{T}}^{(1)}=2} = \begin{pmatrix} 2 & \sqrt{2} \\ \sqrt{2} & 0 \end{pmatrix}, \quad (4.26)$$

where the first basis state is the two-atom state $|0\rangle = |2; 0\rangle$ and the second basis state is the one-molecule state $|1\rangle = |0; 1\rangle$. Diagonalization yields

$$|\phi_0^{\text{MI},g\neq 0}\rangle = \frac{1}{\sqrt{3 - \sqrt{3}}} \left(\frac{1 - \sqrt{3}}{\sqrt{2}} |2; 0\rangle + |0; 1\rangle \right). \quad (4.27)$$

We can calculate the molecular density

$$\begin{aligned} n_{\text{m}} &= \langle \phi_0^{\text{MI},g\neq 0} | \hat{n}_{\text{m}} | \phi_0^{\text{MI},g\neq 0} \rangle \\ &= \frac{1}{\sqrt{3 - \sqrt{3}}}, \end{aligned} \quad (4.28)$$

which is in perfect agreement with Fig. 4.4(a) to interpolate to $t_{\text{a}}/U = 0$. The local von Neumann entropy approaches zero in this limit because the ground state is a product state and thus is not entangled with the rest of the system.

In the opposite limit of $t_{\text{a}}/U \rightarrow \infty$ the molecular density approaches one molecule per site. As discussed previously this is the limit of a molecular or atomic condensate only depending on the value of the detuning $\epsilon_{\text{m}}/t_{\text{a}}$. For a detuning of $\epsilon_{\text{m}} = -6t_{\text{a}} < \tilde{\epsilon}_{\text{m}}$ the state approaches a molecular condensate with decreasing interaction strength U/t_{a} . Hence, we find a unit molecular density and a von Neumann entropy approaching $S_{\text{vN}}^{(1)} \approx 1.27$.

For this transition we find no obvious feature in the local von Neumann entropy in the vicinity of the phase transition (dashed line in Figs. 4.4(a),(b)). The first derivative with respect to the interaction $\partial S_{\text{vN}}^{(1)}/\partial(t_{\text{a}}/U)$ leads to a maximum which saturates at a value far below the actual phase boundary $(U/t_{\text{a}})_{\text{c}} = 1.176$ [43] with increasing system size.

Comparing the von Neumann entropy for different system sizes, however, we find that it is a monotonically increasing function of L in the MI phase and a monotonically decreasing function of L in the MC phase. Qualitatively, the behavior in the MI phase can be explained as a consequence of the finite (exponentially decaying) correlation length [179]: The local entropy increases with the system size until it saturates at a finite value when the system is large enough to support the full correlation length. On the side of the MC phase, we can use

the analytic expression for the weights of the local states in a condensate state Eq. (4.18) and build the derivative explicitly. We concentrate on the MC phase and therefore set $N = L$

$$w_\alpha = \frac{(L-1)^{L-\alpha}}{L^L} L\alpha. \quad (4.29)$$

We want to calculate an upper bound for local von Neumann entropy and therefore use an upper limit to estimate the binomial coefficient

$$Ll \leq \frac{L^\alpha}{\alpha!}. \quad (4.30)$$

Equation (4.18) becomes

$$w_\alpha \leq \left(\frac{L-1}{L}\right)^{L-\alpha} \frac{1}{\alpha}. \quad (4.31)$$

We define

$$F_\alpha(L) = \left(\frac{L-1}{L}\right)^{L-\alpha} \quad (4.32)$$

$$\frac{\partial}{\partial L} F_\alpha(L) = \left(\ln\left(\frac{L-1}{L}\right) + \frac{1}{L-1} - \frac{\alpha}{L(L-1)}\right) F_\alpha(L). \quad (4.33)$$

We can now derive the behavior of the local von Neumann entropy

$$S_{\text{vN}}^{(1)}(L) = - \sum_{\alpha} \frac{F_\alpha(L)}{\alpha!} \ln\left(\frac{F_\alpha(L)}{\alpha!}\right), \quad (4.34)$$

$$\frac{\partial}{\partial L} S_{\text{vN}}^{(1)}(L) = \sum_{\alpha} \frac{F'_\alpha(L)}{\alpha!} (\ln(\alpha!) - \ln(F_\alpha(L)) - 1). \quad (4.35)$$

We are interested in large systems so we go to the asymptotic limit

$$\lim_{L \rightarrow \infty} F_\alpha(L) \approx \frac{1}{e} + \frac{\alpha - 1/2}{eL} + \frac{12\alpha^2 - 5}{24eL^2}, \quad (4.36)$$

$$\lim_{L \rightarrow \infty} F'_\alpha(L) \approx \frac{1}{e} \left(\frac{1}{2} - \alpha\right) \frac{1}{L^2}, \quad (4.37)$$

where all terms were kept up to second order in $1/L$. The derivative of the local von Neumann entropy then becomes

$$\lim_{L \rightarrow \infty} S_{\text{vN}}^{(1)'}(L) \approx \sum_{\alpha} \frac{F'_\alpha(L)}{\alpha!} \ln(\alpha!). \quad (4.38)$$

Inspecting $F'_\alpha(L)$ we see that this quantity is always negative except for $\alpha = 0$. Since the $\ln(\alpha!)$ term kills all terms in the sum with $\alpha < 2$ we see that the derivative of the local von Neumann entropy with respect to system size L is always negative. Plugging in Eqs. (4.36) and (4.37) into Eq. (4.34) we see that $S_{\text{vN}}^{(1)}$ approaches its asymptotic value from above with a $1/L$ correction

$$S_{\text{vN}}^{(1)} \approx a + b \frac{1}{L}, \quad (4.39)$$

where a and b are constants. This result seems to be in contrast to the analytic scaling estimate [180]

$$S_{\text{vN}}(l) = \frac{c}{6}(\ln(L) + \ln(\sin(\frac{\pi l}{L})) + c_1), \quad (4.40)$$

where c_1 is some constant, c denotes the central charge and l is the size of the subsystem. For $l = 1$ (the case considered here) this estimate is a monotonically increasing function of system size. However, an explicit calculation of the local von Neumann entropy in the Bose-Hubbard model also reveals an entropy that goes down with the system size. This is consistent with Ref. [181] where they also find corrections to the scaling Eq. (4.40).

This discussion suggests the study of the L -dependence of the difference between two curves for system sizes L and $2L$

$$\delta S_L(U) = S_{\text{vN},L}^{(1)}(U) - S_{\text{vN},2L}^{(1)}(U), \quad (4.41)$$

where $S_{\text{vN},L}(U)$ is the local von Neumann entropy for system size L at interaction strength U . This quantity is presented in Fig. 4.4(c). The difference in local entropy $\delta S_{\text{vN}}^{(1)}$ is a linear function of the t_a/U in the vicinity of the phase transition. The point where the function changes sign is the point where the monotony changes as a function of L . This reflects the observation that the entropy increases in the MI phase while it decreases in the MC phase. With increasing system size two effects occur: The slope decreases and the point where the monotony changes shifts to the left in the direction of the phase boundary. A naive extrapolation to $1/L = 0$, however, yields an estimate for the critical point that is below the phase boundary [43]. To simplify the numerics we consider the Bose-Hubbard model which corresponds to the $\epsilon_m/t_a \rightarrow \infty$ limit of the BBRM model. We find the exact same behavior of $\delta S_{\text{vN}}^{(1)}(L)$ as for the BBRM model.

4.2.2 Properties of the local reduced density matrix

In this section we study the weight spectrum and the structure of the optimal modes deep in the three phases: MI, MC and AC+MC. Then, we illustrate the change in the optimal mode structure while we tune the system parameters along the two trajectories (see Fig. 4.1) over the two distinct phase transitions.

The difference between optimal modes in the three phases

We begin with the study of the weight spectra at three points deep in the three phases (see the three points in Fig. 4.1). Figure 4.5 illustrates the weight spectrum w_α for (a) the MI phase, (b) the MC phase and (c) the AC+MC phase. In all three phases we find an exponentially decaying structure. The spectrum in the MI phase Fig. 4.5(a) displays a plateau structure. The optimal mode structures $|\langle \alpha | n \rangle|^2$ are displayed in Fig. 4.5 as a function of the bare modes again for all three phases. Generally, the optimal modes are very simple superpositions of the bare occupation number states and for the MC and AC+MC phases they only barely mix different bare modes.

In the MI phase we can gain information about the local reduced density matrix using perturbation theory in the hopping parameter t_a (remember that we set $t_m = 0.5t_a$). We

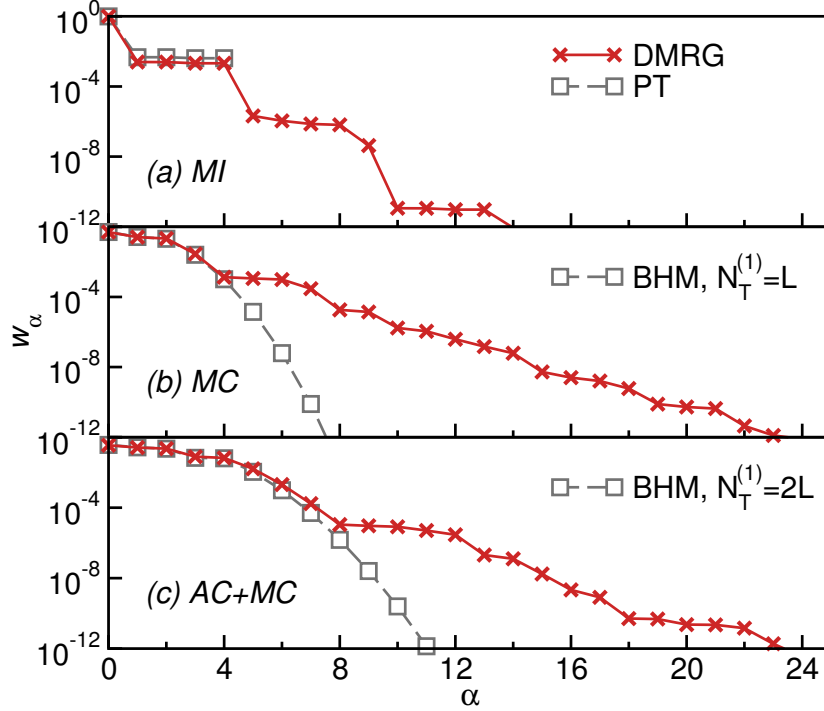


Figure 4.5: Weights of the optimal modes (eigenstates of the local reduced density matrix) in (a) the MI phase, (b) the MC phase and (c) the AC+MC phase calculated using DMRG in a system of size $L = 64$. The open symbols in (a) show results from perturbation theory while in (b) and (c) they represent data from Bose-Hubbard model with $N = L = 64$ (b) and $N = 2L = 128$ (c).

know the exact ground state in the $t_a/U = 0$ limit

$$|\psi_0^{\text{MI},g=U}\rangle = \prod_j |\phi_0^{\text{MI},g=U}\rangle, \quad (4.42)$$

which, since it is a product state, involves the highest weighted optimal mode

$$|\alpha = 0\rangle = |\phi_0^{\text{MI},g=U}\rangle. \quad (4.43)$$

A first approximation to the weight spectrum and the first five optimal modes can be found by calculating the reduced density matrix for the wavefunction in first-order perturbation theory

$$|\tilde{\psi}_0\rangle \approx |\psi_0^{(0)}\rangle + \frac{t_a}{U} |\psi_0^{(1)}\rangle, \quad \rho^{(1)} \approx \text{tr}_E(|\tilde{\psi}_0\rangle\langle\tilde{\psi}_0|). \quad (4.44)$$

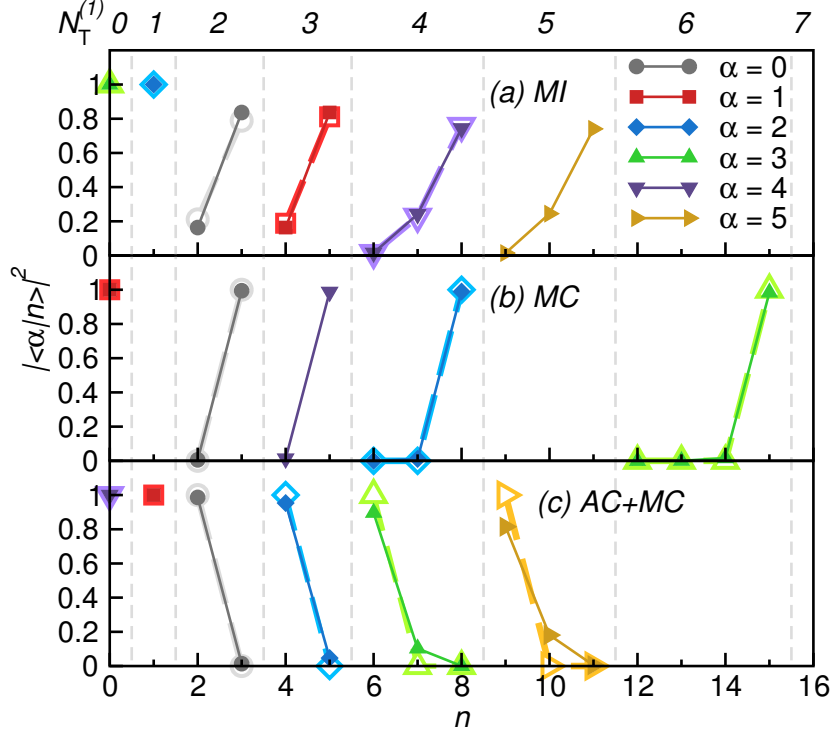


Figure 4.6: Optimal modes (eigenstates of the local reduced density matrix) $|\langle\alpha|n\rangle|$ in (a) the MI phase, (b) the MC phase and (c) the AC+MC phase calculated using DMRG in a system of size $L = 64$. The label n is illustrated in Tab. 4.1. The open symbols in (a) show results from perturbation theory while in (b) and (c) they represent data from Bose-Hubbard model with $N = L = 64$ (b) and $N = 2L = 128$ (c).

The perturbation term is given by the hopping of atoms and molecules

$$H = H_0 + \frac{t_a}{U}V, \quad (4.45)$$

$$H_0 = \sum_j [n_{j,a}(n_{j,a} - 1) + n_{j,m}(n_{j,m} - 1) + n_{j,a}n_{j,m} + m_j^\dagger a_j a_j + m_j a_j^\dagger a_j^\dagger], \quad (4.46)$$

$$V = -t_a \sum_j [a_j^\dagger a_{j+1} + a_{j+1}^\dagger a_j + \frac{1}{2}(m_j^\dagger m_{j+1} + m_{j+1}^\dagger m_j)] \\ = -t_a \sum_j (V_{a,j}^{(0)} + V_{a,j}^{(1)} + \frac{1}{2}(V_{m,j}^{(0)} + V_{m,j}^{(1)})). \quad (4.47)$$

The first-order correction is calculated by

$$|\psi_0^{(1)}\rangle = \sum_{n \neq 0} \frac{\langle\psi_n^{(0)}|V|\psi_0^{(0)}\rangle}{E_0^{(0)} - E_n^{(0)}} |\psi_n^{(0)}\rangle, \quad (4.48)$$

where $|\psi_n^{(0)}\rangle$ is the n -th unperturbed eigenstate of H_0 and $E_n^{(0)}$ is its eigenenergy. The perturbation V couples the local state Eq. (4.27) which has a local occupation number of $N_T^{(1)} = 2$

to states with $N_T^{(1)} = 0, 4$ by application of a molecular hopping term and to states with $N_T^{(1)} = 1, 3$ by application of an atomic hopping term. We therefore need the local eigenstates of H_0 in those subspaces. The Hamiltonian can be easily diagonalized exactly in those subspaces and we find

$$E_0^{N_T=0} = 0 : |\phi_0^{N_T=0}\rangle = |0; 0\rangle, \quad (4.49)$$

$$E_0^{N_T=1} = 0 : |\phi_0^{N_T=1}\rangle = 0.1665|1; 0\rangle, \quad (4.50)$$

$$E_0^{N_T=3} = 0 : |\phi_0^{N_T=3}\rangle = \sqrt{\frac{6}{7}}(-\frac{1}{\sqrt{6}}|3; 0\rangle + |1; 1\rangle), \quad (4.51)$$

$$E_1^{N_T=3} = 7t_a : |\phi_1^{N_T=3}\rangle = \sqrt{\frac{1}{7}}(\sqrt{6}|3; 0\rangle + |1; 1\rangle), \quad (4.52)$$

$$E_0^{N_T=4} \approx -0.5452t_a : |\phi_0^{N_T=4}\rangle = 0.1665|4; 0\rangle - 0.6029|2; 1\rangle \\ + 0.7803|0; 2\rangle, \quad (4.53)$$

$$E_1^{N_T=4} \approx 3.3314t_a : |\phi_1^{N_T=4}\rangle = -0.2902|4; 0\rangle + 0.6231|2; 1\rangle \\ + 0.6231|0; 2\rangle, \quad (4.54)$$

$$E_2^{N_T=4} \approx 13.2138t_a : |\phi_2^{N_T=4}\rangle = 0.9424|4; 0\rangle + 0.3302|2; 1\rangle \\ + 0.0541|0; 2\rangle. \quad (4.55)$$

The states of the full system that are coupled by the perturbation are then given by

$$|\psi_{1,j}^{(0)}\rangle = \cdots \otimes |\phi_0^2\rangle_{j-1} \otimes |\phi_0^3\rangle_j \otimes |\phi_0^1\rangle_{j+1} \otimes |\phi_0^2\rangle_{j+2} \otimes \cdots, \quad (4.56)$$

$$|\psi_{2,j}^{(0)}\rangle = \cdots \otimes |\phi_0^2\rangle_{j-1} \otimes |\phi_1^3\rangle_j \otimes |\phi_0^1\rangle_{j+1} \otimes |\phi_0^2\rangle_{j+2} \otimes \cdots, \quad (4.57)$$

$$|\psi_{3,j}^{(0)}\rangle = \cdots \otimes |\phi_0^2\rangle_{j-1} \otimes |\phi_0^4\rangle_j \otimes |\phi_0^0\rangle_{j+1} \otimes |\phi_0^2\rangle_{j+2} \otimes \cdots, \quad (4.58)$$

$$|\psi_{4,j}^{(0)}\rangle = \cdots \otimes |\phi_0^2\rangle_{j-1} \otimes |\phi_1^4\rangle_j \otimes |\phi_0^0\rangle_{j+1} \otimes |\phi_0^2\rangle_{j+2} \otimes \cdots, \quad (4.59)$$

$$|\psi_{5,j}^{(0)}\rangle = \cdots \otimes |\phi_0^2\rangle_{j-1} \otimes |\phi_2^4\rangle_j \otimes |\phi_0^0\rangle_{j+1} \otimes |\phi_0^2\rangle_{j+2} \otimes \cdots, \quad (4.60)$$

where $|\phi_n^{N_T}\rangle_j$ is the n -th eigenstate of H_0 in the N_T subspace on site j . The states $|\psi_{n,j}^{(0)}\rangle$ are the states that the initial ground state $|\psi_0^{(0)}\rangle$ connects to in first order. We denote the state with reverse order of local states as $|\psi'_{n,j}{}^{(0)}\rangle$. We can now calculate the contributions to the perturbed state from Eq. (4.48)

$$|\psi_0^{(1)}\rangle = -t_a \sum_j \left[\frac{1}{2} (f_1 |\xi_{1,j}^{(0)}\rangle + f_3 |\xi_{3,j}^{(0)}\rangle + f_5 |\xi_{5,j}^{(0)}\rangle + f_3) \right. \\ \left. + g_2 |\xi_{2,j}^{(0)}\rangle + g_4 |\xi_{4,j}^{(0)}\rangle \right], \quad (4.61)$$

where $|\xi_{n,j}^{(0)}\rangle = |\psi'_{n,j}{}^{(0)}\rangle + |\psi_{n,j}^{(0)}\rangle$ and

$$f_i = \frac{\langle \psi_{i,0}^{(0)} | V_{m,0}^{(1)} | \psi_0^{(0)} \rangle}{E_0^{(0)} - E_i^{(0)}}, \quad (4.62)$$

$$g_i = \frac{\langle \psi_{i,0}^{(0)} | V_{a,0}^{(1)} | \psi_0^{(0)} \rangle}{E_0^{(0)} - E_i^{(0)}}. \quad (4.63)$$

We now set up the reduced density matrix using Eq. (4.44). By diagonalization we obtain the first-order approximation to the five most important weights w_α and optimal mode spectra $|\langle \alpha | n \rangle|^2$. Figures 4.5(a) and 4.6(a) illustrate the results (open symbols). Both are very close to the numerically exact data since we are very deep in the large U/t_a limit. The first plateau in Fig. 4.5 emerges in first-order perturbation theory and can be qualitatively explained by the number of local states that the perturbation term couples to the initial state: The unperturbed state has a local occupation number of $N_T = 2$ at every site. To first order, it is coupled to the states with $N_T = 0, 1, 3$ and $N_T = 4$. Comparing to the optimal mode spectra in Fig. 4.6(a) we see that the five most important modes indeed occupy these five local particle number subspaces. The two-fold degeneracy in the $\alpha = 1, 2$ and in the $\alpha = 3, 4$ weights stem from the fact that the first-order perturbation creates the two local modes $|\phi_0^4\rangle$ and $|\phi_0^0\rangle$ as well as the $|\phi_0^3\rangle$ and $|\phi_0^1\rangle$ modes in pairs with the same weight on two neighboring sites. The same reasoning also works to predict the subspaces in which the optimal modes in the second and third plateaus are located when one takes the first and second order subspaces as initial states. The second plateau couples to the first-order states to states in the subspaces $N_T = 0, 1, 2, 3, 4, 5$ and $N_T = 6$. Since the $N_T = 0, 1$ subspaces include one state only and they already lie in the first-order plateau, the second plateau is made from states in the $N_T = 2, 3, 4, 5, 6$ subspaces. Comparison to numerics confirms this assumption. The same procedure works for the third plateau.

We compare the weight spectra in the MC (Fig. 4.5(b)) and AC+MC (Fig. 4.5(c)) phases to the weight spectra of a BHM with the same system parameters and unit (MC) or double filling (AC+MC). These estimates approximate the data in the MC and AC+MC phases well up to a precision of $w_\alpha \approx 10^{-4}$ where the decay of weights is slower in the BBRM model than in a pure BHM. We attribute this to the presence of more than one species in both states together with the effect of the Feshbach term. In the BHM only bare modes exist but their relative importance is given by Eq. (4.18). A comparison of these states with the optimal modes for the MC (Fig. 4.6(b)) and AC+MC (Fig. 4.6(c)) phase reveals that they perfectly describe the order and position of the peak of the first few highest weighted observed optimal modes. However, the $\alpha = 4$ mode in Fig. 4.6(b) is a mixture of an atom and a molecule and therefore can not be described by the approximation via the BHM. The relatively high weight of this mode also shows that the atomic species can not be neglected in this state. The same arguments hold for the AC+MC phase optimal modes where the optimal modes are even stronger effected by the presence of the other species which is reflected in a stronger mixing in the optimal modes (they are less strongly peaked).

Continuous evolution of optimal modes over the phase boundary

We now want to follow the evolution of the optimal modes as the system parameter is tuned while the system stays in the ground state. The parameters are tuned along the two trajectories in Fig. 4.1.

We discuss the transition in the detuning ϵ_m (upper trajectory in Fig. 4.1) first. We have seen that the local von Neumann entropy is sensitive to the location of this transition and we are interested in how the optimal modes correspond to this point. Figure 4.7 shows the eight highest weighted optimal modes as a function of the detuning. Generally, all of them change significantly in the vicinity of the phase boundary which is expected by inspection of the optimal mode structure deep in the two phases Fig. 4.6: at some point a reorganization has to happen. This transition can happen in two ways:

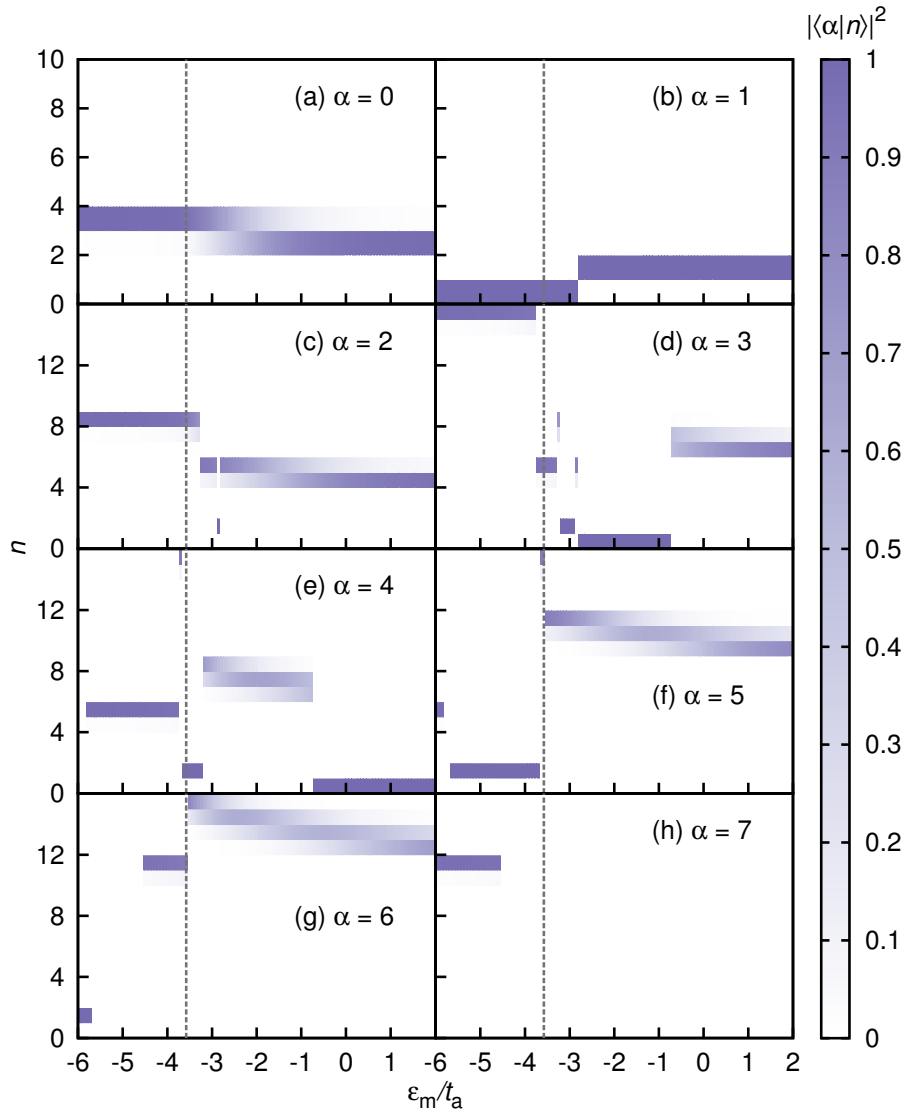


Figure 4.7: (a)-(h) Evolution of the first eight optimal modes $|\alpha\rangle$ along the trajectory from the MC ($\epsilon_m = -6t_a, \frac{t_a}{U} = 3$) to the AC+MC phase ($\epsilon_m = 2t_a, \frac{t_a}{U} = 3$). The figure shows the weights $|\langle\alpha|n\rangle|^2$ of the bare local states $|n\rangle = |N_a^{(1)}(n), N_m^{(1)}(n)\rangle$ contributing to the optimal modes as a function of detuning. DMRG results for $L = 80$. The dashed line indicates the phase boundary [43]. The respective physical state corresponding to the index n is defined in Tab. 4.1.

(i) *A continuous transition.* Provided that both, the initial and final, states are located in the same total local particle subspace labeled by $N_T^{(1)}$ a continuous crossover can happen where the mode changes by continuously shifting weight between bare states. An example is the crossover of the $\alpha = 0$ mode in Fig. 4.7(a): Inspection of Figs. 4.6(b) and (c) reveals that

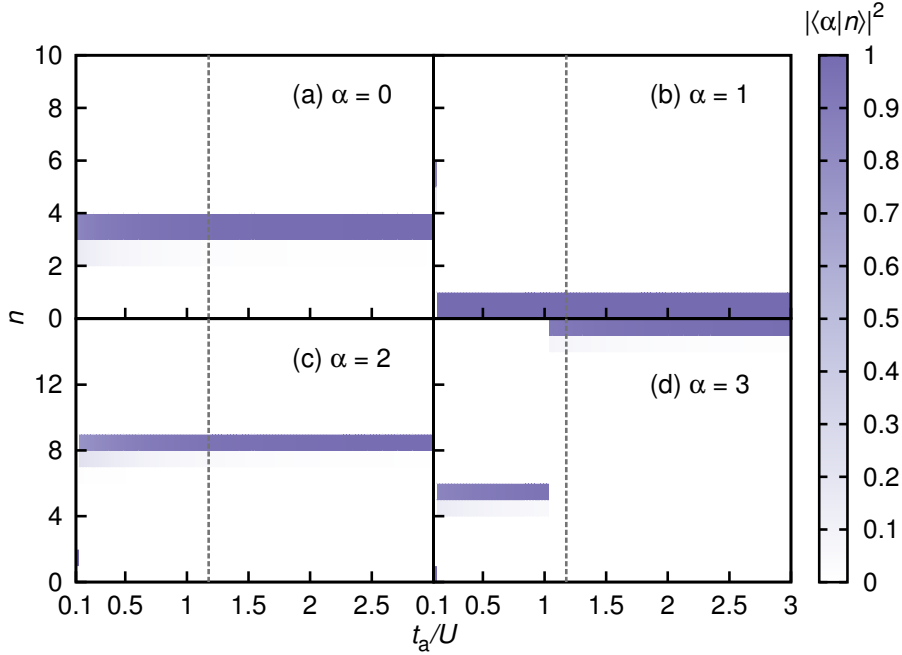


Figure 4.8: (a)-(d) Evolution of the first four optimal modes $|\alpha\rangle$ along the trajectory from the MI ($\epsilon_m = -6t_a, \frac{t_a}{U} = 0.1$) to the MC phase ($\epsilon_m = -6t_a, \frac{t_a}{U} = 3$). The figure shows the weights $|\langle\alpha|n\rangle|^2$ of the bare local states $|n\rangle = |N_a^{(1)}(n), N_m^{(1)}(n)\rangle$ contributing to the optimal modes as a function of t_a/U . DMRG results for $L = 64$. The dashed line indicates the phase boundary [43]. The respective physical state corresponding to the index n is defined in Tab. 4.1.

the highest weighted optimal mode in the MC and AC+MC phases is located in the $N_T^{(1)} = 2$ subspace where the peak in the MC phase is on the $|0;1\rangle$ state and in the AC+MC state it is on the $|2;0\rangle$ state. As the detuning is tuned over the phase transition, the modes transform to the corresponding limit.

(ii) *A level crossing.* If initial and final modes are in different subspaces a continuous transition is impossible. In such a case a level crossing happens: the states need to be reordered which means that states in certain subspaces will become more important while others become less important. As soon as one state becomes less important than another, a level crossing happens which is reflected in the optimal modes by a sudden jump. An example for this behavior is given by Figs. 4.7(b),(c) and (d): The $N_T^{(1)} = 1$ state has a low weight in the MC phase and thus has to ascend the ladder of optimal modes until it reaches its final position as the second most-important mode in the AC+MC phase. The state first emerges as the $\alpha = 3$ state in Fig. 4.7(d) where it stays until, with increasing ϵ_m , it has enough weight to be the third most important $\alpha = 2$ mode in Fig. 4.7(c).

At the phase transition the $\alpha = 0$ mode evolves from the $|0;1\rangle$ state into the $|2;0\rangle$ state. Without further knowledge we can conclude that the MC phase favors molecules while the AC+MC phase favors atoms. Qualitatively, the same happens in other states which are more complicated superpositions of bare modes. In the $\alpha = 5, 6$ modes an interesting feature emerges: the optimal modes change their structure abruptly by jumping from small to large n states. The position of this jump is independent of system size (for our observed system

sizes) and sits right at the phase boundary.

In summary, we see that the change in optimal mode structure happens in the vicinity of the phase boundary and we therefore conclude that the optimal mode structure correlates with the transition.

For the second trajectory that connects states in the MI and MC phases by varying the interaction U/t_a only, we saw that the local von Neumann entropy does not have a clear feature at the transition. Figure 4.8 illustrates the four highest weighted optimal mode structures as a function of t_a/U . Inspection of Fig. 4.6 reveals that apart from the highest weighted mode $\alpha = 0$ no other pair of modes lies in the same particle subspace and, thus, they have to undergo a level crossing. The change in the second and third optimal modes (Figs. 4.8(b),(c)) occurs at a value close to $t_a/U = 0.1$. As in the previous discussion, the $\alpha = 0$ mode lies in the $N_T^{(1)} = 2$ subspace and changes only slightly: with increasing t_a/U the atomic contribution to this mode gets suppressed because the detuning term dominates the occupation ratio. Another feature is shown in Fig. 4.8(d): a jump occurs in the vicinity of the phase transition where the $N_T^{(1)} = 3$ mode drops to a lower weight and the $N_T^{(1)} = 6$ mode moves to its final relative position. As before, the optimal mode structure shows features in the vicinity of the phase boundary and we conclude that it is sensitive to this transition as well.

4.3 Non-Equilibrium properties

In the last part we calculated the ground state expectation values while tuning the system parameters. This can be interpreted as an adiabatic evolution of the system where we start from the ground state in some phase and tune the parameters infinitely slowly in time. In this section we do something more drastic to the system: we again start from the same ground states as previously (see the two start points of the trajectories in Fig. 4.1) but change the parameters suddenly to the values at the end-points of the respective trajectory. This procedure is also called a quantum quench. We study the molecular density, the local von Neumann entropy and the spectrum of the optimal modes as a function of time.

4.3.1 Molecular density and local von Neumann entropy

In this section we illustrate the time-dependence of the $k = 0$ component of the atomic (molecular) quasimomentum distribution function rescaled by the number of atoms (molecules), the molecular density and the local von Neumann entropy after a quench of a ground state deep in the MI (MC) phase to the MC (AC+MC) phase. Also, we calculate the long-time limit of the expectation value of the molecular density which is given by its expectation value in the so-called diagonal ensemble [66]

$$\overline{\langle n_m \rangle}_{\text{diag}} = \sum_n |\langle \psi_0 | \psi_n \rangle|^2 \langle \psi_n | n_m | \psi_n \rangle, \quad (4.64)$$

where $|\psi_n\rangle$ are the eigenstates of the postquench Hamiltonian and $|\psi_0\rangle$ is the initial state before quenching. Additionally, we compare the expectation value of the molecular density in the diagonal ensemble with the one in the canonical ensemble and also we compare the steady-state value of the local von Neumann entropy with its expectation in the diagonal ensemble to see if the system thermalizes. For the calculation of the canonical expectation

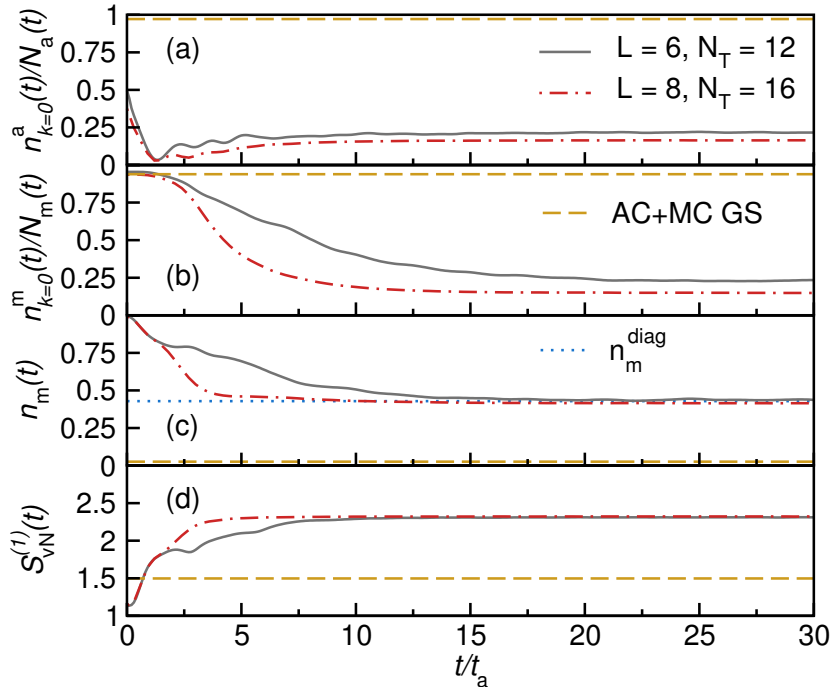


Figure 4.9: Evolution of the $k = 0$ component of the (a) atomic and (b) molecular momentum distribution function, (c) the molecular density and (d) the single-site von Neumann entropy as a function of time along the trajectory from the MC ($\epsilon_m = -6t_a$, $\frac{t_a}{U} = 3$) to the AC+MC phase ($\epsilon_m = 2t_a$, $\frac{t_a}{U} = 3$). The dashed line in (c) gives the expectation value of the molecular density in the diagonal ensemble (Eq. (4.64)) for a system of size $L = 6$ which shows that we reach the long-time steady state in the observed time. The quench energy is $E_q/L = (E - E_0)/L = 4.1227$. ED results for $L = 6, 8$.

value we first extract the canonical temperature T by fixing the expectation value of the energy in the canonical ensemble to the energy of the initial state with respect to the postquench Hamiltonian

$$\langle H \rangle_{\text{can}}(\beta) = \frac{\sum_n E_n e^{-\beta E_n}}{\sum_n e^{-\beta E_n}} \stackrel{!}{=} \langle \psi(t=0) | H | \psi(t=0) \rangle. \quad (4.65)$$

The expectation values of observables \hat{O} in the canonical ensemble are computed from:

$$\langle \hat{O} \rangle = \text{tr}(\rho_{\text{can}} \hat{O}); \quad \rho_{\text{can}} = e^{-\beta H} / Z, \quad (4.66)$$

where Z is the partition function and $\beta = 1/T$. We use Krylov-space time-evolution in a system of size up to $L = 8$ and full diagonalization for the calculation of the diagonal and canonical ensembles in systems of size $L = 6$.

Quench from the MC to the AC+MC phase

The dynamics during the first quench is illustrated in Fig. 4.9 for system sizes $L = 6, 8$. In the first few time steps the $k = 0$ quasimomentum occupations of both species - atoms and

molecules - decrease. The decrease of $n_m^{k=0}$ is consistent with the behavior of the molecular density $n_m = N_m/L$: it decreases in time, which means that atoms are created.

We define the quench energy as the difference between the energy of the initial state in the post-quench Hamiltonian H and the ground state energy of H

$$E_q = E - E_0, \quad (4.67)$$

where $E = \langle \psi_0 | H | \psi_0 \rangle$. The quench energy is finite and so large that the initial state samples primarily states in the bulk of the spectrum of H . So, it is not surprising that the observables are not comparable to their ground state expectation values.

Comparison of the steady-state value of the molecular density and the diagonal ensemble expectation value shows very good agreement which tells us that the molecular density has fully relaxed to its infinite-time value. A comparison between the diagonal ensemble value and the canonical ensemble expectation value shows a relative difference of $(n_m^{\text{diag}} - n_m^{\text{can}})/n_m^{\text{diag}} \approx 9\%$ for $L = 8$. The remaining difference can be attributed to finite size effects [182]. The local von Neumann entropy increases with time until it reaches a steady-state value. We compute the local von Neumann entropy in the canonical ensemble and find that it deviates from the steady-state value $(S_{\text{vN}}^{(1)})_{\text{st}}$ by only $((S_{\text{vN}}^{(1)})_{\text{st}} - (S_{\text{vN}}^{(1)})_{\text{can}})/(S_{\text{vN}}^{(1)})_{\text{st}} \approx 0.01\%$. Increasing the system size lowers the atomic zero-quasimomentum occupation decreases and oscillations vanish.

Quench from the MI to the MC phase

Data for the dynamics of the second quench are shown in Fig. 4.10. The quench energy in this case is small compared to the quench from the MC to the AC+MC case. Because of that, the initial state samples only the low-energy post-quench eigenstate expectation spectrum of the observables. Similar to the case above, the regime in which the observed quantities vary is very short. After that, they reach their steady-state value. The zero-momentum occupation number stays roughly constant both for atoms and molecules. Also, the molecular density changes only by a small fraction and the ratio between atom number and molecule number thus stays constant. The local von Neumann entropy undergoes a drastic increase until it, too, reaches a steady state value. Increasing the size of the system again leads to a decay of oscillations which makes them finite-size effects. We again compare the molecular density to its expectation value in the diagonal ensemble (dashed line in Fig. 4.10(c)). The good agreement between the steady-state value and the diagonal ensemble average indicates that this observable reaches its steady state value in the observed time. Comparison of the diagonal and canonical ensemble averages show a relative difference of $(n_m^{\text{diag}} - n_m^{\text{can}})/n_m^{\text{diag}} \approx 2\%$. For the steady-state value of the local reduced density matrix we find a relative deviation from the value in the canonical ensemble of $((S_{\text{vN}}^{(1)})_{\text{st}} - (S_{\text{vN}}^{(1)})_{\text{can}})/(S_{\text{vN}}^{(1)})_{\text{st}} \approx 5\%$ where we note again that the canonical ensemble average is calculated from a system of size $L = 6$ and is compared to the steady-state value in a system with size $L = 8$.

4.3.2 Post-quench eigenstate expectation values

In this section we describe the time-evolution during a quench from the perspective of the eigenstate thermalization hypothesis (ETH) [66, 183, 184]. Time-evolution is performed under the post-quench Hamiltonian H and we can express the initial state in terms of the eigenstates

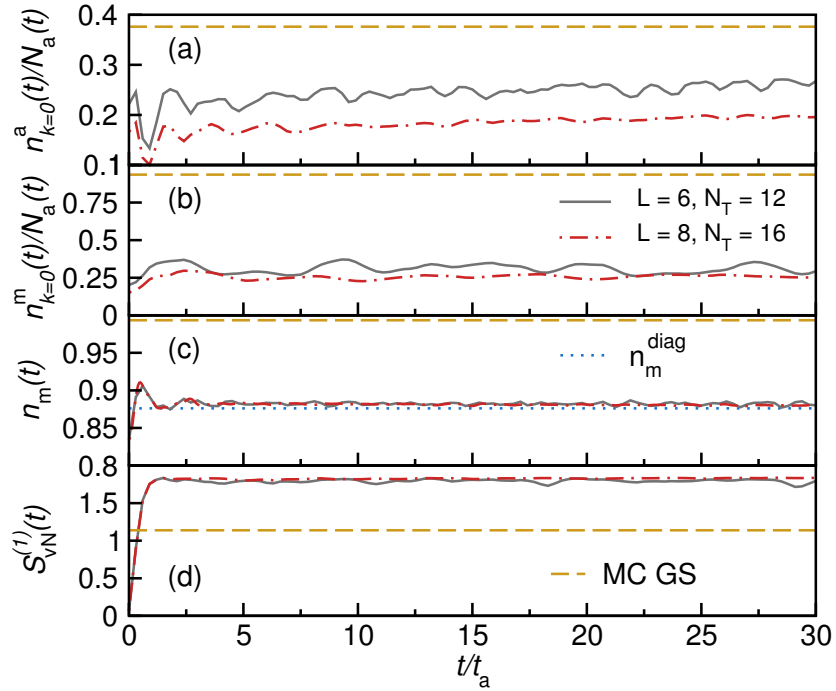


Figure 4.10: Evolution of the $k = 0$ component of the (a) atomic and (b) molecular momentum distribution function, (c) the molecular density and (d) the single-site von Neumann entropy as a function of time along the trajectory from the MI ($\epsilon_m = -6t_a$, $\frac{t_a}{U} = 0.1$) to the MC phase ($\epsilon_m = -6t_a$, $\frac{t_a}{U} = 3$). The dashed line in (c) gives the expectation value of the molecular density in the diagonal ensemble (Eq. (4.64)) for a system of size $L = 6$ which shows that we reach the long-time steady state in the observed time. The quench energy is $E_q/L = (E - E_0)/L = 1.3923$. ED results for $L = 6, 8$.

of this operator

$$|\psi(t=0)\rangle = \sum_n c_n |\psi_n\rangle, \quad (4.68)$$

where $|\psi_n\rangle$ denotes the n -th eigenstate of H . The time-evolution of an observable can then be written

$$\begin{aligned} \langle O \rangle(t) &= \langle \psi(0) | e^{iHt} O e^{-iHt} | \psi(0) \rangle \\ &= \sum_n |c_n|^2 \langle \psi_n | O | \psi_n \rangle \\ &\quad + \sum_{\substack{n, n' \\ n \neq n'}} c_n^* c'_n \langle \psi_n | O | \psi'_n \rangle e^{i(E_n - E'_n)t}, \end{aligned} \quad (4.69)$$

where the first term is the diagonal time-independent part and the second term includes all off-diagonal terms. Please note that we assume a non-degenerate eigenspectrum of H . In the limit of long times only the time-independent part remains while the oscillations cancel via dephasing [66, 185]

$$\overline{\langle O \rangle} = \sum_n |c_n|^2 \langle \psi_n | O | \psi_n \rangle. \quad (4.70)$$

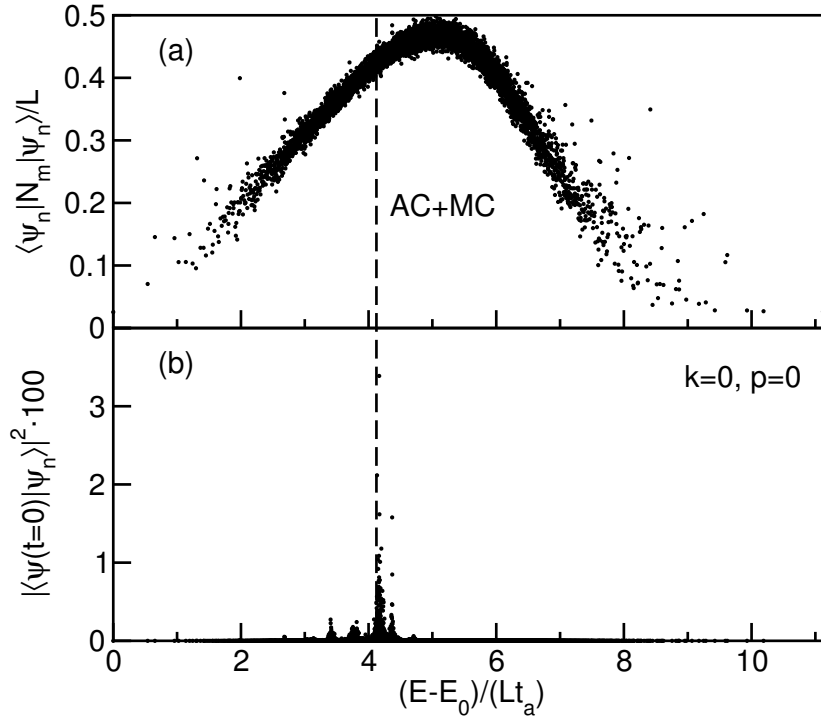


Figure 4.11: (a) Distribution of postquench expectation values of the molecule particle number operator in the AC+MC phase along with (b) the overlaps of the initial state with the eigenstates in a system of size $L = 6$. The dashed line indicates the quench energy. ($\epsilon_m = 2t_a$, $t_a/U = 3$).

This is called the diagonal ensemble average. The statements up to this point are exact and, therefore, have to hold for every observable. In principle this means that knowledge of the initial state together with the eigenspectrum of the system under study is enough to predict the long-time value for an arbitrary observable.

We can now ask when the expectation value in the diagonal ensemble coincides with the one computed from some thermal ensemble. Since for our closed quantum system energy, particle number and volume are fixed it is natural to compare to the expectation value in the microcanonical ensemble

$$\langle O \rangle_m = \frac{1}{\mathcal{N}} \sum_{E-\Delta E < E_n < E+\Delta E} \langle \psi_n | O | \psi_n \rangle \quad (4.71)$$

$$\sum_n |c_n|^2 O_{nn} \stackrel{!}{=} \frac{1}{\mathcal{N}} \sum_{E-\Delta E < E_n < E+\Delta E} O_{nn}, \quad (4.72)$$

where ΔE is a small energy-width around the mean energy E and \mathcal{N} is the number of eigenstates of H in the energy window $E-\Delta E < E_n < E+\Delta E$. The eigenstate thermalization hypothesis makes a statement of how this equality can be fulfilled [66, 183, 184]: The two terms will in general be equal if (i) the $|c_n|^2$ sample just a very narrow energy region (comparable to ΔE) and (ii) the O_{nn} are a sharp distribution and, thus, only a function of energy in the region where $|c_n|^2 \neq 0$.

We discuss the distribution of post-quench eigenstate expectation values of the molecular

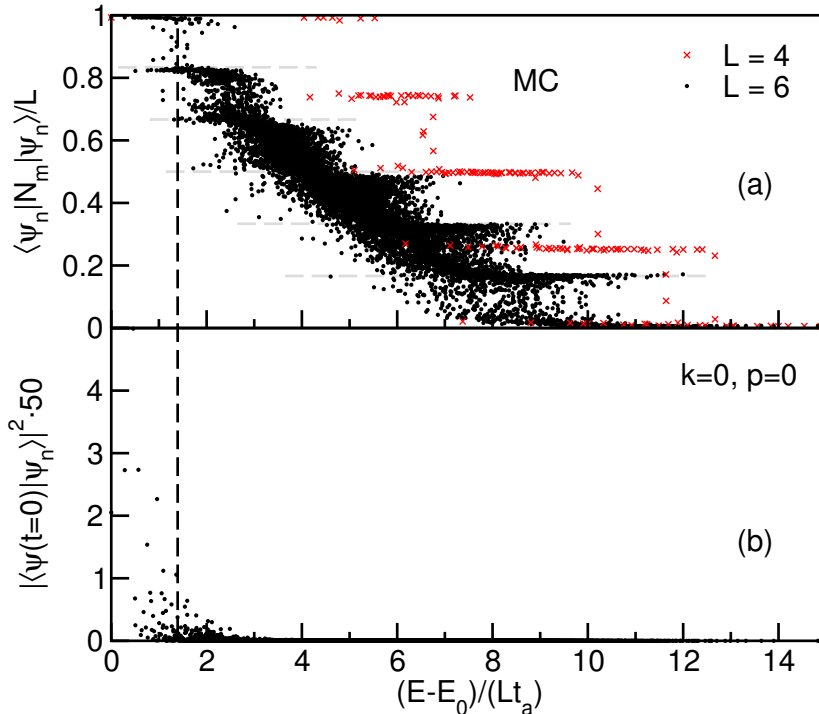


Figure 4.12: (a) Distribution of postquench expectation values of the molecular particle number operator in the MC phase along with (b) the overlaps of the initial state with the eigenstates. The dashed line indicates the quench energy. ($\epsilon_m = 2t_a$, $t_a/U = 3$).

density $\langle \psi_n | n_m | \psi_n \rangle$ for both the quench from the MC to the AC+MC phase and the quench from the MI to the MC phase. Figure 4.11 illustrates this quantity for the quench in the detuning in a system of size $L = 6$. Despite the small size of our system, the distribution of post-quench eigenstate expectation values in Fig. 4.11(a) is a smooth and fairly sharp function for energies in the bulk of the eigenspectrum. The initial state Fig. 4.11(b) is very sharply peaked at an energy $(E - E_0)/L \approx 4t_a$ which is well inside the bulk of the eigenspectrum. We conclude that the criteria for the eigenstate thermalization hypothesis are fulfilled in this case and thus the system thermalizes, which is consistent with our numerical observations.

Figure 4.12 shows the distribution of post-quench eigenstate expectation values for the quench from the MI to the MC phase for the system sizes $L = 4, 6$. The $L = 4$ data shows a clear plateau structure at integer values of the number of molecules. Increasing the system size introduces more states with intermediate molecular particle number, however, a plateau structure is still visible. For the initial state we again find a peaked function of the energy. Comparison to the distribution of post-quench eigenstate expectation values shows that it samples the edge of the spectrum where ETH is expected to work only for very large system sizes [182, 186–188]. Nevertheless, our numerical data indicate a reasonable agreement between the diagonal and thermal ensembles already on our small systems.

4.3.3 Structure of optimal modes

In this final section we study the structure of the optimal modes as a function of time during the two quenches Fig. 4.1. Figure 4.13 illustrates this scenario for the first quench from the

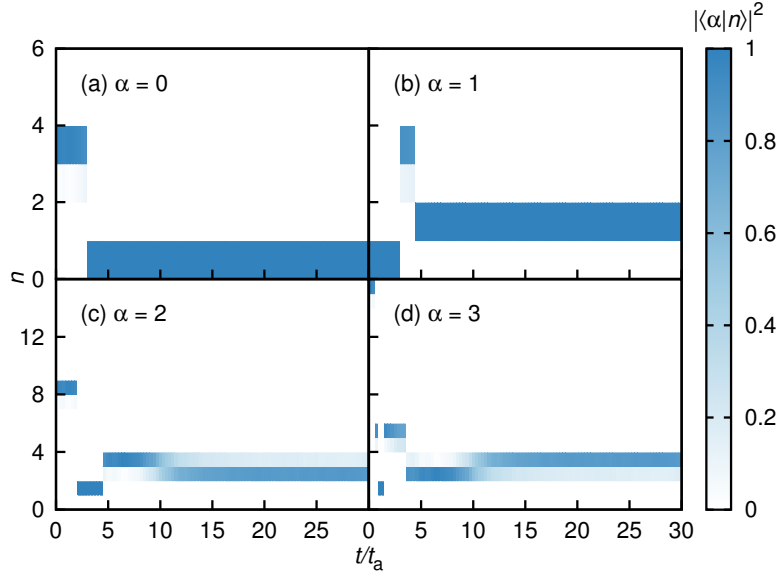


Figure 4.13: (a)-(d) Evolution of the first four optimal modes $|\alpha\rangle$ in time along the trajectory from the MC ($\epsilon_m = -6t_a, \frac{t_a}{U} = 3$) to the AC+MC phase ($\epsilon_m = 2t_a, \frac{t_a}{U} = 3$). The figure shows the weights $|\langle \alpha | n \rangle|^2$ of the bare local states $|n\rangle = |N_a^{(1)}(n), N_m^{(1)}(n)\rangle$ contributing to the optimal modes as a function of t_a/U . ED results for $L = 8$. The respective physical state corresponding to the index n is defined in Tab. 4.1.

MC into the AC+MC phase. For small times t/t_a the optimal-mode structure is the same as deep in the MC phase Fig. 4.6(b) since this is the initial state. Thus, the initial structure has modes in the $N_T^{(1)} = 0, 2, 4, 6$ local particle subspaces. In time they evolve into states in the $N_T^{(1)} = 0, 1, 2$ subspaces. For long times a comparison to Fig. 4.6(c) reveals that only the $\alpha = 1$ (Fig. 4.13(b)) mode has the same form as in the ground state deep in the AC+MC phase while the three other modes evolve to different structures. This is not surprising given the large quench energy for this quench. From the optimal-mode structures we can read off that the contribution of atoms increases: The three most important optimal modes in the steady-state regime are located in the $N_T^{(1)} = 0, 1, 2$ subspaces. Also, the $\alpha = 3, 4$ modes show that the molecular contribution is suppressed with time. The high weight of the $N_T^{(1)} = 0$ implies that there are increased fluctuations in local particle number in the steady state.

Figure 4.14 shows the optimal-mode structures for the second quench from the MI to the MC phase. The evolution from the initial to the steady-state proceeds very rapidly: it takes less than $\sim 2t_a$. This is very similar to the behavior of observables in Fig. 4.10. From Fig. 4.10(c) we also see that the molecular density is not influenced greatly by the quench. The high weight of the $N_T^{(1)} = 0$ mode again implies increased fluctuations in the steady-state.

Generally, the optimal-mode structures vary in the same time-window in which the local von Neumann entropy $S_{vN}^{(1)}$ varies significantly. We want to find out if the local reduced density matrix is indeed thermal and compare the optimal modes in the steady-state to the optimal modes calculated in the canonical ensemble for both quenches. This is done by tracing the

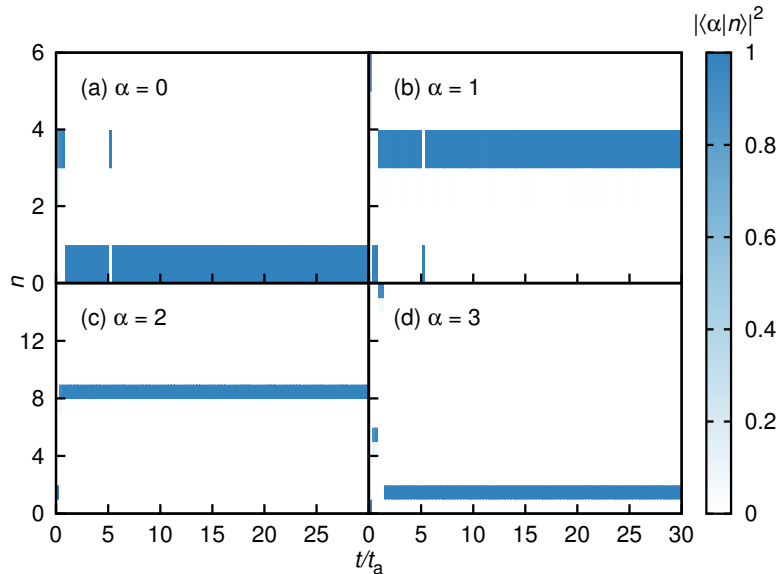


Figure 4.14: (a)-(d) Evolution of the first four optimal modes $|\alpha\rangle$ in time along the trajectory from the MI ($\epsilon_m = -6t_a$, $\frac{t_a}{U} = 0.1$) to the MC phase ($\epsilon_m = -6t_a$, $\frac{t_a}{U} = 3$). The figure shows the weights $|\langle\alpha|n\rangle|^2$ of the bare local states $|n\rangle = |N_a^{(1)}(n), N_m^{(1)}(n)\rangle$ contributing to the optimal modes as a function of t_a/U . ED results for $L = 8$. The respective physical state corresponding to the index n is defined in Tab. 4.1.

canonical density matrix Eq. 4.66 over all but one site

$$\rho_{\text{can}}^{(1)} = \text{tr}_{L-1}(\rho_{\text{can}}). \quad (4.73)$$

We find a strong similarity for both quenches and therefore conclude that the optimal-mode structures are thermal.

4.4 Summary

In this chapter we studied the single-site reduced density matrix in the Bose-Bose resonance model in equilibrium and in quantum quenches. We choose the case of double filling $N_T = 2L$ which has a rich phase diagram [43] and also features non-trivial optimal modes.

We studied the behavior of the local von Neumann entropy in the ground state as a function of the control parameters of our model and found that it displays features at the phase boundaries of this model. At the phase boundary between the MC and AC+MC phases the first derivative of the local von Neumann entropy with respect to the detuning shows a sharp maximum. For the phase transition between the MI and MC phases we found that the local von Neumann entropy behaves differently as a function of system size in the two phases: in the MI phase the entropy is a monotonically increasing function of system size until it saturates from below while in the MC phase we showed that it is a monotonically decreasing function of system size that saturates from above. The point at which the monotony changes is close to the known position of the phase boundary. We also elucidated the behavior of the optimal-mode structure as a function of the control parameters for both trajectories through

the phase diagram. At a point deep in the phases we show that the optimal-mode structure is different and it is thus possible to distinguish the phases by the structure of the first few highest weighted modes. Following the evolution of the optimal-mode structure through the phase diagram we find that a phase transition in our model is reflected by a change of the optimal-mode structure in the vicinity of the phase boundary.

We also considered two quantum quenches along the two trajectories where we start from the ground state in one phase and quench the system over to the final parameters located in a different phase. For these quenches we monitor the fraction of atoms and molecules that are at quasimomentum $k = 0$ (condensed), the density of molecules and the local von Neumann entropy as a function of time. We compute the diagonal and canonical ensemble averages for the molecular density. Both agree very well with the steady-state value obtained from the numerical data. In the first quench, we explain the agreement by the sharply peaked initial state as a function of postquench energy and the sharp distribution of postquench eigenstate expectation values which are the conditions under which the eigenstate thermalization hypothesis applies. Also, we compared the local von Neumann entropy in the steady state to its value computed from the canonical ensemble and find strong agreement. We finally studied the structure of the optimal modes as a function of time. Comparison of the optimal-mode structure in the steady-state and from the canonical ensemble shows that the single-site reduced density matrix is thermal in the steady-state.

Chapter 5

Temporal decay of Néel order in the one-dimensional Fermi-Hubbard model

Many works have considered the time-evolution of order parameters in quenches from ordered into disordered phases [63, 189–193]. One example is the dynamics of the staggered magnetization in quantum magnets which is non-trivial because the Néel state is never an eigenstate of antiferromagnetic Heisenberg models. In a one dimensional setup under time-evolution with an $SU(2)$ -symmetric Hamiltonian the staggered magnetization is expected to decay to zero because spontaneous breaking of a continuous symmetry is prohibited (Mermin-Wagner theorem [63, 194, 195]). This has been studied for the spin-1/2 XXZ chain [64, 196–203] and one observes for the staggered magnetization a temporal power-law decay to zero for the XX case and an exponential decay for the interacting case [64]. Also, due to the integrability of the model, an exact solution for the long-time asymptotic behavior could be obtained [198, 201, 202] and the question of whether the steady state can be described by the generalized Gibbs ensemble could be addressed [204]. Further, the decay of Néel order has been studied in the extended Fermi-Hubbard model [63].

Experiments observing the decay of order include time-resolved spectroscopy experiments [205–207] in which the non-equilibrium relaxation dynamics can be observed directly and ultracold quantum gas experiments [54–58] where excited state lifetimes are so long that the relaxation can be directly followed in real-time [11].

In this project, we study the real-time decay of Néel order in the one-dimensional Fermi-Hubbard model

$$H = -t_0 \sum_{j,\sigma} (c_{j,\sigma}^\dagger c_{j+1,\sigma} + \text{h.c.}) + U \sum_j n_{j,\uparrow} n_{j,\downarrow}, \quad (5.1)$$

where t_0 is the hopping matrix element, U is the onsite repulsion, $c_{j,\sigma}$ annihilates an electron with spin σ and $n_{j,\sigma} = c_{j,\sigma}^\dagger c_{j,\sigma}$ measures the local number of electrons at site j . The initial state is the Néel state

$$|\psi_0\rangle = |\dots, \uparrow, \downarrow, \uparrow, \downarrow, \dots\rangle, \quad (5.2)$$

which is depicted in Fig. 5.1. This fixes the filling to $n = 1/2$. The motivation for this project is twofold: first, it extends previous studies [64] by incorporating charge dynamics

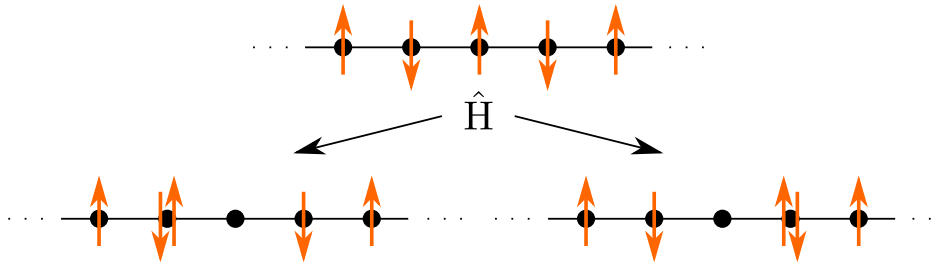


Figure 5.1: The initial setup of our system: the Néel state. A single application of the post-quench Hamiltonian H (Eq. (5.1)) onto the initial state creates doubly occupied sites.

and, second, it is related to two recent experiments on fermions in one dimension [59] and bosons in two dimensions [60]. We want to note here, that the same problem was studied in Ref. [63] which treats the extended Hubbard model.

More specifically, we use the infinite-system size time-evolving block decimation (iTEBD) algorithm [208] to compute the time dependence of the staggered magnetic moment $m_s(t) = (1/2L) \sum_j (-1)^j \langle n_{j,\uparrow} - n_{j,\downarrow} \rangle$, the double occupancy $d(t) = (1/L) \sum_j \langle n_{j,\uparrow} n_{j,\downarrow} \rangle$, nearest neighbor spin- and density-correlations and the von Neumann entropy $S_{vN} = -\text{tr}(\rho_A \ln(\rho_A))$ where ρ_A is the reduced density matrix of one half of the system. We find that the relevant time scale for the relaxation of the double occupancy and the nearest neighbor density correlations is set by the inverse of the hopping matrix element $1/t_0$ (Ref. [63] also finds this scaling for the double occupancy). For the staggered magnetization and nearest-neighbor spin correlations the relaxation is the slower the larger U/t_0 . We attribute this behavior to the existence of two distinct characteristic velocities: the spin- and charge velocities which are related to spin-charge separation at low energies [209]. We also find fingerprints of this separation in the time-dependence of the von Neumann entropy which, in global quantum quenches, is expected to increase linearly in time $S_{vN} \sim t_0 t$ [181, 210, 211]. For the time-dependence of the von Neumann entropy we find two regimes where the linear increase has a different slope: for short times it is governed by charge excitations $S_{vN} \sim t_0 t$ and for longer times we find $S_{vN} \sim t_0 t/U$ (the long-time result is also found in Ref. [63]) which suggests that spin excitations are relevant for which the energy scale is the magnetic exchange constant $J = 4t_0^2/U$ in the limit $U \gg t_0$ [64]. Ref. [63] also measures the charge and spin velocity by adding an excess electron to the initial state and observation of the particle density distribution function as a function of time and arrive at the same conclusion.

Also, we use exact diagonalization (ED) to calculate expectation values of the double occupancy in the diagonal and canonical ensemble. We compare the steady-state value of the double occupancy and the expectation values in the diagonal and canonical ensembles and find that diagonal ensemble average and steady-state values match closely. However, diagonal ensemble average and canonical expectation values are clearly different on the system sizes accessible to ED. We also compute the eigenstate expectation value spectrum for the double occupancy and find that it is a broad distribution in the energy which is in contrast to systems which are expected to thermalize in the framework of the eigenstate thermalization hypothesis [66, 183, 184]. This observation is similar to the behavior of eigenstate expectation values in integrable models describing interacting spinless fermions [186, 212].

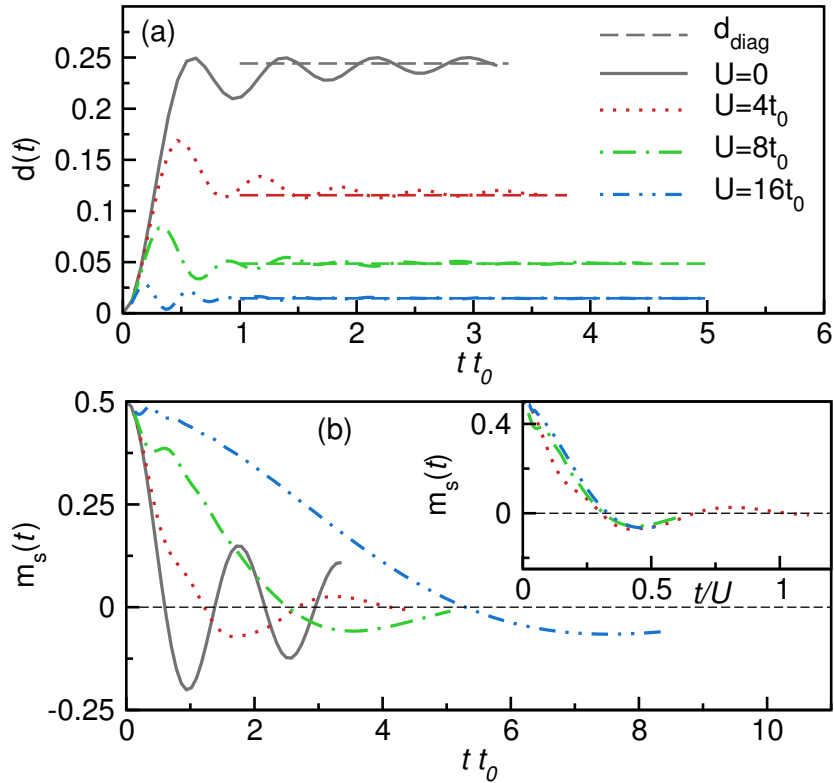


Figure 5.2: Post-quench dynamics of the double occupancy $d(t)$ (a) and staggered magnetization $m_s(t)$ (b) for different choices of interaction strength $U/t_0 = 0, 4, 8, 16$ (iTEBD data). The dashed lines in (a) represent the value from the diagonal ensemble d_{diag} defined in Eq. (5.7) for a system of size $L = 10$ (ED data). The inset in (b) shows $m_s(t)$ plotted against t/U for $U/t_0 > 0$.

5.1 Time evolution and characteristic time scales

Figure 5.2(a) and (b) illustrate the double occupancy $d(t)$ and the staggered magnetization $m_s(t)$ as a function of time calculated by the iTEBD method performed by Andreas Bauer [213]. The dashed lines in Fig. 5.2(a) show the expectation value in the diagonal ensemble Eq. (5.7) calculated by the present author. The relaxation of both quantities proceeds on different time scales. While $d(t)$ reaches the steady-state regime very quickly and almost independently of the value of U , $m_s(t)$ is clearly influenced by the interaction strength. Rescaling the time axis by $1/U$ collapses the data for $U \gtrsim 4t_0$ which is shown in the inset of Fig. 5.2(b). From this we conclude that the relaxation of double occupancy and staggered magnetization happens at the different time-scales $1/t_0$ and U . In terms of the staggered magnetization this suggests that the relaxation-time scale is set by the inverse of the magnetic exchange matrix element $J = 4t_0^2/U$ for large values of U/t_0 . Both quantities also exhibit coherent oscillations. The staggered magnetization is a superposition of two different kinds of oscillations which is most obvious in the case of $U/t_0 = 16$: for very short times an oscillation with a very small period is visible in addition to the oscillations with a much larger period that dominate the relaxation dynamics of $m_s(t)$. The short period oscillations in both $d(t)$

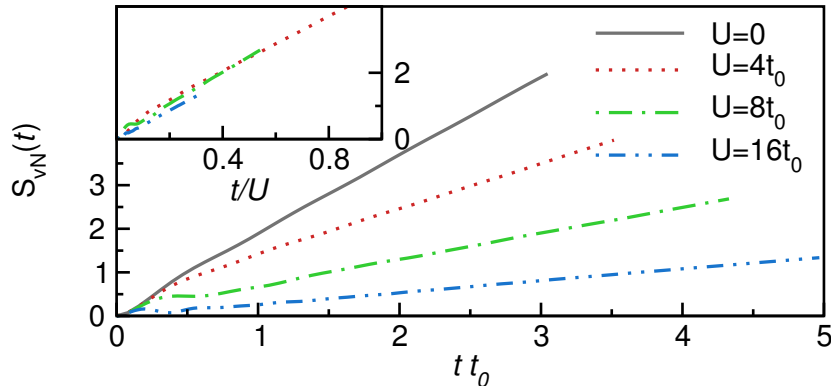


Figure 5.3: The post-quench dynamics of the von Neumann entropy of a central cut through the system $S_{vN}(t)$ for different values of interaction strength $U/t_0 = 0, 4, 8, 16$ (iTEBD data). The inset shows $S_{vN}(t)$ plotted versus t/U .

and $m_s(t)$ are captured by a short-time expansion of the time-evolution operator

$$d(t) = \frac{8t_0^2}{U^2} \sin^2\left(\frac{Ut}{2}\right), \quad (5.3)$$

$$m_s(t) = \frac{1}{2} - \frac{8t_0^2}{U^2} \sin^2\left(\frac{Ut}{2}\right). \quad (5.4)$$

The non-trivial long-period oscillation is found to have period $1/2J$ where $J = 4t_0^2/U$ which follows from the Heisenberg limit $U/t_0 \rightarrow \infty$ [64]. We find the same behavior for two-site charge and spin correlations [62].

The existence of two different relaxation-time scales also leads to an interesting time-evolution of the von Neumann entropy for a cut in the middle of the system. This is shown in Fig. 5.3 where again iTEBD results were computed by Andreas Bauer. The time-evolution can be divided into two distinct regimes where $S_{vN} \sim t$ with a different prefactor. For times $t \lesssim 0.5/t_0$ the prefactor is independent of U , while for $t \gtrsim 0.5/t_0$ the prefactor is clearly U -dependent. Again, rescaling the time-axis by $1/U$ leads to a collapse of the data which is shown in the inset of Fig. 5.3. The prefactor of the linear increase of the von Neumann entropy is related to the existence of gapless modes and given by the characteristic velocities [211]. To show that the U -dependent long-time dynamics of the von Neumann entropy is controlled by spin excitations we compare the prefactor of the linear increase in this regime to the spinon velocity v_s^{BA} which is known from the Bethe ansatz [214–216]

$$v_s^{\text{BA}} = 2t_0 \frac{I_1(2\pi t_0/U)}{I_0(2\pi t_0/U)}, \quad (5.5)$$

where I_0 and I_1 are modified Bessel functions of the first kind. This is shown in Fig. 5.4. Clearly, both c_s and v_s^{BA} have a very similar behavior on U/t_0 which confirms the assumption that the long-time dynamics of the entanglement entropy are controlled by spin excitations.

5.2 Time-averages of double occupancy

In this section we want to analyze the steady-state expectation value of the double occupancy in terms of thermalization. We concentrate the discussion on this quantity because it can be

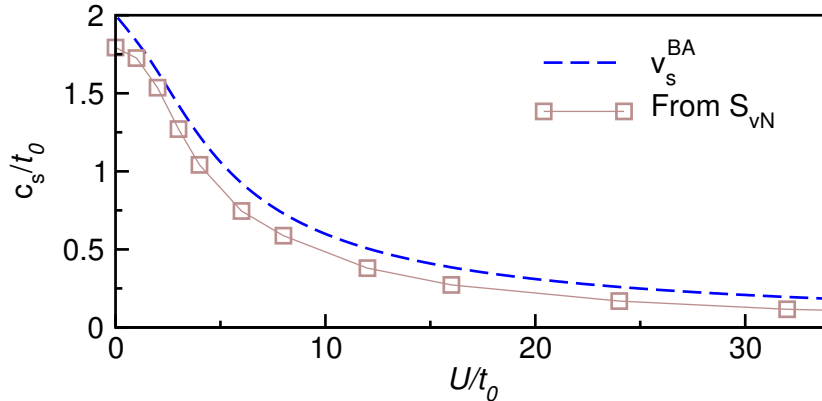


Figure 5.4: Characteristic velocities c_s extracted from the von Neumann entropy $S_{vN}(t)$ in the U -dependent time-regime $t \gtrsim 0.5/t_0$ plotted versus the exact values of the spin velocity known from the Bethe ansatz solution [214].

measured in quantum gas experiments [56, 217]. In Fig. 5.5(a) we compare the steady-state expectation value to the ground-state expectation value and the canonical expectation value (in a system of size $L = 10$) as a function of interaction strength U/t_0 . Generally, all three values behave the same. An interesting observation is that $\bar{d} > d_{gs}$ for the whole observed range of U/t_0 . This is unexpected given the anomalous behavior of the double occupancy as a function of temperature $d(T)$: it first decreases with increasing temperature for small temperatures and later changes monotony for larger temperatures [218, 219]. For very strong interaction $U/t_0 \rightarrow \infty$ the initial state is close to a ground state and, therefore, the system is described by a small temperature and, due to the non-zero t_0/U , the double occupancy is expected to obey $\bar{d} < d_{gs}$ for large values of U/t_0 . We therefore conclude that the $E = 0$ (initial) state always mixes in doublons from the upper Hubbard band. This is confirmed by the following discussion in Sec. 5.3.

We further compare the expectation value in the diagonal and the canonical ensembles in Fig. 5.5(b). Here, we show the relative difference between the two values

$$\Delta d_{\text{rel}} = (d_{\text{diag}} - d_{\text{can}})/d_{\text{diag}}. \quad (5.6)$$

The system is integrable and, therefore, it is not surprising that the diagonal and canonical ensemble averages deviate. We also studied the relative distance as a function of system size for the sizes accessible to ED which showed that it does not get smaller with increasing system size and, thus, we do not observe thermalization. Nevertheless, the behavior of the three values is very similar.

5.3 Connection to eigenstate thermalization hypothesis

In this section we make the connection to the eigenstate thermalization hypothesis (ETH) [66, 183, 184] – a popular framework for understanding thermalization in closed quantum systems. The long-time behavior of observables depends on both, the initial state distribution in the eigenstates of the post-quench Hamiltonian and the eigenstate expectation value spectrum of

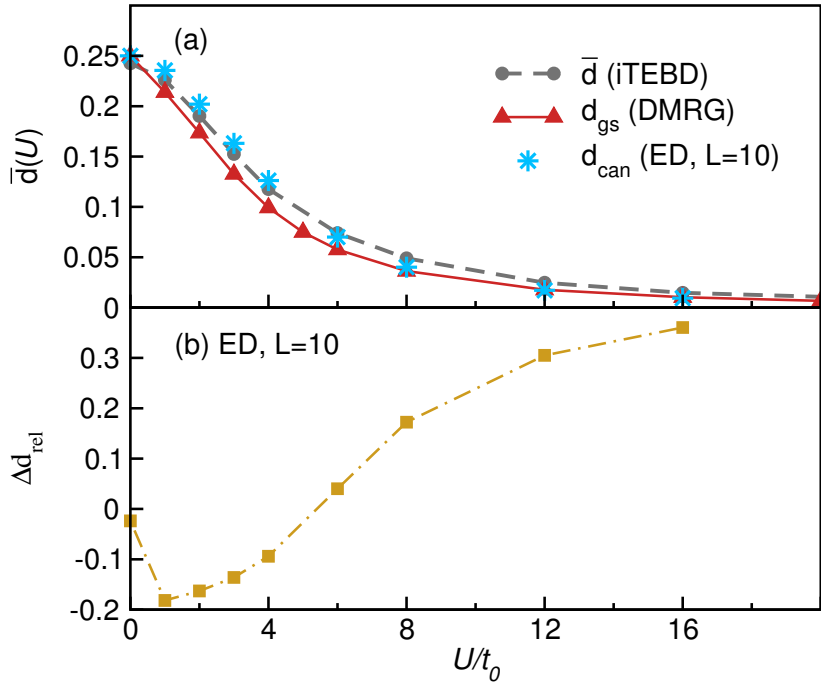


Figure 5.5: (a) Time averages (circles) of the double occupancy as a function of U/t_0 (iTEBD). For comparison, the ground-state expectation value d_{gs} (DMRG, $L = 64$) and the expectation value in the canonical ensemble d_{can} (ED, $L = 10$) are also included. (b) Relative distance between canonical and diagonal ensemble average $\Delta d_{\text{rel}} = (d_{\text{diag}} - d_{\text{can}})/d_{\text{diag}}$.

the observable

$$\langle \hat{O} \rangle_{\text{diag}} = \sum_n |c_n|^2 \langle \psi_n | \hat{O} | \psi_n \rangle. \quad (5.7)$$

Thermalization means that the diagonal ensemble average Eq. (5.7) has to be equal to an ensemble average in the thermodynamic limit. Since our system is closed (energy, number of particles and volume are conserved) we take the microcanonical ensemble as a reference

$$\sum_n |c_n|^2 \langle \psi_n | \hat{O} | \psi_n \rangle \stackrel{!}{=} \frac{1}{\mathcal{N}} \sum_{E-\Delta E < E_n < E+\Delta E} \langle \psi_n | \hat{O} | \psi_n \rangle, \quad (5.8)$$

where the left side of the equation is the diagonal ensemble average and the right side is the microcanonical ensemble average with \mathcal{N} a normalization constant. The ETH states that a system thermalizes if the c_n are strongly peaked and narrow in an energy region where the eigenstate expectation value spectrum $\langle \psi_n | \hat{O} | \psi_n \rangle$ is a very narrow distribution and thus a function of the energy $f(E)$ only in the thermodynamic limit [66, 182]. Figure 5.6 shows both of those quantities, the c_n and $\langle n | \hat{O} | n \rangle$, for four choices of the interaction strength $U/t_0 = 0$ (a), $U/t_0 = 4$ (b), $U/t_0 = 8$ (c) and $U/t_0 = 16$ (d). We find a band structure in the distribution of post-quench expectation values which is inherited from the $U/t_0 \rightarrow \infty$ limit for non-zero interaction strength (Figs. 5.6(b)-(d)). The $E = 0$ state is located at the high-energy edge of the lowest band. This state is at the same time the one with lowest double occupancy and we see that lowering the energy means increasing the double occupancy. Since the initial state is

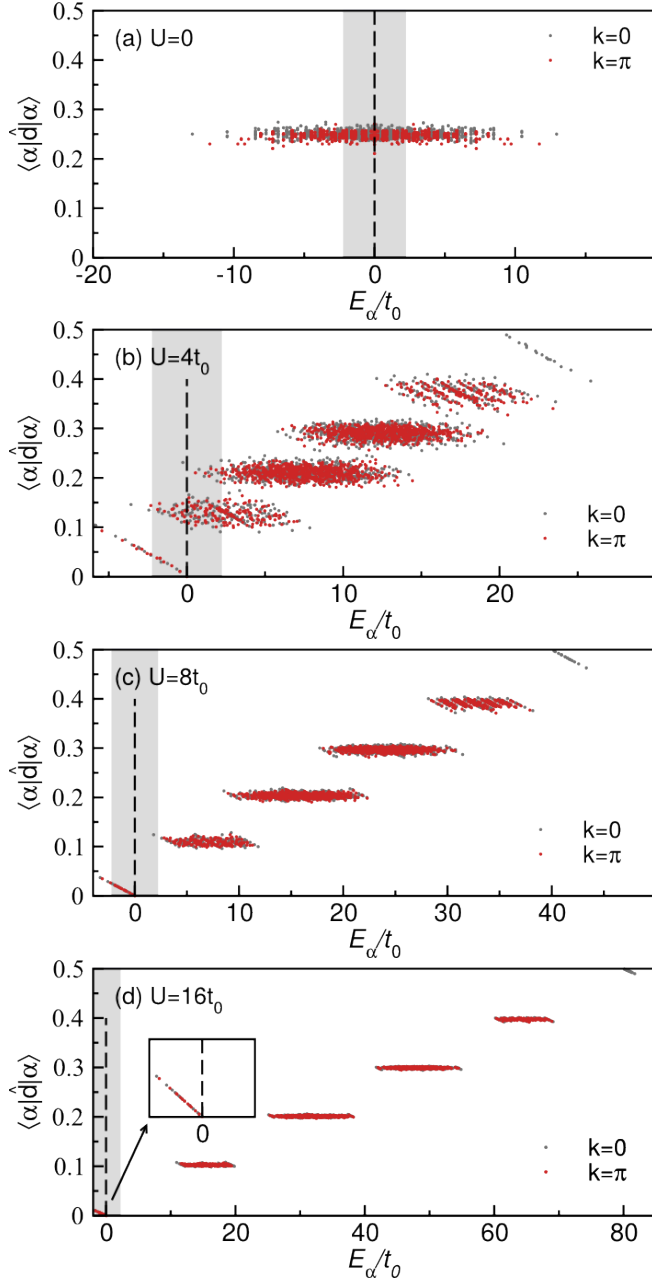


Figure 5.6: Post-quench eigenstate expectation value spectrum for the double occupancy for the interaction strengths $U/t_0 = 0, 4, 8, 16$ (a)-(d) calculated using ED in a system with size $L = 10$. The vertical dashed lines mark the quench energy $E = 0$ for our initial state and the grey shaded area behind it shows the width $\sigma_{\text{diag}} = \sqrt{\langle \psi_0 | H^2 | \psi_0 \rangle}$. The inset in (d) shows a magnified version of the lowest band. Our initial state lives in the $k = 0, \pi$ quasimomentum-subspaces.

not an exact eigenstate of the post-quench Hamiltonian, it has a possibly narrow distribution in the states with energies around $E = 0$. Since the $E = 0$ state is located right at the edge the initial state has to mix in states with a double occupancy from higher bands and this

is the reason why we see $\bar{d} > d_{gs}$ in Fig. 5.5. Due to the band structure the distribution of post-quench expectation values is not a well-defined function of the energy and we therefore do not expect the system to thermalize in the sense of the ETH in the intermediate to strong interaction regime.

5.4 Summary

In this chapter we have presented results on the relaxation dynamics in the one-dimensional Fermi-Hubbard model starting from a perfect Néel state as a function of the interaction strength U/t_0 . As Ref. [63] we find different velocities related to charge and spin quantities. As a main result, we find evidence that the relaxation dynamics of spin-related quantities like staggered magnetization, nearest-neighbor spin correlations as well as of the von Neumann entropy are, in the long time regime, controlled by spin excitations: The slope of the von Neumann entropy $S_{vN} = c_s t$ is very similar to the exact spinon velocity known from the Bethe ansatz. This separation of time scales for double occupancy versus staggered magnetization could be accessible in state-of-the-art quantum gas experiments. We further demonstrated that the time averages of the double occupancy are different from the expectation values in the canonical ensemble. Nonetheless, both quantities exhibit the same qualitative dependence on U/t_0 . Finally, we made a connection to the eigenstate thermalization hypothesis by showing that the eigenstate expectation values of the double occupancy are, in general, broadly distributed with no well-defined dependence on energy only, characteristic for an integrable one-dimensional system.

Chapter 6

Many-body localization in a one-dimensional system of spinless Fermions with attractive interactions

Non-interacting fermions in a one-dimensional disordered system exhibit Anderson localization [71] which means that the system is a perfect insulator and fails to thermalize. A paradigmatic Hamiltonian is

$$H = -t \sum_j (c_j^\dagger c_{j+1} + \text{h.c.}) + \frac{W}{2} \sum_j w_j n_j, \quad (6.1)$$

where c_j is a fermionic annihilation operator, $n_j = c_j^\dagger c_j$ measures the local particle density and the $w_j \in [-1, 1]$ are chosen randomly to get a random potential $Ww_j/2$ on each site. The reason for this behavior is the localized nature of the single-particle eigenstates of the Hamiltonian: Depending on the strength of the disorder potential a single-particle wavefunction $\phi_\alpha(\vec{r})$ of an eigenstate with energy E_α can be classified as localized or extended [68]

$$|\phi_\alpha(\vec{r})|^2 \propto \begin{cases} \frac{1}{\chi_{\text{loc}}^D} e^{-\frac{|\vec{r}-\rho_\alpha|}{\chi_{\text{loc}}}} & \text{localized,} \\ \frac{1}{L} & \text{extended,} \end{cases} \quad (6.2)$$

where χ_{loc} is the localization length which depends on the energy E_α of the state ϕ_α , L is the size of the system, D is the spatial dimensionality of the system and ρ_α denotes the point of maximum amplitude of the state. For one-dimensional systems an arbitrarily small disorder leads to the localization of all eigenstates of the system and a particle being located at one part of the system will never delocalize over the full length of the system and, thus, the system is a perfect insulator. The occupation number n_α of the single-particle eigenstate ϕ_α of the Hamiltonian can be seen as a local integral of motion [220] since

$$H = \sum_\alpha \epsilon_\alpha n_\alpha. \quad (6.3)$$

These properties persist to the more general case of non-vanishing inter-particle interactions [67, 68]. In the case of finite energy densities ($T \neq 0$), one speaks of many-body localization

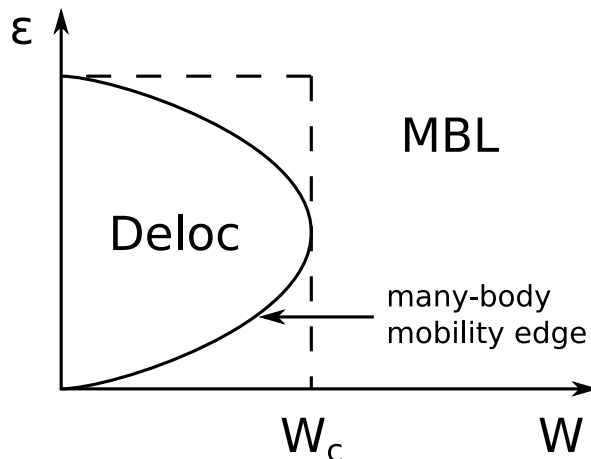


Figure 6.1: A sketch of the MBL phase transition in an interacting system [72]: With increasing disorder strength W more eigenstates of the Hamiltonian transition into the MBL phase. At a critical disorder strength W_c the system is completely in the MBL phase for every temperature. For a given disorder W the mobility edge is defined as the smallest energy density where the system is still in the delocalized phase.

(MBL). With a random disordered potential the Hamiltonian has L quasi-local conserved quantities that spatially extend over a small part of the system [220, 221]. A topic of high interest is the phase transition from an MBL phase to a delocalized phase [222–227]. While any finite disorder in a one-dimensional system of non-interacting electrons leads to Anderson localization the transition to an MBL phase can, in principle, depend on the strength of the disorder and the energy density in the respective eigenstate of the Hamiltonian. In fact, this transition is not fully understood and there is an ongoing discussion [72, 75, 228–230] if such a many-body mobility edge – a region of the phase diagram in the energy density - disorder plane where a part of the eigenstates feature an MBL phase while others are in a delocalized phase – actually exists. The paradigmatic phase diagram for the MBL-delocalized transition is sketched in Fig. 6.1. At the left edge (small disorder) the system is in a delocalized phase and with increasing disorder strength a larger amount of eigenstates transitions to an MBL phase. When reaching a critical disorder strength W_c all eigenstates are localized. The dashed lines show an alternative scenario without a mobility edge: at a critical W_c all eigenstates are in an MBL phase. The MBL transition is also the only known phase transition where the entanglement scaling is fundamentally different in the two phases: the ergodic phase features a volume law scaling while in the MBL phase all eigenstates feature an area law scaling [228, 231, 232].

The MBL phase exists in closed isolated systems which are hard to realize in solid state systems because of the omnipresent coupling of electrons to lattice degrees of freedom. However, ultra-cold quantum gases and systems of trapped ions realize a closed quantum system to a good approximation and allow the investigation of the effect of disorder in many-body systems in the presence of interactions at elevated energy densities [233–238]. Optical lattice experiments with fermions in 1D [233] and strongly interacting bosons in 2D [236] provide evidence that MBL is realized and that the transition can be probed. For a smaller number of degrees of freedom similar conclusions were reached in trapped ion experiments that realize

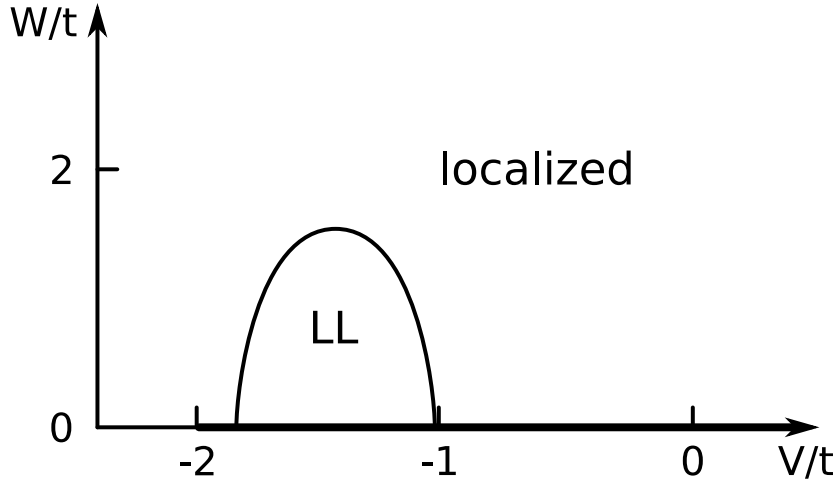


Figure 6.2: Sketch of the phase diagram of the Hamiltonian Eq. 6.6 [74]. For low disorder $W < W_c$ the ground state displays a small region in interaction strength V bounded by $-2t < V < -t$ where it is in a Luttinger-liquid phase. For all other choices of interaction, the system is in a localized phase. In a system with no disorder the groundstate is a Luttinger liquid in the region $-2t < W < 2t$.

a spin-1/2 chain [237].

The quasi-local conserved quantities in the MBL phase can be related to the existence of localized quasi-particles that consist of a localized particle dressed by particle-hole pairs [68, 239]. The existence of such quasiparticles suggests a close analogy of the MBL phase to a zero-temperature Fermi liquid where the quasi-particles are physical electrons dressed with particle-hole pairs. A Fermi liquid at $T = 0$ displays a finite discontinuity at the Fermi edge $0 < \Delta n_k < 1$ which is related to the quasiparticle weight Z_k [65, 240]. It was shown in a recent work [75] that a similar discontinuity is present in the occupation number spectrum of the one-particle density matrix (OPDM) in the MBL phase. The diagonalization of the OPDM – here, in individual many-body eigenstates – yields a basis set in the single-particle subspace and the occupations

$$\rho_{i,j}^{(1)} = \langle \psi_n | c_i^\dagger c_j | \psi_n \rangle, \quad (6.4)$$

$$\rho^{(1)} | \phi_\alpha \rangle = n_\alpha | \phi_\alpha \rangle, \quad (6.5)$$

where $|\phi_\alpha\rangle$ are eigenstates of the OPDM and n_α are their occupations. For non-interacting particles (Anderson insulator), every many-body eigenstate is a Slater determinant and the occupation spectrum (after reordering) is a step function $n_\alpha = 1 - \Theta(\alpha - N)$ where N is the number of particles in the system and $\alpha \geq 1$. This holds irrespective of the disorder strength. In the MBL phase, however, the occupations start to deviate from zero and one in the vicinity of $\alpha = N$ and one observes a discontinuity similar to the one found in the Fermi liquid [75]. This is interpreted as indicating the existence of quasi particles in the MBL phase at all $\epsilon > 0$.

In this project we investigate the delocalization-localization (MBL) transition in a system of spinless fermions with attractive nearest neighbor interactions [74]. To be precise, we

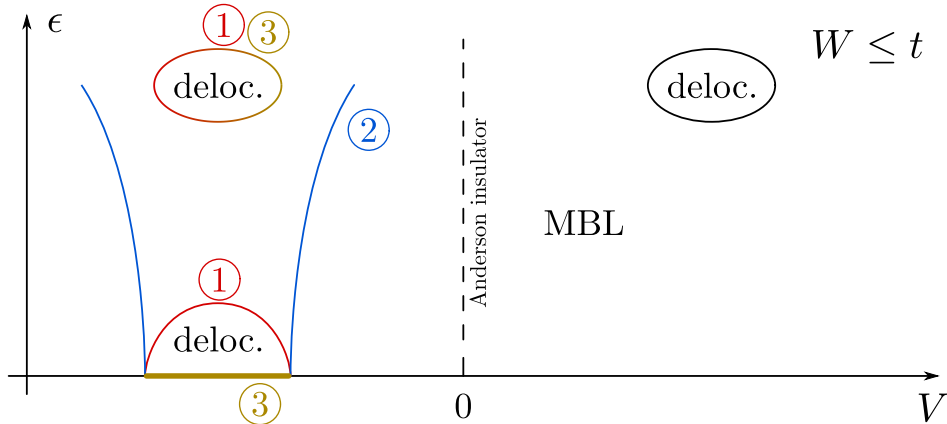


Figure 6.3: A sketch of the possible scenarios of the continuation of the ground-state phase diagram $\epsilon = 0$ to finite energy density. In the first scenario the delocalized phase survives up to a finite energy density forming an inverted many-body mobility edge. In the second scenario the delocalized phase extends into all eigenstates which leads to a finite conductivity at all temperatures. In the third scenario the delocalized phase exists only in the ground state and at high energy density.

consider a system described by the Hamiltonian

$$H = -t \sum_j (c_j^\dagger c_{j+1} + \text{h.c.}) + V \sum_j n_j n_{j+1} + \frac{W}{2} \sum_j w_j n_j, \quad (6.6)$$

where c_j annihilates a fermion and $n_j = c_j^\dagger c_j$ measures the local particle number. The local disorder w_j is taken randomly from a flat distribution $w_j \in [-1, 1]$. It was shown [73, 74] that, for weak disorder, the ground state features a delocalized phase in the attractive regime $V < 0$ of the model. A sketch of the corresponding ground state phase diagram is shown in Fig. 6.2. Qualitatively, the existence of this phase can be explained by the competition between the disorder, hopping and attractive interaction terms. For vanishing interaction strength $V = 0$ the system is an Anderson insulator for any finite non-vanishing disorder strength. As the attractive interaction grows particles can form Cooper pairs which leads to a Luttinger liquid state [65]. Stronger attractive interaction again localizes these pairs. The delocalized region decreases with increasing disorder from both sides. The disorder aids the attractive interaction term by pinning the particles to a smaller region by decreasing the length over which fermions delocalize which enhances the effect of the interaction term and thus leads to the decrease of the delocalized region from both sides.

We study the behavior of two quantities in the vicinity of this phase transition: The largest difference between two adjacent eigenvalues of the one-particle density matrix (OPDM) Eq. (6.5) as well as the von Neumann entropy for a cut in the middle of the system. As discussed above, the eigenvalues of the OPDM feature a steep step in the middle of the spectrum in case of an MBL phase and a much smaller gap for a delocalized phase [75] that vanishes as $L \rightarrow \infty$. The delocalized phase and MBL phase feature a different scaling of entanglement entropy: a volume law in the delocalized phase and an area law in the MBL phase which should be visible in the half-cut von Neumann entropy. Here, we study the von Neumann entropy of the groundstate where the Luttinger-liquid phase features an area-law

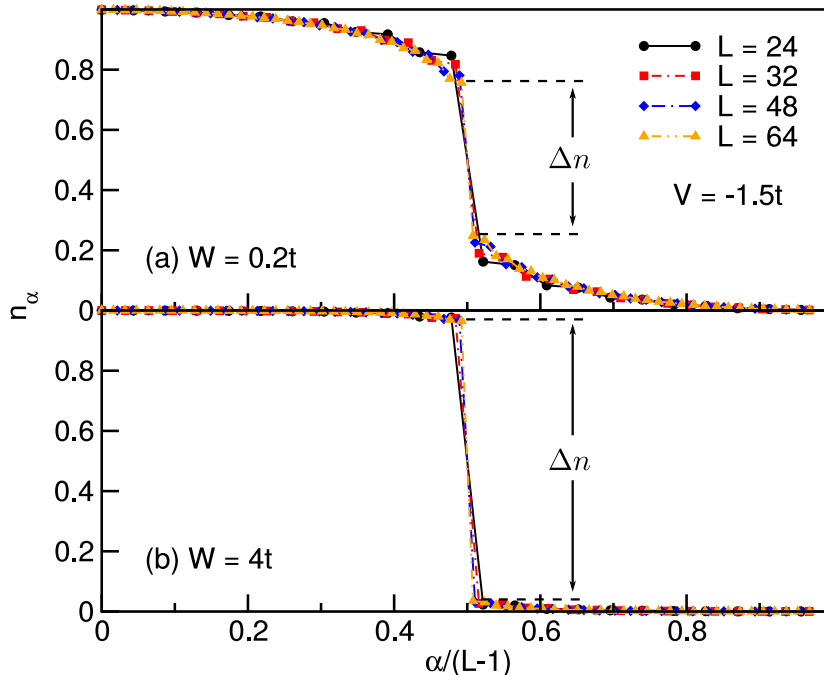


Figure 6.5: The OPDM eigenspectrum n_α for (a) weak disorder potential $W = 0.2t$ and (b) strong disorder potential $W = 4t$ at interaction strength $V = -1.5t$ for a system of size $L = 64$ (DMRG data). For a weak disordered potential (a) the size of the gap Δn decreases with increasing system size while for a strong disorder potential (b) the size of the gap is independent of system size.

exact boundary of this region depends on the value of the disorder strength W) where the ground state is in a Luttinger-liquid phase.

Figure 6.5 shows the eigenspectrum of the OPDM n_α for weak and strong disorder $W = 0.2t, 4t$ in systems of sizes $L = 24, 32, 48, 64$ with interaction strength $V = -1.5t$. For $W = 0.2t$ the system is well inside the Luttinger-liquid phase shown in Fig. 6.2. In this case one expects a Δn in the eigenvalue spectrum that decreases as system size is increased. Figure 6.5(a) supports this expectation and shows a gap that is getting smaller with increasing system size. Figure 6.5(b) shows the OPDM eigenspectrum for a strong disorder $W = 4t$. In this case we expect a distribution close to a step function that does not change with system size which is clearly supported by the data.

Figure 6.6 shows Δn as a function of disorder strength W and interaction strength V . The data show a clear minimum in the vicinity of $V = -2t$ that fades as disorder is increased. We compare the data to results from Ref. [74] (+ symbols) which display the location of the delocalized phase in their measurements and find that the two regions mostly overlap.

We analyze the behavior of Δn for two choices of the disorder strength $W = 0.2t$ (weak disorder) and $W = 4t$ (strong disorder). When tuning the interaction V over the region $-2t < V < -t$ for weak disorder $W = 0.2t$ one crosses two phase transitions: one in the vicinity of $V \approx -1.6t$ and one in the vicinity of $V \approx -t$ (see Fig. 6.2). We expect three regimes in both quantities: a localized phase in the range $V \lesssim -2t$, a delocalized phase at $-2t \lesssim V \lesssim -t$ and another localized phase at $V \gtrsim -t$. In the case of a localized phase we

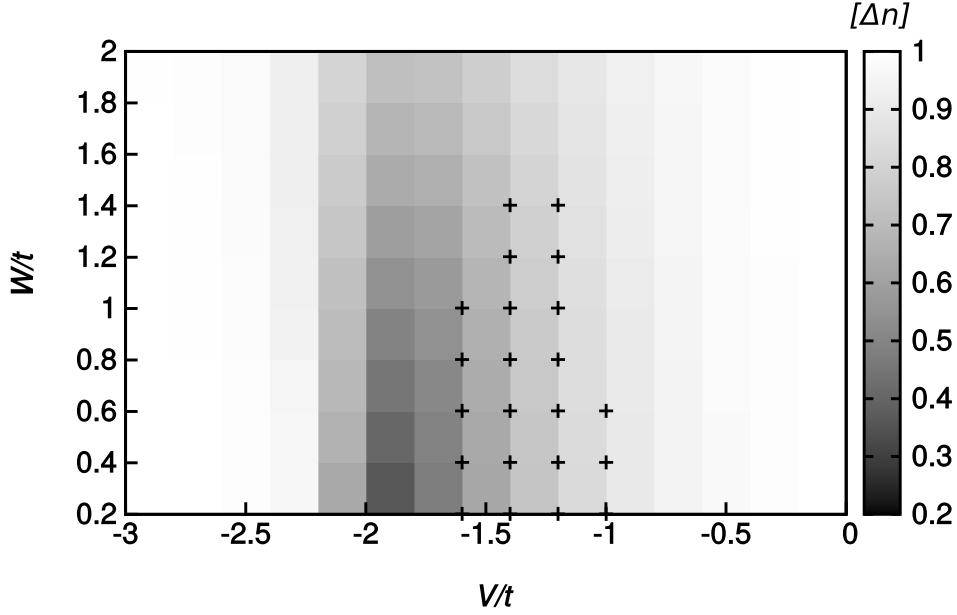


Figure 6.6: The difference in eigenvalues of the OPDM Δn (color) compared to results from Ref. [74] (+ signs) as a function of the interaction strength V and disorder W for a system with hopping parameter set to $t = 1$ and $L = 32$ (DMRG data). A clear feature emerges in this quantity in the vicinity of the domain where the system is in a delocalized phase as found in [74].

expect a non-vanishing gap in the OPDM eigenspectrum close to unity $\Delta n \approx 1$ while for the delocalized phase we expect Luttinger-liquid like behavior $\Delta n \rightarrow 0$ as $L \rightarrow \infty$. For the half-cut von Neumann entropy we expect an area-law scaling $S_{vN} \sim \text{const}$ in the localized regimes because of the localized nature of the excitations and an area-law scaling with logarithmic corrections $S_{vN} \sim \log(L)$ in the Luttinger-liquid phase because the system is in the ground state [241]. Figure 6.7(a) and (b) show the OPDM-eigenvalue difference Δn and the half-cut von Neumann entropy S_{vN} for a system with weak disorder $W = 0.2t$ as a function of V . Both quantities show a peak at $V \approx -2t$ that gets sharper with increasing system size.

The OPDM eigenvalue difference in the weak disorder case $W = 0.2t$ (Fig. 6.7(a)) takes the value $\Delta n = 1$ at $V = 0$ independent of system size which is expected since, at this point, we have free particles which display $\Delta n = 1$ in the disordered phase because the system is an Anderson insulator (it would give the same value without disorder because free particle eigenstates are also eigenstates of the OPDM). For interactions $V < -2t$ we find a large Δn close to the value $\Delta n = 1$ that does not change as system size is increased which is expected in a completely localized phase. In the close vicinity of $V = -2t$ we find a minimum in Δn which depends strongly on the system size. The inset in Fig. 6.7(a) shows the value of Δn at the minimum of the peak at $V_c \approx -1.96875t$ and also at the value $V = 2t$ of the interaction strength versus system size. Naive extrapolation using the function $f(L) = a + b/L + c/L^2$ gives an estimate of a value close to zero for the minimum position and a non-zero value at $V = 2t$ demonstrating a clear difference between those two points. The dependence on system size extends up to a value close to $V = 0$ on both, attractively and repulsively interacting, sides. Comparison to the case with no disorder (dashed line in Fig. 6.7(a)) shows that the two

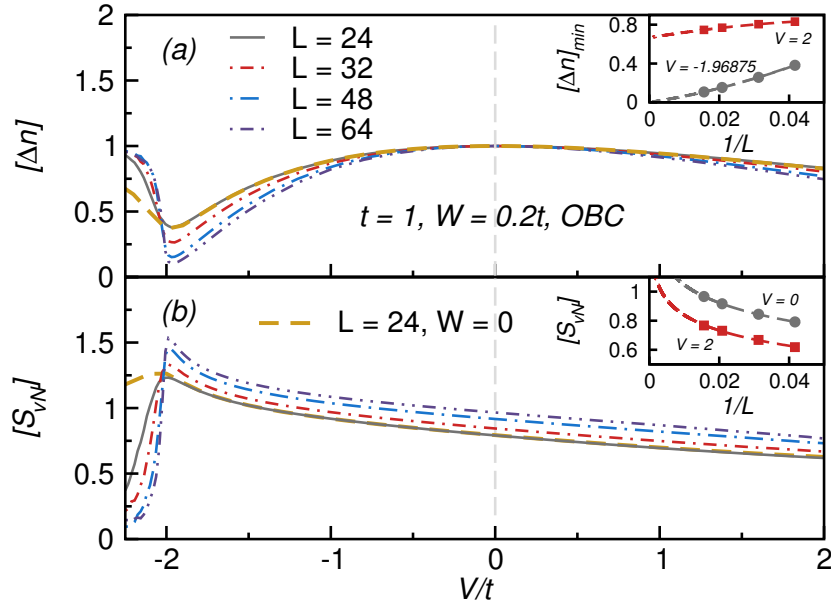


Figure 6.7: (a) The difference in eigenvalues of the OPDM Δn as a function of the interaction strength V for different systems with sizes $L = 24, 32, 48, 64$ and parameters $t = 1, W = 0.2t$. A clear drop in this quantity appears for values of V in the vicinity of the region where the system is in a delocalized phase. The inset shows an extrapolation in $1/L$ to infinite system size for the minimal value at $V = -1.96875t$ and the right edge of the measured spectrum $V = 2t$. For the minimum the used simple extrapolation indicates a drop to zero for $L \rightarrow \infty$ while for the value $V = 2t$ it extrapolates to a finite value. As a fitting function $f(L) = a_0 + a_1/L + a_2/L^2$ was chosen which gives the infinite system extrapolation in a_0 . (b) Half-cut entanglement entropy versus V for $L = 24, 32, 48, 64$.

cases match for all values $V \gtrsim V_c$ and the only difference is in the behavior to the left of V_c where the no-disorder case has a slope that is less steep with decreasing V . This suggests that, for the very low disorder strength $W = 0.2t$, our system sizes are smaller than the localization length $L \leq 64 \leq \chi_{\text{loc}}$ and localization sets in only in the strong attractive interaction regime $V \lesssim 2t$.

The half-cut von Neumann entropy (Fig. 6.7(b)) is a monotonically decreasing function of the interaction strength in the region $V > V_c$. Importantly, it clearly depends on system size in this region. We see that for $V < V_c$ it quickly approaches a small value with decreasing interaction strength similar to the behavior of Δn . The inset in Fig. 6.7(b) shows the value of S_{vN} at $V = 0, 2t$ for the system sizes $L = 24, 32, 48, 64$. For a system in the MBL phase one expects that the half-cut von Neumann entropy saturates at a finite value due to the finite localization length in all many-body eigenstates provided that the system is large enough to support the full correlation length. Clearly, saturation does not happen for the system sizes observed here. In a Luttinger-liquid phase one expects the von Neumann entropy to scale logarithmic with the system size [241]

$$S_{vN}(L) = \frac{c}{6} \ln\left(\frac{L}{\pi}\right) + s_1, \quad (6.7)$$

where c is called the conformal charge and s_1 is a non-universal constant. The data at the

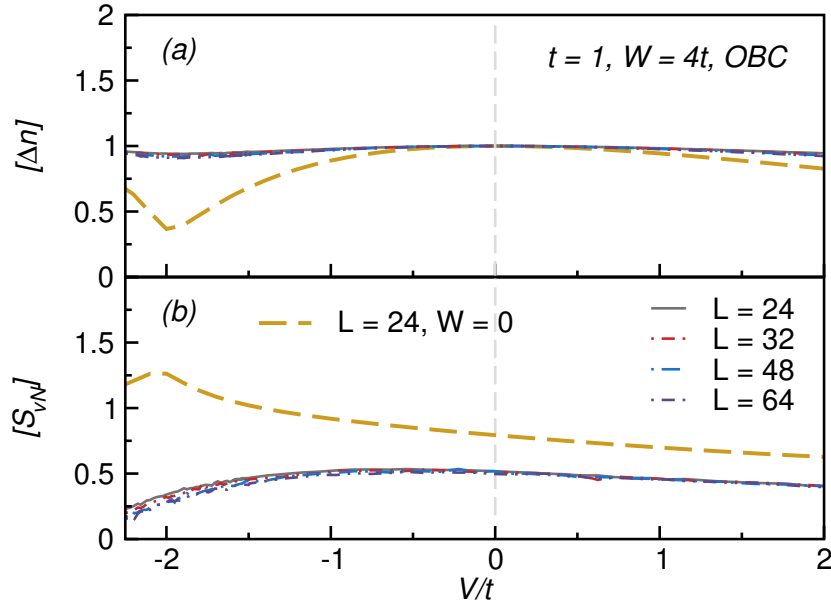


Figure 6.8: (a) The difference in eigenvalues of the OPDM Δn as a function of the interaction strength V for different systems with sizes $L = 24, 32, 48, 64$ and strong disorder $t = 1, W = 4t$. (b) Half-cut entanglement entropy versus V for $L = 24, 32, 48, 64$.

points $V = 0, 2t$ are fitted using Eq. (6.7) which shows perfect agreement for both values of the interaction. This suggests that at the small disorder $W = 0.2t$ the localization length is longer than our observed systems. For values $V < V_c$ the von Neumann entropy settles to a value close to zero for all observed system sizes. We also compare the data of the von Neumann entropy to a system without disorder (dashed line in Fig. 6.7). Again, we find perfect agreement between the disordered and non-disordered systems in this quantity for $V > V_c$ while for $V < V_c$ the von Neumann entropy does not drop to a value close to zero as suddenly as the data for the disordered system. Again, this is evidence that the disorder strength $W = 0.2t$ is too weak to observe effects of localization in the small attractive interaction region $V > -t$.

The variation of Δn and S_{vN} with the interaction strength V in the opposite limit of strong disorder $W = 4t$ is shown in Fig. 6.8. In this case we expect a uniform behavior of both quantities over the whole observed region $-2.25t \leq V \leq 2t$ because disorder is large enough to eradicate the delocalized region. The difference in OPDM eigenvalues is expected to be close to one and the half-cut von Neumann entropy is expected to obey an area law: no logarithmic corrections as system size is changed. Figure 6.8(a) shows Δn and confirms the expectation: the OPDM eigenspectrum is close to a step function and almost independent of the choice of V and independent of system size. The half-cut von Neumann entropy is presented in Fig. 6.8(b). As expected, it saturates at a finite value for most observed values of V . For values of the interaction strength $V \lesssim -1.5t$ the entropy still decreases with increasing system size but seems to saturate with system sizes $L = 48$ and $L = 64$.

6.3 Summary and Outlook

We studied the drop in the OPDM eigenspectrum and the half-cut von Neumann entropy as a function of disorder strength and interaction strength in a system of spinless fermions with attractive interaction in the ground state. For non-zero disorder strength the groundstate phase diagram in the $W - V$ -plane contains two distinct phases [74]: a delocalized phase for $W \lesssim 1.5t$ and $-2t \lesssim V \lesssim -t$ as well as a localized phase for all other choices of W and V . We found that the difference in the OPDM eigenspectrum Δn as a function of W and V resembles the phase diagram found by Ref. [74]. We also measured Δn as a function of V for weak $W = 0.2t$ and strong disorder $W = 4t$. In the weak-disorder case we find clear features in both, Δn and S_{vN} , at the left phase boundary $V \approx 2t$. For $-2t \lesssim V \leq 2t$ we find Luttinger-liquid behavior which suggests that our system sizes are not large enough to see a localized phase in the region $V \gtrsim -1t$ for small disorder, presumably due to a localization length that is larger than our system sizes. For strong disorder $W = 4t$ we find the expected behavior in a localized phase for both quantities: A step function in the OPDM eigenspectrum and a saturation in the half-cut von Neumann entropy due to area-law scaling.

An open question is what happens when the electrons couple to phonons. So far, this question has been posed in the case of the Anderson insulator and it was shown [242, 243] that this coupling leads to delocalization [68] where phonons assist the electrons and allow them to hop between localized states. It is thus an open question if the same holds in the MBL case. This would also be a nice application of the DMRG3S-LBO method (Chap. 1) which is constructed to tackle models with a large local dimension.

Conclusion

In this thesis we have introduced numerical methods for the efficient simulation of quantum many-body systems with bosonic degrees of freedom in equilibrium and out of equilibrium. In detail, we described Krylov space time evolution in a limited functional space and adapted it to work for periodic boundary conditions. For the simulation of the relaxation dynamics of a highly excited charge carrier under the Holstein Hamiltonian we showed that this method is superior to both, standard Krylov space time evolution and the standard time-evolving block decimation methods.

We also discussed how to implement an intermediate step into the time-evolving block decimation method that truncates in the local degrees of freedom and sets up the state in this truncated basis to reduce the computational cost of the most expensive step – the singular value decomposition of a local two-site tensor – by either an order in the bond dimension m or by $(d/d_O)^3$ depending on the state where d_O is the dimension of the truncated local basis [47].

For the computation of the groundstate we introduced a new algorithm that combines the recently developed strictly-single-site density matrix renormalization group algorithm [38] with the concept of local basis optimization [37] which, additionally to the bond update, also optimizes the local (physical) degrees of freedom. The strictly single site DMRG algorithm is an algorithmic improvement over the standard two-site DMRG algorithm because it scales linearly in the local basis dimension instead of with the third power. The local basis optimization scheme reduces the local dimension by truncation of the local degrees of freedom in the so-called optimal-mode basis [36]. The optimized algorithm reduces the scaling from linear in the local dimension d to linear in the optimized local dimension d_O .

The efficiency of the local basis optimization depends on how many optimal-mode states need to be kept in order to reach a good precision. This information is contained in the weight spectrum w_α of those states. We studied the optimal-mode weight spectrum in the groundstate of the Holstein model, the Hubbard-Holstein model and the Bose-Bose resonance model for different choices of model parameters and found that the optimal-mode basis is beneficial in all those cases.

We demonstrated the efficiency of the method on the examples of the Holstein model and the Hubbard-Holstein model. For both models we found a reduction of the computational effort that scales as expected.

We also studied the optimal-mode structure and the local von Neumann entropy, which is a measure of how fast optimal-mode weights decay as a function of their index, in the groundstate and during time evolution as a function of model parameters and time. As a groundstate problem with non-trivial optimal modes we considered the Bose-Bose resonance model which describes bosonic particles that interact via Feshbach interaction allowing them to form molecules. This model has a rich phase diagram [43] and we showed that the optimal-mode structure, as well as, the local von Neumann entropy show features in the vicinity of

the phase boundaries and concluded that the local reduced density matrix in this model is sensitive to phase transitions. This extends earlier work [45, 46] where spin- and fermionic model were considered.

We studied the dynamics of optimal modes and their weights as a function of time, both, in the Holstein model and the BBRM. In both problems we found that the von Neumann entropy relaxes to a steady-state value quickly while it is quasi-constant for the time after this relaxation. Possible oscillatory dynamics of local observables in the steady state regime are thus reflected in the structure of optimal modes which means that, for numerical applications, they need to be updated as time progresses.

The Holstein model is a good testing ground for numerical methods but also describes the interaction between an electron and local optical phonons. We studied the relaxation of a highly excited charge carrier coupled to quantum phonons by monitoring the three observables, kinetic energy of the charge carrier, phonon energy and coupling energy in all coupling regimes. Most notably, we found two distinct regimes depending on the choice of quench parameters: a real net energy transfer from the electron to phonons only happens in the adiabatic case where a single phonon costs less energy than the bandwidth, which is the maximum energy that the electron can give away. For weak electron-phonon coupling we also showed that the relaxation dynamics can be described by a Boltzmann equation which allowed an analytical expression for the relaxation time that depends on all parameters of the model. In the anti-adiabatic case or strong coupling we found coherent oscillations in the phonon energy which are well described by a single-site model.

We also studied thermalization in closed quantum systems. In detail, we found in the observed quenches in the BBRM that optimal mode structure and local von Neumann entropy coincide with expectations from the canonical ensemble which means that the local reduced density matrix thermalizes in this case.

Also, we studied the temporal decay of Néel order in the Fermi-Hubbard model and found evidence that the relaxation dynamics of spin-related quantities like staggered magnetization and nearest-neighbor spin correlations as well as the von Neumann entropy are, in the long-time regime, controlled by spin excitations. Further, we demonstrated that the time-averages of the double occupancy, even though similar, are different from the expectation values in the canonical ensemble.

Finally, we study spinless attractively interacting fermions in a disordered potential. We calculated the largest difference in the one-particle density matrix eigenvalues and the half-cut von Neumann entropy in the groundstate of this model as a function of interaction for different strengths of disorder. We found that those two quantities show a localized phase only for strong attractive interaction strength for our system sizes. For strong disorder we found that the system is in a localized phase for all choices of interaction strength as expected.

The DMRG3S-LBO method we developed is an improvement for groundstate calculations of the Holstein model. Our study of the behavior of the optimal-mode weight spectrum in the BBRM showed that a local basis optimization might also be beneficial for this problem. This would show that the idea of optimal modes also generalizes to non-phononic problems. It would also be interesting to study the effect of a phonon dispersion and additional on-site electronic repulsion on the structure of the optimal modes also for finite fillings in the Hubbard-Holstein model. In the polaron problem non-equilibrium optimal modes are a promising concept for the characterization of dynamics. Here, we focused on the highest

weighted optimal modes, however, also the lower weighted ones have an interesting structure and might carry physical information.

In the case of Anderson localization one knows that the introduction of electron-phonon interactions can lead to delocalization of the charge carrier [68, 242, 243]. An interesting question is what happens when we introduce electron-phonon coupling in the case of interacting fermions. This might also be a testing ground for the methods developed in this thesis and again the structure of phonon optimal modes might be interesting.

Appendix A

Tensor library

In this chapter we describe the general structure of the tensor lib that we developed along this thesis. Chapter 1 gives a detailed description of the various DMRG algorithms we used in tensor notation. The fundamental object in the operations, which algorithms and operations use, is the tensor. Those objects appear with rank three in matrix product states, with rank four in matrix product operators and even higher ranks as temporary objects (such as in a chain of multiple contractions). We can attach a quantum number to all indices occurring in those objects which gives them a natural block structure. Some matrix product states are described by a well-defined global quantum number and are thus sparse in the sense that very few blocks with certain combinations of labels can contain non-zero values. The same holds for matrix product operators that have a well-defined quantum-number flow. The first step to an efficient implementation of the DMRG algorithm is a sparse tensor class where the granularity is on the level of individual blocks rather than on individual numbers.

Seven atomic operations on those tensor objects are necessary for an implementation of a DMRG algorithm: (i) a tensor product operation, (ii) a transpose operation, (iii) an operation to expand one tensor by another, (iv) an operation that reduces the dimension of a tensor in one dimension, (v) a singular value decomposition operation, (vi) an eigen-decomposition operation and (vii) an operation that changes the dimension of a tensor by combining multiple indices into one and vice versa (tensor reshape).

A sketch of the structure of the tensor library is presented in Fig. A.1. The overall structure is split into the data part and the operation part. This split is motivated by the algorithmic nature of this project: we have structured data which is changed by operations that, in combination, represent the algorithm. In this sense the DMRG algorithm is just an operation on a higher level using the lower-level operations and different algorithms just differ in how they combine the lower-level operations.

A.1 A blocky tensor class

The basic object in our implementation is the `gTensor` class which represents a dense tensor. In general, a tensor is defined by its layout and by its entries. For a dense tensor the layout is fully specified by the size of each dimension. A simple example is a matrix which represents a rank-two tensor: the shape is given by the number of rows and columns. Entries are addressed by an array containing the indices.

The next layer is the `bTensor` class which represents the blocky tensor. This class holds

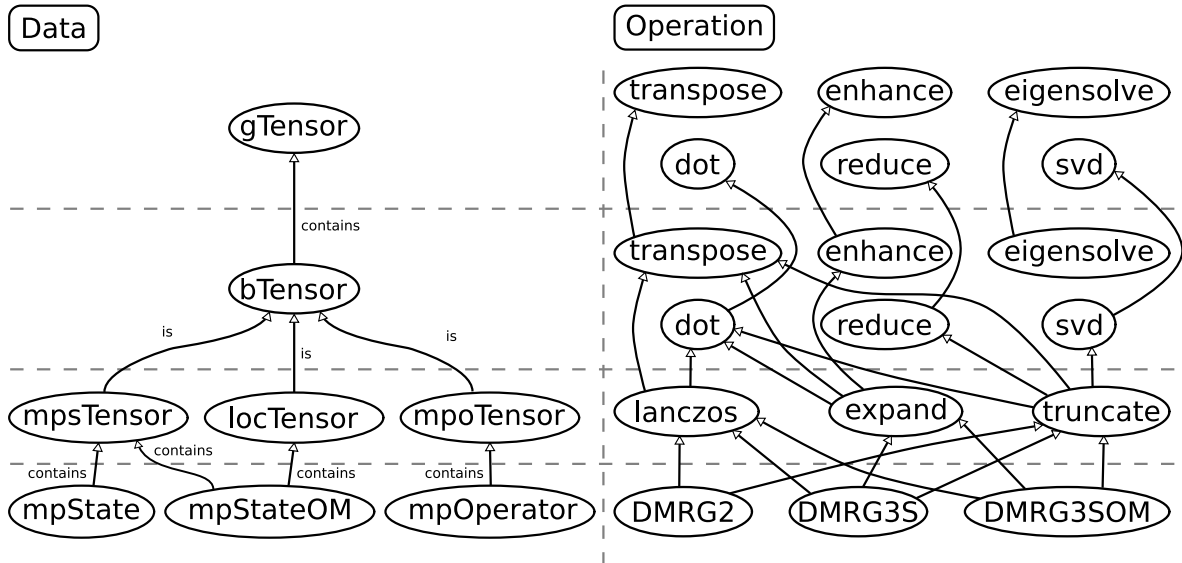


Figure A.1: Sketch of the structure of the tensor library. The data part includes classes that structure the data. The operation part operates on the data.

non-zero blocks in the form of dense tensors. The layout of this class is more complicated: A specific entry in the full tensor is now addressed by two arrays, one that contains the combination of labels that uniquely specify the block that the entry is located in and the actual index inside of the block. The layout of a `bTensor` object is specified by a list containing all the labels together with the internal dimension of the block label. As an example, a matrix that can be blocked into four blocks is specified by a layout that holds two labels for each dimension. This is illustrated in Fig. A.2.

A.1.1 The reshape operation

A very important operation is the tensor-reshape. This operation is used abundantly by the DMRG algorithm because at every site tensors need to be truncated after optimization. For this to happen a rank-three (single-site DMRG) or a rank-four (two-site DMRG) tensor needs to be reshaped into a matrix in order to perform a singular value decomposition. Very importantly, after splitting and truncation of the matrix, one or two of the resulting parts need to be reshaped back into valid rank-three tensors.

For a dense tensor this operation is a mapping of all tuples of indices into new tuples of indices. As an example consider the reshape of a rank-three tensor with shape (d_1, d_2, d_3) into a matrix of shape $(\tilde{d}_1 = d_1, \tilde{d}_2 = d_2 d_3)$

$$\tilde{M}_{\tilde{i}=i, \tilde{j}=j+d_2 k} = M_{i,j,k} \quad \forall i, j, k, \quad (\text{A.1})$$

where \tilde{M} denotes the tensor after reshaping and M denotes the tensor before the reshape operation. In principle, the new shape $(\tilde{d}_1, \tilde{d}_2)$ could be chosen arbitrarily with the only requirement that $\tilde{d}_1 \tilde{d}_2 = d_1 d_2 d_3$ holds, however, this is not easily possible for blocky tensors. A graphical visualization of this mapping is presented in Fig. A.3: The rank-three tensor \tilde{M} is represented as a matrix where the third dimension (into the plane in Fig. A.3) is unfolded

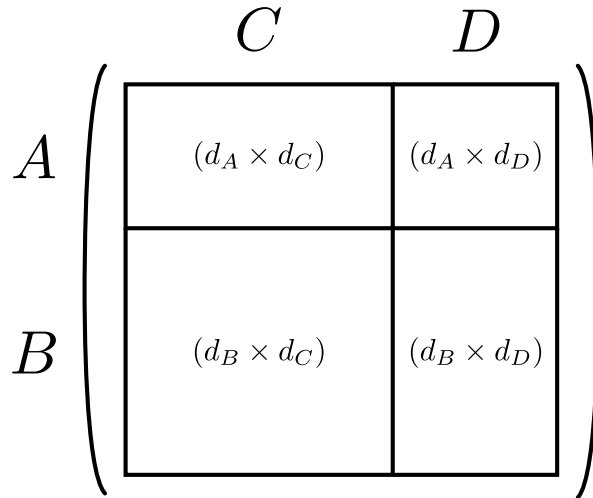


Figure A.2: Sketch of a blocky matrix. The layout consists of the labels and dimensions $(A, d_A), (B, d_B)$ in the row dimension and $(C, d_C), (D, d_D)$ in the column dimension. These four labels can be combined in $(2 \times 2) = 4$ ways. The full row dimension is given by $d_{\text{row}} = d_A + d_B$ and the full column dimension is given by $d_{\text{col}} = d_C + d_D$.

in the second dimension where entries of the rank-three tensor with smaller indices in the third dimension are mapped to the left of entries with larger index in the third dimension.

The same operation can be performed on a blocky tensor. Here, additionally to indices inside a dense block we need a function that maps a set of block labels into a new set of block labels with the reshaped rank. An example is the reshaping of an MPS-tensor $M_{N_{j-1}, N_j}^{n_j}$ into a matrix $\tilde{M}_{\tilde{N}_{j-1}=(N_{j-1}, n_j), \tilde{N}_j=N_j}$ where we group the two indices (N_{j-1}, n_j) together to form a new label \tilde{N}_{j-1} . During a DMRG sweep one normally wants to get this matrix in block-diagonal form to be able to perform an efficient SVD on it. A valid mapping for the first index is $\tilde{N}_{j-1} = N_{j-1} + n_j = N_j$. Different combinations of labels that lead to the same final label have to be stored in the same block just like in the example (Fig. A.3). Two blocks that have different labels in a rank-three tensor can now end up in the same block and thus enhance the dimension of the respective block.

So far, we took a rank-three tensor and made a matrix out of it. For a dense tensor the reverse operation which reshapes the tensor from rank-two to rank-three is trivial because the mapping of indices is bijective. However, for a blocky tensor the mapping of block labels need not be bijective: two different sets of labels can be mapped onto the same new label. To solve this problem we attach two ranks to a blocky tensor object: the current rank and the full rank. Also, the layout keeps the internal structure of the labels which specifies where the data of each block is located. When reshaping a blocky tensor object the reshape always starts from the tensor with its full rank where the layout takes care of where the actual data is stored.

A.1.2 Tensor operations

All previously mentioned fundamental operations are implemented for the tensor classes where the blocky tensor operations utilize the underlying dense-tensor operations. The operations

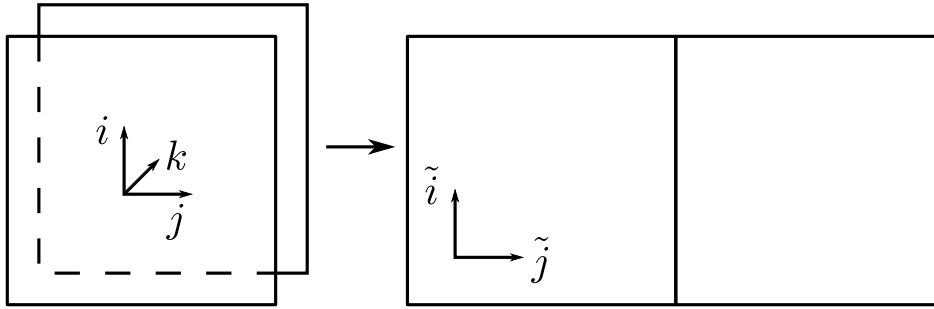


Figure A.3: Sketch of a rank-three tensor that is reshaped into a rank-two tensor (matrix) object. The mapping flattens out the third dimension: the i -index is unaltered $\tilde{i} = i$ while the j and k indices are mapped onto the same dimension $\tilde{j} = j + d_2 k$ where d_2 is the size of the second dimension.

`dot`, `svd` and `eigensolve` on a dense tensor use the LAPACK library. This is straightforward for `svd` and `eigensolve` because those operations are only defined for rank-two tensors. The `dot` operation treats the participating tensors as matrices which enforces the indices to be in the right order when contracting more than one index at the same time. Out of this reason we provide a `transpose` operation which is much cheaper than the `dot`. We tested the LAPACK matrix product operation with a preceding `transpose` against a custom function that performs the tensor contraction directly and found that the former outperforms the direct tensor contraction.

The operations on the blocky tensor implement optimizations for the blockstructure: the `svd` and `eigensolve` operations assume a block-diagonal structure of the tensor which allows a reduction of the computational effort because the operation can then be performed for each block by itself. Also, the `dot` and `transpose` operations only need to consider non-zero blocks since they are trivial for zero-matrices. The two tensor objects described here along with the operations defined for them are completely general and can, in principle, be used for every possible application, including, for example, multidimensional tensor networks.

A.2 The DMRG algorithm

The next layer in our architecture defines the tensor objects and operations that are directly used by DMRG: the MPS-tensor (`mpsTensor`, `locTensor`) and MPO-tensor (`mpoTensor`) classes along with the operations `lanczos`, `expand` and `truncate`. The `lanczos` operation uses the `transpose` and `dot` operations to build up the Krylov space and uses the dense `eigensolve` operation to diagonalize the tridiagonal matrix that is set up internally [78]. The `expand` operation is used for the subspace expansion: it takes two `bTensor` objects and puts all entries in the one tensor into the other, thereby enhancing one of the dimensions (see Ch. 1.2.2). The `truncate` operation is used to reduce one of the dimensions of a tensor. For single-site DMRG it first reshapes the tensor into a matrix to perform an SVD. The singular values are then truncated along with the dimension of the respective index. An important point is that one has to make sure that no block vanishes completely during this truncation since this could modify also the index that is to be kept constant during the truncation. After the truncation the singular values are contracted into the left or right canonical matrix obtained from the SVD which the operation returns. The other tensor is reshaped back into

a rank-three tensor.

The next layer describes the actual MPS (`mpState`, `mpStateOM`) and MPO (`mpOperator`) objects together with the DMRG algorithms (`DMRG2`, `DMRG3S` and `DMRG3SOM`) defined on them. In our implementation an MPS (MPO) is a length- L array of MPS-tensor (MPO-tensor) objects where L is the size of the system. Common to all algorithms that we implemented (DMRG-like as well as TEBD) is the following procedure. The algorithm loops over the system back and forth by an optimization of the tensor at the currently active site followed by a truncation of the bond that has increased during optimization. For the two-site DMRG the optimization includes a contraction of two adjacent single-site tensors and MPO-tensors in the MPS and Hamiltonian MPO to form two-site MPS and MPO tensors, and a Lanczos optimization step that minimizes the global energy in the given environment. The strictly-single-site DMRG algorithm directly optimizes a single tensor and performs a subspace expansion afterwards. Our strictly-single-site DMRG with local basis optimization algorithm (`DMRG3SOM`) performs first an optimization on the local tensor before it continues with the update of the bond index as the `DMRG3S` algorithm in an optimal basis.

Bibliography

- [1] N. W. Ashcroft and N. D. Mermin, *Solid state physics* (Holt, Rinehart and Winston, New York, 1976).
- [2] R. E. Peierls, *Quantum theory of solids* (Clarendon Press, Oxford, 1955).
- [3] L. N. Cooper, Bound Electron Pairs in a Degenerate Fermi Gas, *Phys. Rev.* **104**, 1189 (1956).
- [4] J. Bardeen, L. N. Cooper, and J. R. Schrieffer, Theory of Superconductivity, *Phys. Rev.* **108**, 1175 (1957).
- [5] L. D. Landau, Über die Bewegung der Elektronen in Kristallgitter, *Phys. Z. Sowjetunion* **3**, 644 (1933).
- [6] T. Holstein, Studies of polaron motion: Part I. The molecular-crystal model, *Annals of Physics* **8**, 325 (1959).
- [7] H. Matsueda, S. Sota, T. Tohyama, and S. Maekawa, -, *J. Phys. Soc. Jpn.* **79**, 013701 (2012).
- [8] M. Mitrano, G. Cotugno, S. R. Clark, R. Singla, S. Kaiser, J. Stähler, R. Beyer, M. Dresel, L. Baldassarre, D. Nicoletti, A. Perucchi, T. Hasegawa, H. Okamoto, D. Jaksch, and A. Cavalleri, Pressure-Dependent Relaxation in the Photoexcited Mott Insulator ET – F₂TCNQ: Influence of Hopping and Correlations on Quasiparticle Recombination Rates, *Phys. Rev. Lett.* **112**, 117801 (2014).
- [9] S. Dal Conte, L. Vidmar, D. Golez, M. Mierzejewski, G. Soavi, S. Peli, F. Banfi, G. Ferrini, R. Comin, B. M. Ludbrook, L. Chauviere, N. D. Zhigadlo, H. Eisaki, M. Greven, S. Lupi, A. Damascelli, D. Brida, M. Capone, J. Bonca, G. Cerullo, and C. Giannetti, Snapshots of the retarded interaction of charge carriers with ultrafast fluctuations in cuprates, *Nat Phys* **11**, 421 (2015).
- [10] J. Orenstein, Ultrafast spectroscopy of quantum materials, *Phys. Today* **65**, 44 (2012).
- [11] C. Giannetti, M. Capone, D. Fausti, M. Fabrizio, F. Parmigiani, and D. Mihailovic, Ultrafast optical spectroscopy of strongly correlated materials and high-temperature superconductors: a non-equilibrium approach, *Advances in Physics* **65**, 58 (2016).
- [12] D. Fausti, R. I. Tobey, N. Dean, S. Kaiser, A. Dienst, M. C. Hoffmann, S. Pyon, T. Takayama, H. Takagi, and A. Cavalleri, Light-Induced Superconductivity in a Stripe-Ordered Cuprate, *Science* **331**, 189 (2011).

- [13] L. R. Testardi, Destruction of Superconductivity by Laser Light, *Phys. Rev. B* **4**, 2189 (1971).
- [14] L. Stojchevska, P. Kusar, T. Mertelj, V. V. Kabanov, Y. Toda, X. Yao, and D. Mihailovic, Mechanisms of nonthermal destruction of the superconducting state and melting of the charge-density-wave state by femtosecond laser pulses, *Phys. Rev. B* **84**, 180507 (2011).
- [15] S. L. Dexheimer, A. D. Van Pelt, J. A. Brozik, and B. I. Swanson, Femtosecond Vibrational Dynamics of Self-Trapping in a Quasi-One-Dimensional System, *Phys. Rev. Lett.* **84**, 4425 (2000).
- [16] A. Sugita, T. Saito, H. Kano, M. Yamashita, and T. Kobayashi, Wave Packet Dynamics in a Quasi-One-Dimensional Metal-Halogen Complex Studied by Ultrafast Time-Resolved Spectroscopy, *Phys. Rev. Lett.* **86**, 2158 (2001).
- [17] S. Dal Conte, C. Giannetti, G. Coslovich, F. Cilento, D. Bossini, T. Abebaw, F. Banfi, G. Ferrini, H. Eisaki, M. Greven, A. Damascelli, D. van der Marel, and F. Parmigiani, Disentangling the Electronic and Phononic Glue in a High-Tc Superconductor, *Science* **335**, 1600 (2012).
- [18] J. Hubbard, Electron Correlations in Narrow Energy Bands. III. An Improved Solution, *Proceedings of the Royal Society of London A: Mathematical, Physical and Engineering Sciences* **281**, 401 (1964).
- [19] H. Fehske and S. A. Trugman, Numerical Solution of the Holstein Polaron Problem, *Polarons in Advanced Materials*, volume 103 of Springer Series in Materials Science, 393–461 (Springer Netherlands, 2007).
- [20] S. Klimin and J. Devreese, Feynmans path-integral polaron treatment approached using time-ordered operator calculus, *Solid State Communications* **151**, 144 (2011).
- [21] F. Grusdt and E. Demler, New theoretical approaches to Bose polarons, arXiv:1510.04934 [cond-mat.quant-gas] (2015).
- [22] J. Bonča and S. A. Trugman, Inelastic Quantum Transport, *Phys. Rev. Lett.* **79**, 4874 (1997).
- [23] J. Bonča, S. A. Trugman, and I. Batistić, Holstein polaron, *Phys. Rev. B* **60**, 1633 (1999).
- [24] S. R. White, Density matrix formulation for quantum renormalization groups, *Phys. Rev. Lett.* **69**, 2863 (1992).
- [25] E. Jeckelmann and S. R. White, Density-matrix renormalization-group study of the polaron problem in the Holstein model, *Phys. Rev. B* **57**, 6376 (1998).
- [26] U. Schollwöck, The density-matrix renormalization group, *Rev. Mod. Phys.* **77**, 259 (2005).
- [27] U. Schollwöck, The density-matrix renormalization group in the age of matrix product states, *Annals of Physics* **326**, 96 (2011).

- [28] L. Vidmar, J. Bonča, M. Mierzejewski, P. Prelovšek, and S. A. Trugman, Nonequilibrium dynamics of the Holstein polaron driven by an external electric field, *Phys. Rev. B* **83**, 134301 (2011).
- [29] D. Golež, J. Bonča, L. Vidmar, and S. A. Trugman, Relaxation Dynamics of the Holstein Polaron, *Phys. Rev. Lett.* **109**, 236402 (2012).
- [30] A. N. Rubtsov, V. V. Savkin, and A. I. Lichtenstein, Continuous-time quantum Monte Carlo method for fermions, *Phys. Rev. B* **72**, 035122 (2005).
- [31] M. Hohenadler, Interplay of Site and Bond Electron-Phonon Coupling in One Dimension, *Phys. Rev. Lett.* **117**, 206404 (2016).
- [32] G. Vidal, Efficient Classical Simulation of Slightly Entangled Quantum Computations, *Phys. Rev. Lett.* **91**, 147902 (2003).
- [33] G. Vidal, Efficient Simulation of One-Dimensional Quantum Many-Body Systems, *Phys. Rev. Lett.* **93**, 040502 (2004).
- [34] A. Daley, C. Kollath, U. Schollwöck, and G. Vidal, Time-dependent density-matrix renormalization-group using adaptive effective Hilbert spaces, *J. Stat. Mech.* (2004), P04005 (2004).
- [35] S. R. White and A. E. Feiguin, Real-time evolution using the density matrix renormalization group, *Phys. Rev. Lett.* **93**, 076401 (2004).
- [36] C. Zhang, E. Jeckelmann, and S. R. White, Density Matrix Approach to Local Hilbert Space Reduction, *Phys. Rev. Lett.* **80**, 2661 (1998).
- [37] C. Guo, A. Weichselbaum, J. von Delft, and M. Vojta, Critical and Strong-Coupling Phases in One- and Two-Bath Spin-Boson Models, *Phys. Rev. Lett.* **108**, 160401 (2012).
- [38] C. Hubig, I. P. McCulloch, U. Schollwöck, and F. A. Wolf, Strictly single-site DMRG algorithm with subspace expansion, *Phys. Rev. B* **91**, 155115 (2015).
- [39] S. R. White, Density matrix renormalization group algorithms with a single center site, *Phys. Rev. B* **72**, 180403 (2005).
- [40] A. Weiße and H. Fehske, *Exact Diagonalization Techniques, Computational Many-Particle Physics*, 529–544 (Springer Berlin Heidelberg, Berlin, Heidelberg, 2008).
- [41] C. Zhang, E. Jeckelmann, and S. R. White, Dynamical properties of the one-dimensional Holstein model, *Phys. Rev. B* **60**, 14092 (1999).
- [42] M. Hohenadler, A. O. Silver, M. J. Bhaseen, and B. D. Simons, Quantum phase transitions in bosonic heteronuclear pairing Hamiltonians, *Phys. Rev. A* **82**, 013639 (2010).
- [43] S. Ejima, M. J. Bhaseen, M. Hohenadler, F. H. L. Essler, H. Fehske, and B. D. Simons, Ising Deconfinement Transition between Feshbach-Resonant Superfluids, *Phys. Rev. Lett.* **106**, 015303 (2011).

- [44] M. J. Bhaseen, S. Ejima, F. H. L. Essler, H. Fehske, M. Hohenadler, and B. D. Simons, Discrete symmetry breaking transitions between paired superfluids, *Phys. Rev. A* **85**, 033636 (2012).
- [45] S.-J. Gu, S.-S. Deng, Y.-Q. Li, and H.-Q. Lin, Entanglement and Quantum Phase Transition in the Extended Hubbard Model, *Phys. Rev. Lett.* **93**, 086402 (2004).
- [46] Ö. Legeza and J. Sólyom, Two-Site Entropy and Quantum Phase Transitions in Low-Dimensional Models, *Phys. Rev. Lett.* **96**, 116401 (2006).
- [47] C. Brockett, F. Dorfner, L. Vidmar, F. Heidrich-Meisner, and E. Jeckelmann, Matrix-product-state method with a dynamical local basis optimization for bosonic systems out of equilibrium, *Phys. Rev. B* **92**, 241106(R) (2015).
- [48] F. A. Y. N. Schröder and A. W. Chin, Simulating open quantum dynamics with time-dependent variational matrix product states: Towards microscopic correlation of environment dynamics and reduced system evolution, *Phys. Rev. B* **93**, 075105 (2016).
- [49] L.-C. Ku and S. A. Trugman, Quantum dynamics of polaron formation, *Phys. Rev. B* **75**, 014307 (2007).
- [50] H. Fehske, G. Wellein, and A. R. Bishop, Spatiotemporal evolution of polaronic states in finite quantum systems, *Phys. Rev. B* **83**, 075104 (2011).
- [51] H. Fehske, G. Hager, and E. Jeckelmann, Metallicity in the half-filled Holstein-Hubbard model, *EPL* **84**, 57001 (2008).
- [52] T. Langen, R. Geiger, and J. Schmiedmayer, Ultracold Atoms Out of Equilibrium, *Annual Review of Condensed Matter Physics* **6**, 201 (2015).
- [53] J. Eisert, M. Friesdorf, and C. Gogolin, Quantum many-body systems out of equilibrium, *Nat Phys* **11**, 124 (2015).
- [54] S. Trotzky, Y.-A. Chen, A. Flesch, I. P. McCulloch, U. Schollwöck, J. Eisert, and I. Bloch, Probing the relaxation towards equilibrium in an isolated strongly correlated one-dimensional Bose gas, *Nat Phys* **8**, 325 (2012).
- [55] M. Cheneau, P. Barmettler, D. Poletti, M. Endres, P. Schausz, T. Fukuhara, C. Gross, I. Bloch, C. Kollath, and S. Kuhr, Light-cone-like spreading of correlations in a quantum many-body system, *Nature* **481**, 484 (2012).
- [56] J. P. Ronzheimer, M. Schreiber, S. Braun, S. S. Hodgman, S. Langer, I. P. McCulloch, F. Heidrich-Meisner, I. Bloch, and U. Schneider, Expansion Dynamics of Interacting Bosons in Homogeneous Lattices in One and Two Dimensions, *Phys. Rev. Lett.* **110**, 205301 (2013).
- [57] T. Fukuhara, A. Kantian, M. Endres, M. Cheneau, P. Schausz, S. Hild, D. Bellem, U. Schollwöck, T. Giamarchi, C. Gross, I. Bloch, and S. Kuhr, Quantum dynamics of a mobile spin impurity, *Nat Phys* **9**, 235 (2013).
- [58] T. Fukuhara, P. Schausz, M. Endres, S. Hild, M. Cheneau, I. Bloch, and C. Gross, Microscopic observation of magnon bound states and their dynamics, *Nature* **502**, 76 (2013).

- [59] D. Pertot, A. Sheikhan, E. Cocchi, L. A. Miller, J. E. Bohn, M. Koschorreck, M. Köhl, and C. Kollath, Relaxation Dynamics of a Fermi Gas in an Optical Superlattice, *Phys. Rev. Lett.* **113**, 170403 (2014).
- [60] R. C. Brown, R. Wyllie, S. B. Koller, E. A. Goldschmidt, M. Foss-Feig, and J. V. Porto, Two-dimensional superexchange-mediated magnetization dynamics in an optical lattice, *Science* **348**, 540 (2015).
- [61] S. Hild, T. Fukuhara, P. Schauß, J. Zeiher, M. Knap, E. Demler, I. Bloch, and C. Gross, Far-from-Equilibrium Spin Transport in Heisenberg Quantum Magnets, *Phys. Rev. Lett.* **113**, 147205 (2014).
- [62] A. Bauer, F. Dorfner, and F. Heidrich-Meisner, Temporal decay of Néel order in the one-dimensional Fermi-Hubbard model, *Phys. Rev. A* **91**, 053628 (2015).
- [63] T. Enss and J. Sirker, Light cone renormalization and quantum quenches in one-dimensional Hubbard models, *New Journal of Physics* **14**, 023008 (2012).
- [64] P. Barmettler, M. Punk, V. Gritsev, E. Demler, and E. Altman, Relaxation of Antiferromagnetic Order in Spin-1/2 Chains Following a Quantum Quench, *Phys. Rev. Lett.* **102**, 130603 (2009).
- [65] T. Giamarchi, *Quantum physics in one dimension* (Clarendon ; Oxford University Press, Oxford; New York, 2004).
- [66] M. Rigol, V. Dunjko, and M. Olshanii, Thermalization and its mechanism for generic isolated quantum systems, *Nature* **452**, 854 (2008).
- [67] I. V. Gornyi, A. D. Mirlin, and D. G. Polyakov, Interacting Electrons in Disordered Wires: Anderson Localization and Low- T Transport, *Phys. Rev. Lett.* **95**, 206603 (2005).
- [68] D. Basko, I. Aleiner, and B. Altshuler, Metalinsulator transition in a weakly interacting many-electron system with localized single-particle states, *Annals of Physics* **321**, 1126 (2006).
- [69] V. Oganesyan and D. A. Huse, Localization of interacting fermions at high temperature, *Phys. Rev. B* **75**, 155111 (2007).
- [70] M. Žnidarič, T. Prosen, and P. Prelovšek, Many-body localization in the Heisenberg XXZ magnet in a random field, *Phys. Rev. B* **77**, 064426 (2008).
- [71] P. W. Anderson, Absence of Diffusion in Certain Random Lattices, *Phys. Rev.* **109**, 1492 (1958).
- [72] D. J. Luitz, N. Laflorencie, and F. Alet, Many-body localization edge in the random-field Heisenberg chain, *Phys. Rev. B* **91**, 081103 (2015).
- [73] T. Giamarchi and H. J. Schulz, Anderson localization and interactions in one-dimensional metals, *Phys. Rev. B* **37**, 325 (1988).

- [74] P. Schmitteckert, T. Schulze, C. Schuster, P. Schwab, and U. Eckern, Anderson Localization versus Delocalization of Interacting Fermions in One Dimension, *Phys. Rev. Lett.* **80**, 560 (1998).
- [75] S. Bera, H. Schomerus, F. Heidrich-Meisner, and J. H. Bardarson, Many-Body Localization Characterized from a One-Particle Perspective, *Phys. Rev. Lett.* **115**, 046603 (2015).
- [76] J. M. Zhang and R. X. Dong, Exact diagonalization: the Bose Hubbard model as an example, *Eur. J. Phys.* **31**, 591 (2010).
- [77] E. Jeckelmann and H. Fehske, Exact numerical methods for electron-phonon problems, *Proc. Int. School of Physics "Enrico Fermi", Course CLXI*, Eds. G. Iadonisi, J. Raninger, G. de Filippis, IOS Press Amsterdam 247–284 (2006).
- [78] C. Lanczos, An Iteration Method for the Solution of the Eigenvalue Problem of Linear Differential and Integral Operators, *J. Res. Nat. Bur. Stand.* **45** (1950).
- [79] S. R. White, Density-matrix algorithms for quantum renormalization groups, *Phys. Rev. B* **48**, 10345 (1993).
- [80] M. B. Hastings, An area law for one-dimensional quantum systems, *Journal of Statistical Mechanics: Theory and Experiment* **2007**, P08024 (2007).
- [81] J. Eisert, Entanglement and tensor network states, *Autumn School on Correlated Electrons: Emergent Phenomena in Correlated Matter Jülich, Germany, 23-27. September 2013* (2013). [arXiv:1308.3318\[quant-ph\]](https://arxiv.org/abs/1308.3318).
- [82] C. Holzhey, F. Larsen, and F. Wilczek, Geometric and renormalized entropy in conformal field theory, *Nuclear Physics B* **424**, 443 (1994).
- [83] P. Calabrese and J. Cardy, Entanglement entropy and quantum field theory, *Journal of Statistical Mechanics: Theory and Experiment* **2004**, P06002 (2004).
- [84] I. Affleck, T. Kennedy, E. H. Lieb, and H. Tasaki, Rigorous results on valence-bond ground states in antiferromagnets, *Phys. Rev. Lett.* **59**, 799 (1987).
- [85] S. Östlund and S. Rommer, Thermodynamic Limit of Density Matrix Renormalization, *Phys. Rev. Lett.* **75**, 3537 (1995).
- [86] J. Dukelsky, M. A. Martn-Delgado, T. Nishino, and G. Sierra, Equivalence of the variational matrix product method and the density matrix renormalization group applied to spin chains, *EPL (Europhysics Letters)* **43**, 457 (1998).
- [87] B. Bruognolo, A. Weichselbaum, C. Guo, J. von Delft, I. Schneider, and M. Vojta, Two-bath spin-boson model: Phase diagram and critical properties, *Phys. Rev. B* **90**, 245130 (2014).
- [88] H. Fehske, J. Schleede, G. Schubert, G. Wellein, V. S. Filinov, and A. R. Bishop, Numerical approaches to time evolution of complex quantum systems, *Physics Letters A* **373**, 2182 (2009).

- [89] L. Vidmar, J. Bonča, T. Tohyama, and S. Maekawa, Quantum Dynamics of a Driven Correlated System Coupled to Phonons, *Phys. Rev. Lett.* **107**, 246404 (2011).
- [90] K. Yonemitsu and N. Maeshima, Coupling-dependent rate of energy transfer from photoexcited Mott insulators to lattice vibrations, *Phys. Rev. B* **79**, 125118 (2009).
- [91] G. De Filippis, V. Cataudella, E. A. Nowadnick, T. P. Devereaux, A. S. Mishchenko, and N. Nagaosa, Quantum Dynamics of the Hubbard-Holstein Model in Equilibrium and Non-Equilibrium: Application to Pump-Probe Phenomena, *Phys. Rev. Lett.* **109**, 176402 (2012).
- [92] J. Kogoj, Z. Lenarčič, D. Golež, M. Mierzejewski, P. Prelovšek, and J. Bonča, Multistage dynamics of the spin-lattice polaron formation, *Phys. Rev. B* **90**, 125104 (2014).
- [93] E. H. Lieb and D. W. Robinson, The finite group velocity of quantum spin systems, *Communications in Mathematical Physics* **28**, 251 (1972).
- [94] B. Nachtergaele, Y. Ogata, and R. Sims, Propagation of Correlations in Quantum Lattice Systems, *Journal of Statistical Physics* **124**, 1 (2006).
- [95] B. Nachtergaele, H. Raz, B. Schlein, and R. Sims, Lieb-Robinson Bounds for Harmonic and Anharmonic Lattice Systems, *Communications in Mathematical Physics* **286**, 1073 (2009).
- [96] F. Dorfner, L. Vidmar, C. Brockett, E. Jeckelmann, and F. Heidrich-Meisner, Real-time decay of a highly excited charge carrier in the one-dimensional Holstein model, *Phys. Rev. B* **91**, 104302 (2015).
- [97] G. L. G. Sleijpen and H. A. V. der Vorst, A JacobiDavidson Iteration Method for Linear Eigenvalue Problems, *SIAM Journal on Matrix Analysis and Applications* **17**, 401 (1996).
- [98] A. W. Sandvik, Computational studies of Quantum Spin Systems, *AIP Conf. Proc.* **1297**, 135 (2010).
- [99] S. R. Manmana, A. Muramatsu, and R. M. Noack, Time evolution of onedimensional Quantum Many Body Systems, *AIP Conference Proceedings* **789** (2005).
- [100] C. Moler and C. V. Loan, Nineteen Dubious Ways to Compute the Exponential of a Matrix, Twenty-Five Years Later, *SIAM Review* **45**, 3 (2003).
- [101] K. G. Wilson, The renormalization group: Critical phenomena and the Kondo problem, *Rev. Mod. Phys.* **47**, 773 (1975).
- [102] S. R. White and R. M. Noack, Real-space quantum renormalization groups, *Phys. Rev. Lett.* **68**, 3487 (1992).
- [103] I. Peschel and V. Eisler, *The Conceptual Background of Density-Matrix Renormalization, Computational Many-Particle Physics*, 581–596 (Springer Berlin Heidelberg, Berlin, Heidelberg, 2008).
- [104] A. R. Its, B.-Q. Jin, and V. E. Korepin, Entanglement in the XY spin chain, *Journal of Physics A: Mathematical and General* **38**, 2975 (2005).

- [105] F. Franchini, A. R. Its, B.-Q. Jin, and V. E. Korepin, Ellipses of constant entropy in the XY spin chain, *Journal of Physics A: Mathematical and Theoretical* **40**, 8467 (2007).
- [106] J. Eisert and M. Cramer, Single-copy entanglement in critical quantum spin chains, *Phys. Rev. A* **72**, 042112 (2005).
- [107] M. B. Plenio, J. Eisert, J. Dreißig, and M. Cramer, Entropy, Entanglement, and Area: Analytical Results for Harmonic Lattice Systems, *Phys. Rev. Lett.* **94**, 060503 (2005).
- [108] I. P. McCulloch, From density-matrix renormalization group to matrix product states, *Journal of Statistical Mechanics: Theory and Experiment* **2007**, P10014 (2007).
- [109] S. V. Dolgov and D. V. Savostyanov, Alternating Minimal Energy Methods for Linear Systems in Higher Dimensions, *SIAM Journal on Scientific Computing* **36**, A2248 (2014).
- [110] W. Koller, D. Meyer, Y. no, and A. C. Hewson, First- and second-order phase transitions in the Holstein-Hubbard model, *EPL (Europhysics Letters)* **66**, 559 (2004).
- [111] H. Fehske and E. Jeckelmann, Quantum phase transitions in one-dimensional electron-phonon systems, arXiv:cond-mat/0510741 [cond-mat.str-el] (2005).
- [112] H. Fehske and G. Hager, *Luttinger, Peierls or Mott? Quantum Phase Transitions in Strongly Correlated 1D Electron-Phonon Systems, Metal-to-Nonmetal Transitions*, edited by R. Redmer, F. Hensel, and B. Holst, 1–21 (Springer Berlin Heidelberg, Berlin, Heidelberg, 2010).
- [113] C. Gadermaier, A. S. Alexandrov, V. V. Kabanov, P. Kusar, T. Mertelj, X. Yao, C. Manzoni, D. Brida, G. Cerullo, and D. Mihailovic, Electron-Phonon Coupling in High-Temperature Cuprate Superconductors Determined from Electron Relaxation Rates, *Phys. Rev. Lett.* **105**, 257001 (2010).
- [114] F. Novelli, G. De Filippis, V. Cataudella, M. Esposito, I. Vergara, F. Cilento, E. Sindici, A. Amaricci, C. Giannetti, D. Prabhakaran, S. Wall, A. Perucchi, S. Dal Conte, G. Cerullo, M. Capone, A. Mishchenko, M. Grüninger, N. Nagaosa, F. Parmigiani, and D. Fausti, Witnessing the formation and relaxation of dressed quasi-particles in a strongly correlated electron system, *Nat. Commun.* **5**, 5112 (2014).
- [115] A. Cavalleri, C. Tóth, C. W. Siders, J. A. Squier, F. Ráksi, P. Forget, and J. C. Kieffer, Femtosecond Structural Dynamics in VO₂ during an Ultrafast Solid-Solid Phase Transition, *Phys. Rev. Lett.* **87**, 237401 (2001).
- [116] S. L. Johnson, R. A. de Souza, U. Staub, P. Beaud, E. Möhr-Vorobeva, G. Ingold, A. Caviezel, V. Scagnoli, W. F. Schlotter, J. J. Turner, O. Krupin, W.-S. Lee, Y.-D. Chuang, L. Patthey, R. G. Moore, D. Lu, M. Yi, P. S. Kirchmann, M. Trigo, P. Denes, D. Doering, Z. Hussain, Z.-X. Shen, D. Prabhakaran, and A. T. Boothroyd, Femtosecond Dynamics of the Collinear-to-Spiral Antiferromagnetic Phase Transition in CuO, *Phys. Rev. Lett.* **108**, 037203 (2012).
- [117] D. Afanasiev, B. A. Ivanov, A. Kirilyuk, T. Rasing, R. V. Pisarev, and A. V. Kimel, Control of the Ultrafast Photoinduced Magnetization across the Morin Transition in DyFeO₃, *Phys. Rev. Lett.* **116**, 097401 (2016).

- [118] S. Iwai, M. Ono, A. Maeda, H. Matsuzaki, H. Kishida, H. Okamoto, and Y. Tokura, Ultrafast Optical Switching to a Metallic State by Photoinduced Mott Transition in a Halogen-Bridged Nickel-Chain Compound, *Phys. Rev. Lett.* **91**, 057401 (2003).
- [119] A. Cavalleri, T. Dekorsy, H. H. W. Chong, J. C. Kieffer, and R. W. Schoenlein, Evidence for a structurally-driven insulator-to-metal transition in VO₂: A view from the ultrafast timescale, *Phys. Rev. B* **70**, 161102 (2004).
- [120] P. Monthoux, D. Pines, and G. G. Lonzarich, Superconductivity without phonons, *Nature* **450**, 1177 (2007).
- [121] P. W. Anderson, Is There Glue in Cuprate Superconductors?, *Science* **316**, 1705 (2007).
- [122] V. Z. Kresin and S. A. Wolf, *Colloquium* : Electron-lattice interaction and its impact on high T_c superconductivity, *Rev. Mod. Phys.* **81**, 481 (2009).
- [123] M. P. Allan, K. Lee, A. W. Rost, M. H. Fischer, F. Masee, K. Kihou, C.-H. Lee, A. Iyo, H. Eisaki, T.-M. Chuang, J. C. Davis, and E.-A. Kim, Identifying the 'fingerprint' of antiferromagnetic spin fluctuations in iron pnictide superconductors, *Nat Phys* **11**, 177 (2015).
- [124] O. Ahmadi, L. Coffey, J. F. Zasadzinski, N. Miyakawa, and L. Ozyuzer, Eliashberg Analysis of Tunneling Experiments: Support for the Pairing Glue Hypothesis in Cuprate Superconductors, *Phys. Rev. Lett.* **106**, 167005 (2011).
- [125] N. Ge, C. Wong, R. Lingle, J. McNeill, K. Gaffney, and C. Harris, Femtosecond dynamics of electron localization at interfaces, *Science* **279**, 202 (1998).
- [126] S. Tomimoto, H. Nansei, S. Saito, T. Suemoto, J. Takeda, and S. Kurita, Femtosecond Dynamics of the Exciton Self-Trapping Process in a Quasi-One-Dimensional Halogen-Bridged Platinum Complex, *Phys. Rev. Lett.* **81**, 417 (1998).
- [127] A. D. Miller, I. Bezel, K. J. Gaffney, S. Garrett-Roe, S. H. Liu, P. Szymanski, and C. B. Harris, Electron Solvation in Two Dimensions, *Science* **297**, 1163 (2002).
- [128] C. Gahl, U. Bovensiepen, C. Frischkorn, and M. Wolf, Ultrafast Dynamics of Electron Localization and Solvation in Ice Layers on Cu(111), *Phys. Rev. Lett.* **89**, 107402 (2002).
- [129] N. Dean, J. C. Petersen, D. Fausti, R. I. Tobey, S. Kaiser, L. V. Gasparov, H. Berger, and A. Cavalleri, Polaronic Conductivity in the Photoinduced Phase of 1T-TaS₂, *Phys. Rev. Lett.* **106**, 016401 (2011).
- [130] F. X. Morrissey, J. G. Mance, A. D. Van Pelt, and S. L. Dexheimer, Femtosecond dynamics of exciton localization: self-trapping from the small to the large polaron limit, *J. Phys.: Condens. Matter* **25**, 144204 (2013).
- [131] M. Scherff, J. Hoffmann, B. Meyer, T. Danz, and C. Jooss, Interplay of cross-plane polaronic transport and resistive switching in Pt–Pr_{0.67}Ca_{0.33}MnO₃–Pt heterostructures, *New J. Phys.* **15**, 103008 (2013).
- [132] D. G. Ouellette, P. Moetakef, T. A. Cain, J. Y. Zhang, S. Stemmer, D. Emin, and S. J. Allen, High-density Two-Dimensional Small Polaron Gas in a Delta-Doped Mott Insulator, *Sci. Rep.* **3**, 3284 (2013).

- [133] Y. M. Sheu, S. A. Trugman, L. Yan, J. Qi, Q. X. Jia, A. J. Taylor, and R. P. Prasankumar, Polaronic Transport Induced by Competing Interfacial Magnetic Order in a $\text{La}_{0.7}\text{Ca}_{0.3}\text{MnO}_3/\text{BiFeO}_3$ Heterostructure, *Phys. Rev. X* **4**, 021001 (2014).
- [134] F. Rossi and T. Kuhn, Theory of ultrafast phenomena in photoexcited semiconductors, *Rev. Mod. Phys.* **74**, 895 (2002).
- [135] K. A. Al-Hassanieh, F. A. Reboredo, A. E. Feiguin, I. González, and E. Dagotto, Excitons in the One-Dimensional Hubbard Model: A Real-Time Study, *Phys. Rev. Lett.* **100**, 166403 (2008).
- [136] B. Koopmans, G. Malinowski, F. Dalla Longa, D. Steiauf, M. Fähnle, T. Roth, M. Cinchetti, and M. Aeschlimann, Explaining the paradoxical diversity of ultrafast laser-induced demagnetization, *Nature Mater.* **9**, 259 (2010).
- [137] K. Carva, M. Battiato, D. Legut, and P. M. Oppeneer, Ab initio theory of electron-phonon mediated ultrafast spin relaxation of laser-excited hot electrons in transition-metal ferromagnets, *Phys. Rev. B* **87**, 184425 (2013).
- [138] D. Golež, J. Bonča, M. Mierzejewski, and L. Vidmar, Mechanism of ultrafast relaxation of a photo-carrier in antiferromagnetic spin background Mechanism of ultrafast relaxation of a photo-carrier in antiferromagnetic spin background Mechanism of ultrafast relaxation of a photo-carrier in antiferromagnetic spin background, *Phys. Rev. B* **89**, 165118 (2014).
- [139] E. Iyoda and S. Ishihara, Transient Carrier Dynamics in a Mott Insulator with Antiferromagnetic Order, *Phys. Rev. B* **89**, 125126 (2014).
- [140] M. Eckstein and P. Werner, Ultrafast separation of photo-doped carriers in Mott antiferromagnets, *Phys. Rev. Lett.* **113**, 076405 (2014).
- [141] M. Eckstein and P. Werner, Ultra-fast photo-carrier relaxation in Mott insulators with short-range spin correlations, *Scientific Reports* **6**, 21235 (2016).
- [142] J. Kogoj, M. Mierzejewski, and J. Bonča, Nature of Bosonic Excitations Revealed by High-Energy Charge Carriers, *Phys. Rev. Lett.* **117**, 227002 (2016).
- [143] D. Emin and C. F. Hart, Phonon-assisted hopping of an electron on a Wannier-Stark ladder in a strong electric field, *Phys. Rev. B* **36**, 2530 (1987).
- [144] S. Rott, N. Linder, and G. H. Döhler, Field dependence of the hopping drift velocity in semiconductor superlattices, *Phys. Rev. B* **65**, 195301 (2002).
- [145] P. Werner and M. Eckstein, Field-induced polaron formation in the Holstein-Hubbard model, *Europhys. Lett.* **109**, 37002 (2015).
- [146] A. K. C. Cheung and M. Berciu, Phonon-assisted carrier motion on the Wannier-Stark ladder, *Phys. Rev. B* **88**, 035132 (2013).
- [147] G. Li, B. Movaghar, A. Nitzan, and M. A. Ratner, Polaron formation: Ehrenfest dynamics vs. exact results, *J. Chem. Phys.* **138**, 044112 (2013).

- [148] V. Meden, J. Fricke, C. Wöhler, and K. Schönhammer, Hot electron relaxation in one-dimensional models: exact polaron dynamics versus relaxation in the presence of a Fermi sea, *Z. Phys. B* **99**, 357 (1996).
- [149] J. Fricke, V. Meden, C. Whler, and K. Schnhammer, Improved Transport Equations Including Correlations for Electron Phonon Systems: Comparison with Exact Solutions in One Dimension, *Annals of Physics* **253**, 177 (1997).
- [150] H. Krull, D. Manske, G. S. Uhrig, and A. P. Schnyder, Signatures of nonadiabatic BCS state dynamics in pump-probe conductivity, *Phys. Rev. B* **90**, 014515 (2014).
- [151] V. V. Kabanov and A. S. Alexandrov, Electron relaxation in metals: Theory and exact analytical solutions, *Phys. Rev. B* **78**, 174514 (2008).
- [152] V. V. Baranov and V. V. Kabanov, Theory of the electron relaxation in metals excited by an ultrashort optical pump, *Phys. Rev. B* **89**, 125102 (2014).
- [153] M. Hohenadler, Charge and spin correlations of a Peierls insulator after a quench, *Phys. Rev. B* **88**, 064303 (2013).
- [154] A. F. Kemper, M. Sentef, B. Moritz, C. C. Kao, Z. X. Shen, J. K. Freericks, and T. P. Devereaux, Mapping of unoccupied states and relevant bosonic modes via the time-dependent momentum distribution, *Phys. Rev. B* **87**, 235139 (2013).
- [155] M. Sentef, A. F. Kemper, B. Moritz, J. K. Freericks, Z.-X. Shen, and T. P. Devereaux, Examining Electron-Boson Coupling Using Time-Resolved Spectroscopy, *Phys. Rev. X* **3**, 041033 (2013).
- [156] P. Werner and M. Eckstein, Phonon-enhanced relaxation and excitation in the Holstein-Hubbard model, *Phys. Rev. B* **88**, 165108 (2013).
- [157] E. Jeckelmann, C. Zhang, and S. R. White, Metal-insulator transition in the one-dimensional Holstein model at half filling, *Phys. Rev. B* **60**, 7950 (1999).
- [158] S. Ejima and H. Fehske, Luttinger parameters and momentum distribution function for the half-filled spinless fermion Holstein model: A DMRG approach, *EPL* **87**, 27001 (2009).
- [159] H. Fehske, G. Wellein, G. Hager, A. Weiße, and A. R. Bishop, Quantum lattice dynamical effects on single-particle excitations in one-dimensional Mott and Peierls insulators, *Phys. Rev. B* **69**, 165115 (2004).
- [160] M. Tezuka, R. Arita, and H. Aoki, Density-Matrix Renormalization Group Study of Pairing when Electron-Electron and Electron-Phonon Interactions Coexist: Effect of the Electronic Band Structure, *Phys. Rev. Lett.* **95**, 226401 (2005).
- [161] A. Nocera, M. Soltanieh-ha, C. A. Perroni, V. Cataudella, and A. E. Feiguin, Interplay of charge, spin, and lattice degrees of freedom in the spectral properties of the one-dimensional Hubbard-Holstein model, *Phys. Rev. B* **90**, 195134 (2014).
- [162] A. Weiße, H. Fehske, G. Wellein, and A. R. Bishop, Optimized phonon approach for the diagonalization of electron-phonon problems, *Phys. Rev. B* **62**, 747(R) (2000).

- [163] J. T. Devreese and A. S. Alexandrov, Fröhlich polaron and bipolaron: recent developments, *Rep. Prog. Phys.* **72**, 066501 (2009).
- [164] J. M. Ziman, *Electrons and phonons: the theory of transport phenomena in solids* (Oxford, Clarendon Press, 1960).
- [165] I. G. Lang and Y. A. Firsov, Calculation of the Activation Probability for a Jump of a Small-radius Polaron, *Soviet Journal of Experimental and Theoretical Physics* **27**, 443 (1968).
- [166] P. Zanardi, Quantum entanglement in fermionic lattices, *Phys. Rev. A* **65**, 042101 (2002).
- [167] P. Giorda and P. Zanardi, Ground-state entanglement in interacting bosonic graphs, *Europhys. Lett.* **68**, 163 (2004).
- [168] N. R. Claussen, E. A. Donley, S. T. Thompson, and C. E. Wieman, Microscopic Dynamics in a Strongly Interacting Bose-Einstein Condensate, *Phys. Rev. Lett.* **89**, 010401 (2002).
- [169] E. A. Donley, N. R. Claussen, S. T. Thompson, and C. E. Wieman, Atom-molecule coherence in a Bose-Einstein condensate, *Nature (London)* **417**, 529 (2002).
- [170] P. Makotyn, C. E. Klauss, D. L. Goldberger, E. A. Cornell, and D. S. Jin, Universal dynamics of a degenerate unitary Bose gas, *Nat Phys.* **10**, 116 (2002).
- [171] E. Timmermans, P. Tommasini, M. Hussein, and A. Kerman, Feshbach resonances in atomic Bose-Einstein condensates, *Physics Reports* **315**, 199 (1999).
- [172] M. Holland, J. Park, and R. Walser, Formation of Pairing Fields in Resonantly Coupled Atomic and Molecular Bose-Einstein Condensates, *Phys. Rev. Lett.* **86**, 1915 (2001).
- [173] G. Thalhammer, K. Winkler, F. Lang, S. Schmid, R. Grimm, and J. H. Denschlag, Long-Lived Feshbach Molecules in a Three-Dimensional Optical Lattice, *Phys. Rev. Lett.* **96**, 050402 (2006).
- [174] R. G. Scott, F. Dalfovo, L. P. Pitaevskii, and S. Stringari, Rapid ramps across the BEC-BCS crossover: A route to measuring the superfluid gap, *Phys. Rev. A* **86**, 053604 (2012).
- [175] B. M. Breid and J. R. Anglin, Postadiabatic Hamiltonian for low-energy excitations in a slowly-time-dependent BCS-BEC crossover, *Phys. Rev. A* **88**, 033617 (2013).
- [176] X. Yin and L. Radzihovsky, Postquench dynamics and prethermalization in a resonant Bose gas, *Phys. Rev. A* **93**, 033653 (2016).
- [177] M. J. Bhaseen, S. Ejima, F. H. L. Essler, H. Fehske, M. Hohenadler, and B. D. Simons, Discrete symmetry breaking transitions between paired superfluids, *Phys. Rev. A* **85**, 033636 (2012).
- [178] W. Ding and K. Yang, Entanglement entropy and mutual information in Bose-Einstein condensates, *Phys. Rev. A* **80**, 012329 (2009).

- [179] S. Ejima, H. Fehske, F. Gebhard, K. zu Münster, M. Knap, E. Arrigoni, and W. von der Linden, Characterization of Mott-insulating and superfluid phases in the one-dimensional Bose-Hubbard model, *Phys. Rev. A* **85**, 053644 (2012).
- [180] M. Campostrini, A. Pelissetto, and E. Vicari, Finite-size scaling at quantum transitions, *Phys. Rev. B* **89**, 094516 (2014).
- [181] A. M. Läuchli and C. Kollath, Spreading of correlations and entanglement after a quench in the one-dimensional Bose-Hubbard model, *Journal of Statistical Mechanics: Theory and Experiment* **2008**, P05018 (2008).
- [182] S. Sorg, L. Vidmar, L. Pollet, and F. Heidrich-Meisner, Relaxation and thermalization in the one-dimensional Bose-Hubbard model: A case study for the interaction quantum quench from the atomic limit, *Phys. Rev. A* **90**, 033606 (2014).
- [183] M. Srednicki, Chaos and quantum thermalization, *Phys. Rev. E* **50**, 888 (1994).
- [184] J. M. Deutsch, Quantum statistical mechanics in a closed system, *Phys. Rev. A* **43**, 2046 (1991).
- [185] T. Barthel and U. Schollwöck, Dephasing and the Steady State in Quantum Many-Particle Systems, *Phys. Rev. Lett.* **100**, 100601 (2008).
- [186] M. Rigol, Breakdown of Thermalization in Finite One-Dimensional Systems, *Phys. Rev. Lett.* **103**, 100403 (2009).
- [187] G. Roux, Quenches in quantum many-body systems: One-dimensional Bose-Hubbard model reexamined, *Phys. Rev. A* **79**, 021608 (2009).
- [188] G. Roux, Finite-size effects in global quantum quenches: Examples from free bosons in an harmonic trap and the one-dimensional Bose-Hubbard model, *Phys. Rev. A* **81**, 053604 (2010).
- [189] H.-J. Miesner, D. M. Stamper-Kurn, M. R. Andrews, D. S. Durfee, S. Inouye, and W. Ketterle, Bosonic Stimulation in the Formation of a Bose-Einstein Condensate, *Science* **279**, 1005 (1998).
- [190] R. P. Smith, S. Beattie, S. Moulder, R. L. D. Campbell, and Z. Hadzibabic, Condensation Dynamics in a Quantum-Quenched Bose Gas, *Phys. Rev. Lett.* **109**, 105301 (2012).
- [191] S. Braun, M. Friesdorf, S. S. Hodgman, M. Schreiber, J. P. Ronzheimer, A. Riera, M. del Rey, I. Bloch, J. Eisert, and U. Schneider, Emergence of coherence and the dynamics of quantum phase transitions, *Proc Natl Acad Sci U S A* **112**, 3641 (2015).
- [192] P. Werner, N. Tsuji, and M. Eckstein, Nonthermal symmetry-broken states in the strongly interacting Hubbard model, *Phys. Rev. B* **86**, 205101 (2012).
- [193] N. Tsuji, M. Eckstein, and P. Werner, Nonthermal Antiferromagnetic Order and Nonequilibrium Criticality in the Hubbard Model, *Phys. Rev. Lett.* **110**, 136404 (2013).

- [194] N. D. Mermin and H. Wagner, Absence of Ferromagnetism or Antiferromagnetism in One- or Two-Dimensional Isotropic Heisenberg Models, *Phys. Rev. Lett.* **17**, 1133 (1966).
- [195] P. C. Hohenberg, Existence of Long-Range Order in One and Two Dimensions, *Phys. Rev.* **158**, 383 (1967).
- [196] P. Barmettler, M. Punk, V. Gritsev, E. Demler, and E. Altman, Quantum quenches in the anisotropic spin-Heisenberg chain: different approaches to many-body dynamics far from equilibrium, *New Journal of Physics* **12**, 055017 (2010).
- [197] M. Brockmann, B. Wouters, D. Fioretto, J. D. Nardis, R. Vlijm, and J.-S. Caux, Quench action approach for releasing the Néel state into the spin-1/2 XXZ chain, *Journal of Statistical Mechanics: Theory and Experiment* **2014**, P12009 (2014).
- [198] W. Liu and N. Andrei, Quench Dynamics of the Anisotropic Heisenberg Model, *Phys. Rev. Lett.* **112**, 257204 (2014).
- [199] M. Heyl, Dynamical Quantum Phase Transitions in Systems with Broken-Symmetry Phases, *Phys. Rev. Lett.* **113**, 205701 (2014).
- [200] M. Fagotti, M. Collura, F. H. L. Essler, and P. Calabrese, Relaxation after quantum quenches in the spin- $\frac{1}{2}$ Heisenberg XXZ chain, *Phys. Rev. B* **89**, 125101 (2014).
- [201] B. Wouters, J. De Nardis, M. Brockmann, D. Fioretto, M. Rigol, and J.-S. Caux, Quenching the Anisotropic Heisenberg Chain: Exact Solution and Generalized Gibbs Ensemble Predictions, *Phys. Rev. Lett.* **113**, 117202 (2014).
- [202] B. Pozsgay, M. Mestyán, M. A. Werner, M. Kormos, G. Zaránd, and G. Takács, Correlations after Quantum Quenches in the XXZ Spin Chain: Failure of the Generalized Gibbs Ensemble, *Phys. Rev. Lett.* **113**, 117203 (2014).
- [203] E. J. Torres-Herrera, M. Vyas, and L. F. Santos, General features of the relaxation dynamics of interacting quantum systems, *New Journal of Physics* **16**, 063010 (2014).
- [204] M. Rigol, V. Dunjko, V. Yurovsky, and M. Olshanii, Relaxation in a Completely Integrable Many-Body Quantum System: An *Ab Initio* Study of the Dynamics of the Highly Excited States of 1D Lattice Hard-Core Bosons, *Phys. Rev. Lett.* **98**, 050405 (2007).
- [205] S. Wall, D. Brida, S. R. Clark, H. P. Ehrke, D. Jaksch, A. Ardavan, S. Bonora, H. Uemura, Y. Takahashi, T. Hasegawa, H. Okamoto, G. Cerullo, and A. Cavalleri, Quantum interference between charge excitation paths in a solid-state Mott insulator, *Nat Phys* **7**, 114 (2011).
- [206] H. Ehrke, R. I. Tobey, S. Wall, S. A. Cavill, M. Först, V. Khanna, T. Garl, N. Stojanovic, D. Prabhakaran, A. T. Boothroyd, M. Gensch, A. Mirone, P. Reutler, A. Revcolevschi, S. S. Dhesi, and A. Cavalleri, Photoinduced Melting of Antiferromagnetic Order in $\text{La}_{0.5}\text{Sr}_{1.5}\text{MnO}_4$ Measured Using Ultrafast Resonant Soft X-Ray Diffraction, *Phys. Rev. Lett.* **106**, 217401 (2011).

- [207] L. Rettig, R. Cortés, S. Thirupathaiah, P. Gegenwart, H. S. Jeevan, M. Wolf, J. Fink, and U. Bovensiepen, Ultrafast Momentum-Dependent Response of Electrons in Antiferromagnetic EuFe_2As_2 Driven by Optical Excitation, *Phys. Rev. Lett.* **108**, 097002 (2012).
- [208] G. Vidal, Classical Simulation of Infinite-Size Quantum Lattice Systems in One Spatial Dimension, *Phys. Rev. Lett.* **98**, 070201 (2007).
- [209] T. Giamarchi, *Quantum Physics in One Dimension* (Oxford University Press, 2003).
- [210] G. D. Chiara, S. Montangero, P. Calabrese, and R. Fazio, Entanglement entropy dynamics of Heisenberg chains, *Journal of Statistical Mechanics: Theory and Experiment* **2006**, P03001 (2006).
- [211] P. Calabrese and J. Cardy, Entanglement and correlation functions following a local quench: a conformal field theory approach, *J. Stat. Mech.* (2007), P10004.
- [212] L. F. Santos and M. Rigol, Onset of quantum chaos in one-dimensional bosonic and fermionic systems and its relation to thermalization, *Phys. Rev. E* **81**, 036206 (2010).
- [213] A. Bauer, *Relaxationsdynamik im eindimensionalen Fermi-Hubbard Modell*, Bachelor thesis, Ludwig-Maximilians-Universität München (2014).
- [214] M. Takahashi, Magnetic Susceptibility for the Half-Filled Hubbard Model, *Progress of Theoretical Physics* **43**, 1619 (1970).
- [215] R. Preuss, A. Muramatsu, W. von der Linden, P. Dieterich, F. F. Assaad, and W. Hanke, Spectral Properties of the One-Dimensional Hubbard Model, *Phys. Rev. Lett.* **73**, 732 (1994).
- [216] F. H. L. Essler, H. Frahm, F. Göhmann, A. Klümper, and V. E. Korepin, *The One-Dimensional Hubbard Model* (Cambridge University Press, Cambridge, 2005).
- [217] N. Strohmaier, D. Greif, R. Jördens, L. Tarruell, H. Moritz, T. Esslinger, R. Sensarma, D. Pekker, E. Altman, and E. Demler, Observation of Elastic Doublon Decay in the Fermi-Hubbard Model, *Phys. Rev. Lett.* **104**, 080401 (2010).
- [218] E. V. Gorelik, I. Titvinidze, W. Hofstetter, M. Snoek, and N. Blümer, Néel Transition of Lattice Fermions in a Harmonic Trap: A Real-Space Dynamic Mean-Field Study, *Phys. Rev. Lett.* **105**, 065301 (2010).
- [219] E. V. Gorelik, D. Rost, T. Paiva, R. Scalettar, A. Klümper, and N. Blümer, Universal probes for antiferromagnetic correlations and entropy in cold fermions on optical lattices, *Phys. Rev. A* **85**, 061602 (2012).
- [220] M. Serbyn, Z. Papić, and D. A. Abanin, Local Conservation Laws and the Structure of the Many-Body Localized States, *Phys. Rev. Lett.* **111**, 127201 (2013).
- [221] R. Vosk and E. Altman, Many-Body Localization in One Dimension as a Dynamical Renormalization Group Fixed Point, *Phys. Rev. Lett.* **110**, 067204 (2013).
- [222] A. C. Potter, R. Vasseur, and S. A. Parameswaran, Universal Properties of Many-Body Delocalization Transitions, *Phys. Rev. X* **5**, 031033 (2015).

- [223] R. Vosk, D. A. Huse, and E. Altman, Theory of the Many-Body Localization Transition in One-Dimensional Systems, *Phys. Rev. X* **5**, 031032 (2015).
- [224] M. Serbyn, Z. Papić, and D. A. Abanin, Criterion for Many-Body Localization-Delocalization Phase Transition, *Phys. Rev. X* **5**, 041047 (2015).
- [225] L. Zhang, B. Zhao, T. Devakul, and D. A. Huse, Many-body localization phase transition: A simplified strong-randomness approximate renormalization group, *Phys. Rev. B* **93**, 224201 (2016).
- [226] V. Khemani, S. P. Lim, D. N. Sheng, and D. A. Huse, Critical Properties of the Many-Body Localization Transition, arXiv:1607.05756 [cond-mat.dis-nn] (2016).
- [227] M. Serbyn, Z. Papić, and D. A. Abanin, Thouless energy and multifractality across the many-body localization transition, arXiv:1610.02389 [cond-mat.dis-nn] (2016).
- [228] J. A. Kjäll, J. H. Bardarson, and F. Pollmann, Many-Body Localization in a Disordered Quantum Ising Chain, *Phys. Rev. Lett.* **113**, 107204 (2014).
- [229] Y. Bar Lev, G. Cohen, and D. R. Reichman, Absence of Diffusion in an Interacting System of Spinless Fermions on a One-Dimensional Disordered Lattice, *Phys. Rev. Lett.* **114**, 100601 (2015).
- [230] W. De Roeck, F. Huveneers, M. Müller, and M. Schiulaz, Absence of many-body mobility edges, *Phys. Rev. B* **93**, 014203 (2016).
- [231] B. Bauer and C. Nayak, Area laws in a many-body localized state and its implications for topological order, *Journal of Statistical Mechanics: Theory and Experiment* **2013**, P09005 (2013).
- [232] M. Friesdorf, A. H. Werner, W. Brown, V. B. Scholz, and J. Eisert, Many-Body Localization Implies that Eigenvectors are Matrix-Product States, *Phys. Rev. Lett.* **114**, 170505 (2015).
- [233] M. Schreiber, S. S. Hodgman, P. Bordia, H. P. Lüschen, M. H. Fischer, R. Vosk, E. Altman, U. Schneider, and I. Bloch, Observation of many-body localization of interacting fermions in a quasirandom optical lattice, *Science* **349**, 842 (2015).
- [234] S. S. Kondov, W. R. McGehee, W. Xu, and B. DeMarco, Disorder-Induced Localization in a Strongly Correlated Atomic Hubbard Gas, *Phys. Rev. Lett.* **114**, 083002 (2015).
- [235] P. Bordia, H. P. Lüschen, S. S. Hodgman, M. Schreiber, I. Bloch, and U. Schneider, Coupling Identical one-dimensional Many-Body Localized Systems, *Phys. Rev. Lett.* **116**, 140401 (2016).
- [236] J.-y. Choi, S. Hild, J. Zeiher, P. Schauß, A. Rubio-Abadal, T. Yefsah, V. Khemani, D. A. Huse, I. Bloch, and C. Gross, Exploring the many-body localization transition in two dimensions, *Science* **352**, 1547 (2016).
- [237] J. Smith, A. Lee, P. Richerme, B. Neyenhuis, P. W. Hess, P. Hauke, M. Heyl, D. A. Huse, and C. Monroe, Many-body localization in a quantum simulator with programmable random disorder, *Nat Phys* **12**, 907 (2016).

- [238] P. Bordia, H. Lüschen, U. Schneider, M. Knap, and I. Bloch, Periodically Driving a Many-Body Localized Quantum System, arXiv:1607.07868 [cond-mat.quant-gas] (2016).
- [239] V. Ros, M. Müller, and A. Scardicchio, Integrals of motion in the many-body localized phase, Nuclear Physics B **891**, 420 (2015).
- [240] G. F. Giuliani and G. Vignale, *Quantum Theory of the Electron Liquid* (Cambridge University Press, New York, 2005).
- [241] S. Nishimoto, Tomonaga-Luttinger-liquid criticality: Numerical entanglement entropy approach, Phys. Rev. B **84**, 195108 (2011).
- [242] N. Mott, Introductory talk; Conduction in non-crystalline materials, Journal of Non-Crystalline Solids **8**, 1 (1972).
- [243] B. I. Shklovskii and A. L. Efros, *Electronic Properties of Doped Semiconductors* (Springer, Berlin, 1984).

Acknowledgements

This thesis would not be possible without the support of many people. I want to specially thank

- My PhD advisor PD Fabian Heidrich-Meisner who gave me the opportunity to work as a PhD student in Munich. With the right advice at the right time along with encouragement and, sometimes, demand he was a great advisor.
- Dr. Lev Vidmar for valuable and long discussions on polaron physics along with a lot of advice and a great collaboration on the projects we worked on together.
- Prof. Dr. Eric Jeckelmann and Christoph Brockt for the fruitful collaboration and many meetings and discussions during the last three years.
- Claudius Hubig for many discussions about tensors, algorithms and how to get the most out of both.
- My officemate Dr. Jacopo Nespolo, Jan Stolpp and Jonas Greitemann for many discussions and for proofreading parts of this thesis.
- Cordula Weber for her help with administrative duties and many nice conversations.
- Sabrina and my family who have always supported me.

